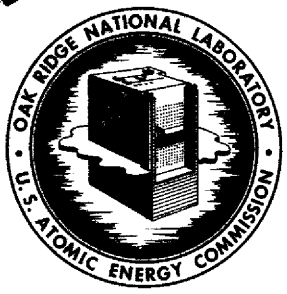

OAK RIDGE NATIONAL LABORATORY
operated by
UNION CARBIDE CORPORATION
for the
U.S. ATOMIC ENERGY COMMISSION

ORNL - TM - 730

100

MSRE DESIGN AND OPERATIONS REPORT

PART III. NUCLEAR ANALYSIS

P. N. Haubenreich
J. R. Engel
B. E. Prince
H. C. Claiborne

ORNL TM-730

Contract No. W-7405-eng-26

MSRE DESIGN AND OPERATIONS REPORT

PART III. NUCLEAR ANALYSIS

P. N. Haubenreich
J. R. Engel
B. E. Prince
H. C. Claiborne

DATE ISSUED

FEB - 3 1964

OAK RIDGE NATIONAL LABORATORY
Oak Ridge, Tennessee
operated by
UNION CARBIDE CORPORATION
for the
U.S. ATOMIC ENERGY COMMISSION

PREFACE

This report is one of a series of reports that describe the design and operation of the Molten-Salt Reactor Experiment. All the reports are listed below. The design and safety analysis reports (ORNL TM-728 and ORNL TM-732) should be issued by spring of 1964, and the others should be issued in the summer of 1964.

ORNL TM-728	MSRE Design and Operations Report, Part I, Description of Reactor Design, by R. C. Robertson.
ORNL TM-729	MSRE Design and Operations Report, Part II, Nuclear and Process Instrumentation, by J. R. Tallackson.
ORNL TM-730*	MSRE Design and Operations Report, Part III, Nuclear Analysis, by P. N. Haubenreich and J. R. Engel.
ORNL TM-731	MSRE Design and Operations Report, Part IV, Chemistry and Materials, by F. F. Blankenship and A. Taboada.
ORNL TM-732	MSRE Design and Operations Report, Part V, Safety Analysis Report, by S. E. Beall.
ORNL TM-733	MSRE Design and Operations Report, Part VI, Operating Limits, by S. E. Beall.
**	MSRE Design and Operations Report, Part VII, Fuel Handling and Processing Plant, by R. B. Lindauer.
**	MSRE Design and Operations Report, Part VIII, Operating Procedures, by R. H. Guymon.
**	MSRE Design and Operations Report, Part IX, Safety Procedures and Emergency Plans, by R. H. Guymon.
**	MSRE Design and Operations Report, Part X, Maintenance Equipment and Procedures, by E. C. Hise.
**	MSRE Design and Operations Report, Part XI, Test Program, by R. H. Guymon and P. N. Haubenreich.
**	MSRE Design and Operations Report, Part XII, Lists: Drawings, Specifications, Line Schedules, Instrument Tabulations (Vols 1 and 2).

*Issued.

**These reports will be the last in the series to be published; report numbers will be given them at that time.

CONTENTS

MSRE DESIGN AND OPERATIONS REPORT

PART III. NUCLEAR ANALYSIS

P. N. Haubenreich
J. R. Engel
B. E. Prince
H. C. Claiborne

ABSTRACT

Preliminary considerations of the effects of core size and fuel-to-moderator ratio on critical mass and fuel concentration led to the specification of a core about 4.5 ft in diameter by 5.5 ft high for the MSRE. The average fuel fraction was set at 0.225, as a compromise between minimizing the critical mass and minimizing the reactivity effects of fuel-salt permeation of the bare graphite moderator.

The nuclear characteristics of the reactor were examined for three combinations of fissile and fertile material (UF_4 and ThF_4) in a molten carrier salt composed of lithium, beryllium, and zirconium fluorides. Fuel A contained ThF_4 (~1 mole %) and highly (~93%) enriched uranium (~0.3 mole %); fuel B contained highly enriched uranium (~0.2 mole %) and no fertile material; and fuel C contained uranium at 35% enrichment (~0.8 mole %) and no thorium. The radial distribution of the thermal neutron flux is strongly influenced by the presence of three control-rod thimbles near the axis of the core, with the result that the radial thermal flux maximum occurs about 8 in. from the axis. The axial distribution is essentially sinusoidal. The magnitude of the thermal flux depends on the choice of the fuel; the maximum varies from 5.6×10^{13} neutrons cm^{-2} sec^{-1} for fuel B (at 10 Mw thermal) to 3.3×10^{13} for fuels A and C. Both the fuel and the moderator temperature coefficients of reactivity are substantially negative, leading to prompt and delayed negative power coefficients. Reactivity coefficients were also calculated for changes in uranium concentration, Xe^{135} concentration, and fuel-salt and graphite densities.

Temperature distributions in the fuel and graphite in the reactor were calculated for the design power level. With the fuel inlet and outlet temperatures at 1175 and 1225°F, respectively, the fuel and graphite reactivity-weighted average temperatures are 1211 and 1255°F, respectively. Fuel permeation of 2% of the graphite volume would increase the graphite weighted average temperature by 7°F. The power coefficient of reactivity with the reactor outlet temperature held constant is −0.006 to −0.008% δk/k per Mw.

Circulation of the fuel at 1200 gpm reduces the effective delayed neutron fraction from 0.0067 to 0.0036.

Xenon poisoning is strongly dependent on the major competing mechanisms of stripping from the fuel in the pump bowl and transfer into the bare graphite. The equilibrium poisoning at 10 Mw is expected to be between −1.0 and −1.7% δk/k.

The fuel contains an inherent neutron source of over 10^5 n/sec due to α,n reactions in the salt. This meets all the safety requirements of a source, but an external source will be increase the flux for convenient monitoring of the subcritical reactivity.

The total worth of the three control rods ranges from 5.6 to 7.6% δk/k, depending on the fuel salt composition. Shutdown margins at 1200°F are 3.5% δk/k or more in all cases. One rod will be used as a regulating rod to control the flux level at low power and the core outlet temperature at high power. In general, the reactor is self-regulating with respect to changes in power demand because of the negative temperature coefficients of reactivity. However, the degree of self regulation is poorer at lower powers because of the low power density and high heat capacity of the system. The control rods are used to improve the power regulation as well as to compensate for reactivity transients due to xenon, samarium, power coefficient, and short-term burnup.

Calculations were made for conceivable reactivity accidents involving uncontrolled control-rod withdrawal, "cold slugs," abnormal fuel additions, loss of graphite, abnormal filling of the reactor, and primary flow stoppage. No intolerable conditions are produced if the reactor safety system (rod drop at 150% of design power) functions for two of the three control rods.

The biological shield, with the possible addition of stacked concrete blocks in some areas, reduces the calculated radiation dose rates to permissible levels in all accessible areas.

1. INTRODUCTION

The design of the MSRE and the plans for its operation require information on critical fuel concentration, reactivity control, kinetics of the chain reaction, nuclear heat sources, radiation sources and levels, activation, and shielding. This part on Nuclear Analysis deals with these topics. Its purpose is to describe fully the nuclear characteristics of the final design of the MSRE and, to some extent, to show the basis for choosing this design. Methods and data used in the calculations are described briefly. Detailed descriptions of the calculations and the sources of the basic data can be found in reports which are cited.

2. PRELIMINARY STUDIES OF CORE PARAMETERS

2.1 Introduction

The original concept of the MSRE core was a cylindrical vessel containing a graphite moderator with small channels through which circulated a molten-salt fuel. During the early stages of MSRE design, the nuclear effects of two important core parameters were surveyed. These were the overall dimensions of the core and the ratio of fuel to graphite in the core. Most of the calculations were for one-region cores, but some calculations were made for cores consisting of two or three concentric regions of differing volume fractions. Critical concentration and inventory of U^{235} and the important coefficients of reactivity were the bases for comparison and for choice of the final design parameters.

Some calculations were made for an alternative core design in which the fuel circulated through INOR-8 tubes in a graphite core. The nuclear characteristics of the reactor were calculated for several combinations of tube diameter and thickness.

All of these computations were performed on the IBM 704, using GNU, a multigroup, diffusion theory code.[1] Data from BNL-325 (ref 2) were used in preparing 34-group cross sections for the computations.[3] The cross sections were averaged over a 1/E spectrum within each group. Those used for thorium and U^{238} in the resonance energy ranges were appropriate for infinite dilution in a moderator, and a temperature of 1200°F was assumed in determining the cross sections for the thermal and last epithermal groups. In all of the calculations except some of those for tubed cores, the core materials were assumed to be homogeneously mixed within a region.

2.2 Effect of Core Size[4]

The effect of core size was explored for cores containing 8 vol % fuel salt having the density and the nominal composition listed for fuel I in Table 2.1. Atomic densities of the constituents other than uranium were computed from this specification, and the GNU code was used to compute the critical concentration of uranium. A graphite density of 1.90 g/cc was assumed.

Table 2.1. Nominal Fuel Compositions and Densities Used in MSRE Survey Calculations

Fuel type		I	II	III
Composition (mole %)	LiF[a]	64	64	70
	BeF_2	31	31	23
	ThF_4	4	0	1
	ZrF_4	0	4	5
	UF_4[b]	1	1	1
Density (g/cc)		2.2	2.2	2.47

[a] 0.003% Li^6, 99.997% Li^7.
[b] 93.5% U^{235}, 6.5% U^{238}.

Computations were made for cores 5.5 and 10 ft high and 3.5, 4.0, 4.5, and 5.0 ft in diameter. Figure 2.1 shows critical concentrations of uranium obtained by these calculations. Also shown in Fig. 2.1 are values of critical mass. These are the masses of U^{235} in a core of the nominal dimensions. (A zero extrapolation distance was assumed.)

2.3 Effect of Volume Fraction in One-Region Cores

2.3.1 First Study[4]

The first survey of the effect of varying volume fraction in a one-region core was for a core 4.5 ft in diameter and 5.5 ft high. Five different fuel volume fractions, ranging from 0.08 to 0.16, were considered. The critical concentrations of uranium were computed, and these were used with the fuel volume fraction and the nominal core dimensions to compute critical masses of U^{235}. Total inventories of U^{235} were also computed, assuming that an additional 46 ft^3 of fuel is required outside the core.

One set of calculations was made with fuel I of Table 2.1. In these calculations the graphite density was assumed to be 1.90 g/cc. Results are shown in Fig. 2.2 by the curves labeled "Composition A."

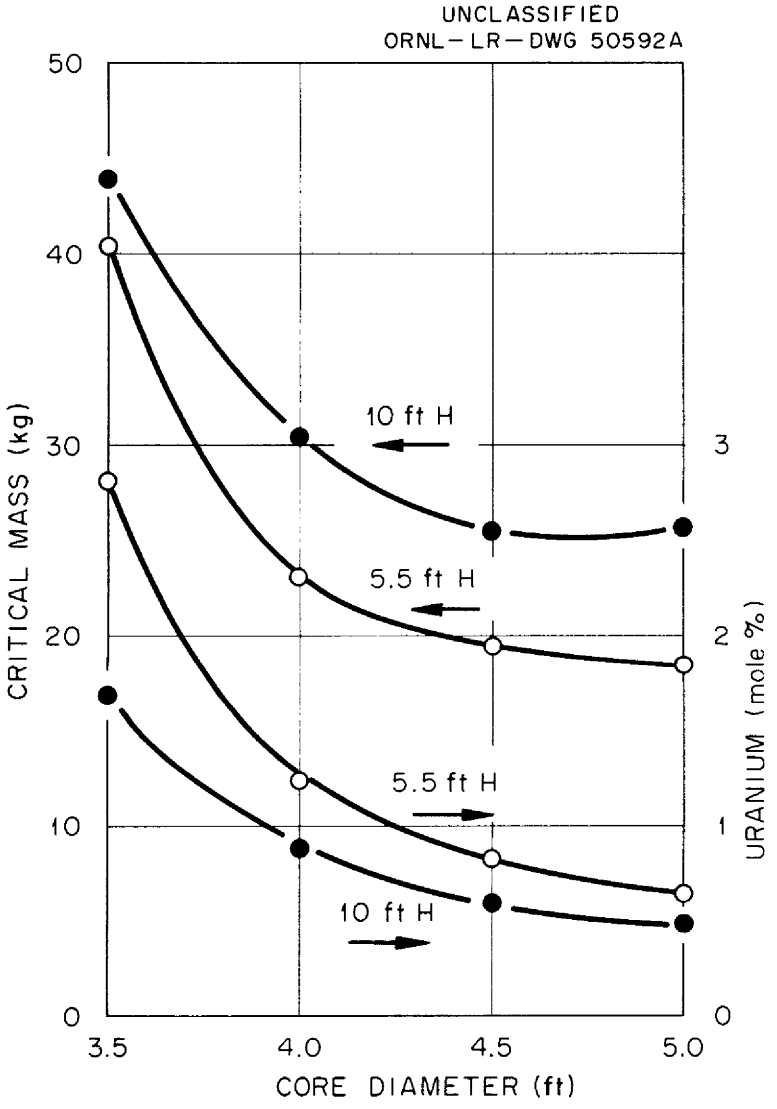

Fig. 2.1. Critical Concentration and Mass as a Function of Core Size.

A similar set of calculations was made with fuel II of Table 2.1, with the results shown in Fig. 2.2 by the curves labeled "Composition B." Not all of the differences in the two sets of curves are attributable to the substitution of zirconium for the thorium in the fuel salt, because a different graphite density, 1.96 g/cc, was used in the calculations for fuel II, which would reduce critical concentrations for this case.

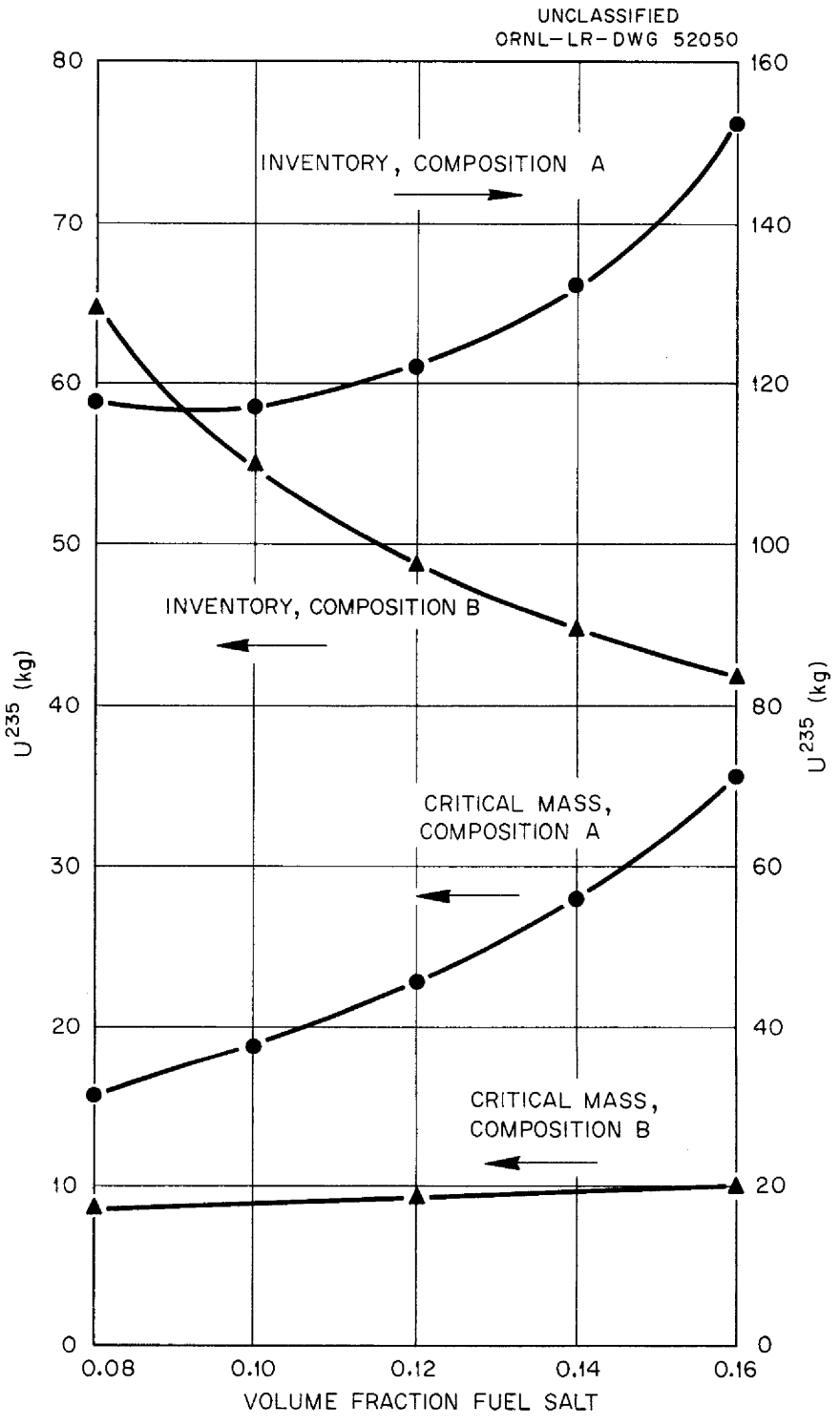

Fig. 2.2. Critical Mass and Total Inventory of U^{235} as Functions of Fuel Volume Fraction, Calculated for Early Fuels.

2.3.2 Second Study[5,6]

After mechanical design and chemistry studies had led to firmer values for the core vessel dimensions and the fuel composition, another study was made of the effect of fuel volume fraction, the results to be used in specifying the fuel channel dimensions. Core dimensions were 27.7-in. radius and 63-in. height, with extrapolation distances of 1 in. on the radius and 3.5 in. on each end added for the criticality calculations. Fuel III of Table 2.1 was used, and a graphite density of 1.90 g/cc was assumed. Fuel volume fractions from 0.08 to 0.28 were considered.

Calculated critical concentrations of uranium are shown in Fig. 2.3. Also shown are inventories of U^{235}, based on a fuel volume of 38.4 ft^3

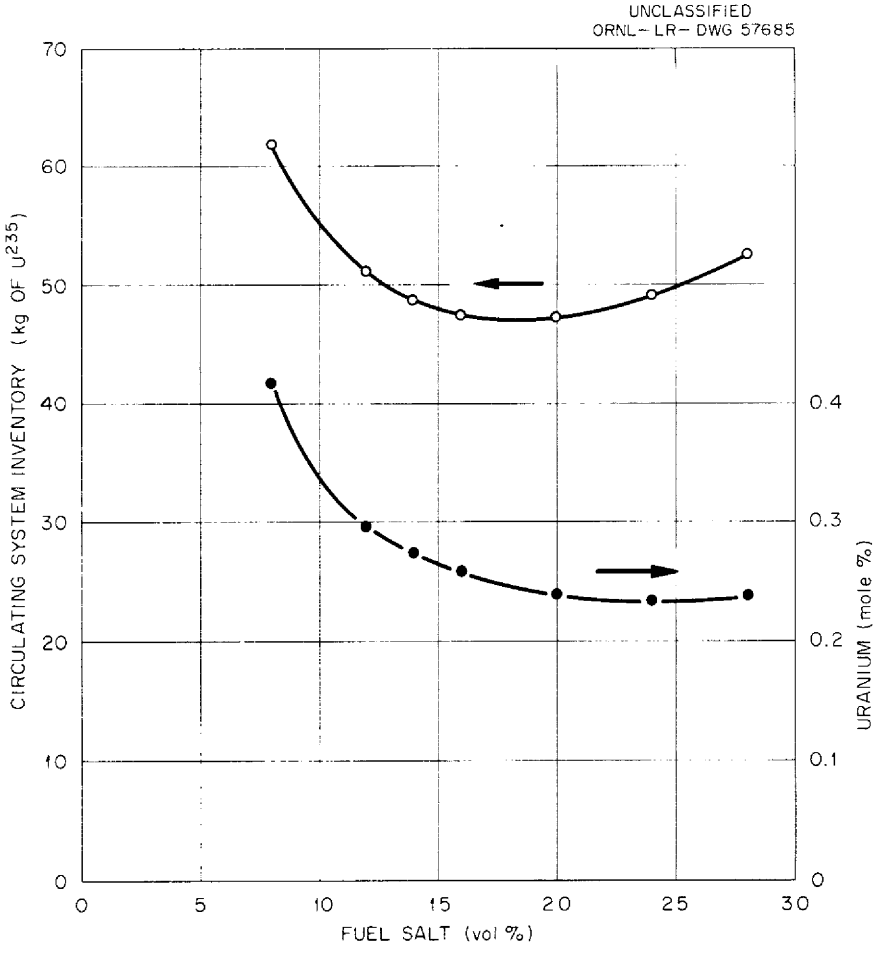

Fig. 2.3. Effect of Fuel Volume Fraction on Critical Concentration and Inventory.

external to the core. The GNU results were also used to compute the reactivity changes resulting from fuel temperature changes and from the permeation of 7% of the graphite volume by fuel salt.* Results are summarized in Table 2.2.

2.4 Two- and Three-Region Cores[5,6]

2.4.1 Channeled Graphite Cores

One way of reducing the critical mass is to use a nonuniform distribution of fuel in the core, with the fuel more concentrated near the

*This fraction was at that time the estimated fraction of the graphite volume accessible to kerosene.

Table 2.2. Effect of Fuel Volume Fraction on Nuclear Characteristics of MSRE[a]

Fuel fraction (vol %)	12	14	16	20	24	28
Critical fuel conc. (mole % U)	0.296	0.273	0.257	0.238	0.233	0.236
Critical mass (kg of U^{235})	11.0	11.8	12.7	14.8	17.4	20.5
System[b] U^{235} inventory (kg)	51.0	48.6	47.4	47.1	48.7	52.4
Fuel temp. coeff. $\times 10^5$ [$(\delta k/k)/°F$]	−3.93	−3.83	−3.70	−3.44	−3.16	−2.86
Permeation effect[c] (% $\delta k/k$)	11.4	9.7	8.3	6.1	4.6	3.5

[a]Core dimensions: 27.7-in. radius, 63-in. height,
Nominal composition of fuel: $LiF-BeF_2-ZrF_4-ThF_4-UF_4$, 70-23-5-1-1 mole %,
Temperature: 1200°F,
Fuel density: 2.47 g/cc,
Graphite density: 1.90 g/cc.

[b]Core plus 38.4 ft^3 of fuel.

[c]Permeation by fuel salt of 7% of graphite volume.

center. This could be done in the MSRE by designing the graphite pieces to give a greater fuel volume fraction toward the center of the core. A reduction in critical mass, if accompanied by an increase in the concentration of U^{235} in the fuel salt, does not necessarily imply a reduction in fissile material inventory in the MSRE because most of the fuel is external to the core.

In order to explore the effects of nonuniform fuel distribution in the MSRE, a set of calculations was made in which the core was subdivided into either two or three regions with different fuel volume fractions. Fuel III of Table 2.1 and graphite having a density of 1.90 g/cc were assumed. Overall dimensions of the core were taken to be 27.7-in. radius and 63-in. height. Radial and axial extrapolation distances of 1 and 3.5 in. were added to these dimensions. The critical fuel concentration, the core inventory (or critical mass), and the total inventory were computed. Flux and power distributions were also obtained.

Three cases of two-region cores were considered. In each the core consisted of two concentric cylindrical regions, with the inner containing 24 vol % fuel and the outer, 18 vol % fuel. Results are summarized in Table 2.3.

Table 2.3. Some Characteristics of Two-Region Reactors

Volume Ratio[a]	Critical Fuel Concentration (mole % U)	Critical Mass (kg of U^{235})	System[b] Inventory (kg of U^{235})
50/50	0.232	15.1	46.5
60/40	0.234	15.7	47.4
70/30	0.236	16.3	48.4

[a]Ratio of inner region (24 vol % fuel) to outer region (18 vol % fuel).

[b]Including 38.4 ft^3 external to the core.

In the three-region cases the core was divided into concentric regions of equal volume. Thirteen cases were calculated, with the results shown in Table 2.4. Although the critical mass was markedly reduced in some cases, this was accompanied by a higher fuel concentration, which raised the fissile material inventory external to the core. As a result, in no case was the total inventory greatly reduced below the minimum for one-region cores.

The heat generation per unit volume of fuel follows closely the shape of the thermal neutron flux in all cases. Table 2.4 shows that the ratio of radial peak to average thermal neutron flux was significantly reduced in some cases. (For a uniform core the ratio is 2.32.) The effect on flux shape is illustrated for some of the cases in Fig. 2.4.

Table 2.4. Some Characteristics of Three-Region Reactors

Fuel Fraction[a] (vol %)	Critical Fuel Concentration (mole % U)	Critical Mass (kg of U^{235})	System[b] Inventory (kg of U^{235})	Thermal Flux Ratio, Radial Peak/Av
25, 13, 7	0.243	11.3	44.2	1.86
40, 13, 7	0.273	16.9	53.8	1.45
10, 13, 7	0.324	10.1	54.0	2.38
25, 20, 7	0.237	12.8	45.1	2.03
25, 6, 7	0.257	10.1	44.9	1.69
25, 13, 10	0.243	12.0	44.8	1.89
25, 13, 4	0.243	10.5	43.3	1.84
40, 20, 7	0.272	18.8	55.6	1.48
10, 6, 7	0.361	8.6	57.5	2.18
25, 20, 10	0.237	13.5	45.7	2.06
25, 6, 4	0.258	9.3	44.2	1.66
40, 13, 10	0.273	17.8	54.8	1.45
10, 13, 4	0.325	9.1	53.0	2.35

[a] In inner, middle, and outer concentric regions of equal volume.

[b] Including 38.4 ft^3 external to the core.

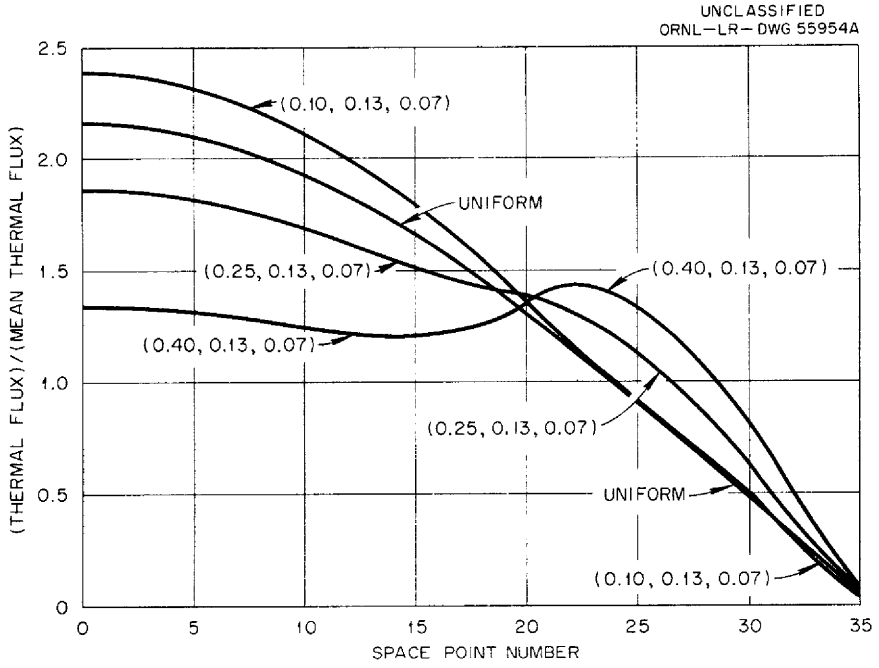

Fig. 2.4. Comparison of Thermal Flux Shapes in Three-Region Reactors. Numbers in parentheses refer to fuel volume fraction in inner, middle, and outer region of reactor, respectively.

Table 2.5. Characteristics of Cores with Lumped Moderator

Moderator	Critical Concentration (mole % U)	Critical Mass (kg of U^{235})
5-in. Reflector Thickness, No Island		
Graphite	1.04	250
Be	0.72	175
BeO	0.76	186
10-in. Reflector Thickness, 1-ft-diam Island		
Graphite	0.67	93
Be	0.25	34
BeO	0.28	39

2.4.2 Cores with Moderator in Reflector and Island[6]

Brief consideration was given to a core which was essentially one large fuel channel, with the moderator confined to a surrounding region

and a central island. Calculations for this type of core were made as an adjunct to those for the multiregion, channeled graphite cores, using the same fuel and overall core dimensions. Three moderators were considered: graphite (ρ = 1.90 g/cc), beryllium (ρ = 1.84 g/cc), and beryllium oxide (ρ = 2.90 g/cc). Typical results are given in Table 2.5.

2.5 Cores Containing INOR-8 Tubes

Nuclear characteristics were also computed for cores in which the fuel was contained in tubes of INOR-8 passing through the core. The preliminary calculations for this type of core treated the fuel, graphite, and INOR-8 of the core as a homogeneous mixture. Results of these calculations were reported in MSRP progress reports.[6,7] In later calculations, hitherto unreported, the GNU code was used to calculate flux distributions and disadvantage factors in a typical cell of fuel, INOR-8, and graphite. When the heterogeneity of the core was taken into account, calculated critical concentrations were increased over those from the homogeneous approximation. Results of the heterogeneous calculations are given in Table 2.6.

2.6 Conclusions

At a very early stage of the design it was decided that the core would be approximately 4.5 ft in diameter and 5.5 ft high after some calculations showed that the critical mass was relatively insensitive to core dimensions around this point (Fig. 2.1).

The volume fraction of fuel in the core was set at 0.225 after calculations showed that a fraction of 0.24 gave the lowest critical concentration of uranium and that the reactivity increase due to fuel permeation of the graphite was much lower around this point than at lower volume fractions. (Four half-channels 0.2- by 1.2-in. in each 2- by 2-in. graphite block were chosen to give a fuel fraction of 0.24; rounding the corners of the channels reduced the fraction to 0.225.)

Only brief consideration was given to cores of two or three regions with differing volume fractions, because calculations showed these had little, if any, advantage over the uniform, one-region core.

Table 2.6. Some Characteristics of Cores with INOR-8 Tubes

Fuel fraction (vol %)	10	10	10	14	14	14	18	18	18
Tube thickness (mil)	40	60	80	40	60	80	40	60	80
Critical fuel conc. (mole % U)	0.74	0.96	1.22	0.64	0.86	1.12	0.62	0.86	1.15
System U^{235} inventory (kg)	128	165	210	118	158	206	122	169	226
Neutron Balance									
Absorptions: INOR	8.7	10.9	12.5	10.7	12.3	13.8	10.6	12.8	14.1
graphite + salt	2.9	2.5	2.1	2.5	2.0	1.7	2.2	1.7	1.4
U^{235}	50.4	50.9	51.3	50.9	51.5	52.2	51.5	52.3	53.3
U^{238}	0.4	0.5	0.6	0.5	0.6	0.7	0.6	0.8	0.9
Th	3.0	2.7	2.5	4.1	3.7	3.3	5.0	4.4	4.0
Fast leakage	24.9	24.5	24.1	24.4	24.5	24.0	25.1	24.4	23.6
Slow leakage	9.7	8.0	6.9	6.9	5.4	4.3	5.0	3.6	2.7

Note: Core radius, 27.7 in.; core height, 63 in.; fuel volume external to core, 40 ft^3; nominal fuel composition, $LiF-BeF_2-ZrF_4-ThF_4-UF_4$, 70-23-5-1-1 mole %; tube OD, 3 in.

3. CRITICALITY, FLUX DISTRIBUTIONS, AND REACTIVITY COEFFICIENTS

3.1 Description of Core

The final design of the core and reactor vessel is shown in the cutaway view in Fig. 3.1. Fuel salt, after entering through a flow distributor, passes down through an annular region between the INOR-8 vessel and the INOR-8 core can to the lower head. The lower head contains anti-swirl vanes which direct the flow inward and a moderator support grid, both of INOR-8. The fuel flows from the lower head up through a lattice of horizontal graphite sticks, through the channeled region of the core and into the upper head. The channeled region of the core consists of 2-in.-square, vertical graphite stringers, with half-channels machined in each face to provide fuel passages. The regular pattern is broken near the axis of the core, where three control rod thimbles and a graphite sample assembly are located. Figure 3.2 shows a typical fuel channel and the section around the core axis.

3.2 Calculational Model of Core

Critical fuel concentrations, flux and power distributions, and reactivity coefficients were calculated for the reactor, taking into account as much detail as was practical. The actual core configuration was represented for the nuclear calculations by a two-dimensional, 20-region model in r-z geometry (cylindrical with angular symmetry). This model is shown in vertical section in Fig. 3.3, indicating the relative sizes and positions of the regions within which the material composition was considered to be uniform. The region boundaries and the volume fractions of fuel, graphite, and INOR-8 in each region are summarized in Table 3.1. The boundaries of each of these "macroscopic" regions were chosen to represent as closely as possible those gross geometrical and material properties which determine the neutron transport in the core. This choice was made within the practical limitations on the number of dimensions and mesh points in the numerical calculations.

Use of two-dimensional geometry resulted in a large saving in computing time, and was considered an adequate representation for most purposes. The major approximation involved was in the representation of the

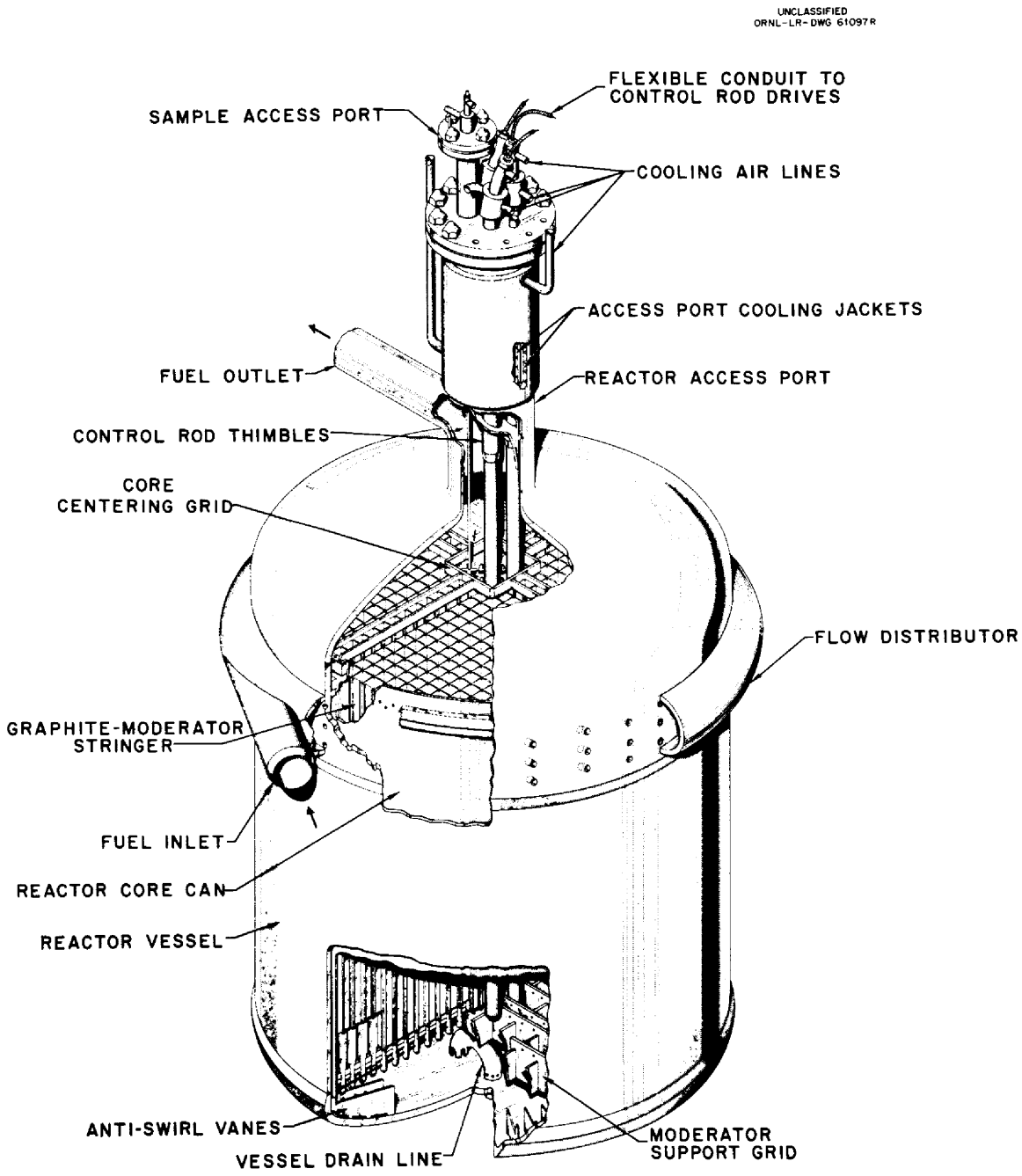

Fig. 3.1. Cutaway Drawing of MSRE Core and Core Vessel.

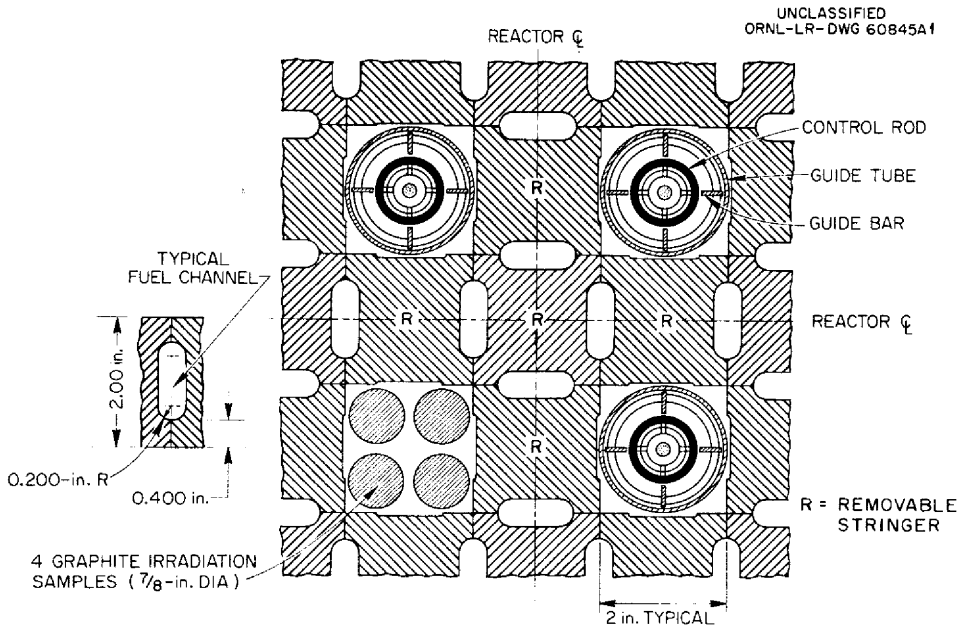

Fig. 3.2. MSRE Control Rod Arrangement and Typical Fuel Channel.

small central region of the core which includes the three control rod thimbles and the graphite specimens. The model contains the same amounts of fuel, graphite, and INOR-8 as the actual core, but the arrangement is necessarily different. The INOR-8 is of the thimbles represented by a 0.10-in.-thick, 6.00-in.-OD annulus, which has a volume and an outside surface area equal to those of the INOR-8 of the three thimbles. Just inside the INOR-8 annulus is a region containing low-density fuel, representing a mixture of the voids inside the thimbles and the extra fuel surrounding the thimbles and the specimens. At the center of the core is a cylinder of normal core composition (0.255 fuel, 0.775 graphite by volume).

Other assumptions made in the calculations are that the temperature is uniform at 1200°F, that there is no permeation of the graphite by the fuel, and that there are no fission product poisons in the core. The graphite was assumed to be pure carbon, with a density of 1.86 g/cc. Reactivity effects due to deviations from these assumptions were tested as perturbations, as described later in this chapter.

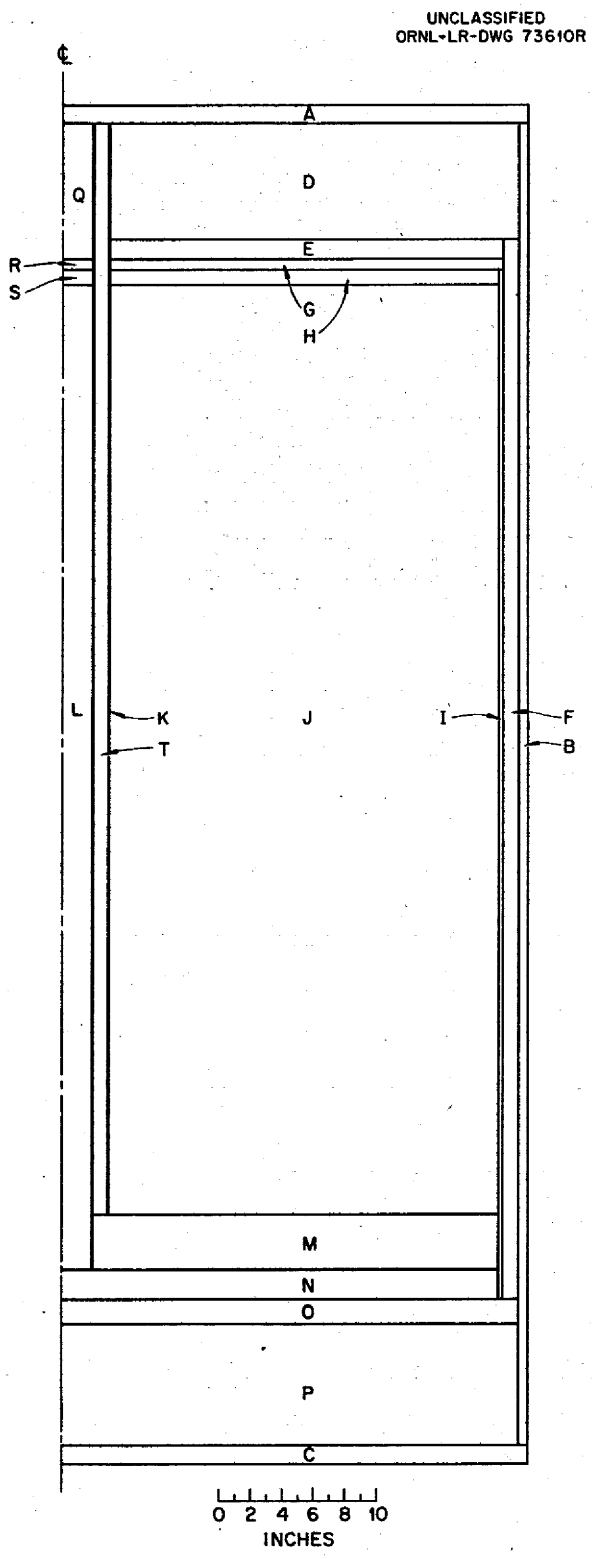

Fig. 3.3. Twenty-Region Core Model for Nuclear Calculations. See Table 3.1 for explanation of letters.

Table 3.1. Twenty-Region Model of MSRE Core Used in Nuclear Calculations
(See Fig. 3.3 for graphical location of regions)

Region	Radius (in.)		Height (in.)		Composition (vol %)			Region Represented
	Inner	Outer	Bottom	Top	Fuel	Graphite	INOR-8	
A	0	29.56	74.92	76.04	0	0	100	Vessel top
B	29.00	29.56	-9.14	74.92	0	0	100	Vessel side
C	0	29.56	-10.26	-9.14	0	0	100	Vessel bottom
D	3.00	29.00	67.47	74.92	100	0	0	Upper head
E	3.00	28.00	66.22	67.47	93.7	3.5	2.8	
F	28.00	29.00	0	67.47	100	0	0	Downcomer
G	3.00	28.00	65.53	66.22	94.6	5.4	0	
H	3.00	27.75	64.59	65.53	63.3	36.5	0.2	
I	27.75	28.00	0	65.53	0	0	100	Core can
J	3.00	27.75	5.50	64.59	22.5	77.5	0	Core
K	2.90	3.00	5.50	74.92	0	0	100	Simulated thimbles
L	0	1.94	2.00	64.59	22.5	77.5	0	Central region
M	1.94	27.75	2.00	5.50	22.5	77.5	0	Core
N	0	27.75	0	2.00	23.7	76.3	0	Horizontal stringers
O	0	29.00	-1.41	0	66.9	15.3	17.8	
P	0	29.00	-9.14	-1.41	90.8	0	9.2	Bottom head
Q	0	1.94	66.22	74.92	100	0	0	
R	0	1.94	65.53	66.22	89.9	10.1	0	
S	0	1.94	64.59	65.53	43.8	56.2	0	
T	1.94	2.90	5.50	74.92	100[a]	0	0	Fuel and voids

[a]Density, 0.46 × density of normal fuel.

3.3 Fuel Properties

The nuclear characteristics of the reactor were calculated for three different fuel salts, described in Table 3.2. (Uranium concentrations are approximate, based on initial estimates of concentrations required for criticality. The exact critical concentrations are given in Sec 3.9.)

3.4 Cross Sections and Effects of Inhomogeneity of Core

The group cross sections to be used in diffusion calculations properly should take into account the effect of fuel composition and lumping on the neutron energy spectra and spatial distributions in the fuel and in the graphite.

Table 3.2. MSRE Fuel Salts for Which Detailed Nuclear Calculations Were Made

Fuel Type	A	B	C
Salt composition (mole %)			
LiF[a]	70	66.8	65
BeF_2	23.7	29	29.2
ZrF_4	5	4	5
ThF_4	1	0	0
UF_4 (approx)	0.3	0.2	0.8
Uranium composition (atom %)			
U^{234}	1	1	0.3
U^{235}	93	93	35
U^{236}	1	1	0.3
U^{238}	5	5	64.4
Density at 1200°F (lb/ft^3)	144.5	134.5	142.7

[a] 99.9926% Li^7, 0.0074% Li^6.

3.4.1 Resonance Neutrons

Fuels A and C contain important amounts of strong resonance absorbers, thorium in fuel A and U^{238} in fuel C. The effective resonance integrals for these materials depend on their concentration in the fuel and on the effective surface-to-volume ratio of the fuel channels. Figure 3.4 illustrates how the effective resonance integral for U^{238} varies over the concentration range of interest for the MSRE. This curve was calculated by Nordheim's numerical integration program for resonance integral computations.[8] In this calculation, the actual two-dimensional transverse section of the MSRE lattice geometry (Fig. 3.2) was approximated by slab geometry with a surface-to-volume ratio of salt equal to the effective

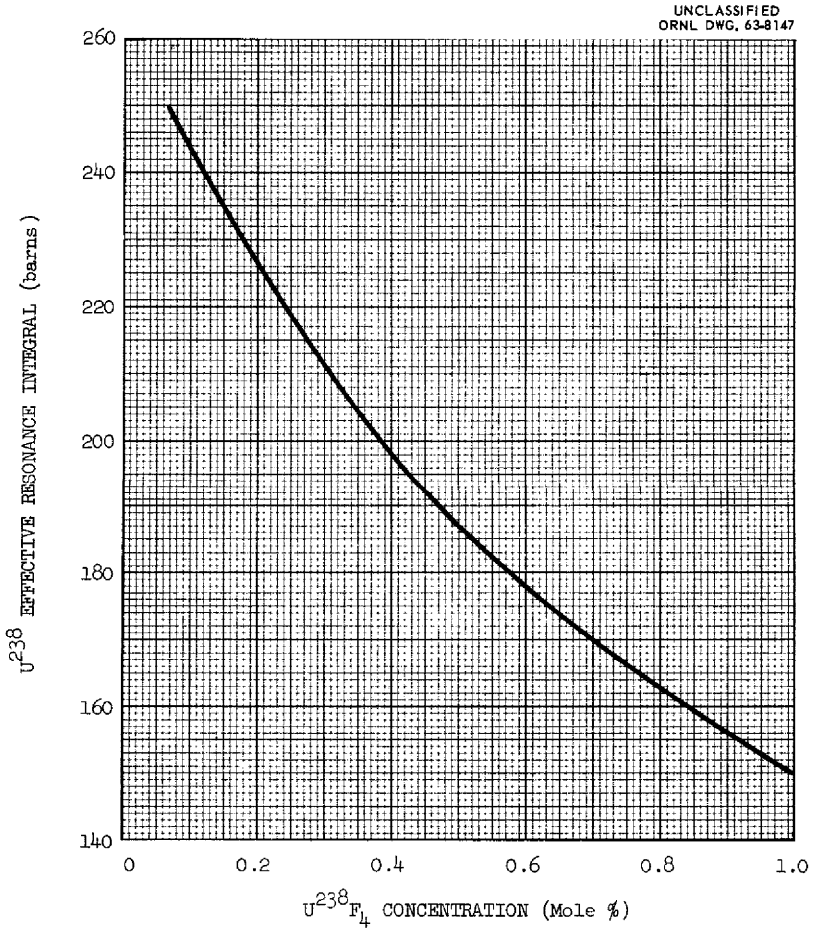

Fig. 3.4. Variation of U^{238} Effective Resonance Integral with $U^{238}F_4$ Concentration in MSRE Lattice.

ratio in the actual lattice. The effective ratio is affected by Dancoff effects (shielding from neighboring channels), which reduces the effective surface-to-volume ratio for resonance capture in the MSRE lattice by about 30%.[9] These calculations of effective resonance integrals were used in initial estimates of the critical concentration of U^{235} in each fuel.

In preparation for the refined calculations of critical concentration, which were to be done by a 33-group diffusion method, a new set of multigroup cross sections was prepared for the core with each of the three fuel compositions. Group cross sections for the 32 fast groups were generated by use of the IBM 7090 program GAM-1.[10] This program is based on a consistent P-1 approximation to the Boltzmann equation for neutron slowing-down, and averages the cross sections over an energy spectrum above thermal which is appropriate for a single-region reactor with a macroscopically uniform composition. Corrections for the shielding effects associated with the fuel channels are automatically included in the GAM-1 program. For the MSRE calculations, a set of cross sections was generated for each fuel composition, assuming a one-region reactor with a lattice like that in the main part of the actual core (22.5 vol % fuel, 77.5 vol % graphite).

A minor complication in the GAM-1 calculation of MSRE cross sections was that the available version of the GAM-1 cross-section library tape did not include Li^6, Li^7, and F^{19}, which are important components of the MSRE fuel. This was circumvented by simulating their effect on the neutron spectrum by the inclusion of an amount of oxygen equivalent in slowing-down power ($\xi\Sigma_s$) to the lithium and fluorine actually present. Fast group cross sections for Li^6, Li^7, and F^{19} were compiled from basic cross-section data, independently of the GAM-1 calculation.

3.4.2 Thermal Neutrons

Average cross sections for the thermal group were calculated by use of two thermalization programs for the IBM 7090. Reference calculations for each fuel at 1200°F were made with THERMOS, which computes the thermal spectrum in a one-dimensional lattice cell.[11] The cell model used was that of a cylindrical graphite stringer, surrounded by an annulus of salt. For other calculations in which the effects of changes in temperature and

thermal cutoff energy were studied, a simpler and more rapid thermalization program was employed, based on the Wilkins "heavy gas" space-independent model.

Lumping reduces the thermal utilization in the MSRE lattice because of the thermal flux depression in the fuel, but this effect is not large. (For salt with the maximum uranium content of interest in the MSRE, 1 mole % UF_4, the flux depression in the fuel was about 3.5%.) Furthermore, the normal temperature of 1200°F is above the temperature at which crystal binding effects in graphite must be considered.[12] For these reasons, it was found that good agreement with the THERMOS model could be obtained by combining the Wilkins thermal spectrum calculation with a one-group P-3 calculation of the spatial disadvantage factor. These approximations were used wherever possible in order to save computer time. For some of the studies of the temperature coefficient of reactivity, however, it was necessary to use the THERMOS program in order to vary the temperature of the fuel channel independently of that of the graphite. These studies are described more fully in Sec 3.7.

3.5 Criticality Calculations

Critical fuel concentrations were computed with MODRIC, a multigroup diffusion program for the IBM 7090.[13] MODRIC is a one-dimensional program with provision for approximating the neutron leakage in the direction transverse to that represented in the one-dimensional model. For the calculation of critical concentration, the reactor was represented by a cylinder with regions and materials corresponding to the midplane of the model shown in Fig. 3.3. Axial leakage was taken into account by the inclusion of a specified axial buckling, based on earlier calculations of the axial flux shape. In the computations for fuels A and B, the concentrations of all uranium isotopes were varied together in all regions to find the critical concentration. For fuel C, the U^{238} concentration was held constant and those of the other uranium isotopes were varied. (Results are summarized in Table 3.5, Sec 3.9.)

In addition to the critical concentration, the MODRIC calculations gave two-group constants for each region represented. These were to be used in a two-group, two-dimensional calculation. It was therefore necessary to perform other MODRIC calculations to include regions missed by the midplane radial calculations. For these calculations the reactor was represented by a multilayer slab, with regions corresponding to an axial traverse through the model of Fig. 3.3, and a radial buckling based on the radial MODRIC calculations. Slabs corresponding to two different traverses were calculated, one corresponding to the core centerline and the other to a traverse just outside the rod thimbles. These axial calculations, using the critical concentrations given by the radial calculations, gave values of k_{eff} between 1.004 and 1.021. This is considered to be good agreement, in view of the fact that the axial calculations are less accurate than the radial because the equivalent transverse buckling is more subject to error in the axial calculations.

The two-group constants obtained from MODRIC were used in calculation of the model of Fig. 3.3 by the two-group, two-dimensional program EQUIPOISE-3.[14,15] These two-group calculations gave k_{eff} of 0.993, 0.997, and 0.993 for fuels A, B, and C, respectively, further confirming the critical concentrations found by the radial MODRIC criticality search.

In all of these calculations it was assumed that the core temperature was uniform at 1200°F, the control rods were withdrawn, and the core contained no fission product poisons. The calculated critical concentrations are therefore those which would be attained during the initial critical experiments with clean, noncirculating fuel and with all rods fully withdrawn. During subsequent operations, the concentration must be higher to compensate for all of the effects (poisons, rods, and the loss of delayed neutrons) which tend to decrease reactivity. The total of these effects is expected to be about 4% $\delta k/k$. Table 3.5 (Sec 3.9) lists the critical concentration for normal operation, which would include these effects. The increases in the critical concentration from the clean critical experiment were computed from values of the concentration coefficient of reactivity $(\delta k/k)/(\delta C/C)$, produced by the MODRIC criticality searches.

3.6 Flux and Fission Distributions

3.6.1 Spatial Distribution

Two-group fluxes and adjoint fluxes were produced by the EQUIPOISE-3 calculations. Figures 3.5–3.8 show the axial and radial distributions for fuels B and C. The fluxes for fuel A are within 2.5% of those for fuel C. The radial distributions are for an axial position that corresponds to the maximum in the thermal flux, which is at a position very close to the core midplane. The axial distributions are at a position 8.4 in. from the core centerline*; this radius corresponds to the maximum value of the thermal flux.

The MODRIC calculations gave spatial flux distributions for each of 33 energy groups. It was necessary to normalize the MODRIC fluxes to correspond to the neutron production at 10 Mw, and the normalization factor was obtained by comparing the MODRIC thermal fluxes with the 10-Mw values computed by EQUIPOISE. (The shapes of the thermal fluxes were very similar.) The high-energy MODRIC fluxes were then multiplied by the normalization factor to obtain the predicted high-energy neutron fluxes in the reactor. Figure 3.9 shows the radial distribution, near the core midplane, of the neutron fluxes with energies greater than 0.18 Mev and with energies greater than 1.05 Mev. Figure 3.10 shows the axial distribution of the same energy groups 3 in. from the core centerline, which is about the location of the rod thimbles and the test specimens. (The values shown in Figs. 3.9 and 3.10 were computed for fuel C, but these very-high-energy fluxes are not sensitive to the fuel composition.)

The spatial distributions of the fission density were obtained from the EQUIPOISE-3 calculations. Figures 3.11 and 3.12 show the axial and radial distributions of the fission density in the fuel, for fuel C. The same calculations also gave total fissions in each region. Table 3.3 summarizes, for fuel C, the fraction of the total fissions which occur in the major regions of the reactor.

---

*The datum plane for the axial distance is the bottom of the horizontal graphite bars at the bottom of the core.

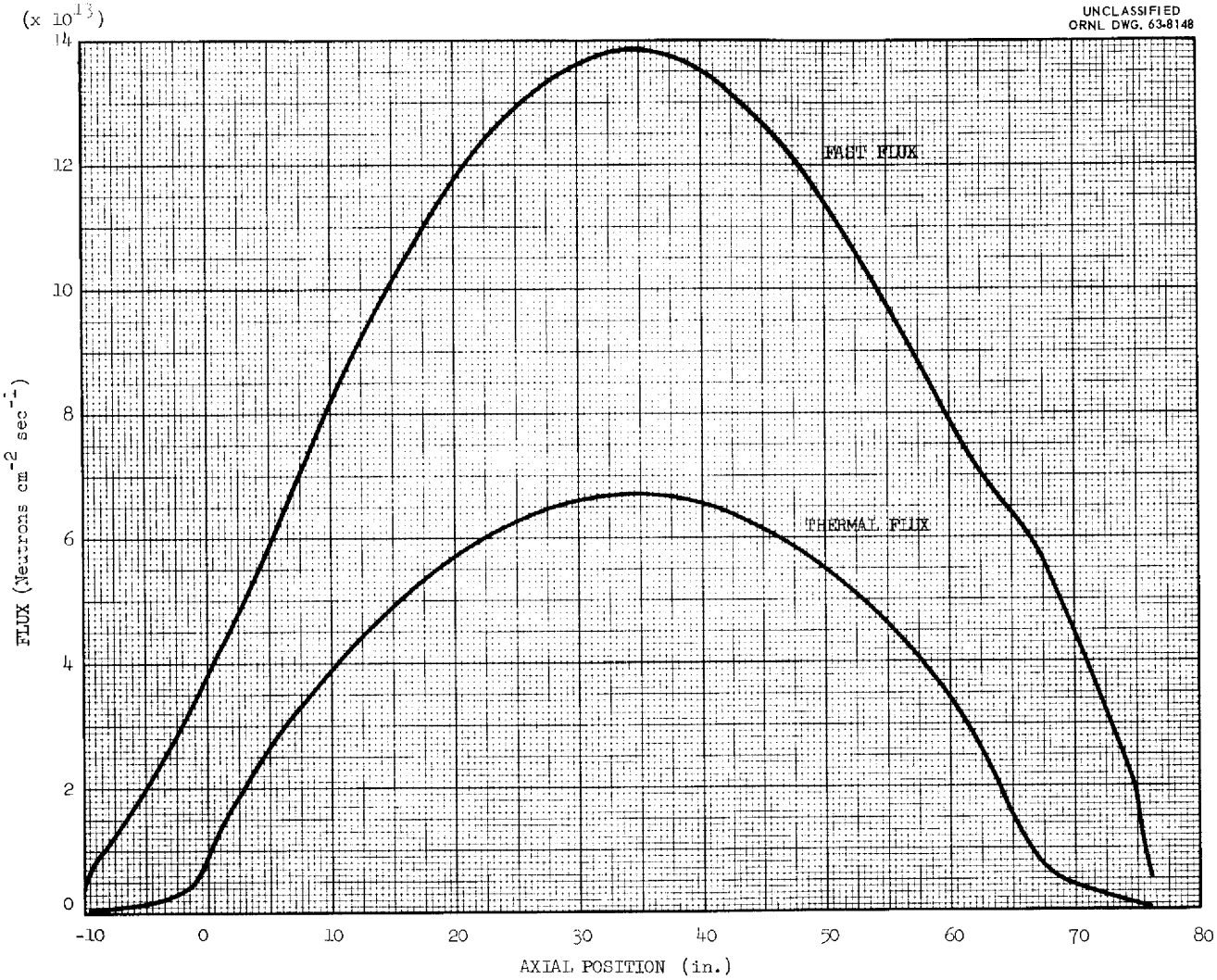

Fig. 3.5. Axial Distribution of Two-Group Fluxes 8.4 in. from Core Center Line, Fuel B.

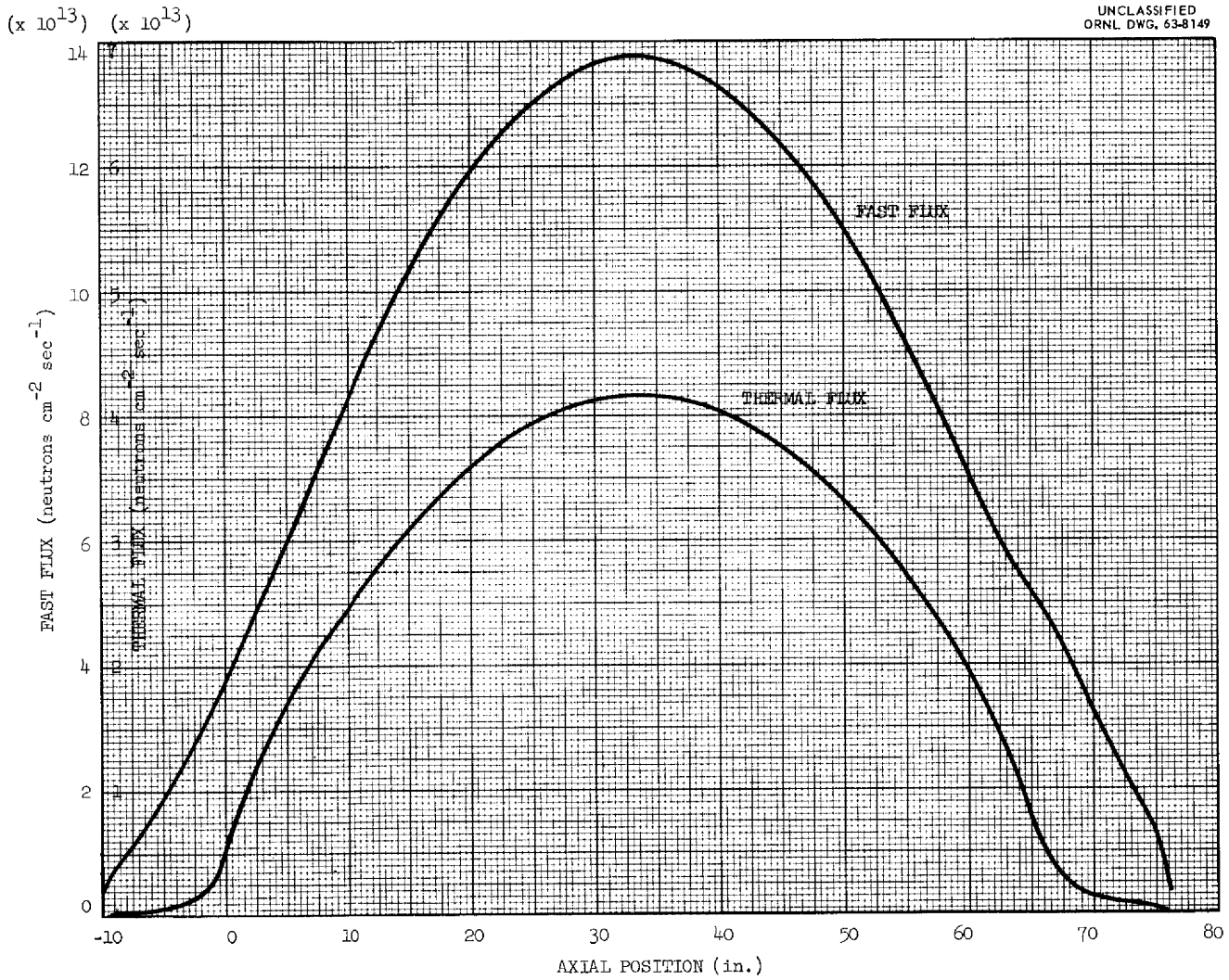

Fig. 3.6. Axial Distribution of Two-Group Fluxes 8.4 in. from Core Center Line, Fuel C.

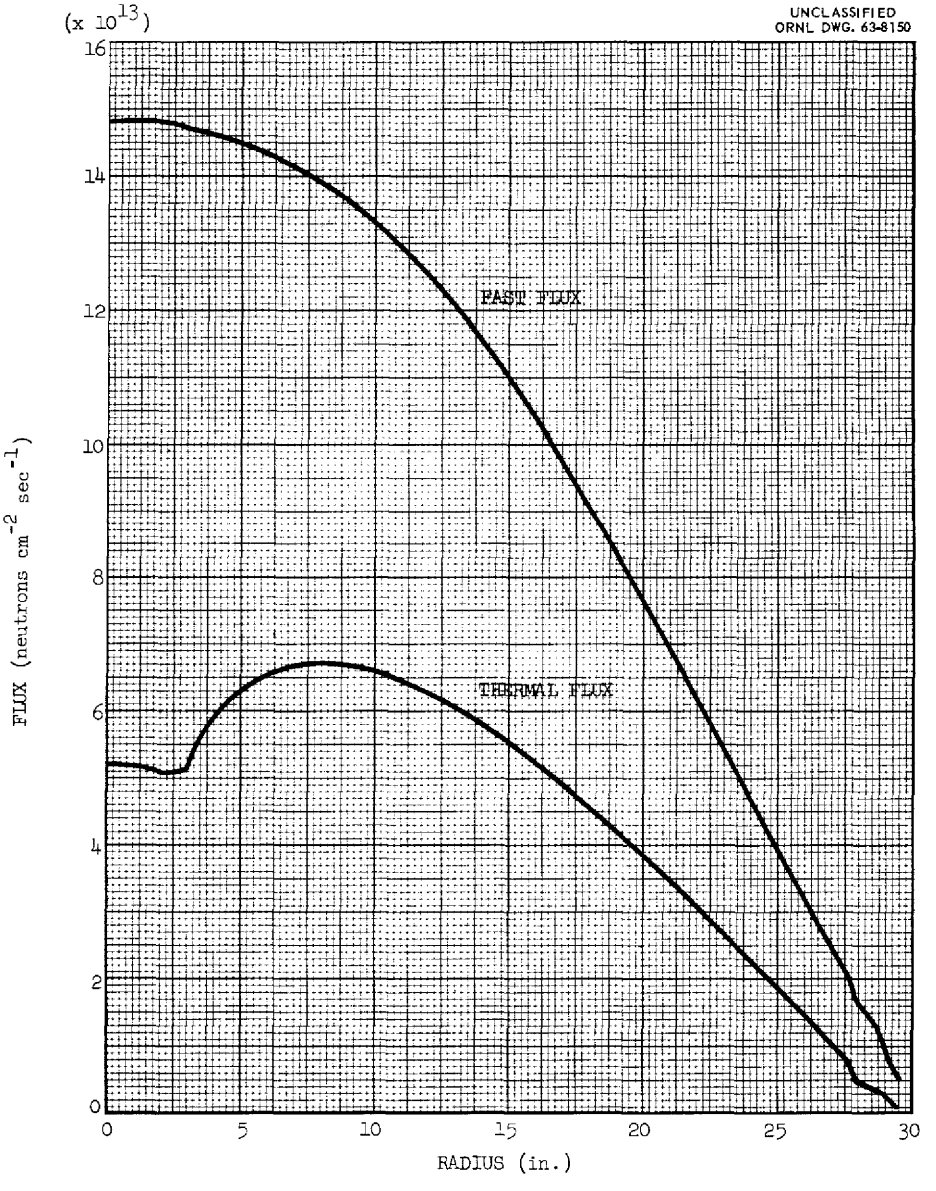

Fig. 3.7. Radial Distribution of Two-Group Fluxes Near Core Midplane, Fuel B.

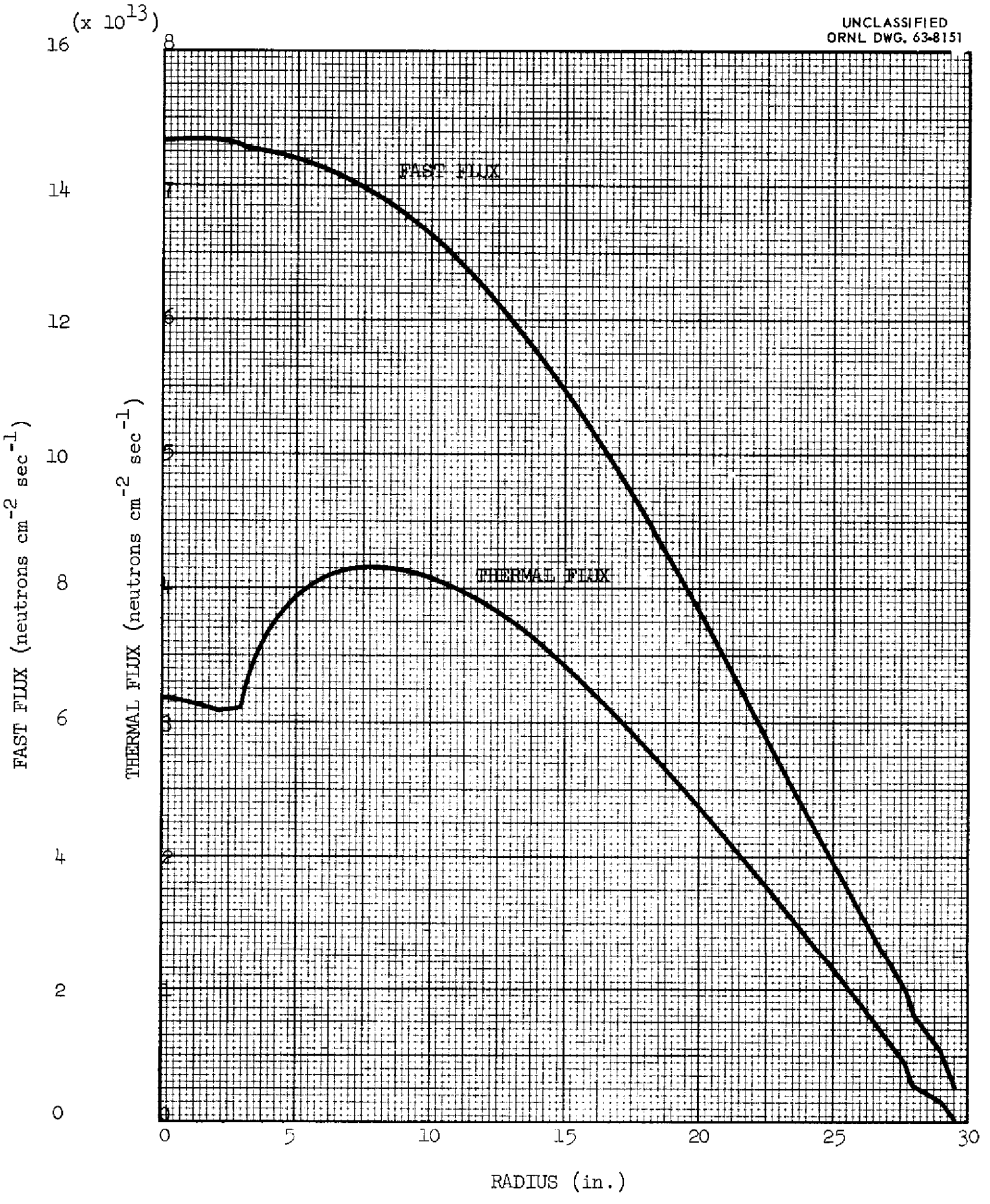

Fig. 3.8. Radial Distribution of Two-Group Fluxes Near Core Midplane, Fuel C.

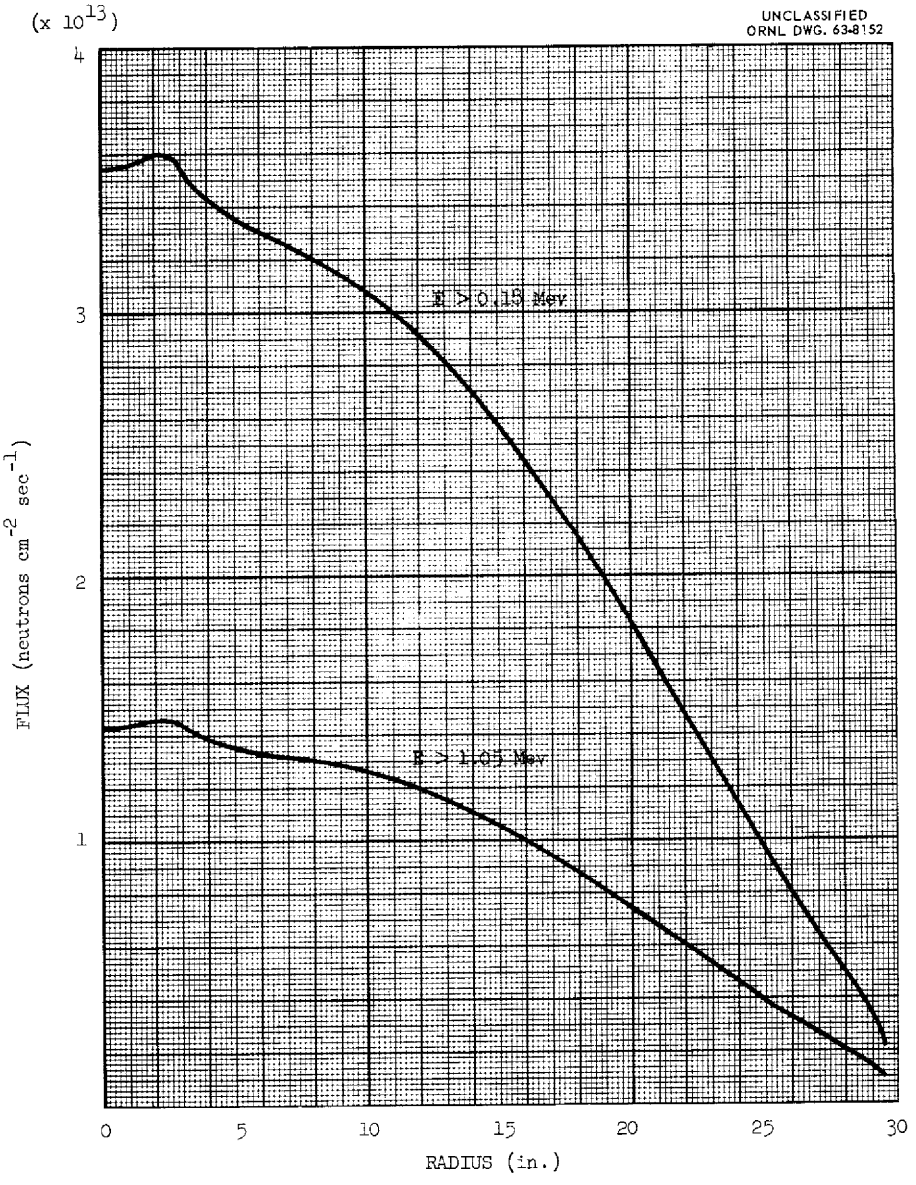

Fig. 3.9. High-Energy Neutron Fluxes: Radial Distribution Near Core Midplane at 10 Mw.

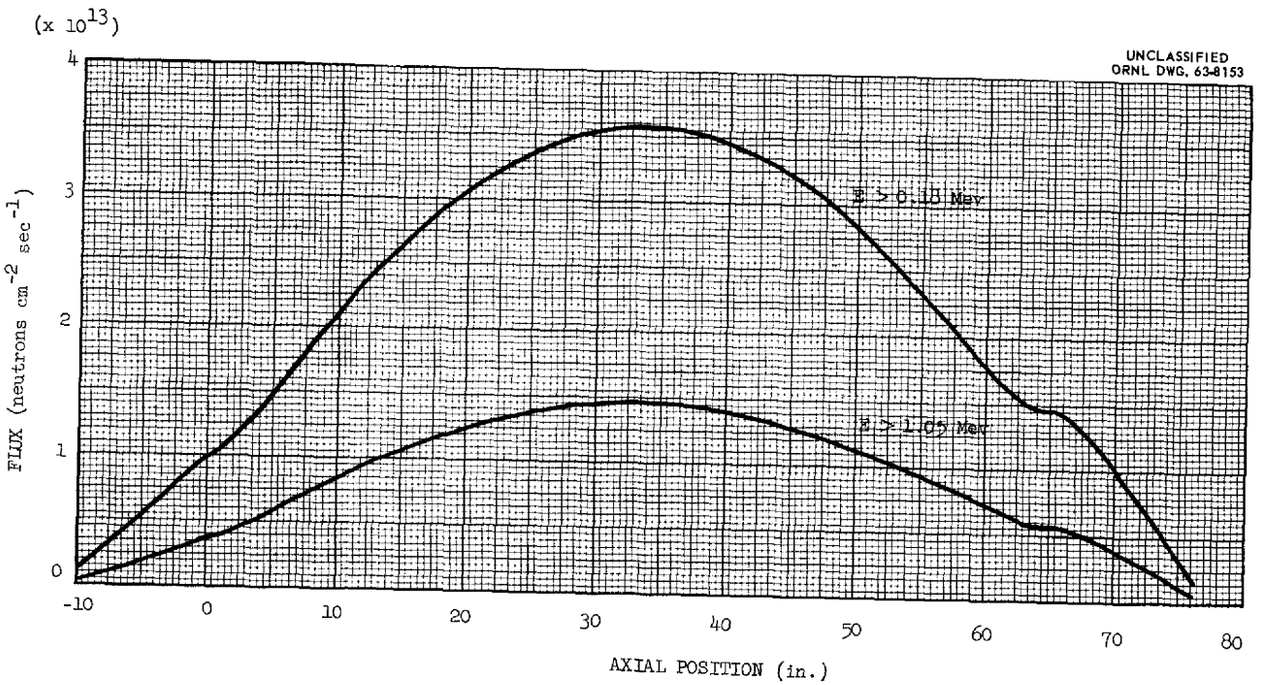

Fig. 3.10. High-Energy Neutron Fluxes: Axial Distribution 3 in. from Core Center Line at 10 Mw.

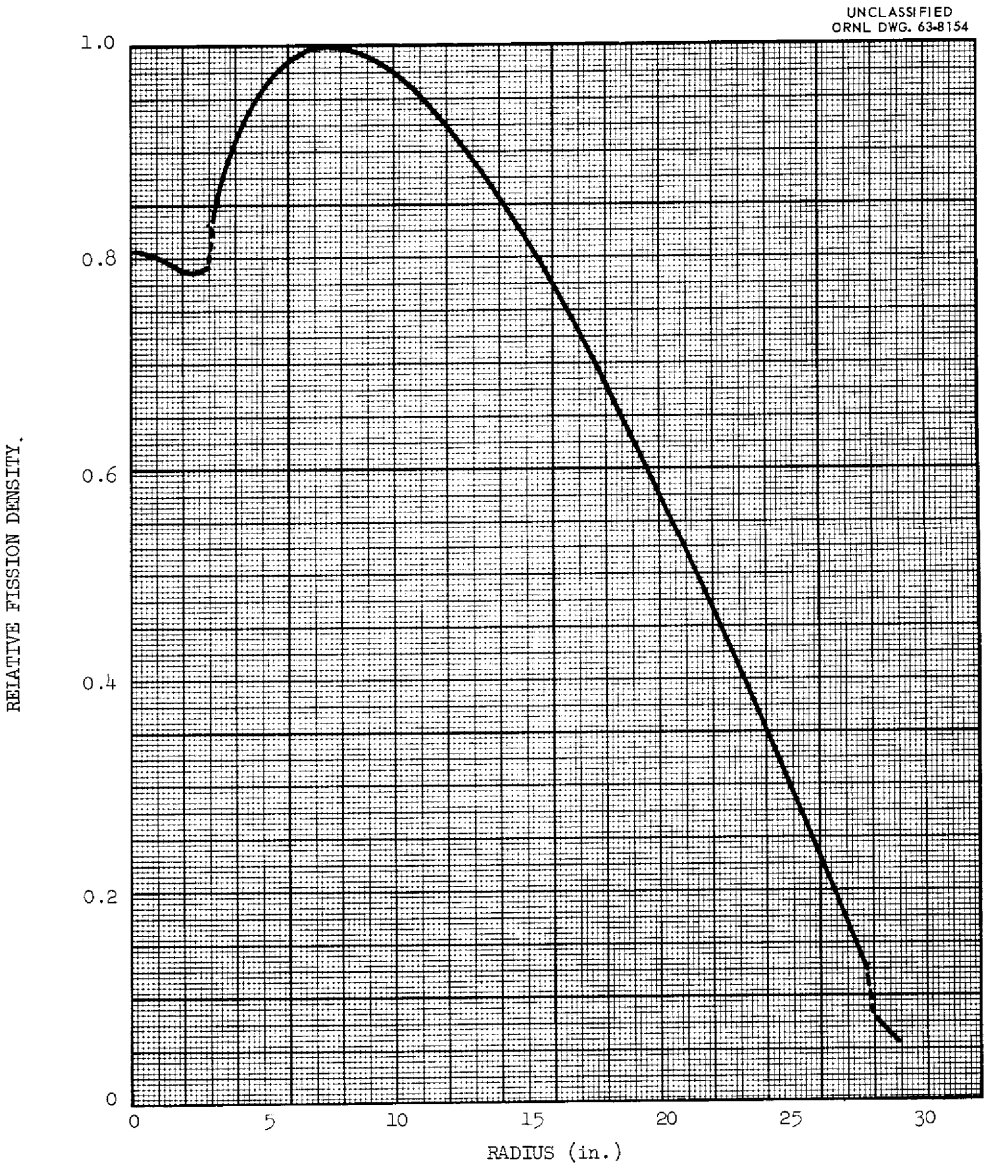

Fig. 3.11. Radial Distribution of Fuel Fission Density Near Core Midplane, Fuel C.

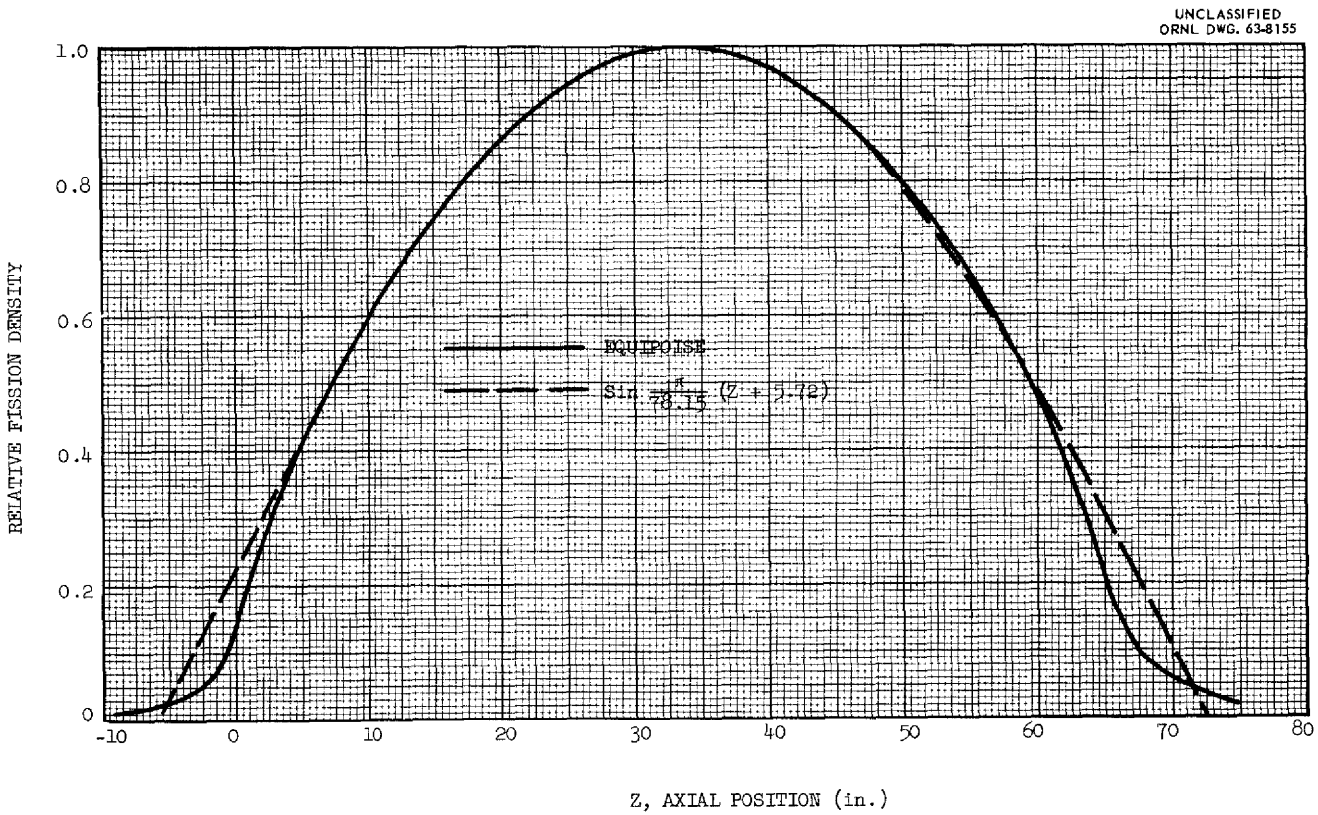

Fig. 3.12. Axial Distribution of Fuel Fission Density 8.4 in. from Core Center Line, Fuel C.

Table 3.3. Fission Distribution by Major Region
(See Fig. 3.3 for graphical location of regions)

Major Region	Regions	Fraction of Total Fissions (%)
Downcomer	F	2.9
Lower head	O, P	2.4
Main core	J, L, M, N, T	89.1
Upper head	D, E, G, H, Q, R, S	5.6

3.6.2 Energy Distribution

The energy distribution of the neutron flux at a given location is influenced by the nuclear properties of the materials in the general vicinity of the point. As a result, the flux spectrum varies rather widely with position and fuel composition. The MODRIC calculations produced average distributions of flux as a function of energy within each reactor region as well as the detailed distributions as functions of position and energy. Figure 3.13 shows the average fluxes, per unit lethargy, in the largest core region (Region J of Fig. 3.3) for each of the 32 nonthermal energy groups. The fluxes are normalized to unit thermal flux in each case. The maximum lethargy of the thirty-second or last epithermal group is 17, which corresponds to a neutron energy of 0.414 ev. This is also the maximum energy (minimum lethargy) of neutrons in the thirty-third or "thermal" group. The effect of the strong resonance absorbers, thorium in fuel A and U^{238} in fuel C, in reducing the flux in the region just above the thermal cutoff is readily apparent.

The distribution of fissions as a function of the lethargy of the neutrons causing fission is the product of the neutron flux and the fission cross section. Figure 3.14 shows the average fission density, per unit lethargy, in the largest core region, normalized to one fission in that region, as a function of neutron energy for fuel C. The resonances in the fission cross section are reflected by the peaks at the higher lethargies (lower energies). Integration of the plot in Fig. 3.14 to a

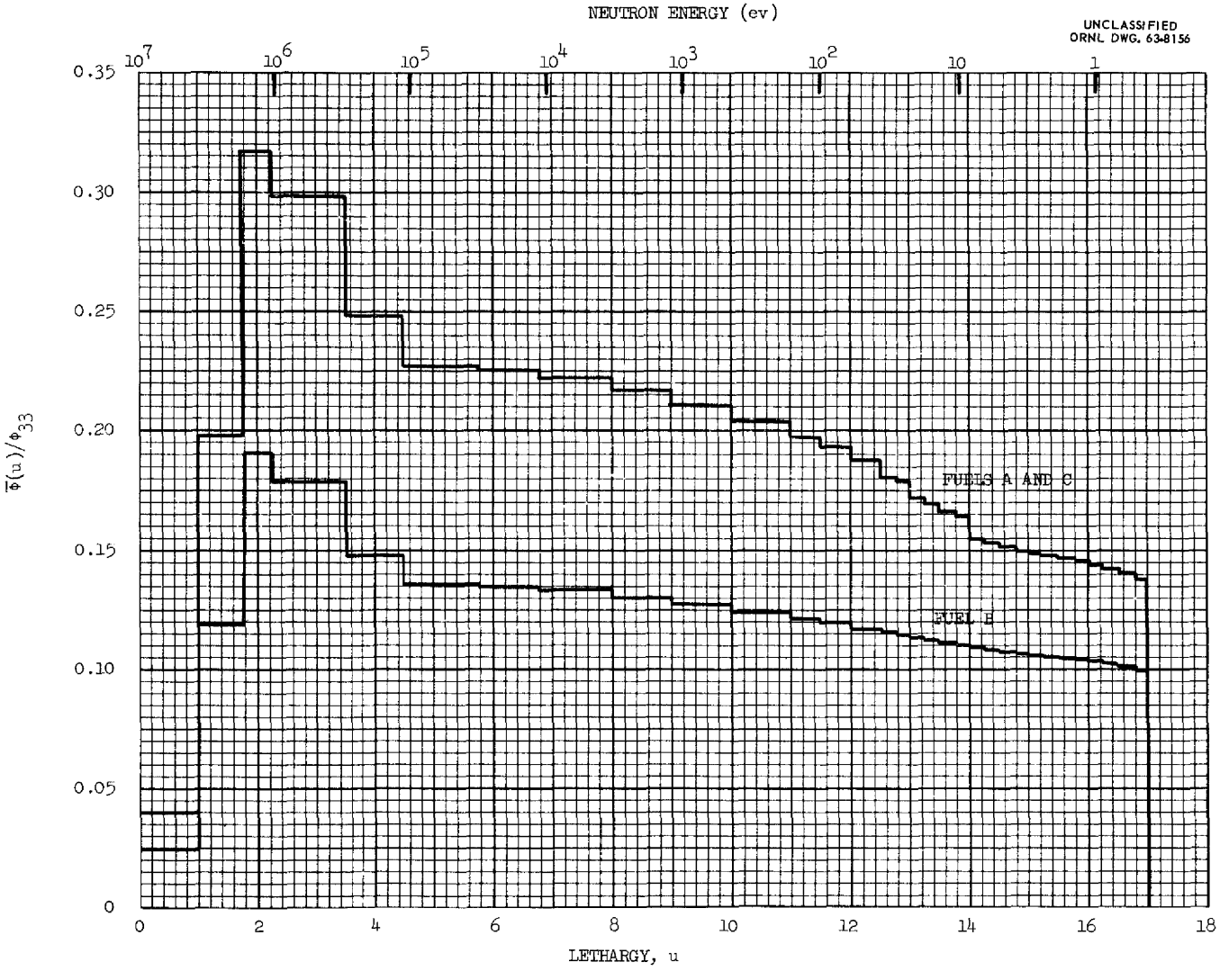

Fig. 3.13. Average Flux Spectra in Largest Core Region.

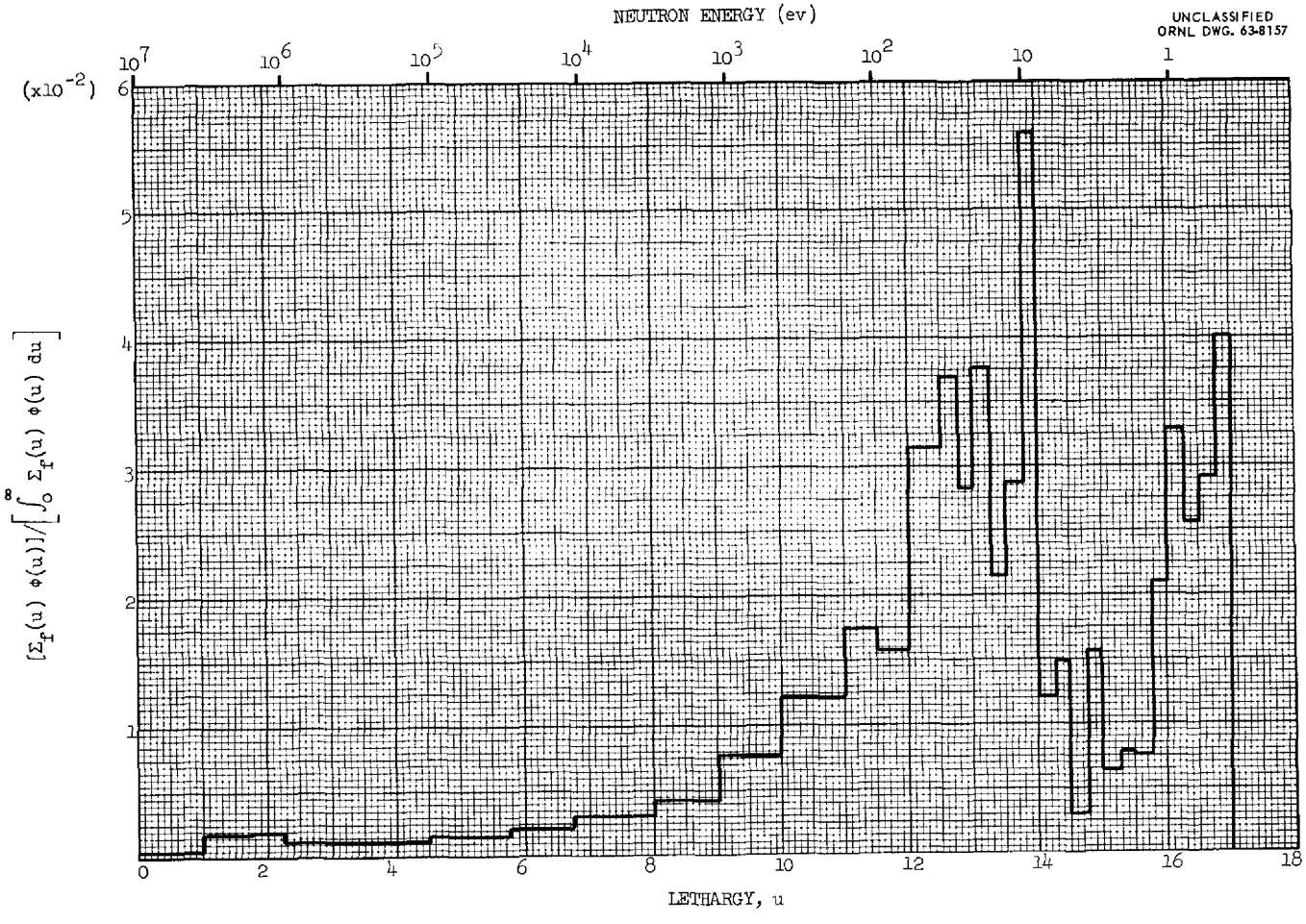

Fig. 3.14. Fission Density as a Function of Lethargy of Neutrons Causing Fission, Fuel C.

given lethargy gives the cumulative fraction of fissions caused by neutrons with less than the specified lethargy. Figure 3.15 illustrates the result of this operation for fuel C in the largest core region. This figure indicates that 17.7% of the fissions in this region are caused by nonthermal neutrons. The average fraction for the entire reactor is 20.2%, indicating that fast fissions account for a relatively larger fraction of the total in other regions. This is particularly true in the upper and lower heads, where the absence of graphite produces a much lower ratio of thermal to fast flux than exists in the main portion of the core.

3.7 Reactivity Effects of Nonuniform Temperature

Changes in the temperature of the core materials influence the reactivity through changes in the neutron leakage and absorption probabilities. The reactivity change between two isothermal conditions can be expressed in terms of a single temperature coefficient of reactivity. When the reactor operates at power, however, the core is not isothermal; in fact, the overall shapes of the temperature distributions in the fuel and in the graphite are quite dissimilar. For this reason, and also because different thermal time constants are involved in fuel and graphite temperature changes, separate consideration of the reactivity effects of these changes is necessary. To delineate the factors governing the reactivity-temperature relation, calculations were first performed using a simplified model of the reactor, that of a single-region cylinder in which composition and temperature were macroscopically uniform. These are discussed in Sec 3.7.1. Analysis based on the multiregion model of Fig. 3.3 is considered in Sec 3.7.2.

3.7.1 One-Region Model

For this analysis, use was made of the GAM-1 program in order to calculate macroscopic cross sections averaged over the energy spectrum above thermal. Cross sections for the thermal group were averaged over a Wilkins spectrum. The lower energy cutoff for the GAM-1 calculation was equal to the upper cutoff for the Wilkins thermal spectrum. The two-group parameters obtained in this way were then used to calculate the

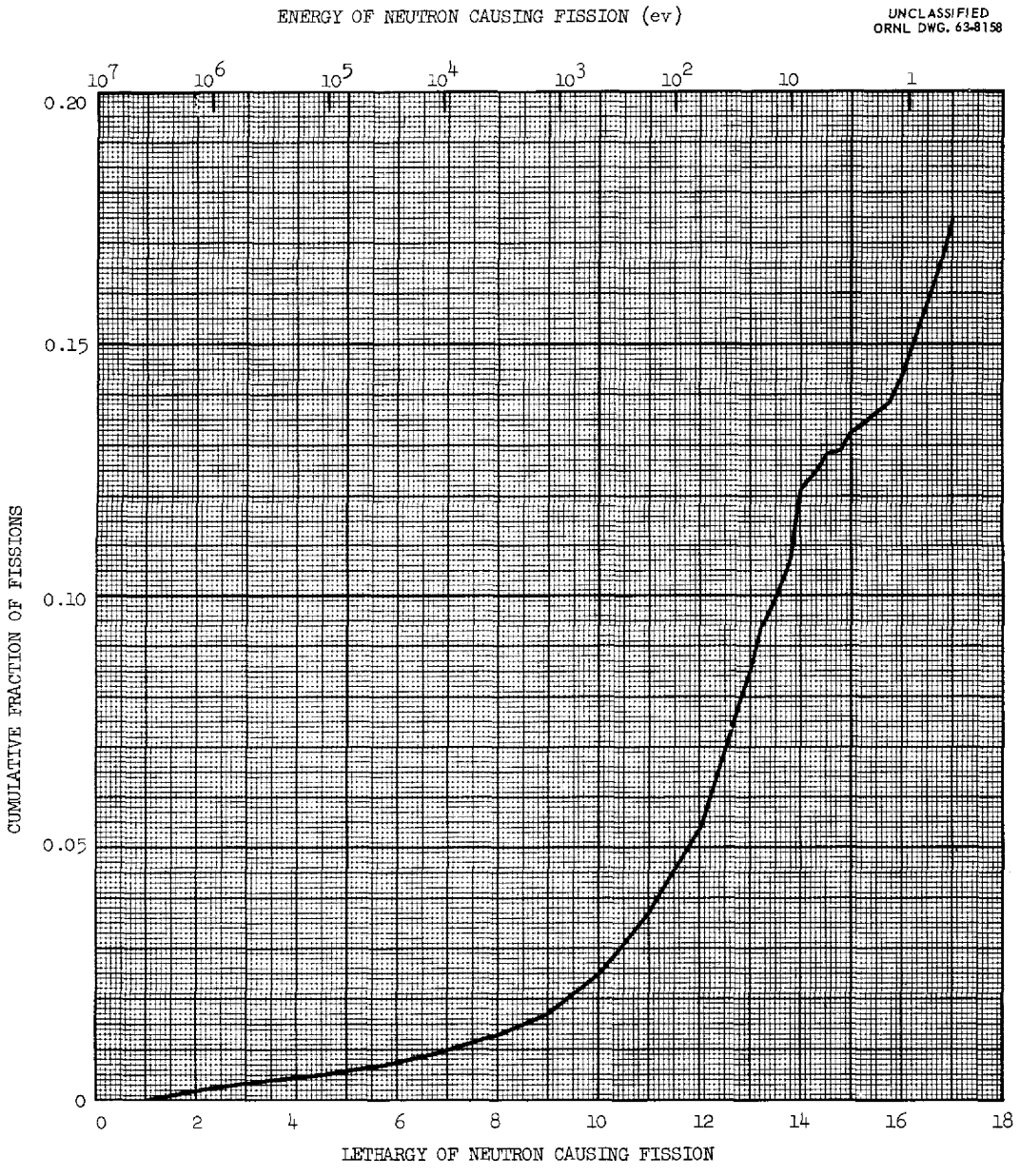

Fig. 3.15. Cumulative Fraction of Fissions Caused by High-Energy Neutrons, Fuel C.

multiplication constant of the cylinder, based on the standard two-group diffusion equations. In this calculation, the geometric buckling used was that of a cylinder, 59 in. in diameter by 78 in. high. Three temperature conditions were considered: (1) salt and graphite at 1200°F, (2) salt at 1600°F, graphite at 1200°F, and (3) salt and graphite at 1600°F. The temperature coefficient of reactivity was obtained from the approximate relation

$$\frac{1}{k}\frac{\partial k}{\partial T} = \frac{k^{(1600)} - k^{(1200)}}{400\ k^{(1200)}} . \qquad (3.1)$$

Two special considerations are of importance in analysis of the MSRE temperature coefficient. The first is the position chosen for the thermal energy cutoff, which is the approximate energy above which thermal motion of moderator atoms may be neglected. Since a cylindrical core of this size has a large neutron leakage fraction, unless the cutoff energy is chosen high enough the total effect of temperature on thermal neutron leakage is underestimated. This effect is indicated in Fig. 3.16, curve (a). Here the total temperature coefficient of reactivity (fuel + graphite) of the core fueled with fuel C is plotted vs the upper energy cutoff of the thermal group. The coefficient tends to become independent of the cutoff energy for cutoffs in excess of about 1 ev.

The second consideration is the effect of the salt temperature on the thermal spectrum. For this calculation, it was necessary to employ the THERMOS program so that the temperatures of the salt channels and graphite could be varied independently. The results of this analysis for fuel C may be seen by comparing curves (b) and (c) in Fig. 3.16. Curve (b) was calculated by neglecting the change in thermal spectrum with salt temperature. This difference is a consequence of the fact that the light elements in the salt, lithium, beryllium, and fluorine, contribute substantially to the total moderation in the MSRE core.

Similar calculations based on the one-region cylindrical model were made for fuels A and B. The values of the reactivity coefficients for all fuels obtained at the asymptotic cutoff energies are summarized in Table 3.4. All calculations were based on the values of volumetric expansion coefficients at 1200°F (see Table 3.4).

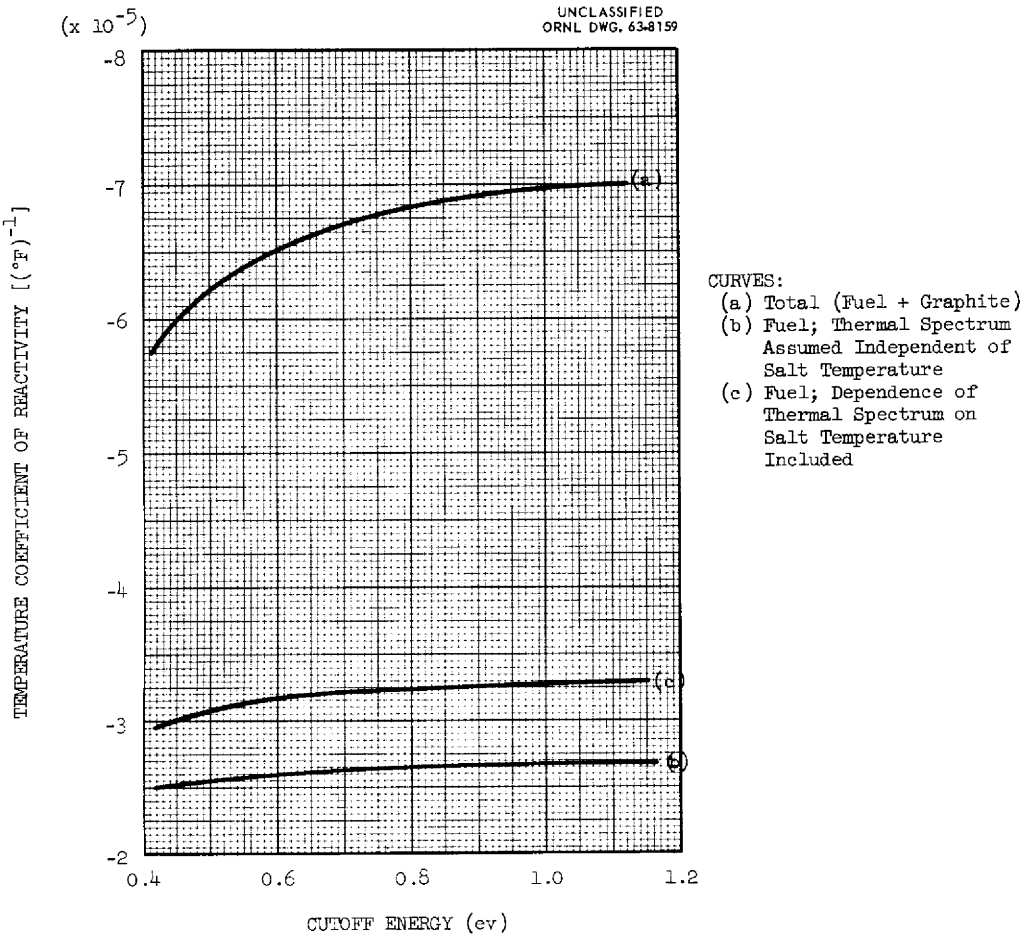

Fig. 3.16. Effect of Thermal Cutoff Energy on Temperature Coefficient of Reactivity, Fuel C.

Table 3.4. Temperature Coefficients of Reactivity Obtained from One-Region Model

(Calculations based on expansion coefficients, at 1200°F, of 1.18×10^{-2} %/°F for salt and 1.0×10^{-3} %/°F for graphite)

	Fuel A	Fuel B	Fuel C
Temperature coefficient of reactivity [(δk/k)/°F]			
Salt	-3.03×10^{-5}	-4.97×10^{-5}	-3.28×10^{-5}
Graphite	-3.36×10^{-5}	-4.91×10^{-5}	-3.68×10^{-5}
Total	-6.39×10^{-5}	-9.88×10^{-5}	-6.96×10^{-5}

3.7.2 Multiregion Model

To study the effects of the macroscopic distribution of materials composition and temperature on the reactivity-temperature relations, use was made of first-order perturbation theory.[16] For this purpose, it is convenient to utilize the concept of a nuclear average temperature. This quantity is defined as follows: At low power, reactor criticality is assumed to be established at isothermal conditions in fuel and graphite. Then, with the graphite temperature held constant, the fuel temperature is varied according to a prescribed distribution, thus changing the reactivity. The fuel nuclear average temperature, T_f^*, is defined as the equivalent uniform fuel temperature which gives the same reactivity change as that of the actual temperature distribution. Similarly, the graphite nuclear average temperature, T_g^*, is defined as the uniform graphite temperature which gives the same reactivity change as the actual graphite temperature profile, with the fuel temperature held constant.

The relations between the nuclear average temperature, T^*, and the temperature distributions, $T(r,z)$, are of the form

$$T_x^* = \frac{\int_{\text{reactor}} T_x(r,z)\, G_x(r,z) r\, dr\, dz}{\int_{\text{reactor}} G_x(r,z) r\, dr\, dz}, \qquad x = f,g, \qquad (3.2)$$

where

$$G_x(r,z) = G_x^{11}\phi_1^*\phi_1 + G_x^{12}\phi_1^*\phi_2 + G_x^{21}\phi_2^*\phi_1 + G_x^{22}\phi_2^*\phi_2 \qquad (3.3)$$

and ϕ_1, ϕ_2, ϕ_1^*, ϕ_2^* are the unperturbed values of the fast and slow fluxes and the fast and slow adjoint fluxes, respectively. The coefficients G^{ij} are constant over each region of the unperturbed reactor in which the nuclear composition is uniform, but vary from region to region. These quantities involve the temperature derivatives of the macroscopic nuclear constants; that is, in obtaining Eq. (3.3), the local change $\delta\Sigma$ in the macroscopic cross sections was related to the local temperature change δT through the approximation

$$\delta\Sigma(r,z) = \frac{\partial\Sigma}{\partial T}\, \delta T(r,z) . \qquad (3.4)$$

This approximation is adequate if the spatial variation in temperature is relatively smooth within a given region.

Temperature coefficients of reactivity which are consistent with the definitions of the nuclear average temperatures were also obtained from perturbation theory. The complete temperature-reactivity relation is expressed as

$$\frac{\delta k}{k} = \alpha_f^* \delta T_f^* + \alpha_g^* \delta T_g^* , \tag{3.5}$$

where

$$\delta T^* = T^* - T_0^* \tag{3.6}$$

and α^* is the appropriate temperature coefficient of reactivity. The fuel and graphite reactivity coefficients are related to the weight functions G(r,z) as follows:

$$\alpha_x^* = \frac{\int_{\text{reactor}} G_x(r,z) r \, dr \, dz}{\int_{\text{reactor}} F(r,z) r \, dr \, dz} , \tag{3.7}$$

where

$$F(r,z) = \nu\Sigma_{f1}\phi_1^*\phi_1 + \nu\Sigma_{f2}\phi_2^*\phi_2 . \tag{3.8}$$

The principal advantage of expressing the reactivity change with temperature in the form of Eq. (3.5) is that the reactivity coefficients, α^*, and the weight functions G(r,z) depend only on the conditions in the unperturbed reactor. Use of this approximation thus simplifies the calculation of the reactivity effects of a large number of temperature distributions.

Reactivity coefficients and temperature weight functions for the fuel salt and graphite were evaluated for the 20-region model of the MSRE core (Fig. 3.3), fueled with fuel C. The resulting weight functions are shown in Figs. 3.17–3.20. These figures correspond to axial and radial traverses of the core which intersect at the approximate position of maximum thermal flux. Corresponding weight functions for fuels A and B do not differ qualitatively from these results. The discontinuities in the weight functions occur as the effective concentrations of salt, graphite,

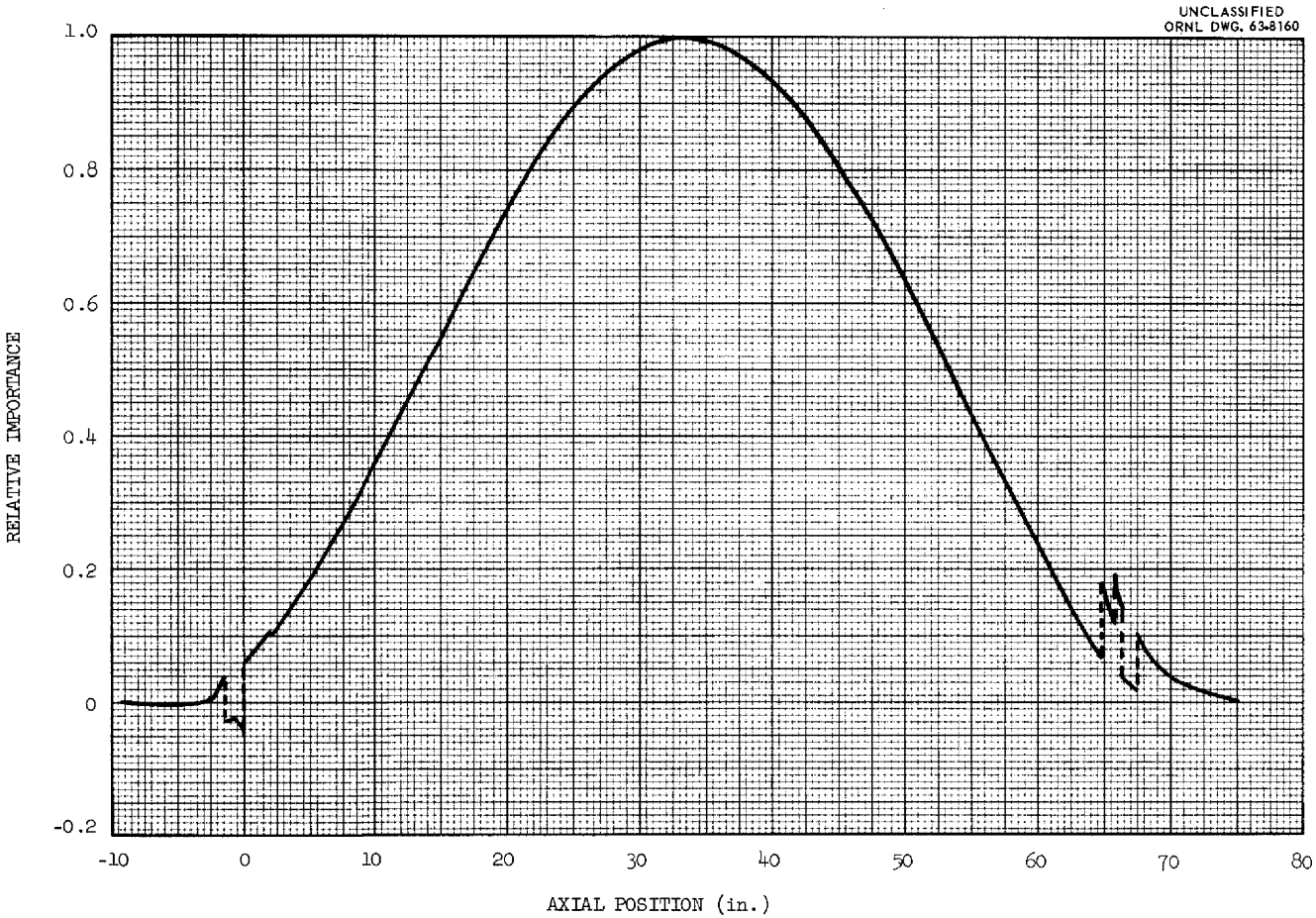

Fig. 3.17. Relative Nuclear Importance of Fuel Temperature Changes as a Function of Position on an Axis Located 8.4 in. from Core Center Line.

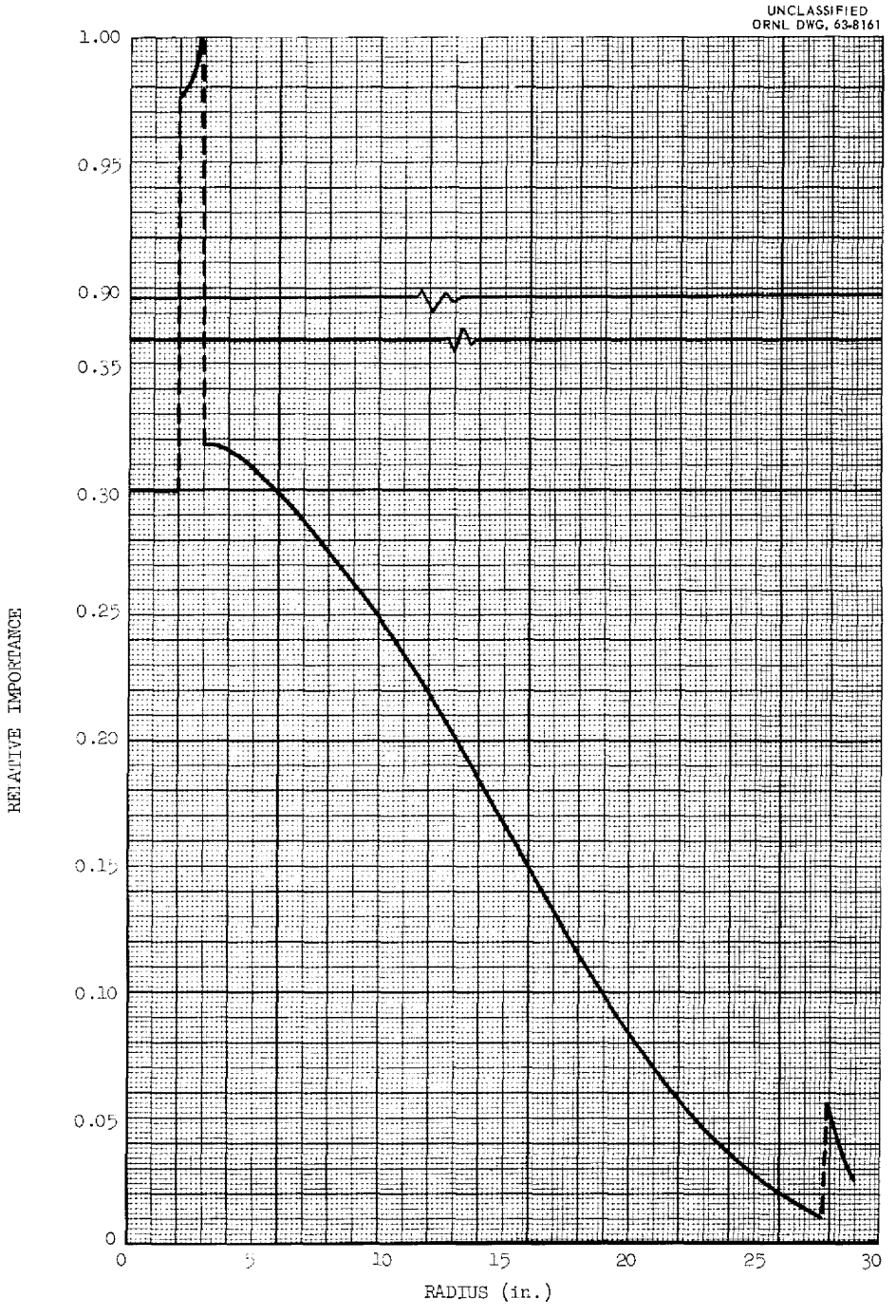

Fig. 3.18. Relative Nuclear Importance of Fuel Temperature Changes as a Function of Radial Position in Plane of Maximum Thermal Flux.

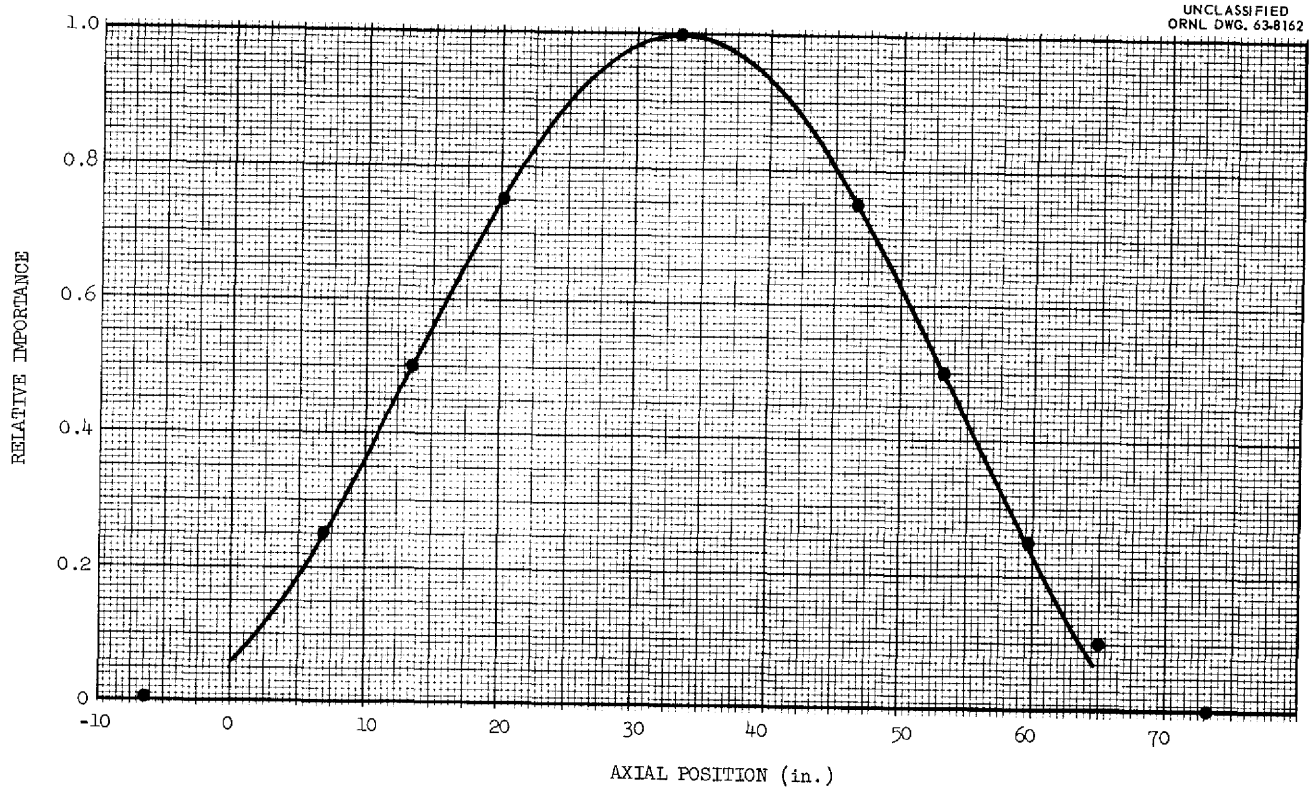

Fig. 3.19. Relative Nuclear Importance of Graphite Temperature Changes as a Function of Position on an Axis Located 8.4 in. from Core Center Line.

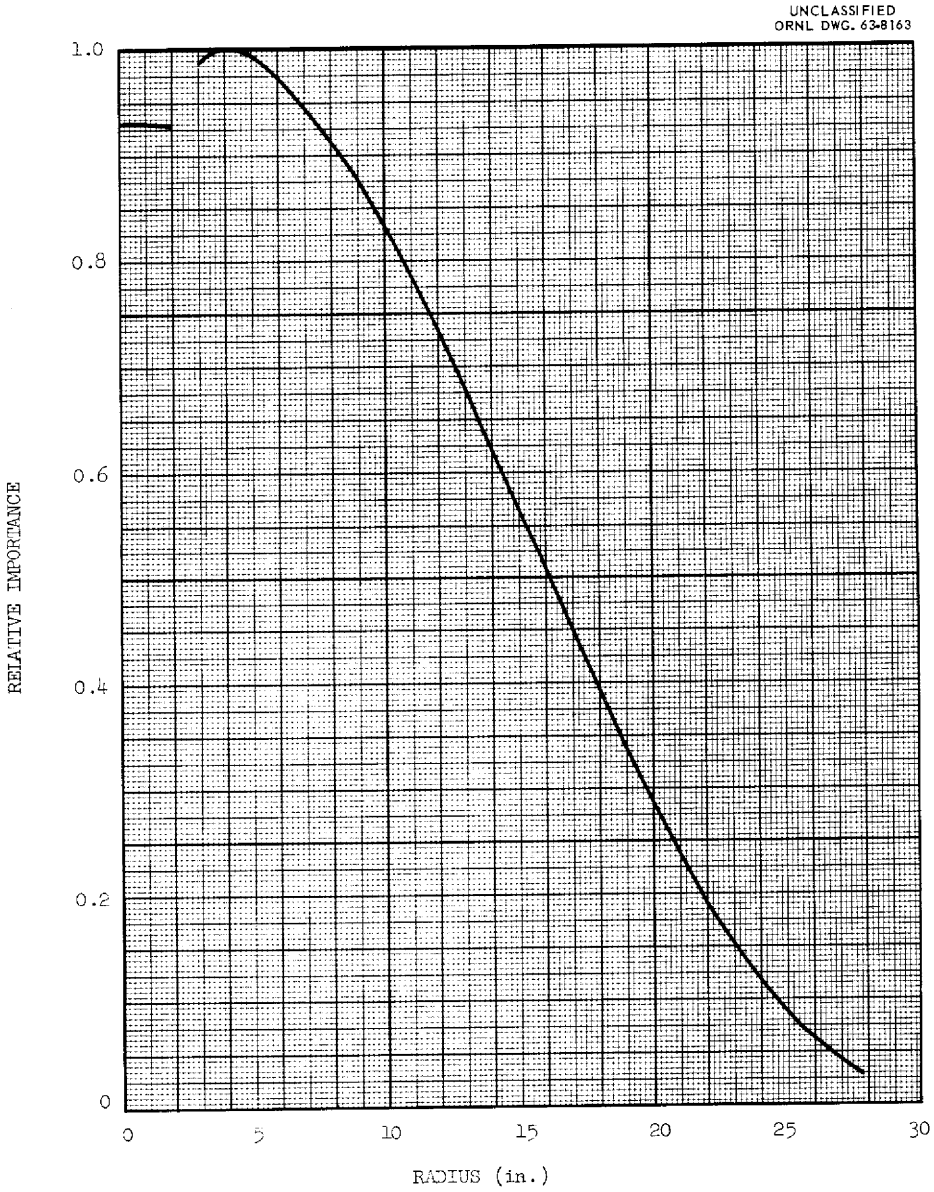

Fig. 3.20. Relative Nuclear Importance of Graphite Temperature Changes as a Function of Radial Position in Plane of Maximum Thermal Flux.

and INOR-8 change from region to region. From the definition of these functions, the point values reflect directly the reactivity effect of a change in fuel or graphite temperature in a unit volume at that point. This occurs through changes in the local unit reaction and leakage rates, reflected in G^{ij} of Eq. (3.3), and through variation in nuclear importance with position, reflected in $\phi_i^* \phi_j$.

Although the method presented above is an attempt to account approximately for macroscopic variations in reactor properties with position, it should be noted the basic model is still highly idealized. The exact nature of the discontinuities in the weight functions would undoubtedly differ from those shown in Figs. 3.17–3.20. Since the reactivity change is an integral effect, however, these local differences tend to be "smeared out" in the quantities determining the operating characteristics. Consider, for example, the large increase in the fuel temperature weighting functions, corresponding to the region of salt plus void surrounding the control rod thimbles. This reflects both the higher average U^{235} concentration and the lack of graphite to dilute the effect of a salt temperature increment on the density of this region. Thus both the average reaction rate and the scattering probability for neutrons entering this region are more sensitive to changes in the salt temperature. However, when integrated over the volume, this region contributes only about 5% to the total fuel temperature coefficient of reactivity.

The temperature coefficients of reactivity obtained from the multiregion model were in reasonably good agreement with the coefficients listed for fuel C in Table 3.4. The fuel coefficient was about 3% smaller and the graphite coefficient about 15% smaller than those of the homogeneous cylinder. The difference in coefficients for the graphite occurs because the volume of the core actually occupied by the graphite is slightly smaller than the effective "nuclear size" of the cylinder. However, the validity of the assumptions concerning the space dependence of the thermal spectrum over the peripheral regions of the core is uncertain, so the values given in Table 3.4 are recommended as design criteria until further studies concerning these corrections can be made.

3.8 Reactivity Effects of Changes in Densities of Fuel Salt and Graphite

Included in the category of reactivity effects of graphite and salt density changes are those due to graphite shrinkage, fuel soakup, entrained gas, and uncertainties in measured values of the material densities at operating conditions. Density coefficients of reactivity were calculated for the simplified, one-region-cylinder model of the core. In these calculations, as in the similar analysis of the temperature reactivity coefficients (Sec 3.7), lattice effects of heterogeneity were considered. The density coefficients relate the fractional change in multiplication constant to the fractional changes in densities;

$$\frac{\delta k}{k} = \beta_s \frac{\delta N_s}{N_s} + \beta_g \frac{\delta N_g}{N_g} . \tag{3.9}$$

The values of the coefficients, β, obtained for the three fuel salts studied are included in Table 3.5. These results directly indicate the reactivity effect of uncertainties in the measured values of the material densities. In order to apply the results to calculate the effects of graphite shrinkage and fuel soakup, some assumptions must be made concerning the changes in the lattice geometry produced by these perturbations. If shrinkage is uniform in the transverse direction across a graphite stringer, and if the center of the stringer remains fixed during contraction, the effect will be to open the gaps between stringers and allow fuel salt to enter the gaps. The homogenized density of the graphite remains constant; however, the effective salt density, N_s, is increased. If v_s and v_g are the volume fractions of salt and graphite in the lattice, the fractional change in salt density is calculated as

$$\delta v_s = -\delta v_g \tag{3.10}$$

and

$$\frac{\delta N_s}{N_s} = \frac{\delta v_s}{v_s} = -\frac{v_g}{v_s}\frac{\delta v_g}{v_g} = \frac{v_g}{v_s} f_1 , \tag{3.11}$$

where f_1 is the fractional decrease in graphite volume due to shrinkage. From Eq. (3.9), the reactivity change is

$$\frac{\delta k}{k} = \beta_s \frac{v_g}{v_s} f_1 = 3.44\, \beta_s\, f_1 \,, \qquad (3.12)$$

in which the salt/graphite volume ratio, 0.225/0.775, has been inserted. Use of the above relation in conjunction with the density coefficients indicates that shrinkage of the graphite by 1% of its volume corresponds to reactivity additions of about 0.65% $\delta k/k$ in fuels A and C and 1.2% $\delta k/k$ in fuel B.

Fuel soakup reactivity additions may also be estimated from Eq. (3.12). For this purpose the graphite shrinkage fraction f_1 need only be replaced by f_2, the porous volume fraction of graphite which is filled with fuel salt.

3.9 Summary of Nuclear Characteristics

The nuclear characteristics of the MSRE have been calculated for three fuel mixtures, designated A, B, and C, which differ primarily in content of fuel and/or fertile material. The distinguishing features of the three fuels are as follows: fuel A contains uranium highly (~93%) enriched in U^{235} and 1 mole % thorium; fuel B contains highly enriched uranium but no fertile material; and fuel C contains about 0.8 mole % uranium with the U^{235} enrichment reduced and no thorium. The characteristics of the reactor with each of the three fuels are summarized in Table 3.5. The uranium concentrations and inventories are listed for the initial, clean, noncirculating, critical condition and for the long-term operating condition. The neutron fluxes are given for the operating uranium concentrations, and the reactivity parameters apply to the initial critical concentration.

Detailed neutron balances were calculated by the computer programs for each of the three fuels. The neutron balance for the reactor filled with fuel C at the clean, critical concentration is summarized in Tables 3.6 and 3.7. Neutron absorptions and leakages associated with various portions of the reactor vessel and its contents are listed in Table 3.6. Table 3.7 gives a detailed breakdown of the neutron absorptions by element in each region of the reactor.

Table 3.5. Nuclear Characteristics of MSRE with Various Fuels

	Fuel A	Fuel B	Fuel C
Uranium concentration (mole %)			
Clean, noncirculating			
U^{235}	0.291	0.176	0.291
Total U	0.313	0.189	0.831
Operating[a]			
U^{235}	0.337	0.199	0.346
Total U	0.362	0.214	0.890
Uranium inventory[b] (kg)			
Initial criticality			
U^{235}	79	48	77
Total U	85	52	218
Operating[a]			
U^{235}	91	55	92
Total U	98	59	233
Thermal neutron fluxes[c] (neutrons cm^{-2} sec^{-1})			
Maximum	3.31×10^{13}	5.56×10^{13}	3.29×10^{13}
Average in graphite-moderated regions	1.42×10^{13}	2.43×10^{13}	1.42×10^{13}
Average in circulating fuel	3.98×10^{12}	6.81×10^{12}	3.98×10^{12}
Reactivity coefficients[d]			
Fuel temperature $[(°F)^{-1}]$	-3.03×10^{-5}	-4.97×10^{-5}	-3.28×10^{-5}
Graphite temperature $[(°F)^{-1}]$	-3.36×10^{-5}	-4.91×10^{-5}	-3.68×10^{-5}
Uranium concentration	0.2526	0.3028	0.1754[e] 0.2110[f]
Xe^{135} concentration in core $(atom/barn\text{-}cm)^{-1}$	-1.28×10^{8}	-2.04×10^{8}	-1.33×10^{8}
Xe^{135} poison fraction	-0.746	-0.691	-0.752
Fuel salt density	0.190	0.345	0.182
Graphite density	0.755	0.735	0.767
Prompt neutron lifetime (sec)	2.29×10^{-4}	3.47×10^{-4}	2.40×10^{-4}

[a] Fuel loaded to compensate for 4% $\delta k/k$ in poisons.

[b] Based on 73.2 ft^3 of fuel salt at 1200°F.

[c] At operating fuel concentration, 10 Mw.

[d] At initial critical concentration. Where units are shown, coefficients for variable x are of the form $(1/k)/(\partial k/\partial x)$; other coefficients are of the form $(x/k)/(\partial k/\partial x)$.

[e] Based on uranium isotopic composition of clean critical reactor.

[f] Based on highly (~93%) enriched uranium.

Table 3.6. Neutron Balance for Fuel C, Clean, Critical
(per 10^5 neutrons produced)

Region	Absorptions					
	U^{235}	U^{238}	Salt[a]	Graphite	INOR	Total
Main core[b]	45,459	7252	4364	795	1380	59,250
Upper head[c]	3,031	928	675	1	131	4,766
Lower head[d]	1,337	449	294	0	1480	3,560
Downcomer	1,496	338	203	0	0	2,037
Core can	0	0	0	0	3635	3,635
Reactor vessel	0	0	0	0	3056	3,056
Total	51,323	8967	5536	796	9682	76,304

Surface	Leakage		
	Fast	Slow	Total
Top	1,991	10	2,001
Sides	19,619	1004	20,623
Bottom	1,068	4	1,072
Total	22,678	1018	23,696

[a]Constituents other than U^{235} and U^{238}.
[b]Regions J, K, L, M, N, and T (Fig. 3.3).
[c]Regions D, E, G, H, Q, R, and S (Fig. 3.3).
[d]Regions O and P (Fig. 3.3).

Table 3.7. Detailed Distribution of Neutron Absorptions with Fuel C

Region[a]	Absorptions per 10^5 Neutrons Produced												
	U^{235}	U^{238}	U^{234}	U^{236}	Li^6	Li^3	Be	Zr	F(n,α)	F(n,γ)	Graphite	INOR	Total
A	0	0	0	0	0	0	0	0	0	0	0	324	324
B	0	0	0	0	0	0	0	0	0	0	0	2578	2,578
C	0	0	0	0	0	0	0	0	0	0	0	154	154
D	1,518	546	8	4	26	13	27	185	115	37	0	0	2,478
E	571	155	3	1	11	6	8	44	30	11	0	123	964
F	1,496	338	7	2	27	17	14	77	39	20	0	0	2,037
G	424	105	2	1	7	4	5	27	17	7	0	0	598
H	494	114	2	1	9	5	5	26	15	7	1	8	687
I	0	0	0	0	0	0	0	0	0	0	0	3635	3,635
J	42,837	6768	160	48	905	510	221	1247	517	480	762	0	54,456
K	0	0	0	0	0	0	0	0	0	0	0	1380	1,380
L	304	58	1	0	6	4	2	11	5	3	7	0	402
M	1,149	199	4	1	23	13	6	37	14	13	20	0	1,480
N	419	85	2	1	8	5	3	17	6	5	6	0	557
O	438	112	2	1	8	5	4	28	12	7	0	790	1,407
P	899	337	5	2	11	8	15	120	44	22	0	690	2,153
Q	19	7	0	0	0	0	0	2	1	0	0	0	30
R	3	1	0	0	0	0	0	0	0	0	0	0	5
S	2	0	0	0	0	0	0	0	0	0	0	0	3
T	750	142	3	1	15	9	5	29	13	9	0	0	976
Total	51,329	8967	199	63	1056	599	315	1850	828	621	796	9682	76,304

[a]Letters refer to designations in Table 3.1 and Fig. 3.3.

4. CONTROL ROD CALCULATIONS

4.1 Control Rod Geometry

The MSRE control element consists basically of a hollow poison cylinder, 1.08 in. OD × 0.12 in. thick. Figure 3.2 illustrates those details of the configuration of the element which are important in determining the reactivity worth of the rods. Three such elements are used, located in a square array about the core center in the positions shown in Fig. 3.2. The fourth position of the array is occupied by a graphite sample assembly.

4.2 Method of Calculation of Rod Reactivity

4.2.1 Total Worth

Several practical simplifications and approximations were necessary in order to estimate the reactivity worth of the control element described above. These were made in accordance with the present "state of the art" in control rod theory, reviewed in ref 17. Several of the computational devices used in the present studies are discussed in this report. The basic physical assumptions involved in the MSRE design calculations are as follows:

a. The Gd_2O_3-Al_2O_3 poison cylinders are assumed to be black to thermal neutrons and transparent to neutrons above thermal energies ($\gtrsim$ 1 ev). The former assumption should be excellent, since the poison material has an absorption-to-scattering ratio in excess of 10^3 in the thermal energy range. The latter assumption is in error, since Gd^{155} and Gd^{157} resonances occur in the epithermal range, and thus have the effect of producing a "gray region" in absorption at these energies. Because these resonances are closely spaced and have large resonance scattering components, it is difficult to obtain meaningful estimates of the resonance self-shielding in the posion tube. Since the total epithermal absorption is expected to be only a fraction of that in the thermal region, this effect was neglected in the calculations.

b. Transmission of thermal neutrons through the INOR-8 thimbles and across the gap between thimble and cylinder was calculated using the P-1 approximation. The average absorption-to-scattering ratio for thermal neutrons traversing the INOR-8 is about 0.1. This means that diffusion theory should be adequate in calculating the thimble transmission, relative to the other simplifications used in the rod worth calculations. The basic mathematical relations involve the control element blackness, B, which is the probability of capture for thermal neutrons incident on the outside surface of the thimble. This expression is[18]

$$B = 1 - \beta \frac{F(\rho_g/L)}{F(\rho_0/L)} , \tag{4.1}$$

where β is the probability that neutrons entering the gap from the thimble miss the central poison cylinder, and ρ_g and ρ_0 are the inner and outer radii of the thimble. The function $F(x)$ is defined in terms of Bessel functions:

$$F(x) = \frac{I_0(x) + a\, K_0(x) + \frac{2D}{L} I_1(x) - \frac{2D}{L} a\, K_1(x)}{I_0(x) + a\, K_0(x) - \frac{2D}{L} I_1(x) + \frac{2D}{L} a\, K_1(x)} ;$$

$$a = \frac{I_1(\rho_g/L) - \frac{L}{2D} \frac{1-\beta}{1+\beta} I_0(\rho_g/L)}{K_1(\rho_g/L) + \frac{L}{2D} \frac{1-\beta}{1+\beta} K_0(\rho_g/L)} .$$

In the above formulas, D and L are the thermal diffusion coefficient and diffusion length in the INOR-8. When the central poison tube is withdrawn, β is equal to unity. With the rod in place, Newmach's approximation for β was used.[19] This is based on the assumption that the angular distribution of neutrons entering the gap is correctly given by P-1 theory. For a black central cylinder, the resulting expression is

$$\beta = \frac{1 - r + f(r)}{1 + r + f(r)} , \tag{4.2}$$

where

$$r = \rho_{rod}/\rho_g \ ,$$

$$f(r) = 1 - \frac{2}{\pi} \sin^{-1} r - \frac{2}{\pi} r\sqrt{1 - r^2} \ .$$

Equations (4.1) and (4.2) were applied to the calculation of the rod reactivity worth by the use of a linear extrapolation distance boundary condition at the control element surface. The extrapolation distance depends not only on the control element blackness, but also on the relative size of the control region.[20] The expression used was

$$\lambda_{ex} = \frac{\phi}{d\phi/dn} = \lambda_{tr} \frac{4}{3B} - g(\rho_0/\lambda_{tr}) \ , \qquad (4.3)$$

where n is the outward normal to the control surface and λ_{tr} is the transport mean free path for thermal neutrons in the core. As indicated in Eq. (4.3), the function g(y) depends only on the ratio of the control radius to the transport mean free path; this function increases from zero at y = 0 to 0.623 for large y. Reference 19, p 725, gives a plot of the value of $\lambda_{ex}/\lambda_{tr}$ vs y for black cylinders (B = 1). This was used to determine g(y) for thermal neutrons incident on the MSRE element.

c. The remaining simplifications in the reactivity worth calculations deal with the geometry of the reactor core and control rod configuration. These calculations of δk/k due to insertion of the central poison cylinders were made using the EQUIPOISE-3 program. Use of this numerical solution method, together with the practical restriction to two-dimensional calculations, required that the reactor-rod configuration be approximated in x-y geometry. The configuration used for a model is shown in Fig. 4.1. This figure represents a horizontal cross section of the core. The basic model is that of a parallelepided with square base. The control regions are represented by regions of square cross section, with the perimeter of each square equal to the actual circumference of the control thimble. Thus the total effective absorptions of the control regions were equal in the model and the actual element. The overall transverse dimension of the core was so chosen that the total geometric

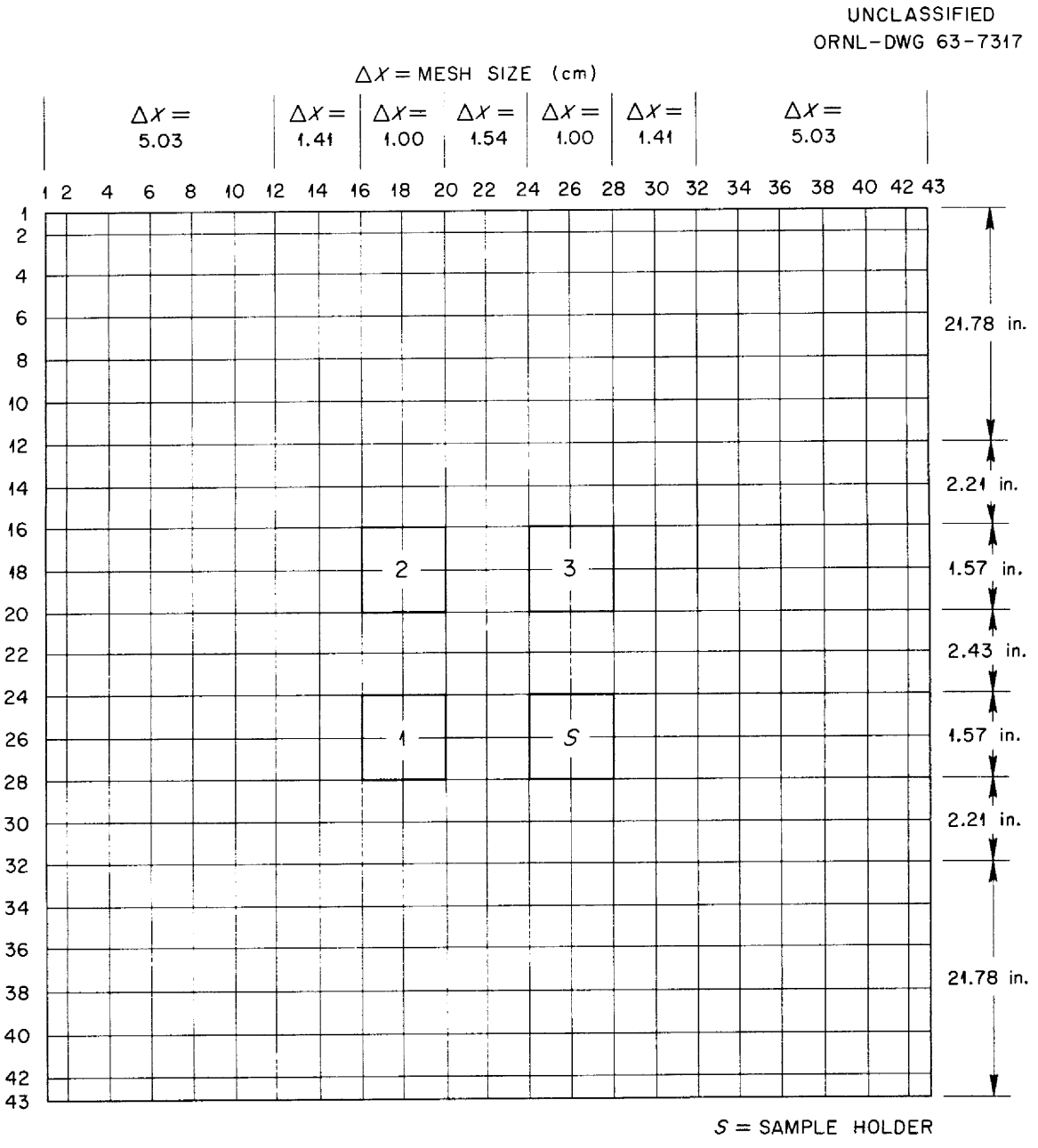

Fig. 4.1. Cross Sectional Model of MSRE Core Used in Equipoise Calculations of Control Rod Worth.

buckling in the transverse (x–y) dimension was equal to the effective radial buckling of the actual cylindrical core. Axial leakage was accounted for by insertion of an effective axial buckling. Because of the limitation of the calculations to two dimensions, it was necessary to assume that the layout shown in Fig. 4.1 extended completely through the active length of the core. In actuality, the maximum penetration distance for the poison cylinders is slightly less than this length.

The model shown in Fig. 4.1 is based on practical limitations concerning the total number of mesh points in the EQUIPOISE program. The attempt was made to adjust the mesh size so that minimum error is obtained in the central region of the core where the control elements are located. This is the region of maximum nuclear importance, and also that of maximum spatial flux variation when the rods are inserted. Representation of the reactor transverse boundary as a square is expected to generate relatively little error in the calculations of the total rod worth.

The effect of the graphite sample holder was neglected in these preliminary calculations. Further studies are planned to examine this effect, and also to improve on some of the above approximations.

4.2.2 Differential Worth

Determination of the worth of partially inserted rods is of importance in setting control rod speeds, in setting limiting rod positions, and in predicting the required rod motion during startup and normal operation. In keeping with the practical restriction to two-dimensional diffusion calculations, a preliminary estimate of the differential worth was based on an r–z geometry model of the core. The three control elements were replaced by a single absorber shell, concentric with the core axis. The relative change in $\delta k/k$ was calculated as a function of the penetration distance of the shell in the core. The radius and thickness of the shell were determined by equating the effective surface-to-volume ratio of the shell to that of the actual elements. The relative change in $\delta k/k$ was then normalized to the total rod worth obtained from the calculations described in Sec 4.2.1.

4.3 Results of Calculations

4.3.1 Total Reactivity Worth

The total control worth of all three rods inserted all the way through the core, obtained from the calculations described in the previous section, is listed in Table 4.1. The worth of the individual rods was also estimated for one of the fuel salts (fuel A), and the results are included in Table 4.1. When converted to represent fractions of the total worth of all three rods, these latter results should be nearly equal for all three fuel salts. Note that the rod worths are not additive, since there is appreciable "shadowing" between the rods. Also, rods 1 and 3 are worth slightly more than rod 2, due to the relatively greater influence of flux depression, caused by thimbles 1 and 3, on the position of rod 2.

4.3.2 Differential Worth

Results of the r-z calculation for the partially inserted rod bank are shown in Fig. 4.2. This is a plot of the fraction of the total axial core height to which the rods are inserted. It is important to note that these results apply to the three rods moving as a unit; effects of moving a single rod with the others held fixed in some partially inserted position are not treated in these calculations.

Table 4.1. Control Rod Worths in the MSRE

Fuel	Rod Configuration	Worth (% δk/k)
A	3 Rods in	5.6
	Rod 1 in, rods 2 and 3 out	2.4
	Rod 2 in, rods 1 and 3 out	2.3
	Rods 1 and 3 in, rod 2 out	4.4
	Rods 1 and 2 in, rod 3 out	4.1
B	3 Rods in	7.6
C	3 Rods in	5.7

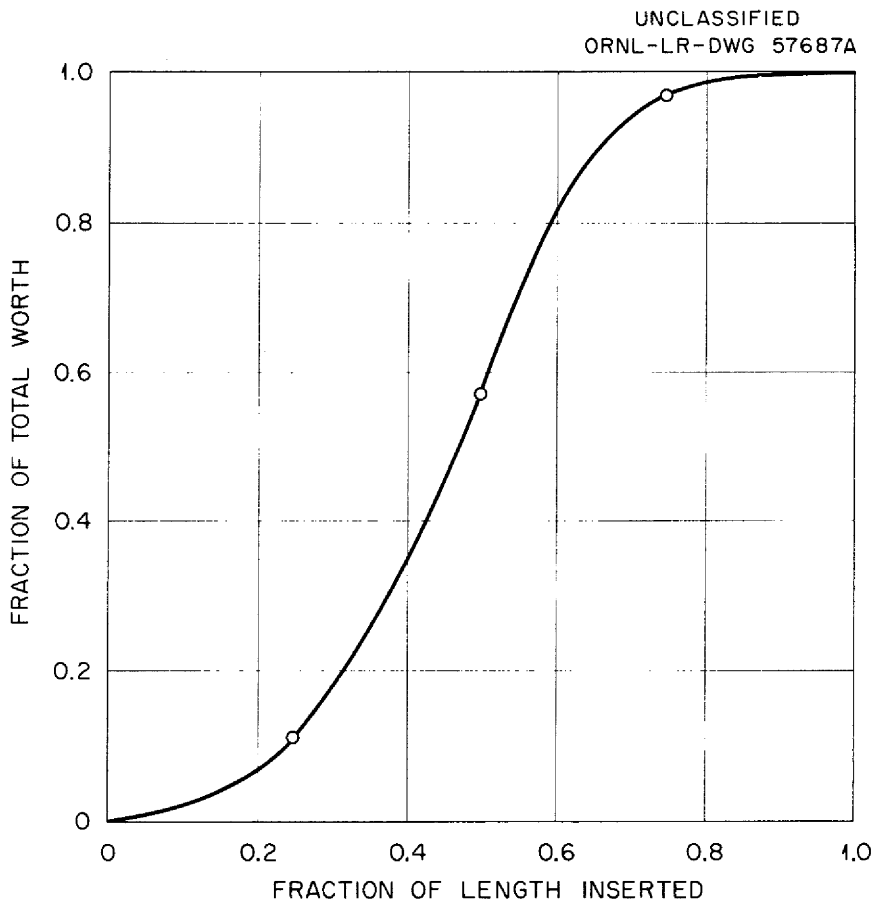

Fig. 4.2. Effect of Partially Inserted Rods.

5. CORE TEMPERATURES

When the reactor is operated at power there is a wide range of temperatures in the graphite and fuel in the core. The temperature distribution cannot be observed experimentally, but some information on the distribution is necessary for the analysis of reactivity changes during power operation. The method by which MSRE core temperatures were predicted is described in detail in ref 21. The calculational method combines the flow distribution in a hydraulic model of the core with the power-density distribution predicted for the nuclear model. The numerical results presented here were computed with the power-density distribution appropriate for fuel C, but calculations for fuels A and B gave practically the same results. (The numerical results in ref 17 were computed for fuel B, with a slightly different model from that used in the calculations whose results are reported here.)

5.1 Overall Temperature Distributions at Power

The temperature distribution in the MSRE core can be regarded as a composite of the overall temperature distributions in the fuel and moderator, upon which are superimposed local temperature variations within individual fuel channels and moderator stringers. The overall temperature distributions are determined by the gross distribution of the power density and the fuel flow pattern. The local variations depend on the fluid flow and heat transfer conditions associated with the individual channels. Since the overall temperature distributions contribute most to the temperature-induced reactivity effects, these are described in detail. Details of local temperature variations are considered only where such consideration is essential to evaluating the overall distribution.

5.1.1 Reactor Regions

A significant fraction of the nuclear power produced in this reactor is generated in the fuel-containing regions of the reactor vessel outside the fuel-graphite matrix which forms the main portion of the

core. These regions contribute to the total temperature rise of the fuel as it passes through the reactor and must, therefore, be included in the core temperature calculations. The 20-region model of the reactor (see Fig. 3.3 and Table 3.1) used for the nuclear calculations was also used to evaluate the core temperatures. The regions designated J, L, M, N, and T were combined to form the main portion of the core, and the remaining fuel-bearing regions were treated separately.

Hydraulic studies on one-fifth-scale and full-scale models of the reactor vessel showed that the vertical fuel velocity varies with radial position in the main portion of the core. The velocity is nearly constant over a large portion of the core, but higher velocities occur near the axis and near the outer radius. To allow for this, three radial regions were used in calculating the temperature distributions in the main portion of the core.

5.1.2 Fuel Temperatures

Nearly all of the nuclear power is removed from the reactor vessel by the circulating fuel stream, so that the fuel temperature rise and flow rate define the operating power level of the reactor. The temperature calculations were based on a nominal power level of 10 Mw, with a 50°F temperature rise across the reactor and a fuel flow rate of 1200 gpm. The reactor inlet and outlet temperatures were set at 1175°F and 1225°F, respectively. These temperatures permit presentation of the distributions in abolute terms, but the shape of the distributions is unaffected by this choice.

Peripheral Regions. – Approximately 14% of the reactor power is produced in or transferred to the fuel-bearing regions surrounding the main portion of the core. Since the temperature rise of the fuel, as it passes through any one of these regions, is small compared with the rise in the main portion of the core, no attempt was made to evaluate, exactly, the fuel temperature distributions in each peripheral region. Instead, the mean temperature rise for each region was calculated from the fraction of the total power produced in the region and the fraction of the total flow rate through it. The inlet temperature for each region

was assumed constant at the mixed-mean outlet temperature of the preceding region. Each peripheral region was assigned an approximate bulk average temperature midway between the inlet and outlet temperatures. Table 5.1 summarizes the flow rates, heat rates, and fuel temperatures in the various reactor regions.

Main Portion of the Core. – The wide variations in fuel temperature, both radially and axially, in the main part of the core necessitate a more detailed description of the temperature distribution.

Table 5.1. Flow Rates, Heat Rates, and Temperatures in Reactor Regions[a]

Region	Flow (gpm)	Heat Rate[b] (kw)	Temperature Rise[b] (°F)	Average Temperature[c] (°F)
D	1142	355.3	1.9	1225.2
E	1142	115.8	0.6	1224.0
F	1200	378.2	1.9	1176.0
G	1142	82.7	0.4	1223.5
H	1142	95.7	0.5	1223.0
J	1142	8121.3	42.7	d
L	17	59.3	20.9	d
M	1183	223.0	1.1	d
N	1200	84.1	0.4	d
O	1200	89.9	0.4	1178.4
P	1200	252.8	1.3	1177.6
Q	17	3.9	1.4	1201.0
R	17	0.7	0.2	1200.2
S	17	0.5	0.2	1200.0
T	41	136.9	20.0	d

[a]Regions not containing fuel are excluded.

[b]At 10 Mw. Includes heat transferred to the fuel from adjoining regions.

[c]With T_{in} = 1175°F, T_{out} = 1225°F.

[d]Actual temperature distribution calculated for this region. See text.

The average temperature of the fuel in a channel at any axial position is equal to the channel inlet temperature plus a rise proportional to the sum of the heat generated in the fuel and that transferred to it from the adjacent graphite as the fuel moves from the channel inlet to the specified point. The heat produced in the fuel follows very closely the radial and axial variation of the fission power density. Since the heat production in the graphite is small, no great error is introduced by assigning the same spatial distribution to this term. Then, if axial heat transfer in the graphite is neglected, the net rate of heat addition to the fuel has the shape of the fuel power density. The fuel temperature rise is inversely proportional to the volumetric heat capacity and velocity. Thus

$$T_f(r,z) = T_f(z = 0) + \int_0^z \frac{(Q_f)_m}{(\rho c_p)_f u} P_f(r,z)\, dz \ , \qquad (5.1)$$

where Q_f is an equivalent specific power which includes the heat added to the fuel from the graphite. The channel inlet temperature, $T_f(z = 0)$, is assumed constant for all channels, and its value is greater than the reactor inlet temperature because of the peripheral regions through which the fuel passes before it reaches the inlet to the main part of the core. The volumetric heat capacity, $(\rho c_p)_f$, is assumed constant, and only radial variations in the fuel velocity, u, are considered. It is further assumed that the radial and axial variations in the power-density distribution are separable:

$$P(r,z) = A(r)\, B(z) \ . \qquad (5.2)$$

Then

$$T_f(r,z) = T_f(z = 0) + \frac{(Q_f)_m}{(\rho c_p)_f} \frac{A(r)}{u(r)} \int_0^z B(z)\, dz \ . \qquad (5.3)$$

If the sine approximation for the axial variation of the power density (Fig. 3.10) is substituted for B(z), Eq. (5.3) becomes

$$T_f(r,z) = T_f(z = 0) + \kappa \frac{A(r)}{u(r)} \left\{ \cos \alpha - \cos \left[\frac{\pi}{78.15} (z + 5.72) \right] \right\} \ . \qquad (5.4)$$

In this expression, κ is a collection of constants,

$$\kappa = \frac{78.15}{\pi} \frac{(Q_f)_m}{(\rho c_p)_f} , \tag{5.5}$$

and

$$\alpha = \frac{\pi}{78.15} (0 + 5.72) . \tag{5.6}$$

The limits within which Eq. (5.4) is applicable are the lower and upper boundaries of the main part of the core, namely, $0 \leq z \leq 64.6$ in. It is clear from this that the shape of the axial temperature distribution in the fuel in any channel is proportional to that of the central portion of the general curve $[1 - \cos \beta]$. The axial distribution for the hottest channel in the MSRE is shown in Fig. 5.1, where it is used to provide a reference for the axial temperature distribution in the graphite.

The radial distribution of the fuel temperature near the core midplane is shown in Fig. 5.2 for the reference conditions at 10 Mw. This distribution includes the effects of the distorted power-density distribution (Fig. 3.11) and the radial variations in fuel velocity. At the reference conditions the main core inlet temperature is 1179°F and the mixed-mean temperature leaving that region is 1222°F. The additional heat required to raise the reactor outlet temperature to 1225°F is produced in the peripheral regions above the main part of the core. The general shape of the radial temperature profile is the same at all axial positions in the main portion of the core.

5.1.3 Graphite Temperature

Since all of the heat produced in the graphite must be transferred to the circulating fuel for removal from the reactor, the steady-state temperature of the graphite is higher than that of the fuel in the adjacent channels. This temperature difference provides a convenient means of evaluating the overall graphite temperature distribution; that is, by adding the local graphite-fuel temperature differences to the previously calculated fuel temperature distribution.

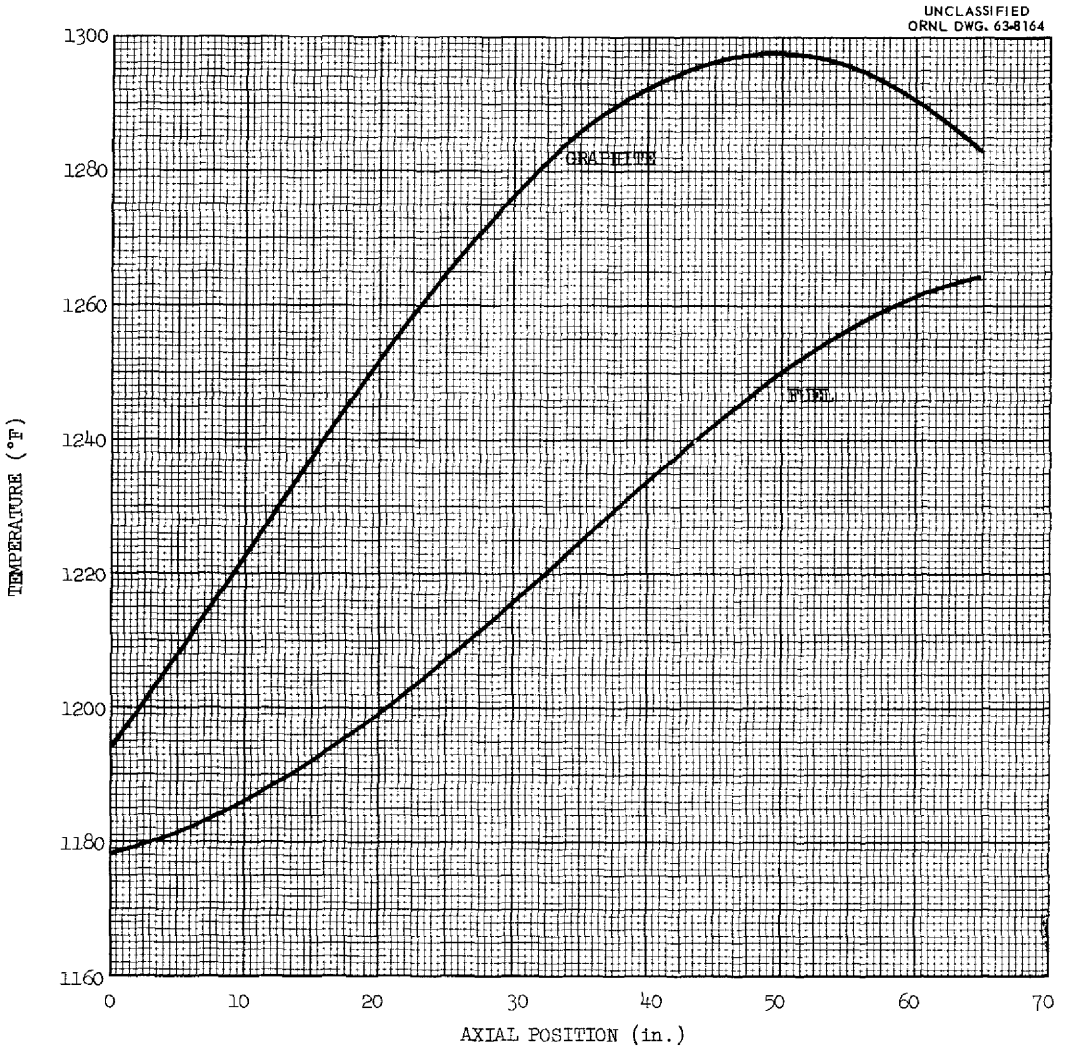

Fig. 5.1. Axial Temperature Profiles in Hottest Channel and Adjacent Graphite Stringer.

Nearly all the graphite in the MSRE (98.7%) is contained in the regions which are combined to form the main portion of the core. Since the remainder would have only a small effect on the system characteristics, the graphite temperature distribution was evaluated for the main part of the core only.

Local Graphite-Fuel Temperature Differences. — In order to evaluate the local graphite-fuel temperature differences, the core was considered in terms of a number of unit cells, each containing fuel and graphite. Axial heat transfer in the graphite was neglected and radially uniform

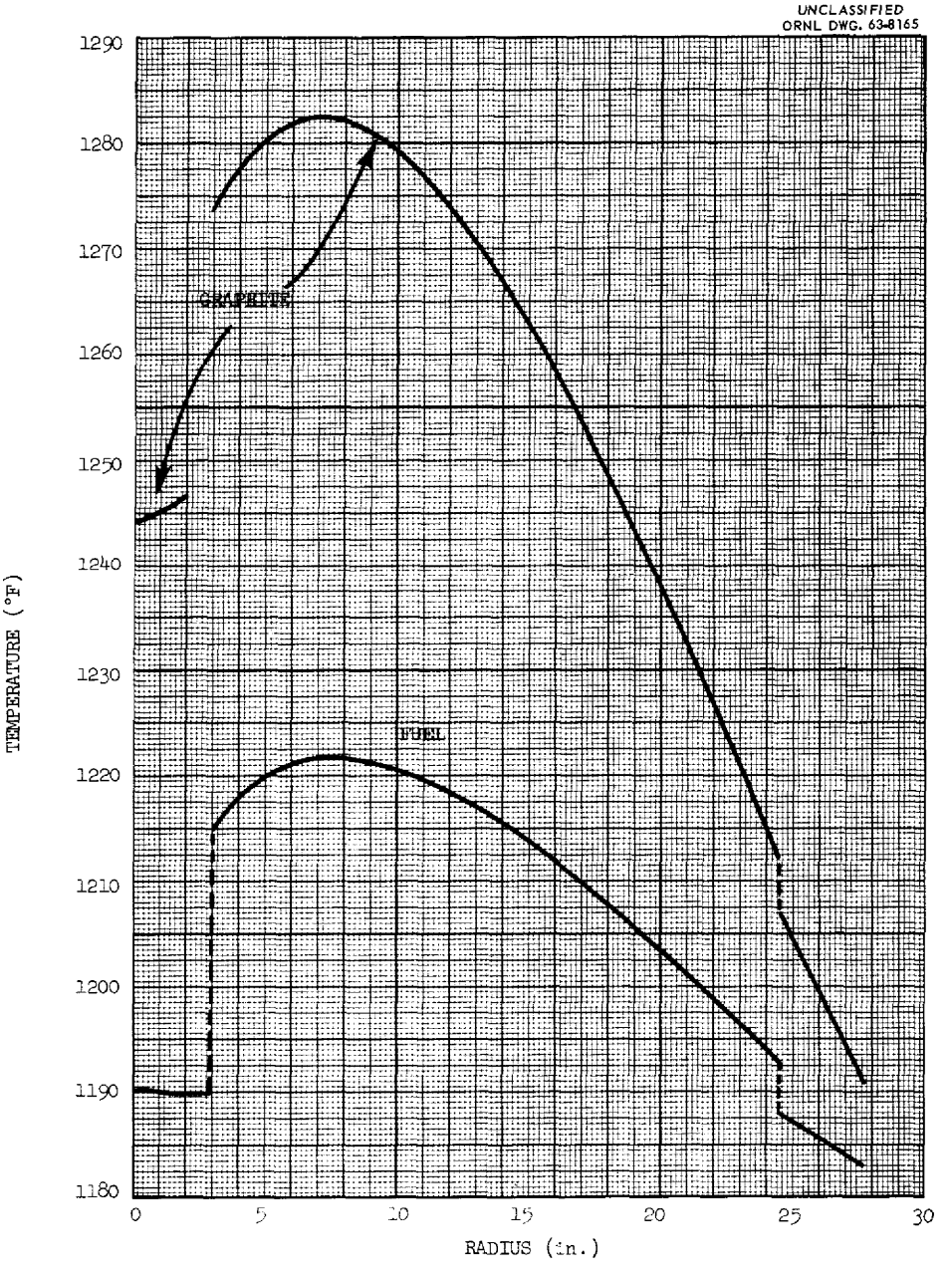

Fig. 5.2. Radial Temperature Profiles Near Core Midplane.

heat generation terms were assumed for the fuel and graphite in each cell. In general, only the difference between the mean temperatures of the graphite stringers and fuel channels was calculated as a function of radial and axial position.

The difference between the mean graphite and fuel temperatures in a unit cell can be broken down into three parts:

1. the Poppendiek effect, which causes the fuel near the wall of a channel to be hotter than the mean for the channel;
2. the temperature drop due to the contact resistance at the graphite-fuel interface; and
3. the temperature drop in the graphite resulting from the internal heat source.

When a fluid with an internal heat source flows through a channel, the lower velocity of the fluid near the channel wall allows that part of the fluid to reach a temperature above the average for the channel. This effect is increased when heat is transferred into the fluid through the channel walls, as is the case in the MSRE. Equations have been developed[22,23] to evaluate the difference between the temperature of the fluid at the wall and the average for the channel. These equations were applied to the reactor, assuming laminar flow in all of the channels. This tends to overestimate slightly the temperature rise in the few channels where the flow may be turbulent.

No allowance was made for a temperature difference due to the contact resistance at the graphite-fuel interface in these calculations. An estimate of this resistance was made by assuming a 1-mil gap, filled with helium, between the graphite and fuel. This rather pessimistic assumption led to a temperature difference which was very small compared with the total.

The difference between the mean temperature of a graphite stringer and the surface temperature was calculated for two simplified geometries: a cylinder with a cross-sectional area equal to that of a stringer and a slab with a half thickness equal to the normal distance from the center of a stringer to the surface of a fuel channel. The value assigned to

the graphite was obtained by linear interpolations between these results on the basis of surface-to-volume ratio.

The local graphite-fuel temperature difference was calculated as a function of position in the core for three degrees of fuel soakup in the graphite: 0, 0.5, and 2.0 vol % of the graphite. In each case, uniform distribution of the fuel within the graphite was assumed. Table 5.2 gives the maximum difference between mean stringer and mean fuel channel temperatures for the three conditions. The distribution of the fuel soaked into the graphite has little effect on the total temperature difference. For 2 vol % permeation, concentration of the fuel near the outer surface of the graphite increased the ΔT by 2°F.

Table 5.2. Maximum Values of Graphite-Fuel Temperature Difference as a Function of Fuel Permeation

Fuel Permeation (vol % of graphite)	0	0.5	2.0
Graphite-fuel temperature difference (°F)			
Poppendiek effect in fuel	55.7	58.3	65.4
Graphite temperature drop	5.5	6.7	9.8
Total	61.2	65.0	75.2

Overall Distribution. – Since the Poppendiek effect and the temperature drop through the graphite are both influenced by the heat generated in the graphite, the spatial distribution of the graphite temperature is affected by the graphite power-density distribution. The graphite power density is treated in detail in Sec. 14.1, for fuel C with no fuel permeation of the graphite. The distribution shown in Figs. 14.1 and 14.2 was used to evaluate the graphite temperatures in Figs. 5.1 and 5.2. Figure 5.1 shows the axial distribution of the mean temperature in a graphite stringer adjacent to the hottest fuel channel. Because of the continuously increasing fuel temperature, the axial maximum in the graphite temperature occurs somewhat above the midplane of the core. The

overall radial distribution of the graphite temperature near the core midplane is shown in Fig. 5.2.

5.2 Average Temperatures at Power

The concept of average temperatures has a number of useful applications in operating and in describing and analyzing the operation of a reactor. The bulk average temperature, particularly of the fuel, is essential for all material balance and inventory calculations. The nuclear average temperatures of the fuel and graphite, along with their respective temperature coefficients of reactivity, provide a convenient means of assessing the reactivity effects associated with temperature changes. Both the bulk average and nuclear average temperatures can be described in terms of the reactor inlet and outlet temperatures, but, because of complexities in the reactor geometry and the temperature distributions, the numerical relations are not obvious.

5.2.1 Bulk Average Temperatures

Bulk average temperatures ($\overline{T}$) were obtained by weighting the overall temperature distributions with the volume fraction of salt or graphite and integrating over the volume of the reactor.

The fuel bulk average temperature was calculated for the fuel within the reactor vessel shell. (The contents of the inlet flow distributor and the outlet nozzle were not included.) A large fraction of the salt in the vessel is in the peripheral regions, where detailed temperature distributions were not calculated. In computing the average for the reactor, average temperatures shown in Table 5.1 were used for these regions. The average temperature in the main part of the core was computed by numerical integration of the calculated temperature distribution. At the reference condition (1175°F inlet, 1225°F outlet), the fuel bulk average temperature for all of the fuel in the reactor vessel was computed to be 1199.5°F. Thus, assuming linear relationships, the fuel bulk average temperature is given by

$$\overline{T}_f = T_{in} + 0.49(T_{out} - T_{in}) \ . \qquad (5.7)$$

Only the graphite in the main portion of the core had to be included in the calculation of the graphite bulk average temperature, since this region contains 98.7% of all the graphite. For fuel C with no permeation, the bulk average graphite temperature at the 10-Mw reference condition is 1229°F. This temperature increases with increasing permeation of the graphite by fuel; earlier calculations of this effect showed a 4.4°F increase in graphite bulk average temperature as the fuel permeation was increased from 0 to 2%.

5.2.2 Nuclear Average Temperatures

The nuclear average temperatures (T^*) of the fuel and graphite were calculated in the same way as the bulk average temperatures, except that the temperature distributions were weighted with their respective nuclear importances as well as with the amounts of material. The temperature weighting functions described in Sec. 3.7.2 include all of the nuclear average weighting factors. These functions were applied to the fuel temperature distribution and resulted in a fuel nuclear average temperature of 1211°F when the inlet temperature is 1175°F and the outlet is 1225°F. With the same inlet and outlet temperatures and no fuel permeation, the graphite nuclear average temperature was calculated to be 1255°F. (With 2% permeation the calculated graphite nuclear average temperature would be higher by 7°F.)

The relations between inlet and outlet temperatures, nuclear average temperatures, and power are all practically linear so that the following approximations can be made:

$$T_{out} = T_{in} + 5.0\ P\ , \tag{5.8}$$

$$T_f^* = \left(\frac{T_{out} + T_{in}}{2}\right) + 1.1\ P = T_{out} - 1.4\ P\ , \tag{5.9}$$

$$T_g^* = \left(\frac{T_{out} + T_{in}}{2}\right) + 5.5\ P = T_{out} + 3.0\ P\ , \tag{5.10}$$

where the temperatures are in °F and P is the power in Mw.

5.3 Power Coefficient of Reactivity

Whenever the reactor power is raised, temperatures of the fuel and graphite throughout the core must diverge. As shown in the preceding sections, the shape of the temperature distributions at power and the relations between inlet, outlet, and average temperatures are inherent characteristics of the system which are not subject to external control. The relation of the temperature distribution at high power to the temperature of the zero-power, isothermal reactor, on the other hand, can be readily controlled by the use of the control rods. When the reactivity effect of the rod poisoning is changed, the entire temperature distribution is forced to shift up or down as required to produce an exactly compensating reactivity effect.* Normally the rods are adjusted concurrently with a power change, to obtain a desired temperature behavior (to hold the outlet temperature constant, for example). The ratio of the change in rod poisoning effect, required to obtain the desired result, to the power change is then called the power coefficient of reactivity.**

Because of the way in which the nuclear average temperature is defined, the effect of fuel temperature changes on reactivity is proportional to the change in the nuclear average temperature of the fuel. Reactivity effects of graphite temperature changes are similarly described by the change in graphite nuclear average temperature. The net effect on reactivity of simultaneous changes in fuel and graphite temperature is

$$\frac{\Delta k}{k} = \alpha_f \Delta T_f^* + \alpha_g \Delta T_g^* \,, \qquad (5.11)$$

where α_f and α_g are the fuel and graphite temperature coefficients of reactivity. The change in rod <u>poisoning</u> is equal in both sign and magnitude to the reactivity effect of the temperature changes. (If the

---

*This statement and the discussion which follows refer to adjustments in rod positions and temperatures which are made in times too short for significant changes in other reactivity effects, such as xenon poisoning.

**Note that the power coefficient does not have a single value, as does a coefficient like the temperature coefficient, because its value depends on the arbitrary prescription of temperature variation with power.

effect of the desired temperature change is to decrease the reactivity, the rod poisoning must be decreased an equal amount to produce the temperature change.) Thus Eq. (5.11) can be used to evaluate the power coefficient of reactivity. When Eqs. (5.9) and (5.10) for T_f^* and T_g^* are substituted, Eq. (5.11) becomes either

$$\frac{\Delta k}{k} = (\alpha_g + \alpha_f)\Delta T_{out} + (3.0\ \alpha_g - 1.4\ \alpha_f)\Delta P \qquad (5.12)$$

or

$$\frac{\Delta k}{k} = (\alpha_g + \alpha_f)\Delta\left(\frac{T_{out} + T_{in}}{2}\right) + (5.5\ \alpha_g + 1.1\ \alpha_f)\Delta P\ . \qquad (5.13)$$

If T_{out} is held constant during power changes (i.e., if ΔT_{out} is zero), the power coefficient is

$$\frac{\Delta k/k}{\Delta P} = 3.0\ \alpha_g - 1.4\ \alpha_f\ . \qquad (5.14)$$

Similarly, if the mean of the inlet and outlet temperatures is to be held constant,

$$\frac{\Delta k/k}{\Delta P} = 5.5\ \alpha_g + 1.1\ \alpha_f\ . \qquad (5.15)$$

If there is no adjustment of reactivity by the control rods, the temperatures must change with power level in such a way that $\Delta k/k$ is zero. (This mode of operation might be called "hands-off" operation, because the rods are not moved.) The power coefficient of reactivity in this case is by definition equal to zero. The change in temperatures from the zero-power temperature, T_0, is found from

$$\frac{\Delta k}{k} = \alpha_f \Delta T_f^* + \alpha_g \Delta T_g^* = 0\ , \qquad (5.16)$$

$$\alpha_f(T_f^* - T_0) = -\alpha_g(T_g^* - T_0)\ . \qquad (5.17)$$

In conjunction with (5.9) and (5.10), this leads to

$$T_f^* = T_0 - \left(\frac{4.4\ \alpha_g}{\alpha_f + \alpha_g} \right) P , \tag{5.18}$$

$$T_g^* = T_0 + \left(\frac{4.4\ \alpha_f}{\alpha_f + \alpha_g} \right) P , \tag{5.19}$$

$$T_{out} = T_0 - \left(\frac{3.0\ \alpha_g - 1.4\ \alpha_f}{\alpha_f + \alpha_g} \right) P . \tag{5.20}$$

Note that the changes with power depend on the values of α_f and α_g, hence on the type of fuel in the reactor.

Thus it has been shown that the power coefficient of reactivity depends on the type of fuel and also on the chosen mode of control. Table 5.3 lists power coefficients of reactivity for three fuels and three modes of control. Also shown are temperatures which would be reached at 10 Mw if the zero-power temperature were 1200°F.

Table 5.3. Power Coefficients of Reactivity and Temperatures at 10 Mw

Mode of Control	Power Coefficient (% δk/k) Mw			Temperatures[a] (°F)			
	Fuel A	Fuel B	Fuel C	T_{out}	T_{in}	T_f^*	T_g^*
Constant T_{out}	−0.006	−0.008	−0.006	1200	1150	1186	1230
Constant $\frac{T_{out} + T_{in}}{2}$	−0.022	−0.033	−0.024	1225	1175	1211	1255
"Hands-off"							
Fuel A	0			1191	1141	1177	1221
Fuel B		0		1192	1142	1178	1222
Fuel C			0	1191	1141	1177	1221

[a]System isothermal at 1200°F at zero power.

6. DELAYED NEUTRONS

The kinetics of the fission chain reaction in the MSRE are influenced by the transport of the delayed neutron precursors. An exact mathematical description of the kinetics would necessarily include, in the equation for the precursor concentrations, terms describing the movement of the precursors through the core and the external loop. In order to render the system of kinetics equations manageable, the transport term was omitted from the equations used in MSRE analysis (see Sec 12.4.1). Thus the equations which were used were of the same form as those for a fixed-fuel reactor. Some allowance for the transport of the delayed neutron precursors was made by substituting "effective" values for delayed neutron yields in place of the actual yields. The kinetics calculations used "effective" yields equal to the contributions of the delayed neutron groups to the chain reaction under steady-state conditions.

6.1 Method of Calculation

In the calculation of the effective contributions during steady power operation, nonleakage probabilities were used as the measure of the relative importance of prompt and delayed neutrons. Spatial distributions for the precursors during steady operation were calculated and were used, together with the energy distribution, in computing nonleakage probabilities.[24]

The MSRE core was approximated by a cylinder with the flux (and precursor production) vanishing at the surfaces. Flow was assumed to be uniformly distributed. With these assumptions, the spatial distribution of precursors of a particular group in the core was found to be of the form

$$S(r,z) = S_0 e^{-\lambda t_c z/H} + \left[S_1 \sin \frac{\pi z}{H} - S_2 \cos \frac{\pi z}{H} + S_2 e^{-\lambda t_c z/H} \right] J_0 \left(\frac{2.4r}{R} \right) . \quad (6.1)$$

(See Sec 6.4 for definition of symbols.)

For the purpose of computing nonleakage probabilities, the spatial distribution of each group was approximated by a series:

$$S(r,z) = \sum_{m=1}^{\infty} \sum_{n=1}^{\infty} A_{mn} J_0 \left(\frac{j_m r}{R} \right) \sin \left(\frac{n\pi z}{H} \right) . \qquad (6.2)$$

The coefficients, A_{mn}, were evaluated from the analytical expression for $S(r,z)$. The nonleakage probability for a group of neutrons was then computed by assigning a nonleakage probability to each term in the series equal to

$$\frac{e^{-B_{mn}^2 \tau}}{1 + L^2 B_{mn}^2} , \qquad (6.3)$$

where

$$B_{mn}^2 = \left(\frac{j_m}{R} \right)^2 + \left(\frac{n\pi}{H} \right)^2 . \qquad (6.4)$$

The energy distribution of each delayed neutron group was taken into account by using an appropriate value for the age, τ, in the expression for the nonleakage probability.

6.2 Data Used in Computation

6.2.1 Precursor Yields and Half-Lives

The data of Keepin, Wimett, and Zeigler for fission of U^{235} by thermal neutrons were used.[25] Values are given in Table 6.1.

6.2.2 Neutron Energies

Mean energies shown in Table 6.1 for the first five groups are values recommended by Goldstein.[26] A mean energy of 0.5 Mev was assumed for the shortest-lived group, in the absence of experimental values.

6.2.3 Age

Prompt neutrons, with an initial mean energy of 2 Mev, have an age to thermal energies in the MSRE core of 292 cm^2 (this value was computed

by a MODRIC multigroup diffusion calculation). The age of neutrons from the different sources was assumed to be proportional to the lethargy; that is,

$$\tau_i = \frac{\log (E_i/E_{th})}{\log (E_{pr}/E_{th})} \tau_{pr} . \qquad (6.5)$$

Computed values of τ_i are given in Table 6.1.

Table 6.1. Delayed Neutron Data

Group	1	2	3	4	5	6
Precursors half-life (sec)	55.7	22.7	6.22	2.30	0.61	0.23
Fractional yield of precursors, $10^4\beta_i$ (neutrons per 10^4 neutrons)	2.11	14.02	12.54	25.28	7.40	2.70
Neutron mean energy (Mev)	0.25	0.46	0.40	0.45	0.52	0.5
Neutron age in MSRE (cm^2)	256	266	264	266	269	268

6.2.4 MSRE Dimensions

The computation of B^2 for the nonleakage probabilities used R = 27.75 in. and H = 68.9 in. The volume of fuel within these boundaries is 25.0 ft^3. At a circulation rate of 1200 gpm, residence times are 9.37 sec in the core and 16.45 sec in the external loop. A thermal neutron diffusion length appropriate for a core with highly (~93%) enriched uranium and no thorium was used (L^2 = 210 cm^2).

6.3 Results of Computation

The core residence time, in units of precursor half-lives, ranges from 0.2 to 41. Because of this, the shapes of the delayed neutron sources in the core vary widely, as shown in Fig. 6.1, when the fuel is circulating. (The source strength is normalized to a production rate of

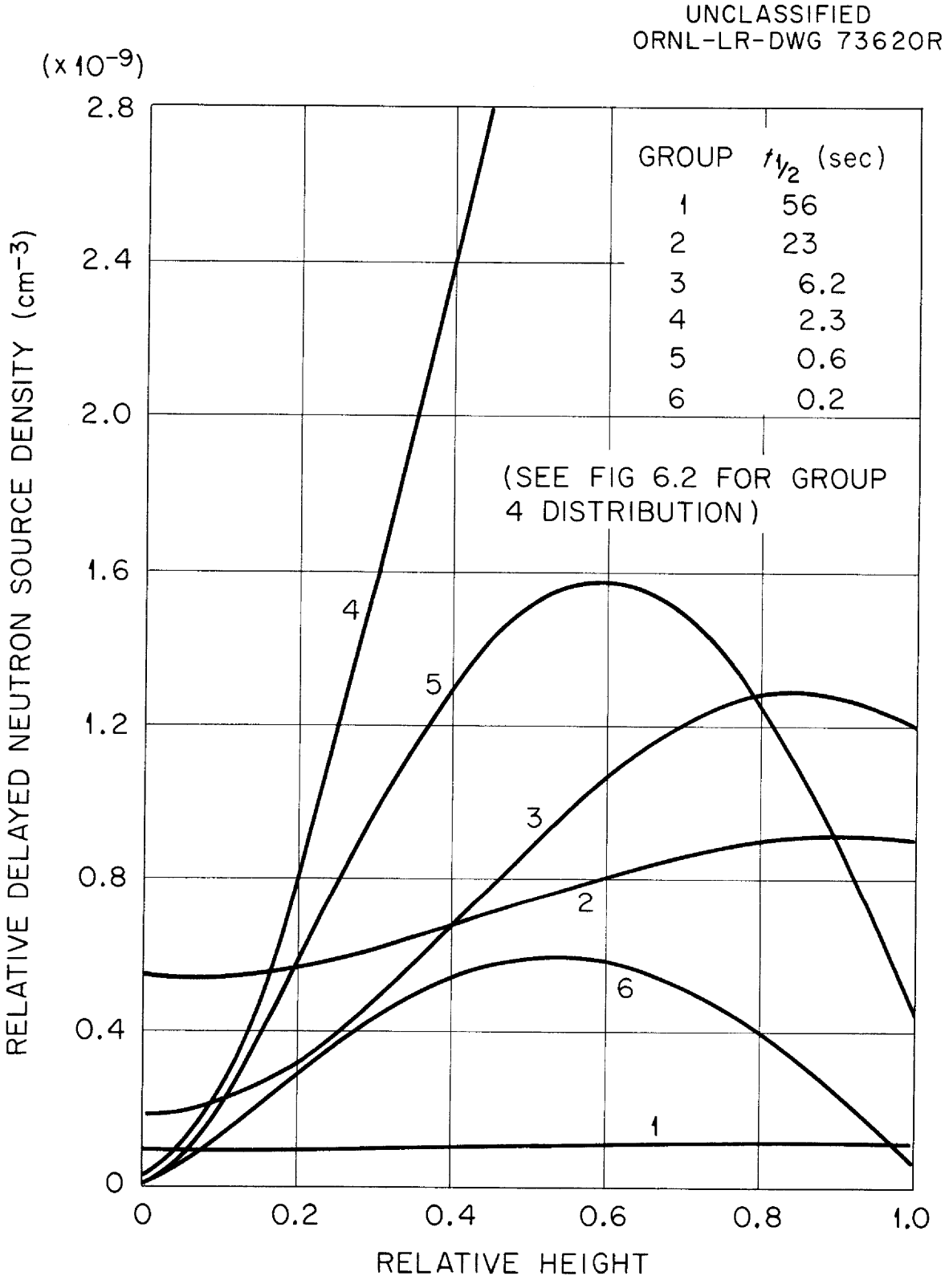

Fig. 6.1. Axial Distribution of Delayed Neutron Source Densities in an MSRE Fuel Channel. Fuel circulating at 1200 gpm.

1 neutron/sec in the reactor.) Figure 6.2 compares source distributions for one group under circulating and static conditions. The reduction in the number of neutrons emitted in the core is indicated by the difference in areas under the curves. A greater probability of leakage under circulating conditions is suggested by the shift in the distribution, which reduces the average distance to the outside of the core.

Table 6.2 summarizes important calculated quantities for each group. The total effective fraction of delayed neutrons is 0.00362 at a 1200-gpm circulation rate and is 0.00666 in a static core. The total yield of precursors is 0.00641.

Table 6.2. Delayed Neutrons in MSRE at Steady State

Group	1	2	3	4	5	6
Circulating:						
θ_i	0.36	0.37	0.46	0.71	0.96	0.99
P_i/P_{pr}	0.68	0.72	0.87	0.91	1.01	1.03
β_i^*/β_i	0.25	0.27	0.40	0.67	0.97	1.02
$10^4\beta_i^*$	0.52	3.73	4.99	16.98	7.18	2.77
Static:						
P_i/P_{pr}	1.06	1.04	1.04	1.04	1.03	1.03
$10^4\beta_i^*$	2.23	14.57	13.07	26.28	7.66	2.80

6.4 Nomenclature for Delayed Neutron Calculations

A_{mn}	Coefficient in series representation of S
B^2	Geometric buckling
E	Initial mean neutron energy
E_{th}	Thermal neutron energy
H	Height of core

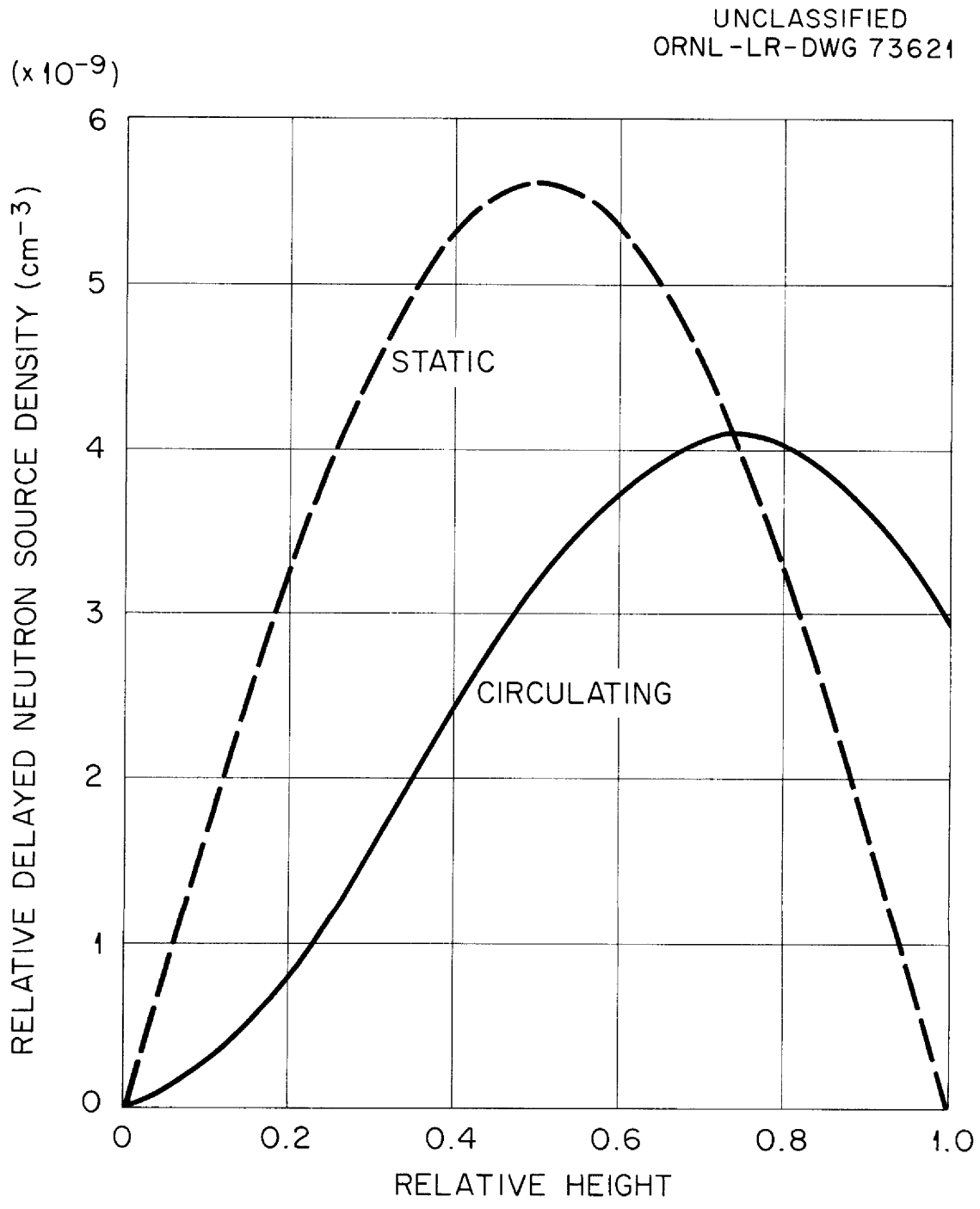

Fig. 6.2. Effect of Fuel Circulation on Axial Distribution of Source Density of Group 4 Delayed Neutrons. Fuel circulating at 1200 gpm.

J_0	Bessel function of first kind
j_m	mth root of $J_0(x) = 0$
L	Neutron diffusion length
P	Nonleakage probability
r	Radial distance from core axis
R	Outside radius of core
S	Neutron source per unit volume of fuel
t_c	Residence time of fuel in core
z	Axial distance from bottom of core
β_i	Fractional yield of neutrons of group i
β_i^*	Effective fraction of neutrons of group i
θ_i	Fraction of group i emitted in core
λ	Precursor decay constant
τ	Neutron age

7. POISONING DUE TO XENON-135

Changes in the concentration of Xe^{135} in the core produce changes in reactivity that are about as large as those from all other factors combined.* In order to use the net reactivity behavior during power operation to observe changes in such factors as burnup, fuel composition, and graphite permeation, the xenon poisoning must be calculated quite accurately from the power history.

7.1 Distribution of Iodine and Xenon

The first step in calculating the xenon poisoning is to calculate the behavior and distribution of I^{135} in all parts of the reactor. (This information is, of course, necessary because most of the Xe^{135} is formed by decay of I^{135}.) From this one proceeds to calculate the concentration of Xe^{135} in the fuel salt, in various parts of the graphite, and elsewhere throughout the reactor.

A number of production and destruction mechanisms for both xenon and iodine which involve the chemical and physical behavior of the isotopes can be postulated and described mathematically, at least in principle. Some of these mechanisms can be eliminated immediately as insignificant, while others can be shown to be highly significant. There remain, however, a number of mechanisms whose significance probably cannot be evaluated until after the reactor has been operated and the operation carefully analyzed.

7.1.1 Sources of Iodine and Xenon in Fuel

The only significant source of I^{135} in the circulating fuel is the direct production from fission; the iodine precursors in this chain have half-lives too short to have any significant effect.

The principal sources of Xe^{135} in the fuel are the decay of I^{135} in the fuel and direct production from fission. However, a third potential source exists if iodine is trapped on metal surfaces in the primary loop,

---

*See list of reactivity shim requirements, Table 9.1.

and the xenon formed by the decay of this iodine does not immediately return to the circulating stream. In this case, the xenon must be treated separately from that produced by decay of iodine in the circulating stream, because the delay in the return of the xenon to circulation changes the destruction probabilities.

7.1.2 Removal of Iodine and Xenon from Fuel

The principal removal mechanism for iodine is radioactive decay. However, consideration must also be given to the possibility of iodine migration into the graphite and to metal surfaces. If these processes occur, they will modify the overall xenon behavior. Volatilization or stripping of iodine in the pump bowl and destruction by neutron capture are both regarded as insignificant.

There are a number of competing mechanisms for the removal of xenon from the fuel. The most important of these are stripping in the pump bowl and migration to the graphite. Of lesser importance, but still significant, are decay of and neutron capture by xenon in the fuel itself. Decay of xenon trapped on metal surfaces must also be considered.

7.1.3 Sources of Iodine and Xenon in Graphite

Unless permeation of the graphite by fuel occurs, the only source of iodine in the graphite is migration from the fuel. If fuel permeation does occur, the direct production of iodine in the graphite by fission must be considered.

The major source of xenon in the graphite is migration from the fuel. Other sources which may or may not be important are decay of iodine in the graphite and direct production from the fission of fuel soaked into the graphite.

7.1.4 Removal of Iodine and Xenon from Graphite

Because of the low neutron absorption cross section of I^{135}, the only mechanism for its removal from the graphite is by radioactive decay to Xe^{135}. In the case of xenon, both decay and neutron capture are important.

In all cases where the transfer of an isotope from one medium to another is involved, only the net transfer need be considered; therefore, these can be regarded as one-way processes, with the direction of transfer being indicated by the sign of the term.

7.1.5 Detailed Calculations

A set of simultaneous differential equations has been developed to describe, in mathematical terms, all of the mechanisms discussed above. These equations also take into account radial and axial variations in the fuel flow pattern throughout the core and within individual fuel channels, as well as the overall distribution of the neutron flux. The equations can, theoretically at least, be programmed for solution by a large computer to give detailed spatial distributions of iodine and xenon in the core. An actual solution of the equations requires detailed information about a number of the chemical and physical parameters of the system, which is not currently available. However, some qualitative comments can be made about the nature of the results that can be expected.

The distribution of xenon in the fuel within the core will probably be relatively uniform, because of the mixing in the external loop and the fact that most of the xenon is produced from iodine that was formed in earlier passes through the core. Some depletion may occur along the region near the centerline of the core, because of the higher neutron flux and because the higher fuel turbulence facilitates transfer to the graphite. However, the mixed-mean concentration at the core outlet must be somewhat higher than at the inlet to allow for stripping in the pump bowl and decay in the external loop.

The overall radial distribution of xenon in the graphite may exhibit a minimum, due to burnout, at the radius corresponding to the maximum in the thermal flux. This minimum is reinforced by the fact that the flux maximum occurs in the low-velocity region of the core, where transfer from the fuel is slowest. In the axial direction, the highest xenon concentrations will probably occur near the inlet to the core; the neutron flux is low in this region, and turbulence near the entrance of the fuel channels tends to promote transfer from the fuel. This distribution may, however, be significantly affected by axial diffusion in the graphite stringers.

7.1.6 Approximate Analysis

In order to provide a basis for estimating the reactivity effect of Xe^{135} in the reactor, an approximate analysis of the steady-state xenon distribution was made.[27] For this approach, the scope of the problem was reduced to include only the major behavior mechanisms. It was assumed that all of the iodine remains with the fuel in which it is produced; this completely eliminated iodine from the steady-state mathematical expressions. The core was divided into four radial regions on the basis of fuel velocity, and an overall mass-transfer coefficient was calculated for xenon transfer from fuel to graphite in each region. Axial variations in xenon concentration in both fuel and graphite were neglected. Average xenon burnup rates were calculated on the basis of the average thermal neutron flux in the reactor. Fuel permeation of the graphite was neglected.

Because of uncertainties in the physical parameters, the xenon behavior was calculated for relatively wide ranges of the following variables:

1. Stripping efficiency in the pump bowl. The ultimate poisoning effect of the xenon is most sensitive to this quantity, which also has the greatest degree of uncertainty associated with it. The entire range, from 0 to 100% efficiency, was considered.

2. Fuel-to-graphite mass-transfer coefficient. This quantity can be calculated with reasonable confidence but the xenon poisoning is relatively sensitive to the results. Values differing by a factor of 2 from the expected value were considered.

3. Diffusion coefficient for xenon in graphite. The uncertainty associated with this quantity is quite large but its effect on the poisoning, within the range of expected values, is small. Two values, differing by a factor of 100, were considered.

The xenon poisoning is determined primarily by the xenon which diffuses into the graphite. Nearly all of the xenon that does not migrate to the graphite is stripped out in the pump bowl, leaving only a small fraction ($<1\%$ of the total) to be destroyed by neutron absorption or radioactive decay in the fuel. The xenon migration to the graphite is

not significantly affected by the choice of fuel, because all three fuels have similar physical properties. However, the choice of fuel has some effect on the poisoning, because this determines the flux level in the reactor at design power (see Table 3.5). This is illustrated by the fact that 49% of the Xe^{135} that enters the graphite is destroyed by neutron absorption at the flux level associated with 10-Mw operation with fuels A and C, whereas 62% is destroyed by this mechanism with fuel B.

Figure 7.1 illustrates the effect of stripping efficiency on the fraction of Xe^{135} produced in the reactor which migrates to the graphite. This figure also shows the effect of changing the diffusion coefficient, D, in the graphite by a factor of 100. It is expected that the average value of the graphite diffusion coefficient in the MSRE will be between the values shown. Figure 7.2 shows the effects of increasing and decreasing the mass-transfer coefficient, K, by a factor of 2 from the expected value, K_0. The curves in Fig. 7.2 are based on the higher of the two graphite diffusion coefficients.

7.2 Reactivity Effects of Xenon-135

Once the spatial distribution of xenon in circulation and that retained on the graphite has been calculated, it is possible to relate theoretically the xenon reactivity effect to the poison distribution. This relation is most conveniently expressed in terms of a reactivity coefficient and an importance-averaged xenon concentration.[28] The method for calculating these quantities is similar to that used in obtaining the reactivity effect of temperature (Sec 3.7). In the case of xenon, however, the weight function for the poison concentration is proportional to the product $\phi_2^*\phi_2$:

$$N_{Xe}^* = \frac{\int_{graphite} N_{Xe}^g \phi_2^* \phi_2 \, dV_g + \int_{salt} N_{Xe}^s \phi_2^* \phi_2 \, dV_s}{\int_{reactor} \phi_2^* \phi_2 \, dV}, \qquad (7.1)$$

where N_{Xe}^* is the importance-averaged concentration per unit reactor volume, and N_{Xe}^g and N_{Xe}^s are the local concentrations, per unit volumes of graphite and salt, respectively. The quantity N_{Xe}^* is also the uniform

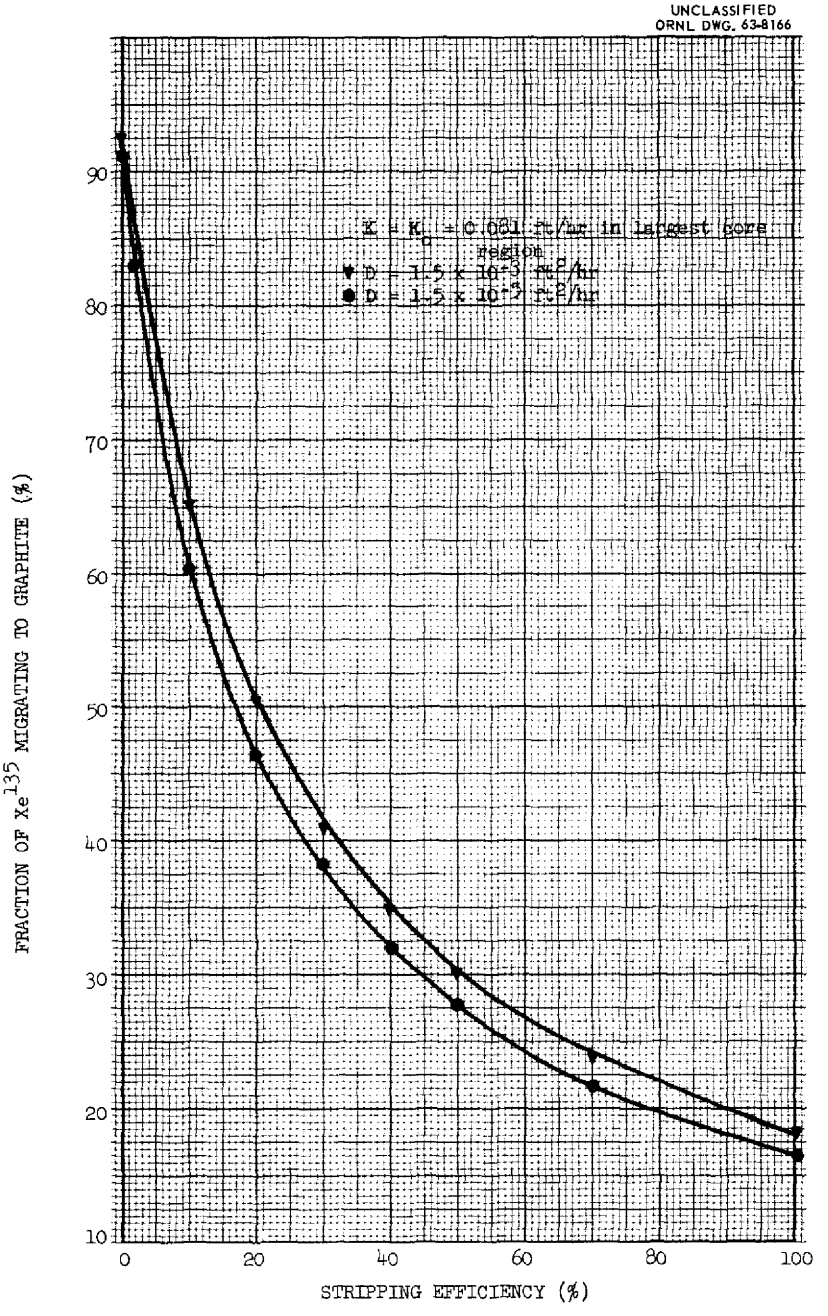

Fig. 7.1. Effect of Stripping Efficiency and Graphite Diffusion Coefficient on Xenon-135 Migration to Graphite.

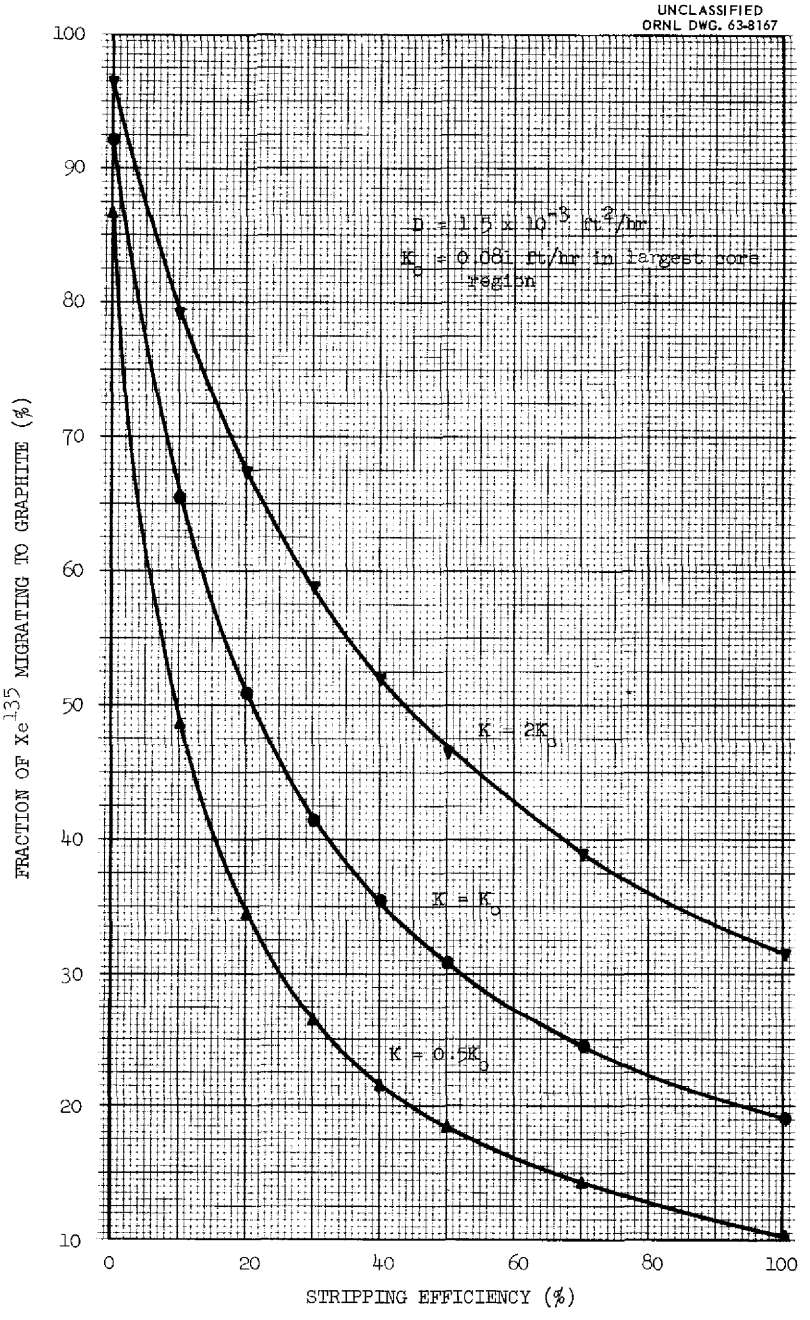

Fig. 7.2. Effect of Mass-Transfer Coefficient on Xenon-135 Migration to Graphite.

equilibrium concentration of xenon in the reactor, which produces the same reactivity change as the actual distribution. In relating N^*_{Xe} to the total reactivity change, it is convenient to define a third quantity, the effective thermal poison fraction, P^*_{Xe}. This is the number of neutrons absorbed in xenon per neutron absorbed in U^{235}, weighted with respect to neutron importance:

$$P^*_{Xe} = \frac{\sigma_{Xe} \int_{reactor} \phi^*_2 \phi_2 \, dV}{\int_{reactor} (N_{25}\sigma^{25}_1 \phi^*_1 \phi_1 + N_{25}\sigma^{25}_2 \phi^*_2 \phi_2) \, dV} N^*_{Xe} , \qquad (7.2)$$

where

N_{25} = concentration of U^{235}, per unit reactor volume,

$\sigma^{25}_{1,2}$ = U^{235} microscopic absorption cross section for fast (1) and thermal (2) neutrons,

σ_{Xe} = xenon thermal absorption cross section.

The relation between total xenon reactivity and P^*_{Xe} is given by[28]

$$\left(\frac{\delta k}{k}\right)_{Xe} = \frac{\int_{reactor} (N_{25}\sigma^{25}_1 \phi^*_1 \phi_1 + N_{25}\sigma^{25}_2 \phi^*_2 \phi_2) \, dV}{\int_{reactor} (\nu\Sigma_{f1} \phi^*_1 \phi_1 + \nu\Sigma_{f2} \phi^*_1 \phi_2) \, dV} P^*_{Xe} . \qquad (7.3)$$

Thus, if knowledge of the xenon distribution can be obtained from separate experiments or calculations, the calculation of the total xenon reactivity involves three steps: (a) obtaining N^*_{Xe} from Eq. (7.1), (b) calculating P^*_{Xe} from N^*_{Xe} by use of Eq. (7.2), and (c) calculating $\delta k/k$ from Eq. (7.3). Alternatively, the above relations may be used in a reverse manner if knowledge of the distribution is inferred from reactivity measurements at power.

The numerical values of the xenon reactivity coefficients obtained for the three fuels under consideration are given in Table 3.5. Both the coefficients relating $\delta k/k$ to the poison fraction and to the importance-averaged xenon concentration are listed.

Xenon concentrations calculated by the approximate method described in Sec 7.1.6 were used with the reactivity coefficients to obtain estimates of the xenon poisoning in the MSRE. Since the simplified analysis used only the average neutron flux, the calculated xenon concentrations

were space-independent and, therefore, independent of the importance-weighting functions. (The weighted average of a constant function is the same constant, regardless of the shape of the weighting function.) It may be noted that peaking in the xenon distribution toward the center of the core would make the importance-weighted average concentrations higher than the calculated values, while peaking toward the outside of the core would have the opposite effect.

Xenon reactivity effects were calculated for all three fuels; the results are listed in Table 7.1. The expected values are based on a graphite diffusion coefficient of 1.5×10^{-5} ft^2/hr and the calculated mass-transfer coefficients. The minimum and maximum values were obtained by applying the most favorable and unfavorable combinations of these two variables, within the limits discussed in Sec 7.1.6. The reactivity effects for fuels A and C are the same because the average thermal fluxes are the same and the reactivity coefficients do not differ within the accuracy of these calculations. The higher reactivity effect with fuel B is to be expected, because of the higher flux associated with this mixture. Changes in pump bowl stripping efficiency would have the same relative effect on fuel B as is shown for fuels A and C.

Table 7.1. Reactivity Effects of Xe^{135}

	Fuel A or C			Fuel B
Pump bowl stripping efficiency (%)	25	50	100	50
Reactivity effect (% δk/k)				
Expected	−1.2	−0.7	−0.5	−0.9
Minimum	−1.0	−0.5	−0.3	−0.5
Maximum	−1.7	−1.2	−0.9	−1.5

8. POISONING DUE TO OTHER FISSION PRODUCTS

Many fission products other than Xe^{135} contribute appreciably to the neutron absorptions in the reactor after long operation at high power. There are a few stable or long-lived fission products with high cross sections, the most important of which is Sm^{149}. The poisoning effect of this group of fission products saturates in a period of a few weeks or months, but undergoes transients following power changes. In addition, there is a slowly rising contribution to the poisoning from lower-cross-section nuclides which continue to build up throughout power operation.

8.1 Samarium-149 and Other High-Cross-Section Poisons

Samarium-149 is the next most important fission product poison after Xe^{135}, having a yield of 0.0113 atom/fission and a cross section of about 40,000 barns. Unlike Xe^{135}, it is a stable nuclide, so that once the reactor has been operated at power, some Sm^{149} poison will always be present. The poison level changes, however, following power changes.

Samarium-149 is the end product of the decay chain

$$Nd^{149} \xrightarrow{2h} Pm^{149} \xrightarrow{53.1h} Sm^{149} \text{ (stable)} ,$$

For all practical purposes the effect of Nd^{149} on the time behavior of Sm^{149} can be neglected. If it is further assumed that there is no direct yield of Sm^{149}, and no burnup of Pm^{149}, the equations governing the Sm^{149} concentration are

$$\frac{dN_{Pm}}{dt} = y\Sigma_F\bar{\phi} - N_{Pm}\lambda ,$$

$$\frac{dN_{Sm}}{dt} = N_{Pm}\lambda - N_{Sm}\sigma_{Sm}\bar{\phi} .$$

These equations can be solved to obtain the poisoning, P, due to the Sm^{149} in a thermal reactor:

$$P \equiv \frac{N_{Sm}\sigma_{Sm}}{\Sigma_U} = \frac{N_{Sm}\sigma_{Sm}}{\Sigma_F}\frac{\Sigma_F}{\Sigma_U} .$$

The reactivity effect of the Sm^{149} is simply related to P, in the case of a thermal reactor, by

$$\frac{\delta k}{k} = -fP \ ,$$

where f is the thermal utilization factor in the core.

Figures 8.1–8.3 show the type of behavior which can be expected of the Sm^{149} effect in the MSRE. Figure 8.1 shows the transient following a step increase to 10 Mw from a clean condition. The steady-state poisoning is independent of power level, but the rate of buildup is a function of the power, in this situation. This curve was calculated using $\bar{\phi} = 1 \times 10^{13}$, $\sigma_{Sm} = 4 \times 10^4$, $y = 0.0113$, and $f\Sigma_F/\Sigma_U = 0.8$. When the power is reduced the Sm^{149} builds up, because the rate of production from Pm^{149} decay is temporarily higher than the burnup of Sm^{149}. Figure 8.2 shows the reactivity transient due to Sm^{149} buildup after a reduction to zero power from the steady state approached in Fig. 8.1. After the Sm^{149} has built up to steady state at zero power, a step increase back to $\bar{\phi} = 1 \times 10^{13}$ results in the transient shown in Fig. 8.3.

In addition to the simple production of Sm^{149} through Pm^{149}, some may be produced by successive neutron captures and beta decays in a chain beginning with Pm^{147}. This source can become important after a long time at a high flux.

Other high-cross-section poisons which are important are Sm^{151}, Gd^{155}, Gd^{157}, Eu^{155}, and Cd^{113}. The effect of these nuclides amounts to about 0.2 of that of the Sm^{149}, and saturates in roughly the same length of time. Some of these fission products have relatively short-lived parents, so that they undergo transients similar to Sm^{149} after changes in power.

8.2 Low-Cross-Section Poisons

The large majority of the fission products may be regarded as an aggregate of stable, low-cross-section nuclides. The effective thermal cross section and resonance integral of this aggregate depend in an involved manner on the energy spectrum of the flux, the fuel nuclide, and the amount of fuel burnup which has occurred.[29,30] At low fuel burnup, in a thermal reactor fueled with U^{235}, a good approximation is that each

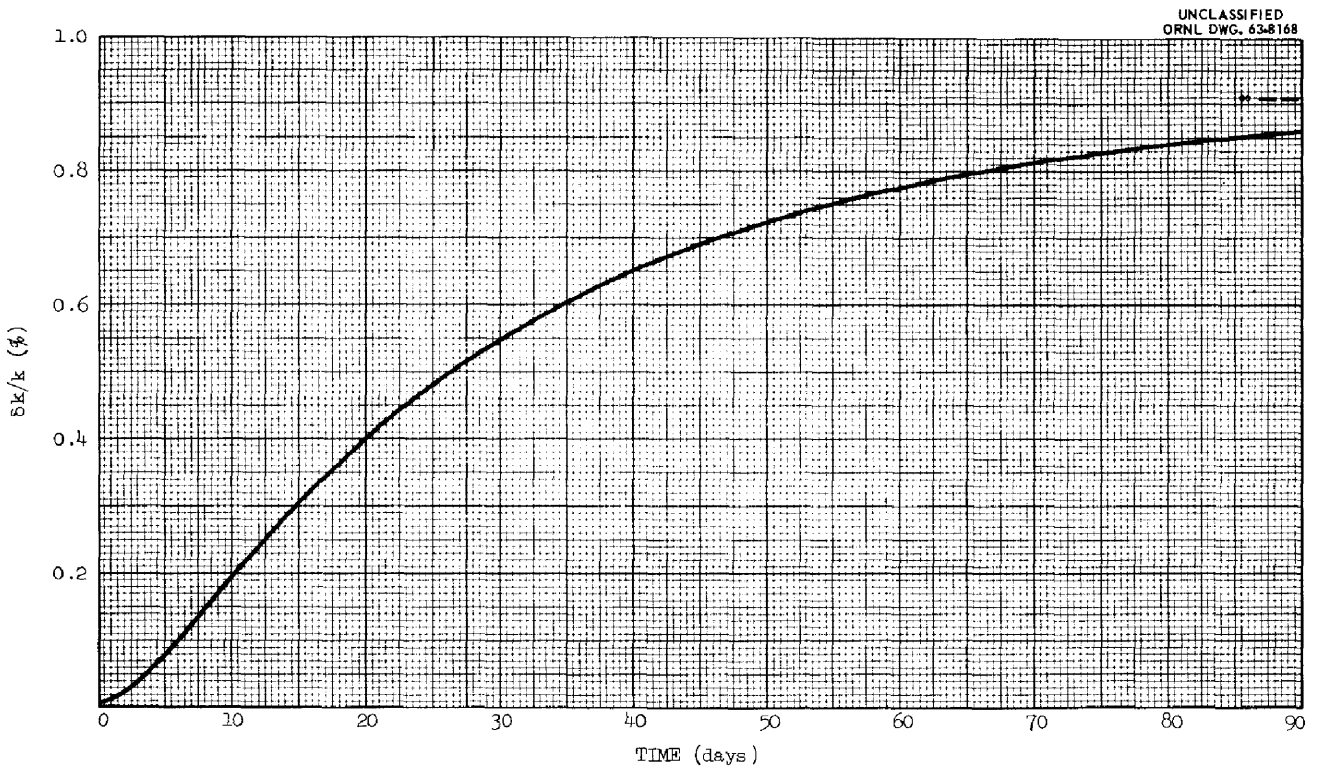

Fig. 8.1. Sm^{149} Poisoning at $\overline{\phi} = 1 \times 10^{13}$ After Startup with Clean Fuel.

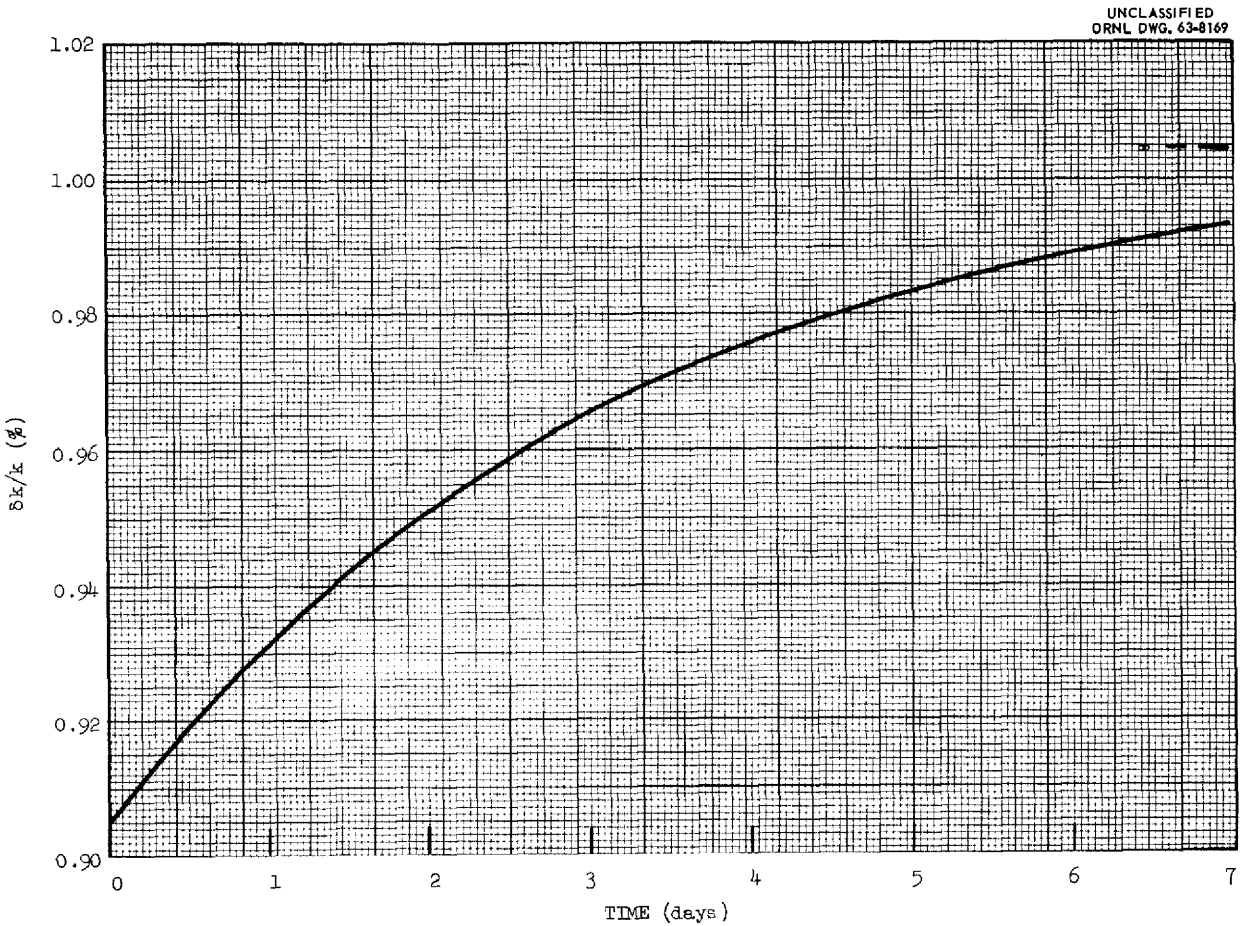

Fig. 8.2. Sm^{149} Poisoning at Zero Power After Reaching Steady State at $\bar{\phi} = 1 \times 10^{13}$.

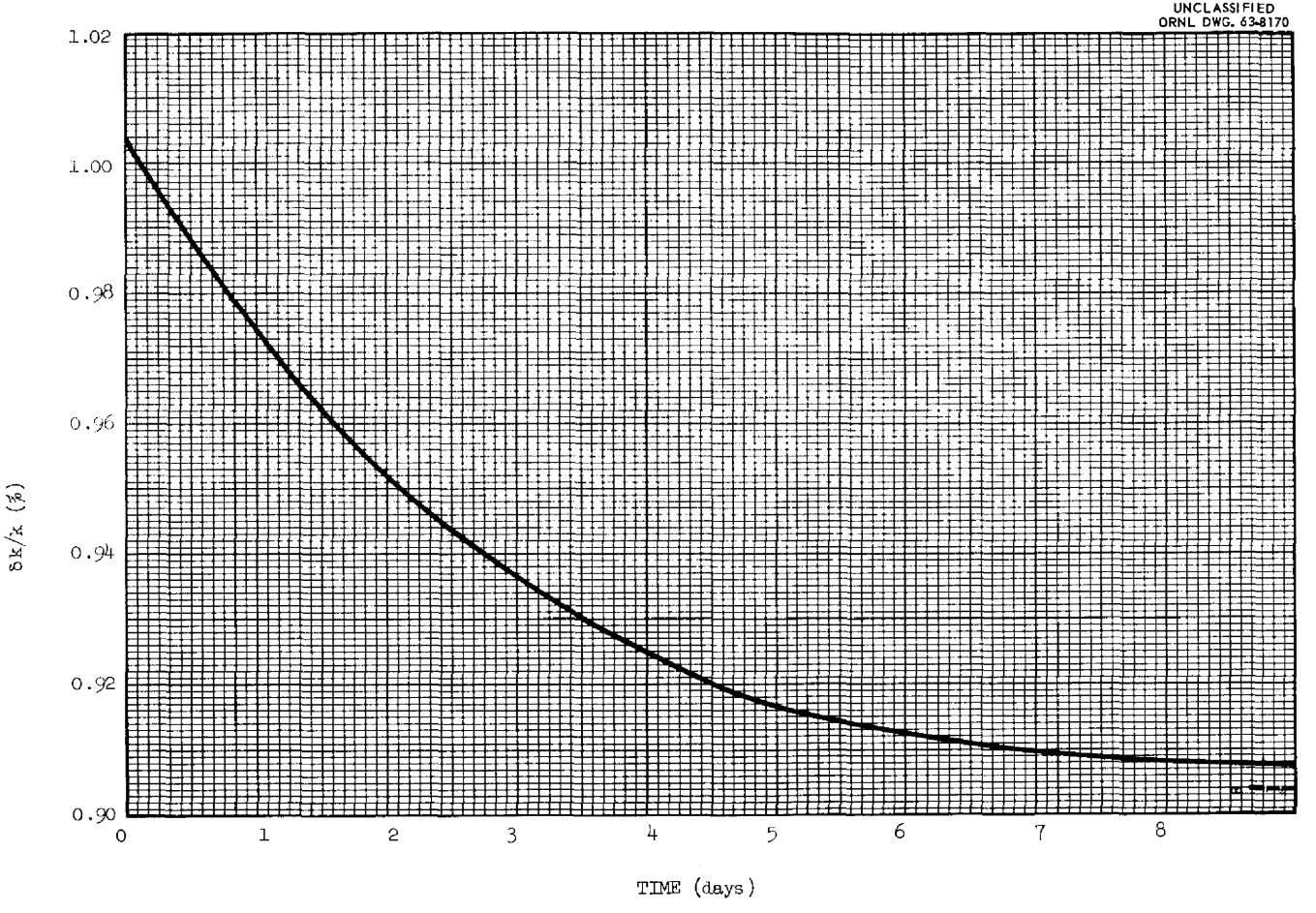

Fig. 8.3. Sm^{149} Poisoning After Step to $\bar{\phi} = 1 \times 10^{13}$ from Peak Low-Power Poisoning.

fission produces one atom with a cross section of 43 barns and a resonance integral of 172 barns.[31] In a predominantly thermal reactor with a thermal flux of 1×10^{13}, the poisoning effect of this group of fission products increases initially at a rate of about 0.003% $\delta k/k$ per day.

9. EMPLOYMENT OF CONTROL RODS IN OPERATION

The control rods are used to make the reactor subcritical at times, to regulate the nuclear power or fuel temperature, and to compensate for the changes in reactivity which occur during a cycle of startup, power operation, and shutdown. The manner in which the control rods are employed is dictated by their sensitivity and total worth, the reactivity shim requirements, and certain criteria related to safe and efficient operation. These factors and a normal program of rod positions during an operating cycle are summarized briefly here.

9.1 General Considerations

The drive mechanisms for the three rods are identical, and each rod has practically the same worth. Thus any one of the rods can be selected to be part of the servo control system which controls the reactor fission rate at power below 1 Mw or the core outlet temperature at higher powers. The other two rods are moved under manual control to shim the reactivity as required. The servo-controlled rod is called the regulating rod; the other two, shim rods. All rods are automatically inserted or dropped under certain conditions, so that all perform safety functions. (For a description of control and safety systems see Part II. Nuclear and Process Instrumentation.)

The criteria for the rod employment are as follows:

1. The reactivity is limited by fuel loading to the minimum required for full-power operation. Thus, at full power, with maximum poison and burnup, the rods are withdrawn to the limits of their operating ranges.

2. The maximum withdrawal of the shim rods is set at 54 in. to avoid waste motion at the beginning of a rod drop.

3. The normal operating range of the regulating rod is limited by the reduced sensitivity at either end to between 15-in. and 45-in. withdrawal. (In this range the rod changes reactivity at 0.002 to 0.04% $\delta k/k$ per sec while being driven at 0.5 in./sec.)

4. Rod movements are programmed to minimize error in calculated rod worth due to interaction or shadowing effects.

5. While the core is being filled with fuel, the rods are withdrawn so that the reactor, when full, will be subcritical by about 1.0% δk/k. This allows the source multiplication to be used to detect abnormalities, and provides reserve poison which can be inserted in an emergency.

6. Before the circulating pump is started, the rods are inserted far enough to prevent any cold slug from making the reactor critical.

9.2 Shim Requirements

The reactivity changes due to various causes during an operating cycle depend, for the most part, on the type of fuel in the reactor. The amounts of rod poison which must be withdrawn to compensate for various effects are summarized in Table 9.1. Equilibrium samarium poisoning and the slow growth of other fission products and corrosion products are compensated by fuel additions rather than by rod withdrawal.

The largest single item in Table 9.1, the xenon poisoning, depends on the flux, the stripper efficiency, the xenon diffusivity in the graphite, and the fuel-graphite xenon transfer. The tabulated values of xenon effect were calculated for a stripper efficiency of 50%, xenon diffusivity in the graphite of 1.5×10^{-5} ft^2/hr, and a mass transfer coefficient of 0.08 ft/hr. There is considerable uncertainty in these factors, and the

Table 9.1. Rod Shim Requirements

Cause	Effect (% δk/k)		
	Fuel A	Fuel B	Fuel C
Loss of delayed neutrons	0.3	0.3	0.3
Entrained gas	0.2	0.4	0.2
Power (0–10 Mw)	0.06	0.08	0.06
Xe^{135} (equilibrium at 10 Mw)	0.7	0.9	0.7
Samarium transient	0.1	0.1	0.1
Burnup (120 g of U^{235})	0.03	0.07	0.03
Total	1.4	1.9	1.4

xenon effect could be as little as one-third or as much as twice the values tabulated.

9.3 Shutdown Margins

When the rods are withdrawn to the limits set by criteria 2 and 3, the combined poison of the three rods is 0.5% δk/k. The useful worth of the rods, from full insertion to the upper end of their operating ranges, is therefore less than the total worth (Table 4.1) by 0.5% δk/k.

The minimum shutdown margin provided by the rods is the difference between the useful worth of the rods and the shim requirements (Table 9.1). (The shutdown margin will be greater than the *minimum* whenever any of the effects in Table 9.1 are present.) Minimum shutdown margins for fuels A, B, and C are 3.7, 5.2, and 3.8% δk/k, respectively. These margins are equivalent to reductions in critical temperatures of 580, 530, and 550°F, respectively. If the 10-Mw equilibrium xenon poisoning were twice the values shown in Table 9.1, the minimum shutdown margins would correspond to critical temperature reductions of 470, 440, and 450°F, respectively. Thus criterion 6 is easily satisfied by fully inserting the rods before the pump is started.

9.4 Typical Sequence of Operations

At the beginning of an operating cycle, when the core is being filled with fuel, the rods are positioned so that the reactor should be slightly subcritical when full. The rod poisoning which is necessary at this time depends on the total shim requirements and the current effects of samarium and burnup. (Xenon and other factors causing reactivity loss during operation will not normally be present during a fill.) Assuming that the shim requirements are as shown in Table 9.1 and that the fuel has peak samarium, no xenon, and no burnup during a fill, the rods would be positioned to poison 2.8, 3.3, or 2.8% δk/k with fuels A, B, and C, respectively. This would leave 2.8, 4.3, or 2.9% δk/k in reserve, to be inserted if abnormal conditions should require a rod scram. If the shim requirements are greater than shown in Table 9.1, the reserve is accordingly less. During the fill all three rods will be at equal withdrawal.

This is to provide the best protection if only two of the three rods drop when called for.

Before the pump is started, all three rods are fully inserted to give full protection against a cold slug making the reactor critical. (The rod position indicators can also be calibrated at this time.)

After the pump is running, the shim rods are withdrawn to a predetermined point, and then the reactor is made critical by slowly withdrawing the regulating rod. The amount of shim rod withdrawal is chosen to make the critical regulating rod position well below the position of the shim rods but within the range of adequate sensitivity. (The regulating rod and shim rod tips are kept separated to reduce the nonlinearities in worth which result from the regulating rod tip moving into and out of the shadow of the shim rods.)

After the power is raised and more rod poison must be withdrawn, the shim rods are withdrawn together, if they are not already fully withdrawn, until they reach the maximum desirable withdrawal. The regulating rod is then allowed to work its way up, under control of the servo system, to shim for further reactivity changes.

Table 9.2 summarizes rod positions and poisoning during the typical operating cycle with fuel C in the reactor.

Table 9.2. Rod Positions During Typical Operation, Fuel C

Condition	Rod Position (in. withdrawn)		Rod Poisoning (% δk/k)		
	Regulating	Shims	Regulating	Shims	Total
Filling core (1% subcritical)	28.5	28.5	0.9	1.9	2.8
Starting fuel pump	0	0	1.9	3.8	5.7
Going critical, no Xe, peak Sm, no burnup	28.4	54	1.2	0.1	1.3
At 10 Mw, no Xe, peak Sm, no burnup	29.4	54	1.1	0.1	1.2
At 10 Mw, equilibrium Xe and Sm, no burnup	39.3	54	0.6	0.1	0.7
At 10 Mw, equilibrium Xe and Sm, 120 g of U^{235} burnup	39.9	54	0.5	0.1	0.6

10. NEUTRON SOURCES AND SUBCRITICAL OPERATION

10.1 Introduction

When the reactor is subcritical, the fission rate and the neutron flux will depend on the neutron source due to various reactions and the multiplication of these source neutrons by fissions in the core. The fuel itself is an appreciable source of neutrons due to (α,n) reactions of alpha particles from the uranium with the fluorine and beryllium of the salt. There is also a contribution from spontaneous fission. Thus the core will always contain a source whenever the fuel is present. After high-power operation the internal source will be much stronger, because of photoneutrons produced by the fresh fission products. For the initial startup, an external source can be used to increase the flux at the chambers used to monitor the approaxh to criticality.

10.2 Internal Neutron Sources

10.2.1 Spontaneous Fission

An absolutely reliable source of neutrons is the spontaneous fission of the uranium in the fuel. Uranium-238 is the most active, in this regard, of the uranium isotopes in the MSRE fuel. If fuel C, containing 0.8 mole % uranium of 35% enrichment, is used, the spontaneous fission source will be about 10^3/neutrons sec. If highly (~93%) enriched uranium is used, the spontaneous fission source will be very small. Table 10.1 lists the specific emission rate of neutrons due to spontaneous fission of each isotope.[32] Also shown are the amounts of uranium in the core (clean, critical loading) and the resulting total spontaneous fission neutron sources for the fuels whose compositions are given in Table 3.1.

10.2.2 Neutrons from (α,n) Reactions in the Fuel

Alpha particles from uranium decay interact with some of the constituents of the fuel salt to produce a strong internal source of neutrons.[33] All of the uranium isotopes are alpha-radioactive and any of the uranium alphas can interact with the fluorine and the beryllium in the fuel salt to produce neutrons. The more energetic of the alpha particles can also

Table 10.1. Neutron Source from Spontaneous Fissions in MSRE Core[a]

Isotope	Specific Emission Rate [n/(kg·sec)]	Fuel A		Fuel B		Fuel C	
		M_c[b] (kg)	Source (n/sec)	M_c[b] (kg)	Source (n/sec)	M_c[b] (kg)	Source (n/sec)
U^{234}	6.1	0.3	2	0.2	1	0.2	1
U^{235}	0.51	27.0	14	16.5	8	26.4	13
U^{236}	5.1	0.3	2	0.2	1	0.2	1
U^{238}	15.2	1.5	22	0.9	13	47.5	722
			40		23		737

[a]"Effective" core, containing 25 ft^3 of fuel salt.

[b]Mass in core at clean, critical concentration.

produce neutrons by interaction with lithium, but the yield is negligible in comparison with that from fluorine and beryllium. Table 10.2 summarizes the specific yields and gives the neutron source in the core for the clean, critical loading with different fuels. About 97% of the neutrons are caused by alpha particles from U^{234}. Thus the (α,n) source is proportional to the amount of U^{234} present.

10.2.3 Photoneutrons from the Fuel

Gamma rays with photon energies above 1.67 Mev can interact with the beryllium in the fuel salt to produce photoneutrons. This source is unimportant before operation, when only the uranium decay gammas are present, but after operation at significant powers, the fission product decay gammas produce a strong, long-lived neutron source.

Figures 10.1 and 10.2 show the rate of photoneutron production in the MSRE core after operation at 10 Mw for periods of 1 day, 1 week, and 1 month. The source is proportional to the power, and the source after periods of nonuniform power operation can be estimated by superposition of sources produced by equivalent blocks of steady-power operation.

Table 10.2. Neutron Sources from (α,n) Reactions in MSRE Core[a]

Isotope	E_α (Mev)	Alpha Production [α/(sec·kg)]	Fuel A		Fuel B		Fuel C	
			Yield (n/10^6 α)	Source (n/sec)	Yield (n/10^6 α)	Source (n/sec)	Yield (n/10^6 α)	Source (n/sec)
U^{234}	4.77	1.64×10^{11}	7.0	3.3×10^5	7.8	2.3×10^5	7.6	2.8×10^5
	4.72	0.64×10^{11}	6.6	1.2×10^5	7.3	0.8×10^5	7.1	1.0×10^5
U^{235}	4.58	0.79×10^7	5.4	1.1×10^3	6.0	0.8×10^3	5.9	1.2×10^3
	4.47	0.24×10^7	4.7	0.3×10^3	5.3	0.2×10^3	5.2	0.3×10^3
	4.40	6.56×10^7	4.3	7.5×10^3	4.8	5.2×10^3	4.7	8.1×10^3
	4.20	0.32×10^7	3.2	0.3×10^3	3.7	0.2×10^3	3.6	0.3×10^3
U^{236}	4.50	1.72×10^9	4.9	2.4×10^3	5.5	1.7×10^3	5.4	2.1×10^3
	4.45	0.63×10^9	4.5	0.8×10^3	5.1	0.6×10^3	5.0	0.7×10^3
U^{238}	4.19	0.95×10^6	3.1	4	3.6	3	3.5	1.6×10^2
	4.15	0.28×10^6	2.9	1	3.4	1	3.3	0.4×10^2
				4.6×10^5		3.2×10^5		3.9×10^5

[a]"Effective" core, containing 25 ft^3 of fuel salt of clean, critical concentration.

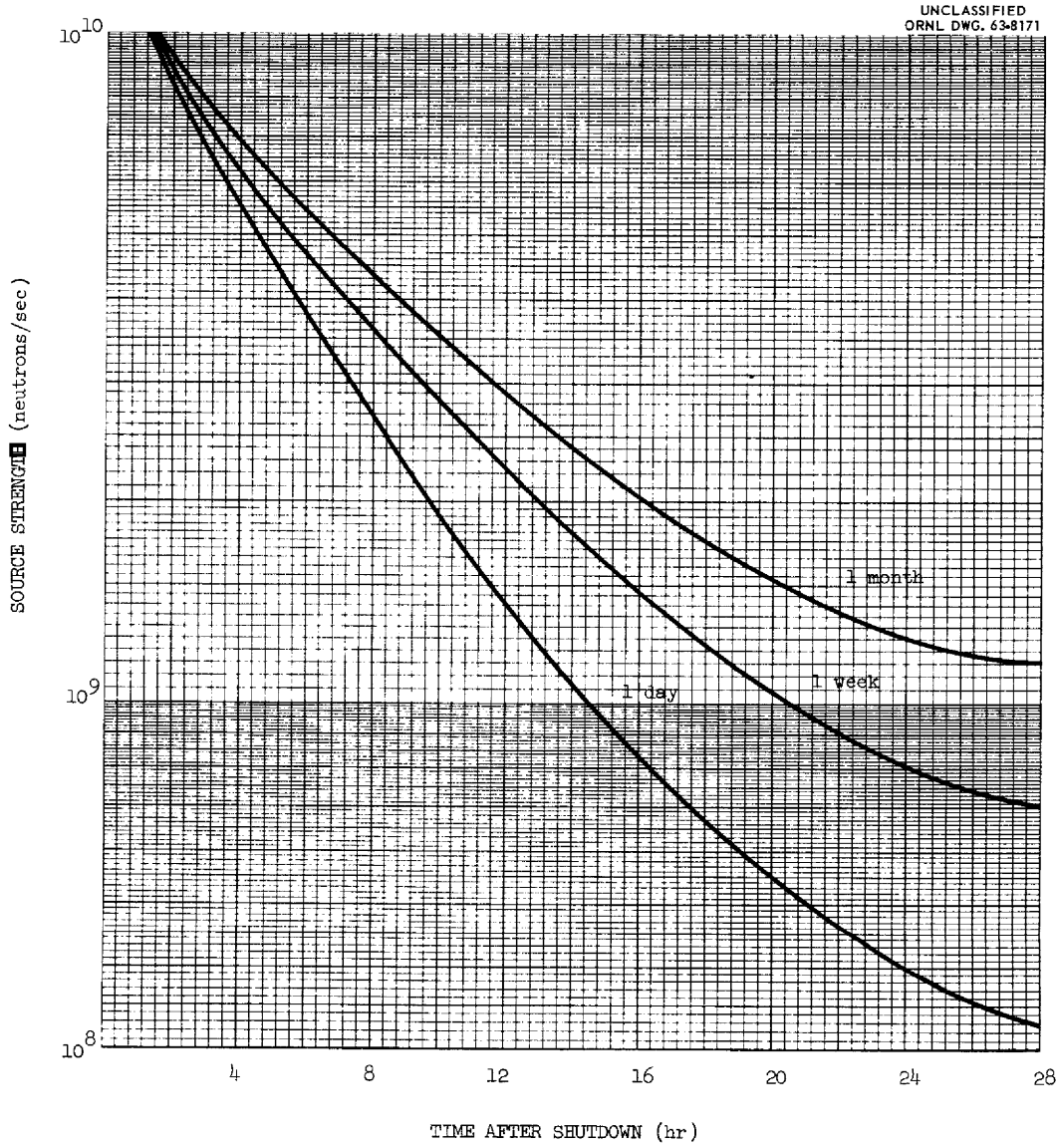

Fig. 10.1. Photoneutron Source in MSRE Core After Various Periods at 10 Mw.

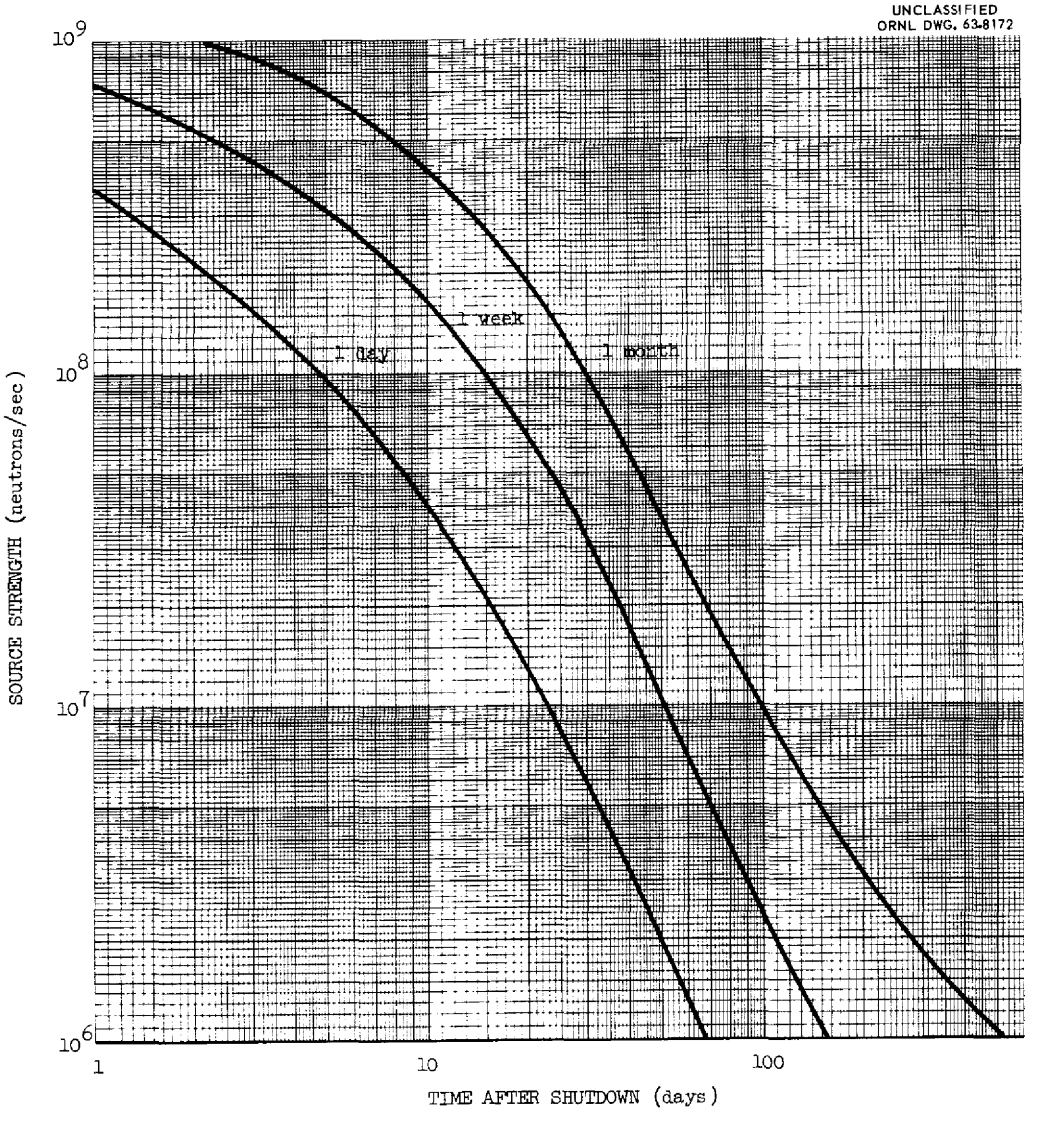

Fig. 10.2. Photoneutron Source in MSRE Core After Various Periods at 10 Mw.

The gamma-ray source used in the calculations is group IV of Blomeke and Todd,[34] which includes all gamma rays above 1.70 Mev. The probability of one of these gamma rays producing a photoneutron was approximated by the ratio of the $Be^9(\gamma,n)$ cross section to the total cross section for gamma-ray interaction in a homogeneous mixture with the composition of the core. A $Be^9(\gamma,n)$ microscopic cross section of 0.5 mb was used, and the total cross section was evaluated at 2 Mev. These assumptions lead to a conservatively low estimate of neutron source strength.

10.3 Provisions for External Neutron Source and Neutron Detectors

10.3.1 External Source

For reasons which will be described later, it is desirable to supplement the inherent, internal source with a removable, extraneous source. Therefore, a thimble is provided inside the thermal shield on the opposite side of the reactor from the nuclear instrument shaft. The thimble is a 1-1/2-in. sched 40 pipe of type 304 stainless steel, extending vertically down to about 2 ft below the midplane of the core. It is mounted as close as possible to the inner surface of the shield for maximum effectiveness.

10.3.2 Neutron Detectors

A nuclear instrument shaft is provided for all the permanently installed neutron detecting instruments. This is a water-filled 3-ft-diam tube which slopes down to the inner surface of the thermal shield with separate, inner tubes for the various chambers. The shaft contains ten tubes, of which seven will be used for routine power operation (two wide-range servo-operated fission chambers, two compensated ion chambers, and three safety chambers). This leaves three tubes in which auxiliary or special-purpose chambers could be installed. Any chamber in the instrument shaft is in a sloping position, with the upper end farther from the core (and hence, in a lower flux) than the lower end. As a result, a long chamber in the instrument shaft is exposed to a lower average flux than a shorter one.

Two vertical thimbles, similar to the source thimble but made of 2-in. sched 10 pipe, are installed in the thermal shield to accommodate temporary neutron detectors. The two detector thimbles are located 120 and 150° from the source thimble, one on either side of the permanent nuclear instrument shaft. The advantage of these vertical thimbles is that they place the entire length of a chamber close to the inner surface of the thermal shield, where it is exposed to a higher average neutron flux.

10.4 Neutron Flux in Subcritical Reactor

Changes in the reactivity of the subcritical reactor can be monitored if the fissions caused by the source neutrons produce a measurable neutron flux at the detectors mounted outside of the reactor vessel. The flux at a chamber depends on the source – its strength, the energy of the neutrons, and, in the case of an external source, its location both with respect to the core and with respect to the chamber. The flux also depends on the amount of multiplication by fissions and the shape of the neutron flux distribution in the core, which is determined by the location of the source and the value of k in the core.

The count rate produced by a given chamber depends on the chamber sensitivity as well as on the neutron flux. Of interest in establishing the neutron-source requirements are the sensitivities of the chambers which will be used to observe the behavior of the reactor under subcritical conditions. The fission chambers, which will be used to monitor routine approaches to critical (as well as power operation) are 6 in. long and have a counting efficiency of 0.026 count per neutron/cm^2. In addition, BF_3 chambers are available; they will be used during the initial critical experiments (and possibly to monitor routine reactor fills). These have a sensitive length of 26-1/4 in. and a counting efficiency of 14 counts per neutron/cm^2.

The steady-state flux in the core and thermal shield with a source in the thermal shield source tube was calculated[35] for two core conditions: the first, with no fuel in the core; the second, with the core filled with fuel salt containing 0.76 of the clean, critical uranium concentration. In the latter case k_{eff} was calculated to be 0.91. Contri-

butions from the internal neutron source were neglected. The calculated ratios of thermal neutron fluxes at the chambers to the source strength (neutrons/cm^2 per source neutron) are given in Table 10.3. As a first approximation, the ratios of flux or count rate to source strength at k_{eff} above 0.9 can be assumed to change in proportion to the inverse of $(1 - k_{eff})$.

When the multiplication is high, that is, when $(1 - k_{eff})$ is quite small, most of the neutrons are produced by fissions in the core, with a spatial source distribution close to the fission distribution in a critical reactor. The relation between the core power, or fission rate, in the critical core and the flux in the thermal shield was calculated in the course of the thermal shield design, using DSN, a multigroup, transport-theory code. For the case of a thick, water-filled thermal shield, when the core power is 10 Mw, the predicted thermal neutron flux reaches a peak, 1 in. inside the water, of 1.2×10^{12} neutrons cm^{-2} sec^{-1}. The ratio of peak flux to power is 1.2×10^{5} neutrons cm^{-2} sec^{-1} per watt, or 1.5×10^{-6} neutrons cm^{-2} sec^{-1} per neutron/sec produced in the core. It was estimated that a 6-in.-long chamber at maximum insertion in the instrument shaft would be exposed to an average flux of roughly 1×10^{-7}

Table 10.3. Fluxes Produced at Neutron Chambers by an External Source

Location	Chamber Length (in.)	Average Flux/Source Strength {[n/(cm^2·sec)]/(n/sec)}	
		No Fuel	k_{eff} = 0.91
		$\times 10^{-6}$	$\times 10^{-6}$
120° thimble	Any	13	18
150° thimble	Any	4	9
Instrument shaft (~180°)	6	2	7
	26	0.6	1.7

neutrons cm^{-2} sec^{-1} per neutron/sec produced. For a 26-in.-long chamber, the corresponding value is about 3×10^{-8}. A chamber in one of the vertical tubes just inside the inner wall of the thermal shield would be exposed to an average flux of about 3×10^{-7} neutrons cm^{-2} sec^{-1} per neutron/sec produced in the core.

With both an external and an internal source present, the flux at a particular location in the thermal shield can be roughly approximated by an expression of the form

$$\phi = bS_{ex} + \frac{f_{ex}S_{ex}}{1 - k} + \frac{f_{in}S_{in}}{1 - k} . \qquad (10.1)$$

The quantities S_{ex} and S_{in} are the strengths of the external and internal sources, respectively. The factors f_{ex} and f_{in} indicate the fraction of neutrons, produced in the core from the corresponding source neutrons, which reach the location in question. Since these factors depend on the flux shape, the values vary somewhat with k_{eff}. The factor b is proportional to the fraction of the neutrons from the external source which reach the thermal shield without first entering the core, that is, by scattering around the core. This factor is essentially independent of k_{eff}.

The calculation of the flux distribution with an external source and no fuel in the core indicated that f_{ex} is essentially zero for this condition. Also, when there is no fuel in the reactor, $S_{in} = 0$. Thus, for this condition Eq. (10.1) reduces to

$$\phi = bS_{ex} . \qquad (10.2)$$

This expression permits direct evaluation of b for various locations from the above calculation.

When the reactor is near critical, the variation in f_{ex} and f_{in} with k can be neglected to obtain approximate values for these quantities. The value of f_{in} for various locations was obtained from the critical flux distribution, and f_{ex} was obtained from the distribution at $k_{eff} = 0.91$.

The values obtained for the factors at the various proposed neutron chamber locations are listed in Table 10.4. These factors can be used to

Table 10.4. Flux/Source Factors in MSRE

Location	Chamber Length (in.)	b (cm^{-2})	f_{ex} (cm^{-2})	f_{in} (cm^{-2})
		$\times 10^{-6}$	$\times 10^{-7}$	$\times 10^{-7}$
120° thimble	Any	13	5	3
150° thimble	Any	4	5	3
Instrument shaft	6	2	4	1
	26	0.6	1	0.3

estimate the flux at the chambers for different source conditions either when the reactor is empty or when it is near critical ($k_{eff} \geq 0.95$).

10.5 Requirements for Source[35]

A neutron source must perform several functions in the operation of a reactor, and each function places different requirements on the source.

10.5.1 Reactor Safety

The most important function of a neutron source in the reactor has to do with reactor safety. If an adequate source is present, the statistical fluctuations in the level of the fission chain reaction will be negligibly small and the level will rise smoothly as the reactivity is increased to make the reactor critical. Furthermore, when the reactor becomes supercritical, the level will be high enough that temperature feedback becomes effective, and safety actions can be taken before enough excess reactivity can be added to cause a dangerous power excursion.

As shown in Secs 12.2 and 12.7, the strength of the inherent (α-n) source is enough to satisfy the safety requirements for a source. This is convenient because the (α-n) source will always be present whenever there is any chance of criticality. This assurance of an adequate internal source eliminates the usual safety requirement that an extraneous

source be installed and its presence proved by significant count rates on neutron chambers before a startup can begin.

10.5.2 Preliminary Experiments

An extraneous source and sensitive neutron chambers are useful in the MSRE primarily because they comprise a means of monitoring the reactivity while the reactor is subcritical, or of following the nuclear power behavior at levels below the range of the ionization chambers which provide information at high power.

For the initial critical experiment, it is desirable to have a significant neutron count rate before any fuel is added to the reactor. This guarantees that the condition of the reactor can be monitored at all times during the experiment. Table 10.5 lists the external source strength required to produce a count rate of 2 counts/sec on the various chambers with no fuel in the reactor.

10.5.3 Routine Operation

After the preliminary experiments, only the chambers in the nuclear instrument shaft will be available to monitor the reactor flux.

The function of the neutron source in routine operation is to permit monitoring the flux during reactor startups so that the operation is orderly. A normal startup of the MSRE involves two separate steps: (1) filling the reactor with fuel salt and (2) withdrawing the control rods

Table 10.5. External Source Required for 2 Counts/sec with No Fuel in Reactor

Location	Chamber Type	Counting Efficiency {(counts/sec)/[n/(cm^2·sec)]}	Source Strength (n/sec)
120° thimble	BF_3	14	1×10^4
150° thimble	BF_3	14	4×10^4
Instrument shaft	Fission	0.026	4×10^7
	BF_3	14	2×10^5

to make the reactor critical. Although the first operation will normally leave the reactor subcritical, it is desirable to monitor the flux during this step to ensure that no abnormal conditions exist. This requires that a significant count rate exist before the fill is started, and the source requirements are the same as for the initial critical experiment. The second phase of the startup involves changing the multiplication constant from about 0.95 (the shutdown margin attainable with the control rods) to 1.0. This operation should, if possible, be monitored by instruments which are still useful after criticality is attained; in the MSRE, these instruments are the servo-operated fission chambers. A source of 8×10^6 neutrons/sec is required to produce a count rate of 2 counts/sec on a fully inserted fission chamber when $k = 0.95$.

10.6 Choice of External Source

The source requirements of the MSRE can be met in a number of ways. One of the most desirable sources from the standpoint of cost and ease of handling is the Sb-Be type, and such a source that meets the calculated requirements can be easily obtained. However, Sb^{124} has only a 60-day half-life, so the initial intensity of such a source must be substantially greater if frequent replacement is to be avoided. The calculated requirements can also be met with a Pu-Be source. Such a source would be more expensive, and there is a containment problem because of the plutonium content. On the other hand, the long half-life of plutonium would eliminate the problems associated with source decay.

Because the flux calculations are subject to substantial errors, the final specification of the source will be based on measurements to be made shortly after the reactor vessel containing the core graphite is installed inside the thermal shield. (The construction and startup schedule is such that there is time for procurement of a source after these measurements and before the source is needed for nuclear operation.)

11. KINETICS OF NORMAL OPERATION

Studies of the kinetic behavior of the reactor fall into two categories. One deals with the behavior in normal operation, when the reactor is subjected only to moderate changes in load demand and to small, random disturbances or "noise." The concern here is with stability — absolute and relative. (Absolute stability means that a disturbance does not lead to divergent oscillations; relative stability refers to the magnitude and number of oscillations which occur before a transient dies out.) The other category of kinetics studies treats the response of the system to large or rapid changes in reactivity such as might occur in abnormal incidents. Studies of the first kind are covered in this chapter. The next chapter deals with safety studies, or kinetics under abnormal conditions.

11.1 Very Low Power

When the MSRE is operated at very low power, with the temperature held constant by the external heaters, the fission chain reaction is controlled by the control rods alone. The kinetic behavior of the fission rate under this condition is determined by the prompt neutron lifetime and the effective delayed neutron fractions and is not unusual in any way. The neutron lifetime is between 2 and 4×10^{-4} sec, depending on the fuel salt composition. (For comparison, the lifetime in most water-moderated reactors is between 0.2 and 0.6×10^{-4} sec, and large, graphite-moderated reactors have lifetimes of about 10×10^{-4} sec.) Although the effective delayed neutron fractions are considerably lower than in a fixed-fuel reactor using U^{235}, this presents no important problem of control.

11.2 Self-Regulation at Higher Power

When the reactor power is high enough to have an appreciable effect on fuel and graphite temperatures, the power becomes self-regulating. That is, because of the negative temperature coefficients of reactivity,

the nuclear power tends to follow the heat extraction, or load, without external control by the rods. The kinetic behavior under these conditions is governed by the fuel and graphite temperature coefficients of reactivity, power density, heat capacity, heat transfer coefficients, and transport lags in the fuel and coolant circuits.

11.2.1 Coupling of Fuel and Graphite Temperatures

One characteristic of the MSRE which profoundly influences the self-regulation is the rather loose coupling between the fuel and the graphite temperatures. This is caused by a low ratio of heat transfer to thermal inertia and a disproportion of heat generation between the fuel and graphite.

Heat transfer between the graphite and fuel is about 0.020 Mw per °F of temperature difference. The total heat capacity of the graphite is 3.7 Mw-sec per °F of temperature change. The ratio of heat transfer to graphite heat capacity is only about 0.005°F/sec per °F. This means that with a temperature difference of 100°F between the fuel and the graphite, the heat transferred is only enough to raise the graphite temperature at 0.5°F/sec.

The heat capacity of the fuel in the core is 1.7 Mw-sec/°F, less than half that of the graphite. But 93% of the fission heat is generated in the fuel; only 7% in the graphite. Thus, the core fuel temperature tends to change much more rapidly than that of the graphite whenever there is an imbalance between the heat generation and the heat removal from the core. Such imbalances would occur, for example, in any power excursion or undershoot, or whenever the fuel inlet temperature changes.

The difference in the time responses of the fuel and graphite temperatures makes it necessary to treat them separately in any analysis of the MSRE kinetics.

11.2.2 Transport Lags and Thermal Inertia

The kinetic behavior of the reactor is determined not only by the core characteristics but also by the characteristics of the entire heat-removal system, which includes the radiator, the coolant salt loop, the fuel-coolant heat exchanger, and the fuel circulating loop.

The coolant loop contains 44 ft^3 of salt, with a total heat capacity of 2.9 Mw-sec/°F. At an 850-gpm circulation rate, the loop circuit time is 23 sec. There is 67 ft^3 of fuel salt in circulation, having a total heat capacity of 4.6 Mw-sec/°F. The fuel circulation rate is 1200 gpm, giving a circuit time of 25 sec. There is also additional thermal inertia due to the metal of the piping and heat exchanger.

Because the circuit times are rather long and the heat capacities are large compared with the normal operating power, the system response to changes in heat removal at the radiator is rather slow.

11.2.3. Simulator Studies

The kinetics and stability of normal operation were studied by a detailed simulation of the entire reactor system with an analog computer. By this method it was feasible to include the many effects of fluid mixing, loop transit times, heat capacities, heat transfer-ΔT relations, temperature coefficients of reactivity for the fuel and graphite, and the reactivity-power relations.

Studies of operation at power without external control of the reactivity were carried out with two different analog representations of the reactor. In the first model, the core was represented as a single major region comprised of two subregions of fuel and one subregion of graphite. Figure 11.1 is a schematic diagram which shows the treatment of the thermal effects in the fuel and graphite in this model. In the second model, the core was subdivided into nine major regions, as shown in Fig. 11.2. Thermal effects were treated separately for each major region by the same relations used for the single major region in the first model of the core. The purpose of the subdivision of the core was to better approximate some of the effects of spatial variation of the power generation, fuel and graphite temperatures, and the nuclear importance in the actual core. Temperatures in each of the nine regions were weighted to obtain the averages which determine the net effect on reactivity.

Figures 11.3 and 11.4 show the response of the system with the nine-region core model to changes in simulated power demand in the absence of external control action. In both cases the demand was changed by changing

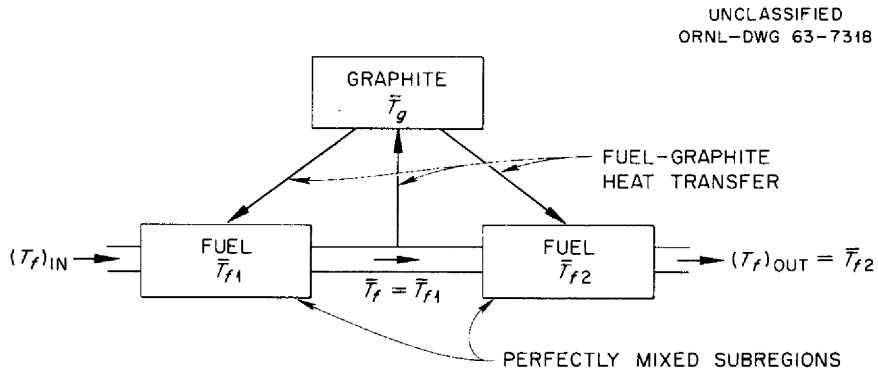

Fig. 11.1. Analog Model of Reactor-Core Region. Nuclear power is produced in all three subregions.

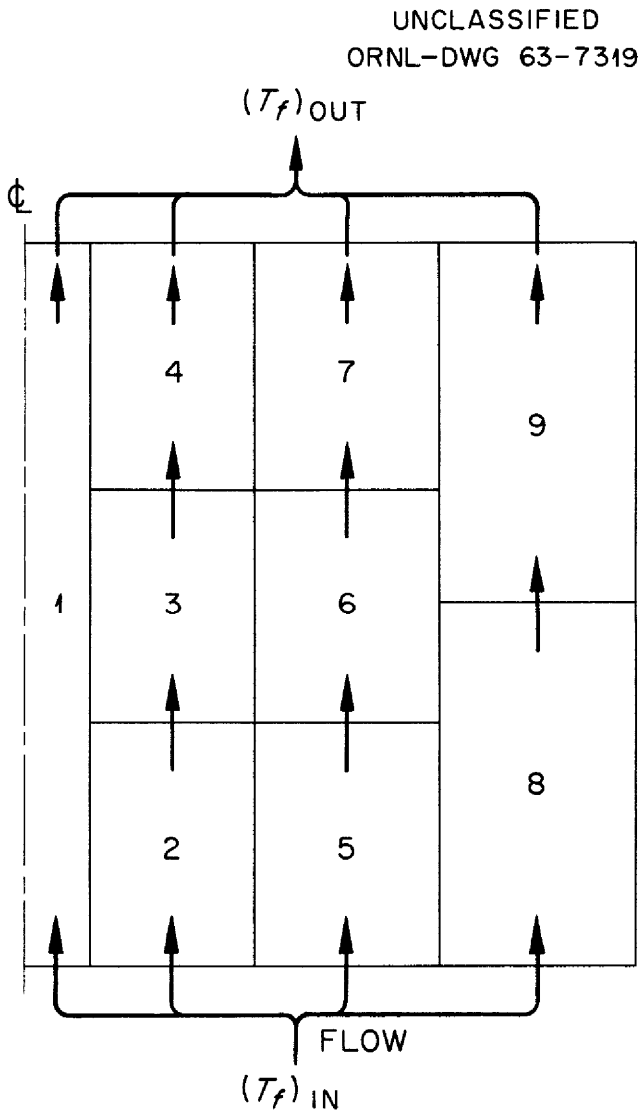

Fig. 11.2. Schematic Breakdown of 9-Region Analog Model.

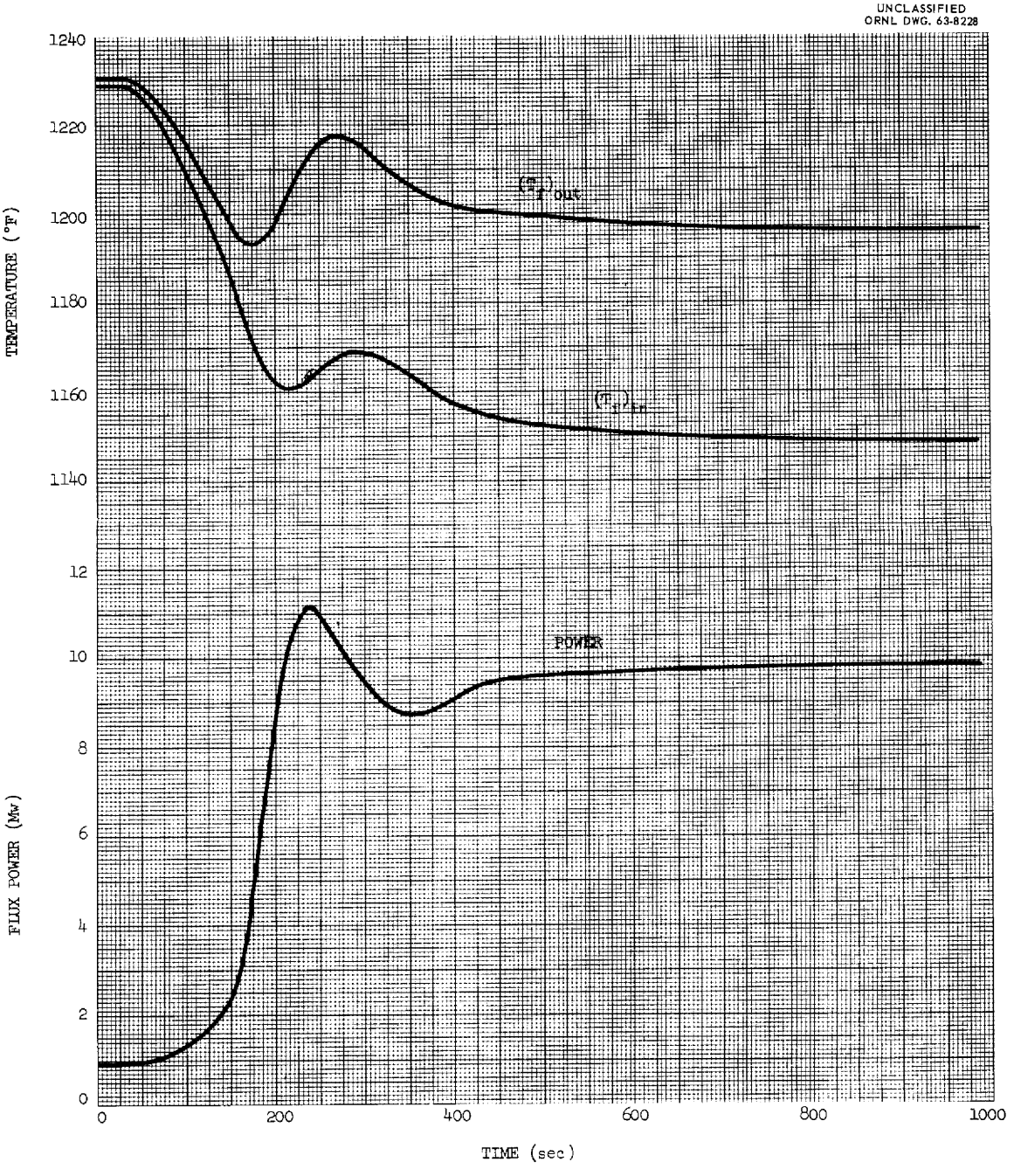

Fig. 11.3. Response of 9-Region Model of MSRE to an Increase in Power Demand.

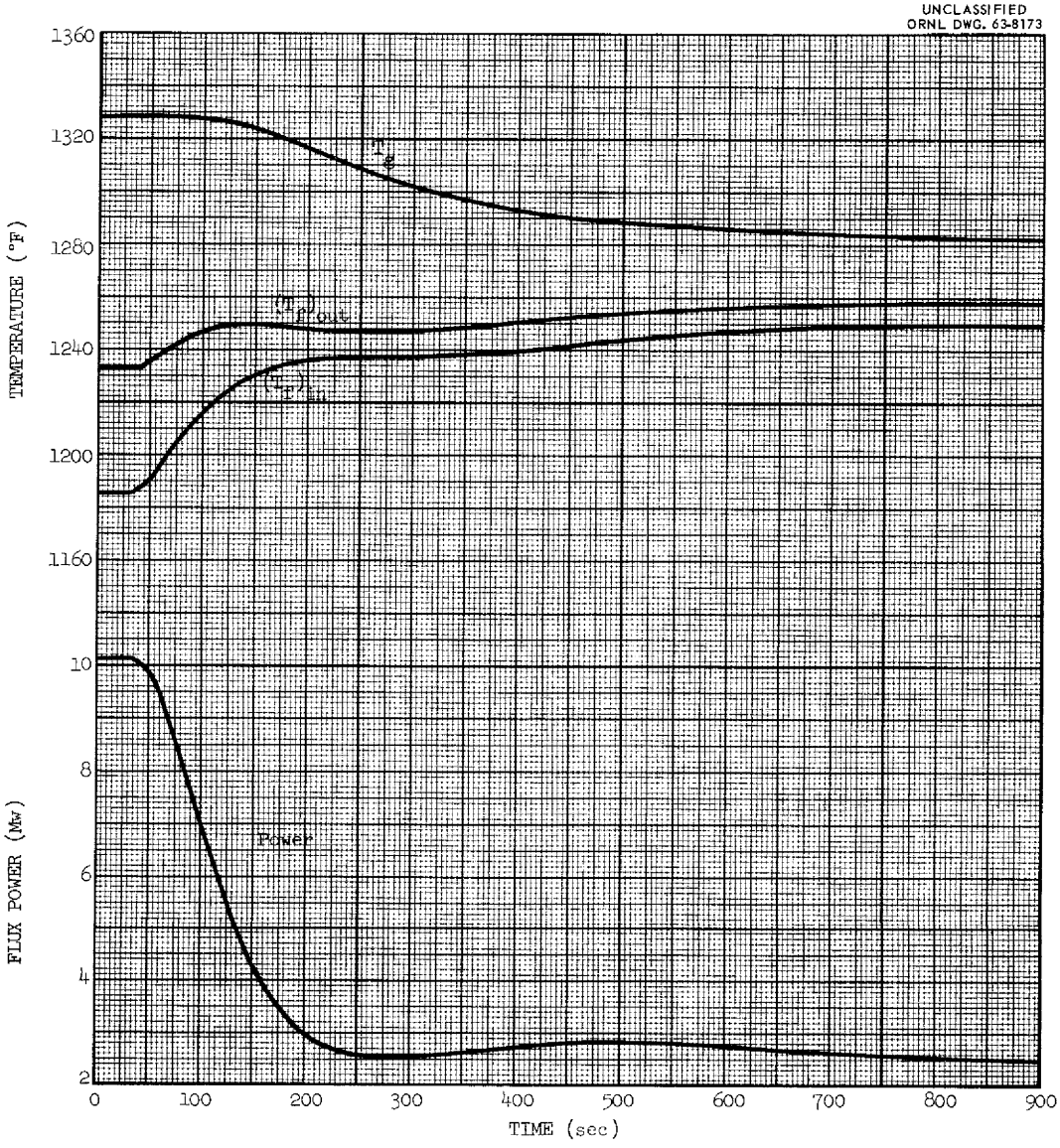

Fig. 11.4. Response of 9-Region Model of MSRE to a Decrease in Power Demand.

the simulated air flow through the radiator, the ultimate heat sink in the reactor system. For the power increase in Fig. 11.3, the simulated air flow was raised from 3% to 100% of the design value at 0.5%/sec. As shown, there was a moderate power overshoot and about 15 min was required for the power and the fuel temperatures to approach steady-state values. The response to a decrease in air flow to 8% of the design value at 3%/sec is shown in Fig. 11.4. In this simulator test, the temperature of the graphite in an important region of the core (region 3 in Fig. 11.2) was recorded.

Besides showing the transient response of the reactor system, Fig. 11.4 illustrates the shift in steady-state temperatures at different powers which results if there is no adjustment of the control rods. This shift comes about because the heat generated in the graphite must be transferred to the fuel for removal from the core, causing the fuel and graphite temperatures to diverge. Since the temperature coefficients of reactivity of both the fuel and the graphite are negative, the tendency of the graphite temperature to rise at higher powers forces the fuel temperature to decrease to keep the net reactivity change zero.

Figures 11.5 and 11.6 show the response of the simulated nuclear power in the one-region core model to changes in power demand similar to those used to produce Figs. 11.3 and 11.4. It may be noted that the simulation involving the simpler core model shows a significantly greater tendency toward sustained power oscillation at low powers. The reason for the different results is not clear. The reactor system models differed in several respects beside the core, and, because the calculations were done at different stages of the reactor design, they used somewhat different values for the current reactor design data.

Despite the differences in the simulator results, an important conclusion can be drawn from them. That is: although the negative temperature coefficients of reactivity make the reactor capable of stable self-regulation, an external control system is desirable because the reactor is loosely coupled and sluggish, particularly at low power. (Neither of the models included compressibility effects due to entrained gas, but inclusion of these effects would probably not change the conclusion.)

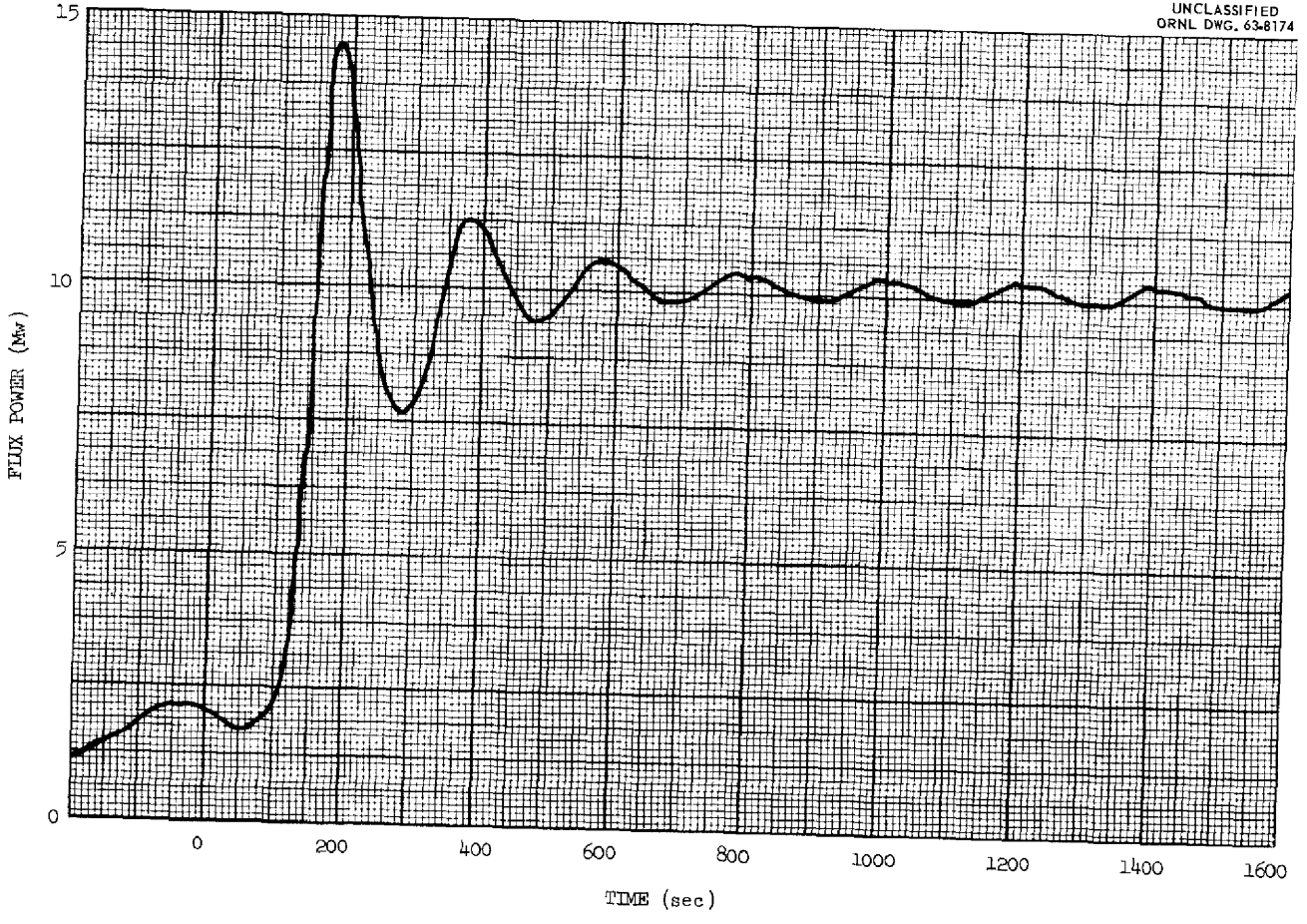

Fig. 11.5. Response of 1-Region Model of MSRE to an Increase in Power Demand.

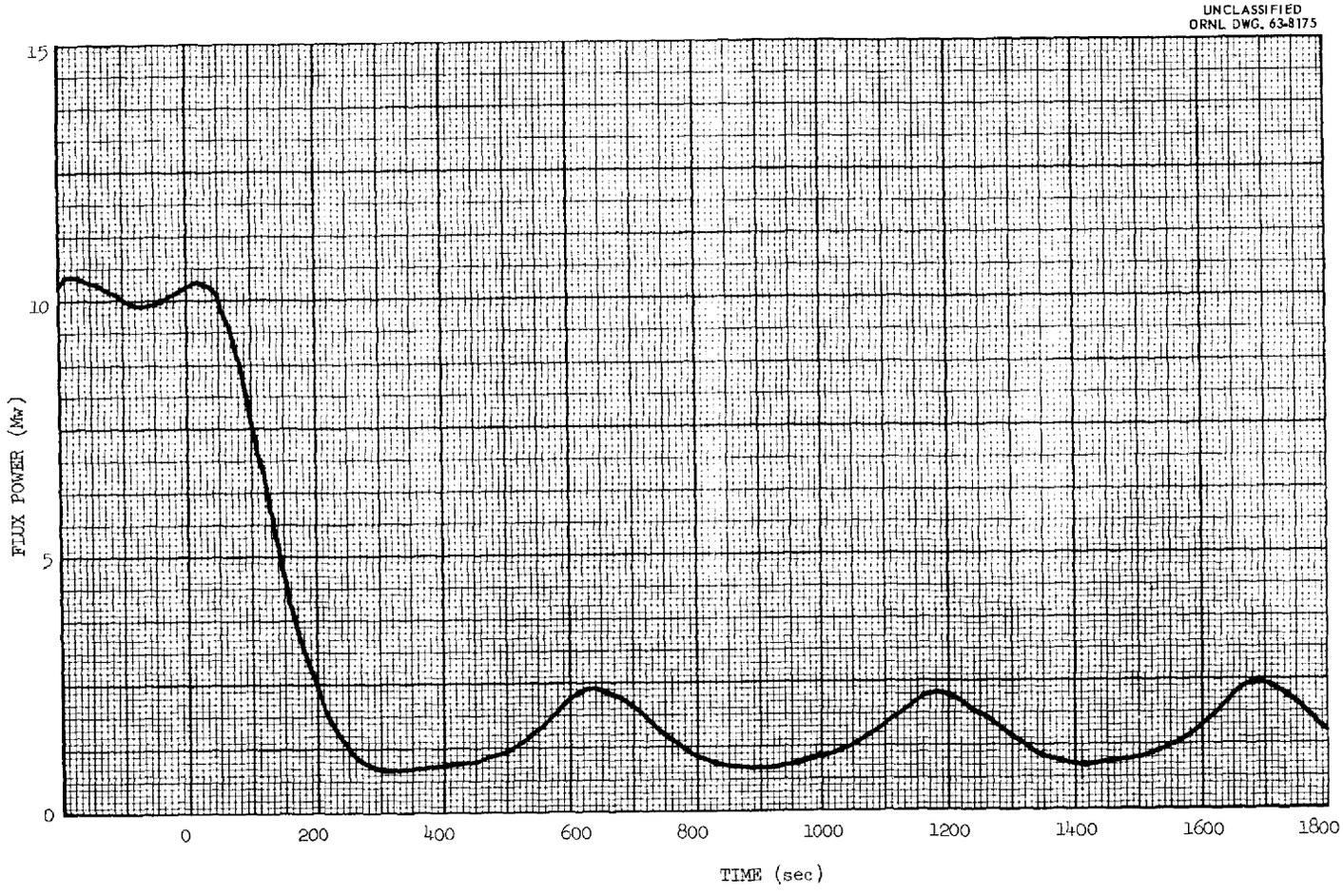

Fig. 11.6. Response of 1-Region Model of MSRE to a Decrease in Power Demand.

11.3 Operation with Servo Control

In order to eliminate possible oscillations and to obtain the desired steady-state temperature-power relations, a servo control system was designed for use in operation at powers above 1 Mw. One control rod is used as part of a servomechanism which regulates the nuclear power as required to keep the fuel temperature at the reactor vessel outlet within narrow limits. Simulator tests showed that the servo control system was capable of holding the fuel outlet temperature practically constant during load changes betwee 1 and 10 Mw in times of the order of 5 to 10 min without significant overshoot of the nuclear power.

At powers below 1 Mw, the servo control is switched to control the flux, or nuclear power, at a set point, and the temperature is controlled by manual adjustment of the radiator heat removal. Adjustment of the external heaters may also be used at times.

The design and performance of the servo control system are described in detail in Part II. Nuclear and Process Instrumentation.

12. KINETICS IN ABNORMAL SITUATIONS — SAFETY CALCULATIONS

12.1 Introduction

There are several conceivable incidents which could result in reactivity increases larger or faster than those encountered in normal operation of the reactor. Each of these incidents must be examined from the standpoint of reactor safety, to determine whether there is a possibility of damage to the reactor or hazard to personnel. Because the concern is safety, a conservative approach must be used. If the analysis of an incident indicates that the consequences may be intolerable, then protection must be provided to guard against damage and ensure the safety of reactor operation. (Control and safety systems are described in Part II. Nuclear and Process Instrumentation.)

12.2 General Considerations

The most likely form of damage from excessive reactivity additions in the MSRE is breach of the control rod thimbles in the core by a combination of high fuel temperature and the high pressure produced in the core by the rapid thermal expansion of the fuel.

The severity of the power, temperature, and pressure transients associated with a given reactivity incident depends upon the amount of excess reactivity involved, the rate at which it can be added, the initial power level, the effectiveness of the inherent shutdown mechanisms, and the efficacy of the reactor safety system. All of these factors depend to some extent on the fuel composition, because this determines the magnitude of the various reactivity coefficients and the control rod worth (see Tables 3.5 and 4.1).

In general, equivalent physical situations lead to larger amounts of reactivity and greater rates of addition with fuel B than with either A or C. This is a consequence of the larger values of the reactivity coefficients and control rod worth, the absence of the poisoning effect of thorium or U^{238}, and the lower inventory of U^{235} in the core.

The power and temperature transients associated with a given reactivity incident increase in severity as the initial power level is reduced. The reason for this is that, when the reactor becomes critical at very low power, the power must increase through several orders of magnitude before the reactivity feedback from increasing system temperatures becomes effective. Thus, even slow reactivity ramps can introduce substantial excess reactivity if the reactor power is very low when $k_{eff} = 1$.

The power level in the MSRE when the reactor is just critical depends on the strength of the neutron source, the shutdown margin prior to the approach to criticality, and the rate at which reactivity is added to make the reactor critical. The minimum neutron source strength which must be considered is 4×10^5 neutrons/sec, which is the rate of production in the core by (α-n) reactions in the fuel salt. Ordinarily the effective source will be much stronger, because an external Sb-Be source will normally be used to supply about 10^7 neutrons/sec to the core and, after the reactor has operated at high power, fission product gamma rays will generate up to 10^{10} photoneutrons/sec in the core. The ratio of the nuclear power at criticality to the source strength varies only ±10% for reactivity addition rates between 0.05 and 0.1% $\delta k/k$ per second and for the maximum shutdown margins attainable in the MSRE. For these conditions, the power level at criticality is about 2 mw if only the inherent (α-n) source is present, and is proportionately higher with stronger sources. The power level at criticality increases for lower rates of reactivity addition.

The principal factor in the inherent shutdown mechanism for the MSRE is the negative temperature coefficient of reactivity of the fuel salt. Since most of the fission heat is produced directly in the fuel, there is no delay between a power excursion and the action of this coefficient. The graphite moderator also has a negative temperature coefficient of reactivity; but this temperature rises slowly during a rapid power transient, because only a small fraction of the energy of fission is absorbed in the graphite. As a result, the action of the graphite temperature coefficient is delayed by the time required for heat transfer from the fuel to the graphite. Since fuel B has the largest negative temperature

coefficient of reactivity, a given reactivity incident produces smaller excursions with this fuel than with either of the other two.

The MSRE safety system causes the three control rods to drop by gravity when the nuclear power reaches 15 Mw or when the reactor outlet temperature reaches 1300°F. In the analysis of reactivity incidents, conservative values were assumed for delay time and rod acceleration, namely, 0.1 sec and 5 ft/sec^2, respectively. It was also assumed that one of the three rods failed to drop when called for.

12.3 Incidents Leading to Reactivity Addition

In the MSRE the conceivable incidents which could result in significant additions of reactivity include the following:

1. uncontrolled rod withdrawal,
2. cold-slug accident,
3. abnormal concentration of uranium during fuel additions,
4. displacement of graphite by fuel salt,
5. premature criticality while the core is being filled,
6. fuel pump power failure.

Estimates of the maximum addition rates and total reactivity associated with the first four incidents, together with the initial conditions postulated, are summarized in Table 12.1. Brief descriptions of these postulated incidents and the bases for the rates listed in Table 12.1 are as follows.

1. Simultaneous, continuous withdrawal of all three rods is initiated, starting with the reactor critical at 1200°F and the rod tips near the position of maximum differential worth. The rod withdrawal speed is 0.5 in./sec and the maximum differential worth was obtained from Fig. 4.2.

2. The cold-slug accident occurs when the mean temperature of the core salt decreases rapidly because of the injection of fluid at abnormally low temperature. Such an accident would be created by starting the fuel circulating pump at a time when fuel external to the core has been cooled well below that in the core, if such a situation were possible. A detailed study was made for a case in which fuel at 900°F is

Table 12.1. Maximum Expected Reactivity Additions in Postulated Operating Incidents

Incident	Description	Maximum Estimated Reactivity Rate [(% δk/k)/sec]	Maximum Total Reactivity (%)	Initial Power Level Assumed in Accident (w)
1	Uncontrolled withdrawal of 3 rods	0.10	3–4[a]	0.002[b]
2	Cold-slug accident[c]	0.16	1.5	1000
3	Abnormal concentration of uranium during fuel addition at pump bowl	0.12	0.37	0.01
4	Graphite stringer breakage	0.02	0.22	0.01

[a]Determined by maximum operating excess reactivity (~4%).

[b]Power at $k_{eff} = 1$ for minimum neutron source.

[c]900°F fuel salt pumped into core, which is initially critical at 1200°F.

pumped at 1200 gpm into the core, which is initially critical at a uniform temperature of 1200°F. The maximum reactivity addition rate in this case depends on heat transfer between salt and graphite and transient nuclear heating before the core is filled. The product of the salt temperature reactivity coefficient and the temperature decrease (300°F) divided by the core fluid residence time gives the rough estimate of reactivity addition rate listed in Table 12.1.

3. A maximum of 120 g of highly enriched uranium can be added as frozen salt at the pump bowl. An upper limit on the transient caused by a batch going into circulation was found by assuming that the fresh salt failed to mix gradually and passed through the core as a "front" of highly concentrated uranium. The rate listed in Table 12.1 is the maximum rate of addition, accounting for the change in nuclear importance as the concentrated salt moves upward through the channels. The total reactivity added would increase to a maximum when the uranium is near the center of the core, then decrease as the fuel exits.

4. Replacement of graphite by fuel produces a reactivity increase. Breakage of a graphite stringer into two pieces while fuel is circulating through the core could allow the upper section to float upward and fuel salt to move into the space about the fracture, were it not for the restraining rods and wires through the lower and upper ends of the stringers. An upper limit of the potential reactivity increase due to loss of graphite was calculated by assuming that the entire central graphite stringer was replaced by fuel salt. The total reactivity, listed in Table 12.1, is small, compared with that in the other incidents, and requires a time approximately equal to the core residence time for its addition.

Incidents 5 and 6 are not included in Table 12.1, since the conditions important to these incidents cannot be simply characterized by a reactivity addition rate.

In brief, the filling accident is postulated to occur as follows: When the reactor is shut down, the fuel salt is drained from the core. During the subsequent startup, the fuel salt and graphite are preheated and the control rods are positioned so that the reactor remains subcritical while filling. Criticality with the core only partially filled

could result, however, if the core or salt temperature were abnormally low, the fuel salt were abnormally concentrated in uranium, or the control rods were fully withdrawn.

In the case of the fuel pump power failure, there is an increase in reactivity because delayed neutron precursors are no longer swept out of the core when the pump stops. More important, from the standpoint of rising temperatures, is the sudden decrease in heat removal from the core.

From the reactivity additions listed in Table 12.1, it is apparent that of the four incidents listed, the rod withdrawal and the cold-slug accident are potentially the most serious. The analysis of these incidents and of the filling accident and the pump stoppage are described in the sections which follow.

12.4 Methods of Analysis

The general method used to estimate the consequences of the various incidents was numerical integration, by means of a digital computer, of the differential equations describing the nuclear, thermal, and pressure behavior of the reactor. In the development of the methods of analysis, realistic rather than pessimistic approximations were made wherever possible. The conservatism necessary in an appraisal of safety was then introduced by the choice of the initial conditions for the postulated incidents.

The mathematical procedures developed for the analysis of the MSRE kinetics are described in this section. Symbols used in this description are defined in Sec 12.4.4.

12.4.1 Reactivity-Power Relations

The time dependence of the nuclear power was described by the well-known relation

$$\dot{P} = \frac{k(1 - \beta) - 1}{\ell} P + \sum_{i=1}^{N} \lambda_i \Gamma_i \ . \qquad (12.1)$$

Six groups of neutrons were included in the summation. The effective number of precursors (actually, the latent power associated with their decay was represented by the equation for fixed-fuel or noncirculating reactors:

$$\dot{\Gamma}_i = \frac{\beta_i P}{\ell} - \lambda_i \Gamma_i \ . \qquad (12.2)$$

An allowance was made for the effects of circulation on the contribution of delayed neutrons by using reduced values of β_i (see Chap. 6).

The effective multiplication constant, k, was represented by the sum of several terms:

$$k = 1 + k_{ex} - \alpha_f(T_f^* - T_f^{*0}) - \alpha_g(T_g^* - T_g^{*0}) \ . \qquad (12.3)$$

Here k_{ex} is the reactivity added by all means other than changes in the fuel and graphite temperatures. Temperature effects are represented by the last two terms in (12.3): $\alpha_f(T_f^* - T_f^{*0})$ is the reactivity effect of changes in fuel temperature, which responds rapidly to power changes, and $\alpha_g(T_g^* - T_g^{*0})$ is the effect of the graphite temperature, which responds more slowly.

The equations given above are intrinsically space-independent approximations in which the response of the reactor is characterized by the time behavior of the total power, a single temperature for the fuel and another for the graphite, and the two parameters α_f and α_g. In order to complete the mathematical description of the reactor kinetics, the fuel and graphite temperature distributions must be reduced to a single characteristic temperature for each, which are related to the heat generation rate, P. The relations must necessarily involve heat removal from the core, heat capacities of the fuel and the graphite, and heat transfer between fuel and graphite.

12.4.2 Power-Temperature Relations

Two different models were used to approximate the exact thermal relations in the core.

The first power-temperature model assumed that the effective average temperature in the core was simply a weighted average of the inlet and outlet fuel temperatures:

$$T_f^* = \theta T_{fo} + (1 - \theta)T_{fi} \ . \tag{12.4}$$

It was also assumed that the nuclear average temperatures for the fuel and graphite were identical with the bulk average temperatures, which are governed by

$$S_f \dot{\overline{T}}_f = (1 - \gamma)P - WC_p(T_{fo} - T_{fi}) + h(\overline{T}_g - \overline{T}_f) \tag{12.5}$$

and

$$S_g \dot{\overline{T}}_g = \gamma P - h(\overline{T}_g - \overline{T}_f) \ . \tag{12.6}$$

These approximations were combined with the neutron kinetics equations in an IBM 7090 program called MURGATROYD.[36]

In the second model, an approximate calculation was made of the time dependence of the spatial temperature distributions of the fuel and graphite. These temperature distributions were then weighted with respect to nuclear importance in order to obtain single nuclear average temperatures for the fuel and graphite. The average temperatures then determined the reactivity feedback. In calculating the temperature profiles, the <u>shape</u> of the core power distribution was assumed to be time-independent; however, the <u>magnitude</u> of the total power varied in accordance with Eq. (12.1).

The temperature distributions as a function of time were calculated by replacing the macroscopic heat balance Eqs. (12.5) and (12.6) by "local" heat balances on salt and graphite in the individual channels:

$$u \frac{\partial T_f}{\partial z} + \frac{\partial T_f}{\partial t} = \frac{\Phi_f}{\rho_f C_f} + \frac{h(T_g - T_f)}{a_f \rho_f C_f} \ , \tag{12.7}$$

$$\frac{\partial T_g}{\partial t} = \frac{\Phi_g}{\rho_g C_g} - \frac{h(T_g - T_f)}{a_g \rho_g C_g} \ , \tag{12.8}$$

$$T = T(r,z,t), \qquad \Phi = \Phi(r,z,t) .$$

Note that the fluid temperature equation is now a partial differential equation, because of the presence of the transport term $u(\partial T_f/\partial z)$. The shape of the axial power distribution was assumed to be sinusoidal:

$$\Phi_f(r,z,t) = \frac{(1-\gamma)\, F(r)\, P(t)}{V_f} \frac{\pi}{2} \sin \frac{\pi z}{H} , \tag{12.9}$$

$$\Phi_g(r,z,t) = \frac{\gamma\, F(r)\, P(t)}{V_g} \frac{\pi}{2} \sin \frac{\pi z}{H} . \tag{12.10}$$

With the above approximations, it was possible to reduce the procedure of solving (12.7) and (12.8) to numerical integrations over only the time variable. The temperature at any point along the channel depends on the temperature distribution along the channel at the time the fuel enters the channel and the subsequent power-time history. The power-time relation was again obtained by integrating Eqs. (12.1) and (12.2). However, the temperature feedback terms are now based on nuclear average temperatures, in which the fuel and graphite temperature profiles at time t are weighted with respect to nuclear importance [see Eq. (3.2) for the general definition of the nuclear average temperature]. Using the sinusoidal approximation for the axial variation of the importance function and I(r) to represent the radial variation of the importance:

$$T_j^*(t) - T_{fi} = \frac{\int_0^R \int_0^H [T_j(r,z,t) - T_{fi}]\, I(r) \sin^2 \frac{\pi z}{H}\, r\, dr\, dz}{\int_0^R \int_0^H I(r) \sin^2 \frac{\pi z}{H}\, r\, dr\, dz} , \tag{12.11}$$

$$j = f,\ g .$$

With the further assumption that heat conduction effects are small compared with the heat generation terms, the radial dependence of the temperature rise is proportional to the radial power density, so that (12.11) may be further simplified:

$$T_j^*(t) - T_{fi} = F_R^* \frac{\int_0^H [T_j(z,t) - T_{fi}] \sin^2 \frac{\pi z}{H} \, dz}{\int_0^H \sin^2 \frac{\pi z}{H} \, dz}, \qquad (12.12)$$

$$j = f, g ,$$

where

$$F_R^* = \frac{\int_0^R F(r) \, I(r) \, r \, dr}{\int_0^R I(r) \, r \, dr} . \qquad (12.13)$$

The procedure for solution of the kinetics equations thus consists of calculating the temperature profiles from Eqs. (12.7) and (12.8), the nuclear average temperature from Eq. (12.12), and the power-time behavior from Eqs. (12.1), (12.2), and (12.3). An IBM 7090 program, ZORCH, was designed to obtain the solution of this set of equations by numerical approximation methods.[37]

12.4.3 Temperature-Pressure Relations

During any excursion in the fuel temperature, the pressure in the core will rise and fall as the fuel expands and contracts. These changes result from the inertial effect of acceleration of the fuel salt in the reactor outlet pipe leading to the pump bowl, changes in friction losses in the pipe, and the compression of the gas space in the pump bowl. If the fluid is assumed to be incompressible, so that there is no effect of pressure on reactivity, the hydrodynamics equations can be solved independently of the power-temperature equations. A simplified model of the primary salt system, similar to that utilized by Kasten and others for kinetics studies relating to the Homogeneous Reactor Test,[38] was used for approximate calculations of the pressure rise. It is assumed that the fluid density can be adequately approximated by a linear dependence on the temperature:

$$\rho(\bar{T}_f) = \rho^0 + \frac{\partial \rho}{\partial T_f} (\bar{T}_f - \bar{T}_f^0) , \tag{12.14}$$

where $\bar{T}_f$ is the bulk average temperature of the salt in the reactor core. The other basic relations required for calculation of the pressure rise are the force balance on the fluid in the outlet pipe and the equation of continuity for the core salt:

$$\frac{M}{144 g_c} \dot{U} = A(p_c - p_p - fU^2) , \tag{12.15}$$

$$\dot{\rho} = - \frac{A}{V_f} \rho^0 (U - U^0) . \tag{12.16}$$

The compression of the gas in the pump bowl is assumed to be adiabatic:

$$p_p V_p^n = p_p^0 (V_p^0)^n . \tag{12.17}$$

The resulting equation for the pressure rise is[36]

$$p_c - p_c^0 = C_1[\dot{x} + C_2 y + C_3 \dot{y} (1 + C_4 \dot{y})] . \tag{12.18}$$

In this expression x and y are the dimensionless power and the dimensionless fluid temperature, defined as

$$x = P/P^0 , \tag{12.19}$$

$$y_f = \frac{S_f(\bar{T}_f - \bar{T}_{fo})}{(1 - \gamma)P^0}, \tag{12.20}$$

and the constants are defined as

$$C_1 = - \frac{V_f}{A} \frac{1}{\rho^0} \frac{\partial \rho}{\partial T_f} \frac{M(1 - \gamma)P^0}{144 g_c A S_f} , \tag{12.21}$$

$$C_2 = p_p^0 \frac{(nA)\ 144 g_c A}{V_p^0 M}, \tag{12.22}$$

$$C_3 = 2U_f^0 \frac{144 g_c A}{M}, \tag{12.23}$$

$$C_4 = -\frac{V_f(1-\gamma)P^0}{2AU^0 S_f \rho^0} \frac{\partial \rho}{\partial \bar{T}_f}. \tag{12.24}$$

The first term on the right hand side of (12.18) arises from acceleration of fluid in the outlet pipe, the second results from the compression of the pump bowl gas, and the last represents the pressure drop due to friction loss in the pipe. This equation is the basic approximation for the transient core pressure rise utilized in the kinetics programs ZORCH and MURGATROYD.

12.4.4 Nomenclature for Kinetics Equations

A	Cross-sectional area of outlet pipe
a_f	Cross-sectional area of fuel channel
a_g	Cross-sectional area of graphite stringer
C_1	Constant defined by Eq. 12.21
C_2	Constant defined by Eq. 12.22
C_3	Constant defined by Eq. 12.23
C_4	Constant defined by Eq. 12.24
f	Friction loss in outlet pipe
F	Radial distribution of power density
F_R^*	Importance-weighted average of F
g_c	Dimensional constant, $(ft \cdot lb_{mass})/(sec^2 \cdot lb_{force})$
H	Height of core
h	Heat transfer factor, graphite to fuel
I	Radial distribution of nuclear importance
k	Multiplication factor
k_{ex}	Reactivity added by external means
ℓ	Neutron lifetime
M	Mass of fuel in outlet pipe to pump
N	Number of delayed neutron groups
n	Ratio of specific heats

P	Power
p_c	Pressure in core
p_p	Pressure in pump bowl
R	Radius of core
r	Radial distance from core center line
S_f	Total heat capacity of fuel in core
S_g	Total heat capacity of graphite
T_f	Local temperature of fuel
T_g	Local temperature of graphite
T_f^*	Nuclear average temperature of fuel
T_g^*	Nuclear average temperature of graphite
$\overline{T}_f$	Bulk average temperature of fuel
$\overline{T}_g$	Bulk average temperature of graphite
T_{fi}	Fuel inlet temperature
T_{fo}	Fuel outlet temperature
t	Time
u	Velocity of fuel in a channel
U	Velocity of fuel in outlet pipe
V_f	Volume of fuel in core
V_g	Volume of graphite in core
V_p	Volume of gas in pump
WC_p	Heat capacity of fuel flow
x	Normalized power
y	Normalized fuel temperature
z	Axial distance from bottom of core
α_f	Fuel temperature coefficient of reactivity
α_g	Graphite temperature coefficient of reactivity
β_i	Fraction of neutrons in delayed group i
β	Total fraction of delayed neutrons
γ	Fraction of heat produced in graphite
Γ_i	Latent power associated with delay group i
θ	Temperature weighting factor
λ_i	Decay constant for group i
ρ	Density
ρC	Volumetric heat capacity
Φ	Power density

Superscript 0 refers to initial conditions

12.5 MSRE Characteristics Used in Kinetics Analysis

Table 12.2 summarizes the properties of the MSRE which affect the kinetics and gives the values which were used in the last analysis.

Table 12.2. MSRE Characteristics Affecting Kinetic Behavior

	Fuel Salt		
	A	B	C
Prompt neutron lifetime (sec)	2.29×10^{-4}	3.47×10^{-4}	2.40×10^{-4}
Temperature coefficients of reactivity [$(\delta k/k)/°F$]			
Fuel	-3.03×10^{-5}	-4.97×10^{-5}	-3.28×10^{-5}
Graphite	-3.36×10^{-5}	-4.91×10^{-5}	-3.68×10^{-5}
Fuel density (lb/ft^3)	144	134	143
Delayed neutron fraction			
Static		0.0067	
Circulating		0.0036	
Residence times (sec)			
Core		9.37	
External to core		16.45	
Fraction of heat generation			
In fuel		0.933	
In graphite		0.067	
Core heat capacity [(Mw-sec)/°F]			
Fuel		1.74	
Graphite		3.67	
Graphite-to-fuel heat transfer (Mw/°F)		0.020	
Core fuel volume (ft^3)		25.0	
Fuel volumetric expansion coefficient ($°F^{-1}$)		1.18×10^{-4}	
Length of line to pump bowl (ft)		16.0	
Cross sectional area of line (ft^2)		0.139	
Friction loss in line [$psi/(ft/sec)^2$]		0.020	
Pumb bowl initial pressure (psig)		5	
Volume of gas in pump bowl (ft^3)		2.5	
Ratio of specific heats of helium (C_p/C_v)		1.67	

12.6 Preliminary Studies

12.6.1 Early Analysis of Reactivity Incidents[39]

An early study was made in which each of the accidents described in Sec 12.3 was analyzed, using the space-independent kinetics program MURGATROYD to calculate power, temperature, and pressure excursions. Some calculations of the response of the reactor to arbitrary step and ramp additions of reactivity were also made, in order to better define the limits which would lead to internal damage to the core. The nuclear characteristics used in this study were similar to those listed in Table 12.2 for fuel A.

The results of the preliminary study indicated that none of the accidents analyzed could lead to catastrophic failure of the reactor. The extreme cases of cold-slug accidents, filling accidents, and uncontrolled rod withdrawal led to predicted core temperatures high enough to threaten internal damage. Because each of these accidents could happen only by compound failure of protective devices, and because in each case there existed means of corrective action independent of the primary protection, damage was considered to be very unlikely in the cases considered.

The calculated response to arbitrary step and ramp additions of reactivity indicated that damaging pressures could occur only if the addition were the equivalent of a step of about 1% δk/k or greater, well beyond the severity of foreseeable accidents.

12.6.2 Comparison of MURGATROYD and ZORCH Results

After the digital program ZORCH became available, some kinetics calculations were made to compare the excursions predicted by this method with those computed with MURGATROYD. As expected, differences were found in the calculated power, temperature, and pressure excursions obtained from the two kinetics programs. The differences arise because the approximations used in MURGATROYD for the nuclear average temperature and the rate of heat removal from the reactor are poor during a rapid power transient, whereas these quantities are treated much more realistically in ZORCH.

An example of the differences in MURGATROYD and ZORCH results is illustrated in Fig. 12.1, where the power and temperature transients following a prompt-critical step in reactivity are compared. Because ZORCH computes a spatial temperature distribution and gives the greatest weight to the most rapidly rising temperatures, its nuclear average temperature rises more rapidly than the fuel bulk average temperature or the temperature computed by MURGATROYD. The power excursion is therefore cut off at a lower peak than that calculated by MURGATROYD. The integrated power is also less in the ZORCH results, causing a smaller rise in the mixed-mean temperature of the fuel leaving the core (T_o in Fig. 12.1). The highest temperature in Fig. 12.1, $(T_o)_{max}$, is the temperature predicted by ZORCH for the outlet of the hottest fuel channel. This fuel would mix in the upper head of the reactor vessel with cooler fuel from other channels before reaching the outlet pipe.

12.7 Results of Reactivity Accident Analyses

The results of the most recent analyses of the important reactivity accidents are described in this section.

12.7.1 Uncontrolled Rod Withdrawal Accident

This accident is most severe when criticality is achieved with all three control rods moving in unison at the position of maximum differential worth. Since this condition is within the range of combinations of shutdown margin and rod worth for all three fuels, it was used as a basis for analyzing this accident. The maximum rates of reactivity addition by control-rod withdrawal are 0.08, 0.10, and 0.08% $\delta k/k$ per second when the system contains fuels A, B, and C, respectively. The initial transients associated with these ramps were calculated for fuels B and C starting with the reactor just critical at 0.002 w and 1200°F. (The transients for fuel A would be practically the same as for fuel C.)

The first 15 sec of the transients in some of the variables are shown in Figs. 12.2 and 12.3 for fuels B and C respectively. The curves illustrate the behavior of the power, the fuel and graphite nuclear average temperatures, T_f^* and T_g^*, the temperature of the fuel leaving the

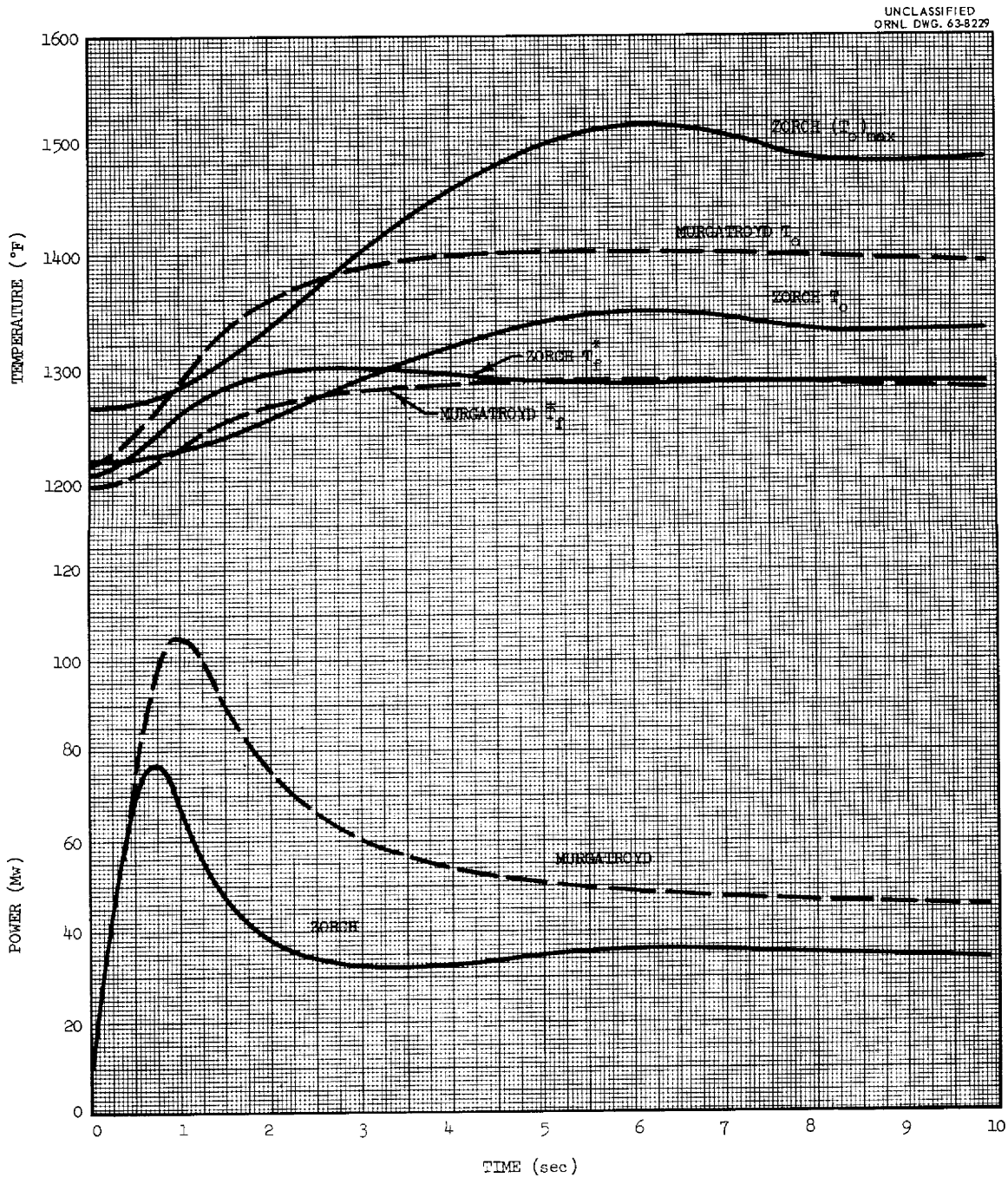

Fig. 12.1. Power and Temperature Transients Following a Prompt Critical Step in Reactivity; Fuel A; Comparison of ZORCH and MURGATROYD Kinetics Models.

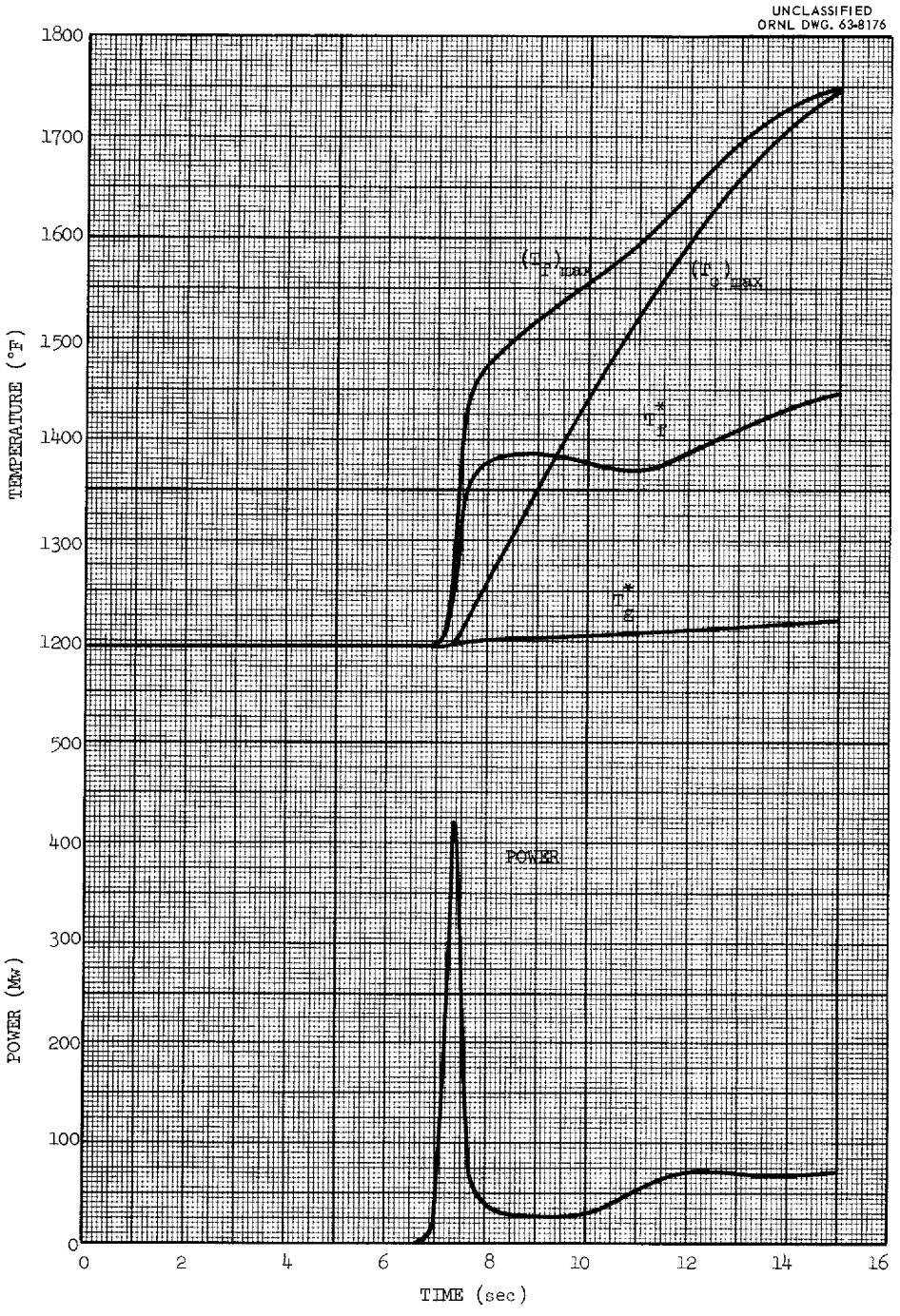

Fig. 12.2. Power and Temperature Transients Produced by Uncontrolled Rod Withdrawal, Fuel B.

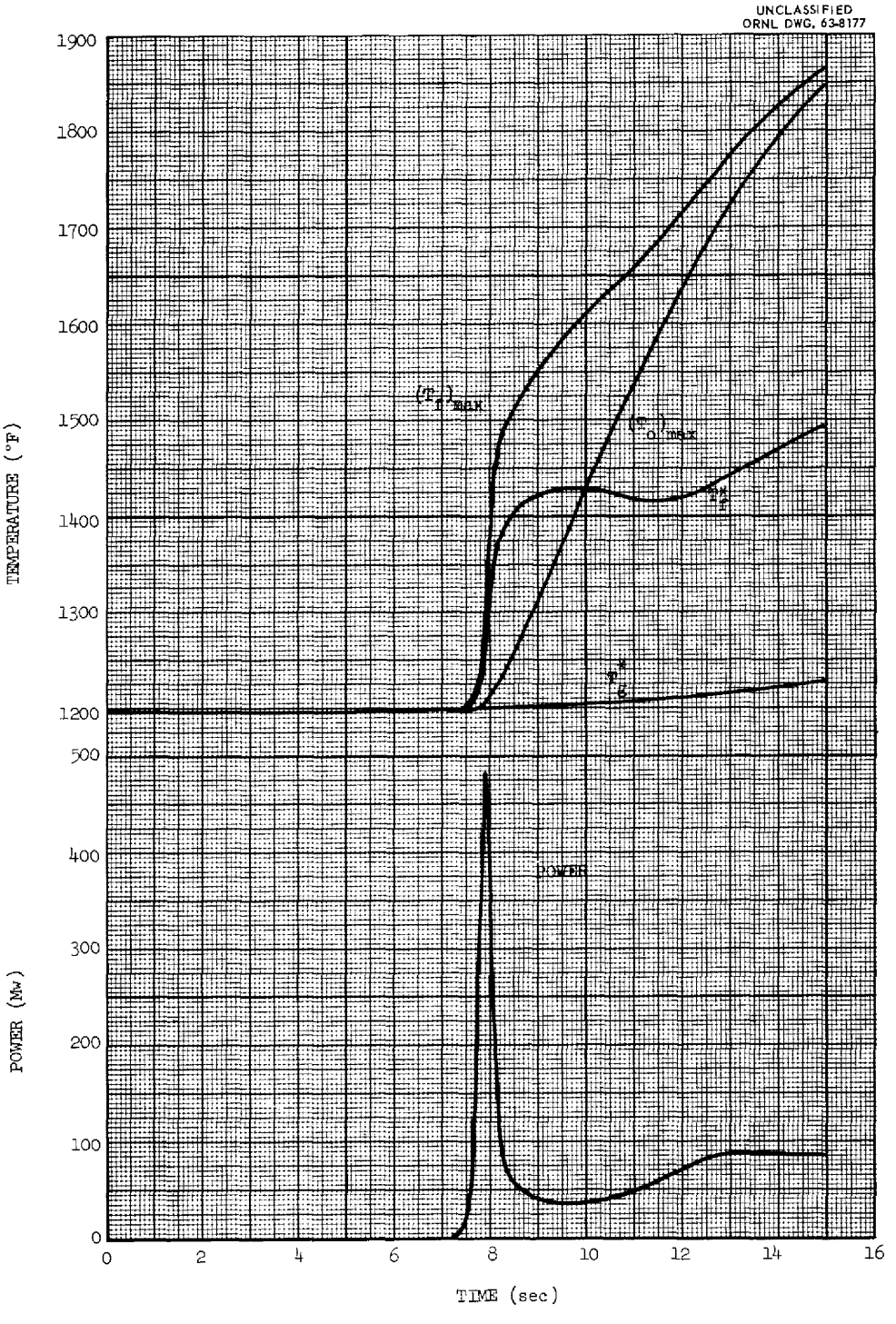

Fig. 12.3. Power and Temperature Transients Produced by Uncontrolled Rod Withdrawal, Fuel C.

hottest channel, $(T_o)_{max}$, and the highest fuel temperature in the core, $(T_f)_{max}$.

Although the rate of reactivity addition was lower for fuel C than for fuel B, the excursions were more severe for fuel C because of the smaller fuel temperature coefficient of reactivity and the shorter prompt neutron lifetime associated with this mixture. The power excursion occurred somewhat later with fuel C because of the greater time required to reach prompt criticality at the lower ramp rate.

During steady operation the maximum fuel temperature occurs at the outlet of the hottest channel. However, during severe power excursions which are short compared with the time of transit of fuel through the core, the maximum fuel temperature at a given time may be at a lower elevation in the hottest channel, where the power density is relatively higher. This is illustrated by the difference between the maximum fuel temperature and the temperature at the outlet of the hottest channel during and immediately after the initial power excursion. These two temperatures then converged as the fuel was swept from the region of maximum power density toward the core outlet, while the power was relatively steady. The rise in the mixed-mean temperature of the fuel leaving the core is about half of that shown for the hottest fuel channel.

The transient calculations were stopped before the fuel that was affected by the initial power excursion had traversed the external loop and returned to the core. The trends shown in Figs. 12.2 and 12.3 would continue until the core inlet temperature began to rise, about 16 sec after the initial excursion in the outlet temperature. At that time, the power and the outlet temperatures would begin to decrease; the nuclear average temperatures would continue to rise as long as rod withdrawal were continued. However, the rise in graphite temperature resulting from heat transfer from the fuel would reduce the rate of rise of the fuel nuclear average temperature.

It is clear from Figs. 12.2 and 12.3 that intolerably high fuel temperatures would be reached in this accident if complete withdrawal of the control rods were possible. Since the reactor safety system provides for dropping the control rods on high power, the accident involving fuel C was also examined in the light of this action. It was assumed that only

two rods dropped (0.1 sec after the flux reached 15 Mw, with an acceleration of 5 ft/sec^2), while the third continued to withdraw. The initial transients for this case are shown in Fig. 12.4. The flat portion in the maximum fuel temperature reflects the time required for the fuel that was heated by the initial excursion to pass out of the core. Dropping two control rods in this accident reduced the temperature excursions to insignificant proportions from the standpoint of reactor safety. Since the reactor cannot be made critical by withdrawing only one control rod, failure of the rod-drop mechanism on one rod does not impair the safety of the system.

The core pressure transients were small in all of the rod withdrawal accidents. With no corrective action, the pressure increases were 18 and 21 psi for the cases involving fuels B and C, respectively. Simulation of the control-rod drop limited the pressure excursion with fuel C to 8 psi.

12.7.2 Cold-Slug Accident

The kinetic behavior was calculated for a postulated incident in which one core-volume of fuel at 900°F suddenly entered the core, which was initially critical at 1200°F and 1 kw. The resulting power-temperature transients are summarized in Fig. 12.5, as calculated for fuel salt B. The maximum values reached for power and temperature were higher for this case than for salt C. The maximum pressure achieved was about 6 psi with either salt.

The temperature plots given in Fig. 12.5 exhibit the following features: There was an initial 300°F drop in the reactor inlet temperature, which remained at 900°F until the core was filled with the cooler fluid. As the volume of the core occupied by the cold slug became larger, the fuel nuclear average temperature decreased slowly, adding reactivity. When the reactivity approached prompt critical, the reactor period became small and substantial nuclear heating occurred. This caused the fuel nuclear average temperature to rise sharply and limit the power excursion. The additional heat generation was reflected as a rise in the channel outlet temperature. At the time the leading edge of the cold slug reached

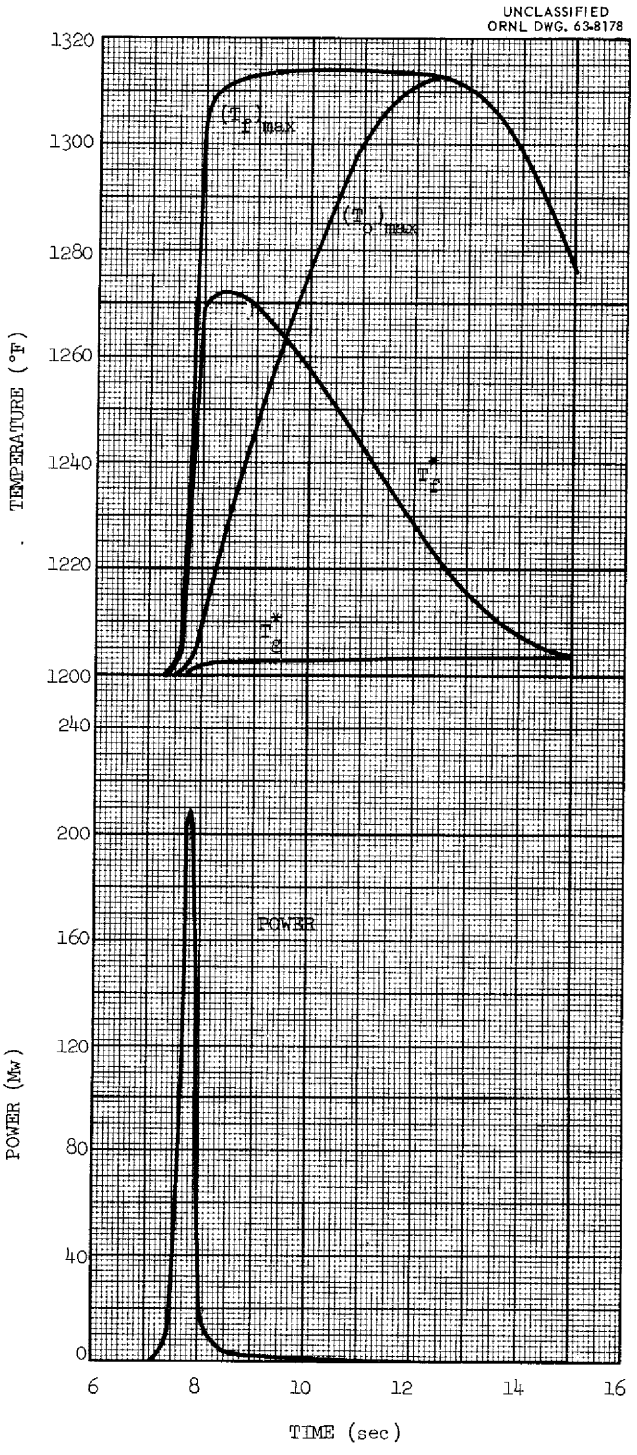

Fig. 12.4. Effect of Dropping Two Control Rods at 15 Mw During Uncontrolled Rod Withdrawal, Fuel C.

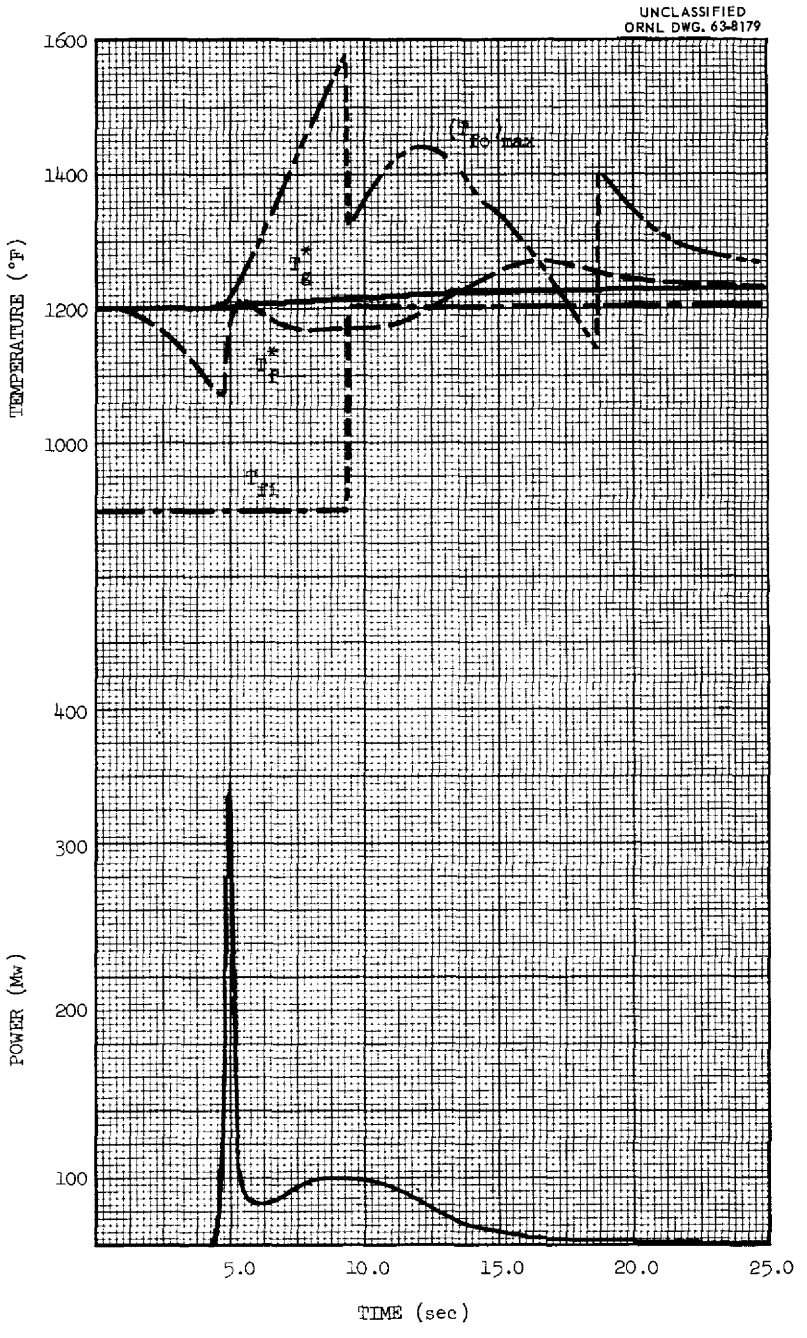

Fig. 12.5. Power and Temperature Transients Following a 900°F Cold Slug Accident; Fuel Salt B; No Corrective Action.

the top of the core, there was a sharp drop in the channel outlet temperature. Simultaneously, the reactor inlet salt temperature returned to 1200°F as the available amount of cold fluid was exhausted. The channel outlet passed through a maximum upon arrival of the fluid heated at the center of the core by the initial power transient, then decreased until finally the rise in salt inlet temperature was again reflected (about 9.4 sec later) as a rise in the channel outlet temperature.

It is apparent that the excursions in temperature and pressure resulting from the nuclear incident are less important than the rapid rates of change of temperature calculated for the incident. The latter could result in large transient stresses in the inlet and outlet piping and in the fuel pump.

12.7.3 Filling Accident

Conditions Leading to Filling Accident. – Normal procedure for startup of the MSRE requires that the reactor and fuel be heated by electric heaters to near the operating temperature before the fuel is transferred from the drain tank to the core. The control rods normally are partially inserted during a fill, so that the reactor is subcritical at normal temperature with the core full of fuel. Criticality is attained by further rod withdrawal after the fuel and coolant loops have been filled and circulation has been started.

Criticality could be reached prematurely during a startup while the core is being filled if: (a) the control rods were withdrawn from the positions they normally occupy during filling; (b) the core temperature were abnormally low; or (c) the fuel were abnormally concentrated in uranium. Interlocks and procedures are designed to prevent such an accident. If, despite the precautions, the reactor were to become critical under such conditions, there would be a power excursion, the size of which would depend on the source power and the rate of reactivity addition. The core temperature would rise rapidly during the initial power excursion; then, if fuel addition were continued, it would rise in pace with the increase in critical temperature. The consequences of a number of filling accidents were analyzed, and the principal results are summarized in this section. Detailed description of these studies is contained in ref 40.

Reactivity Addition. — The amount of reactivity available in a filling accident depends on the conditions causing the accident and the characteristics of the fuel salt. In the case of filling the reactor with the control rods fully withdrawn, the excess reactivity is limited to the amount in the normal fuel loading. Only about 3% δk/k will be required for normal operation (see Table 9.1), and the uranium concentration in the fuel will be restricted by administrative control to provide no more than required. Filling at the normal rate with all rods fully withdrawn results in a reactivity ramp of 0.01% δk/k per second when k = 1. The power excursion associated with this ramp is well within the range of control of the rod safety system. Full insertion of any two of the three control rods is adequate for shutdown of the full core.

In filling the fuel at an abnormally low temperature, excess reactivity is added by means of the negative temperature coefficient of the fuel. For fuel B (the mixture with the largest negative temperature coefficient of reactivity), cooling the salt to the liquidus temperature (840°F) provides 1.9% excess reactivity. The reactivity addition rate at k = 1 is 0.006%/sec. The shutdown margin provided by the control rods is 5.2%.

In the case of filling of the reactor core with fuel abnormally concentrated in uranium, the mechanism assumed to cause the incident is that of selective freezing of fuel in the drain tank. The crystallization paths of all three salt mixtures under consideration are such that large quantities of salt can be solidified, under equilibrium conditions,* before uranium (or thorium) appears in the solid phase. Selective freezing, therefore, provides one means by which the uranium concentration can be increased while the salt is in the drain tank. Since the reactor vessel is the first major component of the fuel loop that fills on salt additions, approximately 40% of the salt mixture can be frozen in the drain tank before it becomes impossible to completely fill the core.

The changes in liquid composition as selective freezing proceeds depend on the initial composition and the conditions of freezing. Figure 12.6 shows the atomic concentrations in the remaining melt for fuel A as

*Very slow cooling.

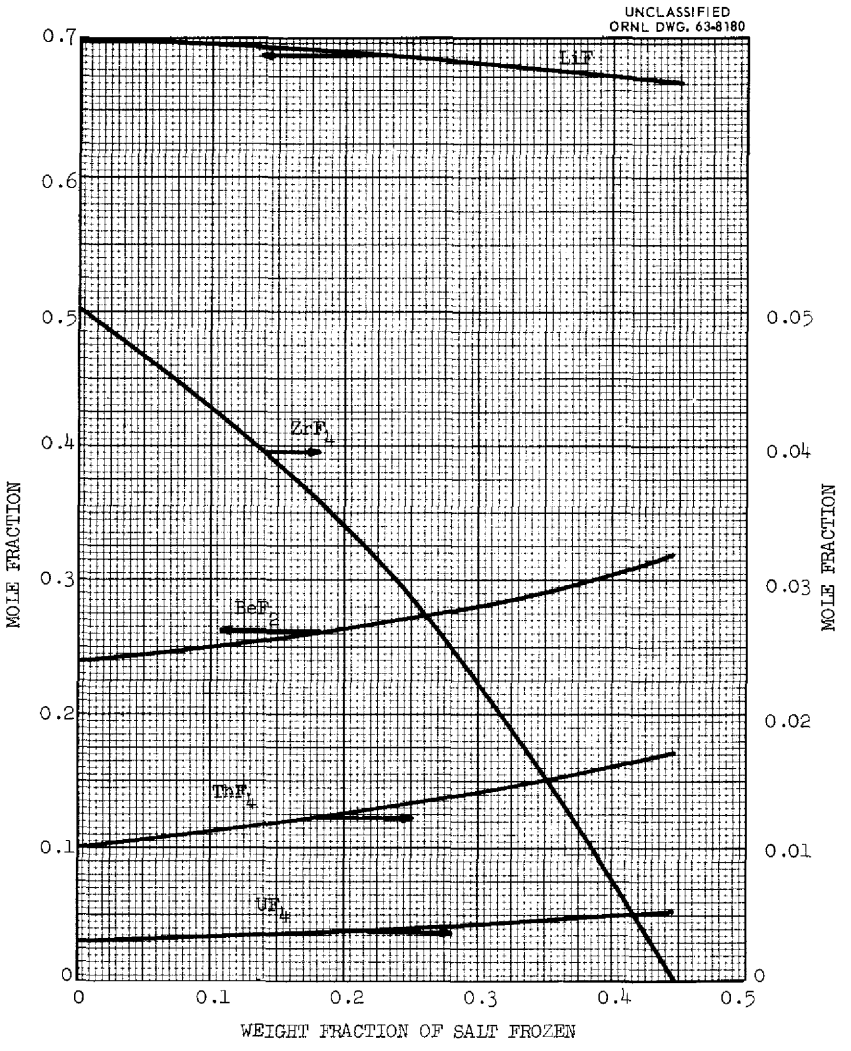

Fig. 12.6. Liquid Composition Resulting from Selective Freezing of Fuel Salt A in Drain Tank.

a function of the fraction of salt frozen. The curves are based on the assumption that only the equilibrium primary solid phase, $6LiF \cdot BeF_2 \cdot ZrF_4$, appears.

The effect on premature criticality was evaluated for each of the three salts with 39%, by weight, frozen in the drain tank as $6LiF \cdot BeF_2 \cdot ZrF_4$.* Under these conditions the full reactor at 1200°F had about 4% excess reactivity for fuels A and C and 15% for fuel B. Fuels A and C

*The composition of the solid phase has little effect on the nuclear calculations as long as it does not include fissile or fertile material.

contain significant amounts of thorium and U^{238}, respectively, which remain in the melt with the U^{235} during selective freezing. The poisoning effect of these species greatly reduces the severity of the filling accident when they are present. The excess reactivities in this accident, with so much selective freezing, exceed the shutdown margin of the control rods. Thus it is necessary to stop the filling process to prevent a second reactivity excursion after the rods have been dropped. The accident involving fuel B is the most severe; the reactivity addition rate for this case is 0.025% $\delta k/k$ per second at $k = 1$, compared with 0.01%/sec for fuels A and C.

Corrective Actions. — Control rod drop and stoppage of fuel addition are considered as means for limiting the power excursion and stopping the addition of reactivity. In the first case, dropping the rods on high flux signal (15 Mw power) was found to be more than adequate for any filling accident in which the available excess reactivity does not exceed the shutdown margin of the rods. For the more severe accidents, it is necessary to supplement the rod drop by stopping the fill to prevent further reactivity addition.

Filling the reactor is accomplished by admitting helium, at 40 psig supply pressure, to a drain tank and forcing the liquid fuel up through the drain line into the primary system. Figure 12.7 is a simplified flowsheet of the reactor fill, drain, and vent systems showing only those features which pertain directly to the filling accident. All valves are shown in the normal positions for filling the reactor from fuel drain tank No. 1. Three independent actions are available to stop the addition of fuel to the primary loop:

1. Opening HCV-544 equalizes the loop and drain tank pressure.
2. Opening HCV-573 relieves the pressure in the drain tank by venting gas through the auxiliary charcoal bed to the stack.
3. Closing HCV-572 stops the addition of helium to the drain tank.

During a filling accident all three actions would be attempted simultaneously to ensure stopping the fill. The first two actions, in addition to stopping the fill, allow the fuel in the primary loop to run back to the drain tank. Stopping the gas addition only stops the fill, but the salt flow does not stop instantaneously.

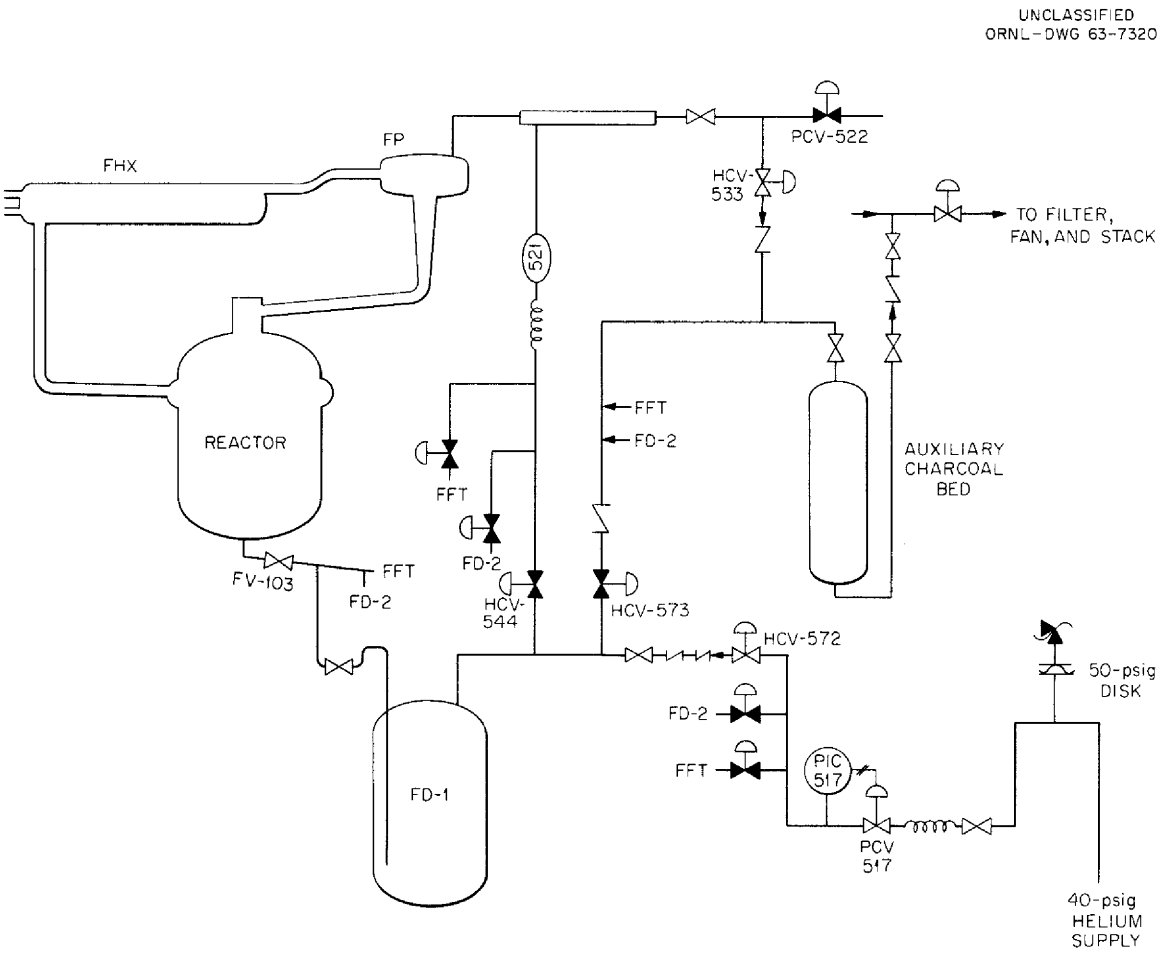

Fig. 12.7. System Used in Filling Fuel Loop.

During filling, the flowing fuel in the drain line experiences a small pressure drop. In addition, the gas displaced from the primary loop must flow out to the stack through equipment which imposes some pressure drop. Consequently, the pressure in the drain tank at any point in the filling operation is greater than that required to maintain the liquid-level difference under static conditions. As a result, when gas addition is stopped, the fuel level in the primary loop coasts up until the dynamic head losses have been replaced by an increase in the static head difference between loop and drain tank. If this coast-up occurs during a filling accident, the additional excess reactivity associated with the higher level must be compensated for by the system.

Temperature Coefficient of Reactivity. – The temperature coefficient of reactivity of the fuel in the partially filled core differs substantially from that in the full system. In the full system, the thermal expansion of the salt expels fuel from the core. The effective size of the core, however, remains essentially constant. Thermal neutron leakage also increases, and both of these factors tend to reduce reactivity. In the partially full core, fuel expansion increases the effective height of the core. This tends to offset the decrease in reactivity due to increased radial neutron leakage. The effective temperature coefficient of reactivity of fuel B with the core 60% full is approximately -0.4×10^{-5} $(°F)^{-1}$, compared with -5.0×10^{-5} $(°F)^{-1}$ for the full core. The temperature coefficient of the graphite is not significantly affected by the fuel level.

Maximum Filling Accident. – Only the most severe of the postulated filling accidents was analyzed in detail. It was assumed that the uranium in fuel B was concentrated to 1.6 times the normal value by selective freezing of 39% of the salt in the drain tank. Several other abnormal situations were postulated during the course of the accident, as follows:

1. The helium supply pressure was assumed to be 50 psig, the limit imposed by the rupture disk in the supply system, rather than the normal 40 psig. This pressure gave a fill rate of 0.5 ft^3/min when criticality was achieved and produced a level coast-up of 0.2 ft after gas addition was stopped.

2. It was assumed that only two of the three control rods dropped on demand during the initial power excursion.

3. It was assumed that two of the three actions available for stopping the fill failed to function. Only the least effective action, stopping the gas addition, was used in the analysis. This allowed the fuel level to coast up and make the reactor critical after the two control rods had been dropped to check the initial power excursion.

The power and temperature transients associated with the accident described above were calculated with the aid of both digital and analog computers. Since the useful range of an analog computer is only about two decades for any variable, the initial part of the power transient was calculated with the digital kinetics program MURGATROYD. The digital

calculation was stopped at 10 kw when the power began to affect system temperatures, and the digital results were used as input to start the analog calculation. Since it was clear that the reactor would go critical again after the control rods had been dropped, the analog simulation included the compensating effects of the fuel and graphite temperature coefficients of reactivity. Because of the small fuel coefficient, it was necessary to use a highly detailed model to represent heat transfer from the fuel to the graphite during the transient.

The results of the maximum fill accident simulation are shown graphically in Figs. 12.8 and 12.9. Figure 12.8 shows the externally imposed reactivity transient exclusive of temperature compensation effects. The essential features are the initial, almost-linear rise which produced the first power excursion as fuel flowed into the core, the sharp decrease as the rods were dropped, and the final slow rise as the fuel coasted up to its equilibrium level. Figure 12.9 shows the power transient and some pertinent temperatures. The fuel and graphite nuclear average temperatures are the quantities which ultimately compensated for the excess reactivity introduced by the fuel coast-up. The maximum fuel temperature refers to the temperature at the center of the hottest portion of the hottest fuel channel. The initial power excursion reached 24 Mw before being checked by the dropping control rods, which were tripped at 15 Mw. This excursion is not particularly important, because it did not result in much of a fuel temperature rise. After the initial excursion, the power dropped to about 10 kw and some of the heat that had been produced in the fuel was transferred to the graphite. The resultant increase in the graphite nuclear average temperature helped to limit the severity of the second power excursion. Reactivity was added slowly enough by the fuel coast-up that the rising graphite temperature was able to limit the second power excursion to only 2.5 Mw. The maximum temperature attained, 1354°F, can be tolerated for long times.

12.7.4 Fuel Pump Power Failure

The consequences of interruption of fuel circulation while the reactor is at high power were determined by analog computer simulation of

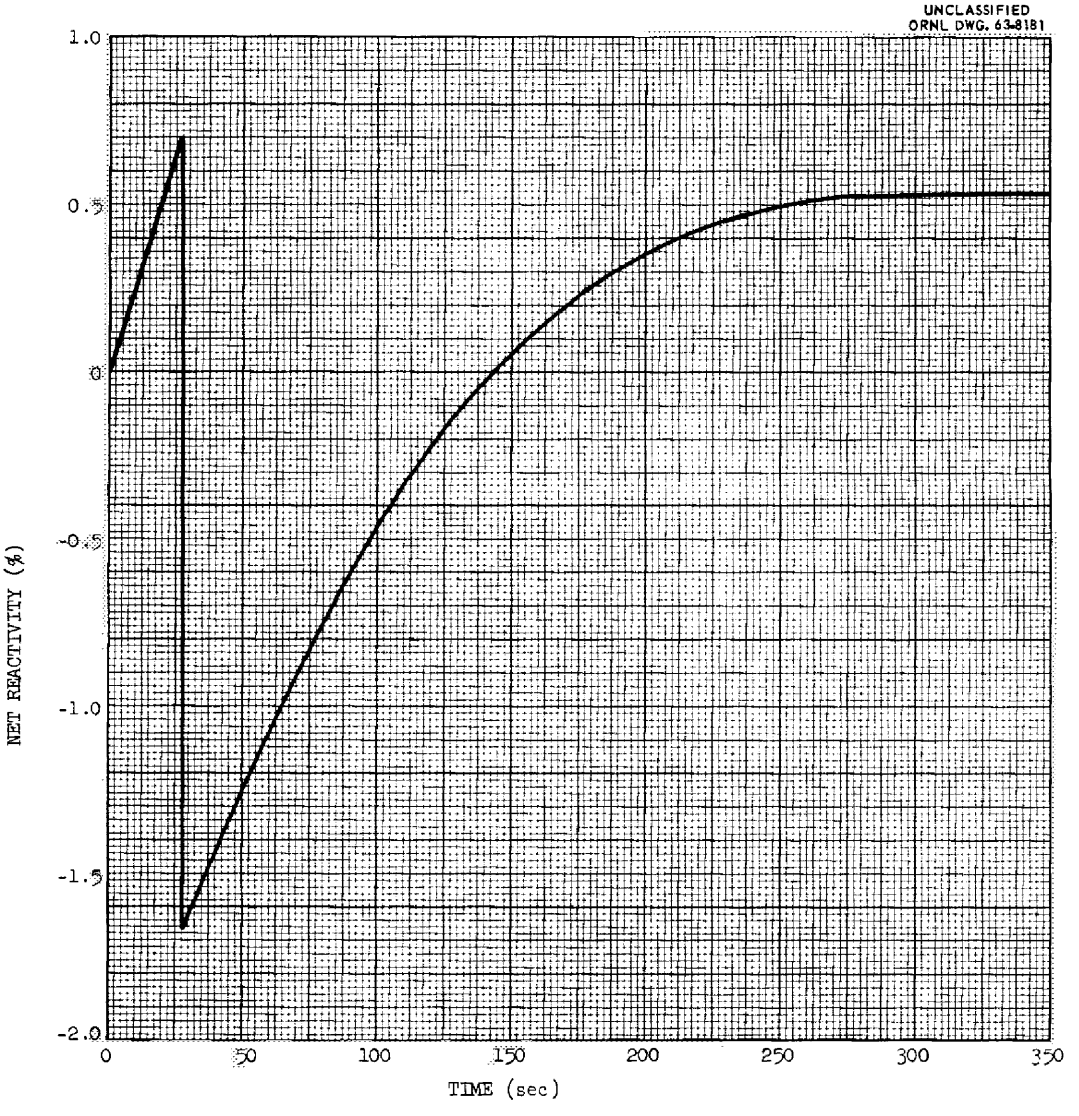

Fig. 12.8. Net Reactivity Addition During Maximum Filling Accident.

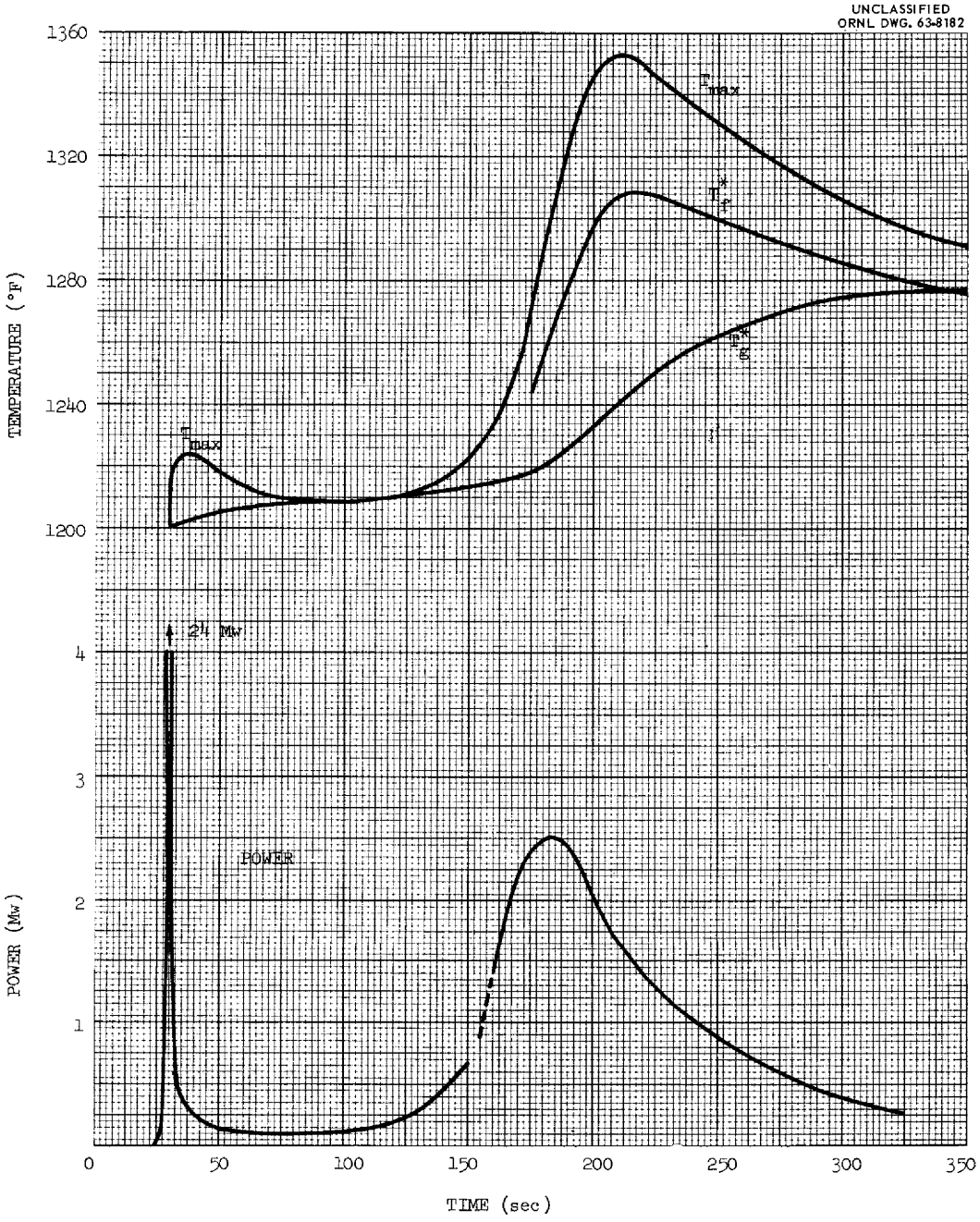

Fig. 12.9. Power and Temperature Transients Following Maximum Filling Accident.

the nuclear, heat transfer, and thermal convection equations for the system. Failure of the fuel pump power supply, with subsequent coast-down of the flow, was simulated by causing the circulation rate to decrease exponentially with a 2-sec time constant until it reached the thermal circulation rate determined by the temperature rise across the core. As the fuel circulation rate decreased, the effective delayed neutron fraction was increased by 0.003 and the heat transfer coefficient in the heat exchanger was reduced.

Figure 12.10 shows the results of a simulated fuel pump failure at 10 Mw, with no corrective action. The gain in delayed neutrons caused the initial rise in the power. The decrease in heat removal from the core, coupled with the high production, caused the core outlet temperature to rise. As the fuel flow and the heat transfer in the heat exchanger fell, the continued heat extraction at the radiator caused the coolant salt temperature to decrease and reach the freezing point in less than 2 min. (The behavior in simulator tests at lower power was similar, but the coolant temperature remained above the freezing point if the initial power was less than 7 Mw.)

Practical measures can be taken to prevent freezing of the coolant salt or overheating of the core in the event of fuel pump failure. These consist of closing the radiator doors and inserting the control rods. Figure 12.11 shows simulator results for a case in which these actions were taken rather slowly, yet proved effective. One second after the pump power was cut, a negative reactivity ramp of −0.075% δk/k per second was initiated, simulating insertion of the control rods at normal driven speed. Beginning 3 sec after the pump power failure, the simulated heat removal from the radiator tubes was reduced to zero over a period of about 30 sec.

12.7.5 Conclusion

The results of the analyses described here form part of the basis for a comprehensive analysis of the safety of the reactor system. The credibility and the importance of each accident are evaluated and discussed in the Safety Analysis Report.

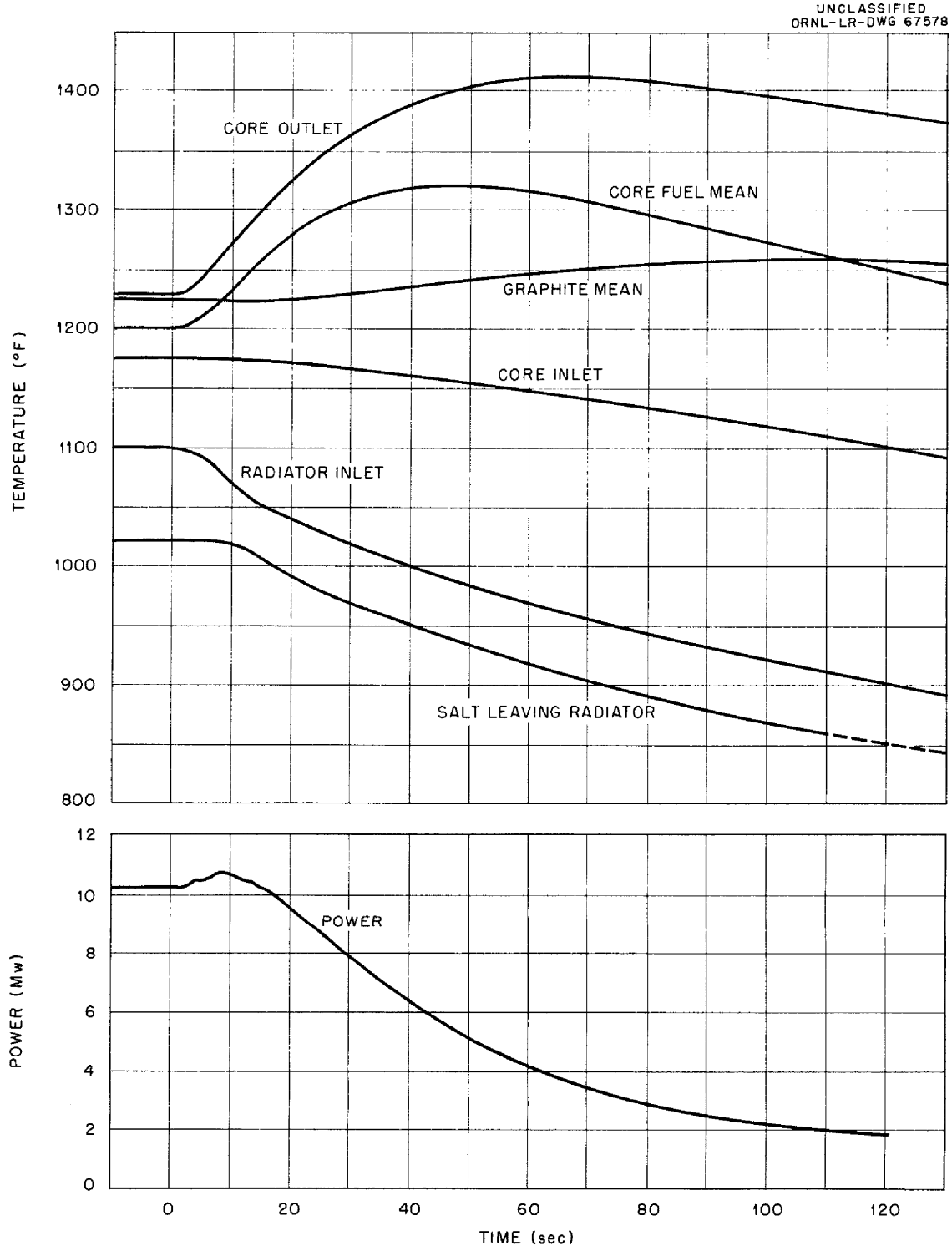

Fig. 12.10. Power and Temperature Transients Following Fuel Pump Power Failure at High Power; No Corrective Action.

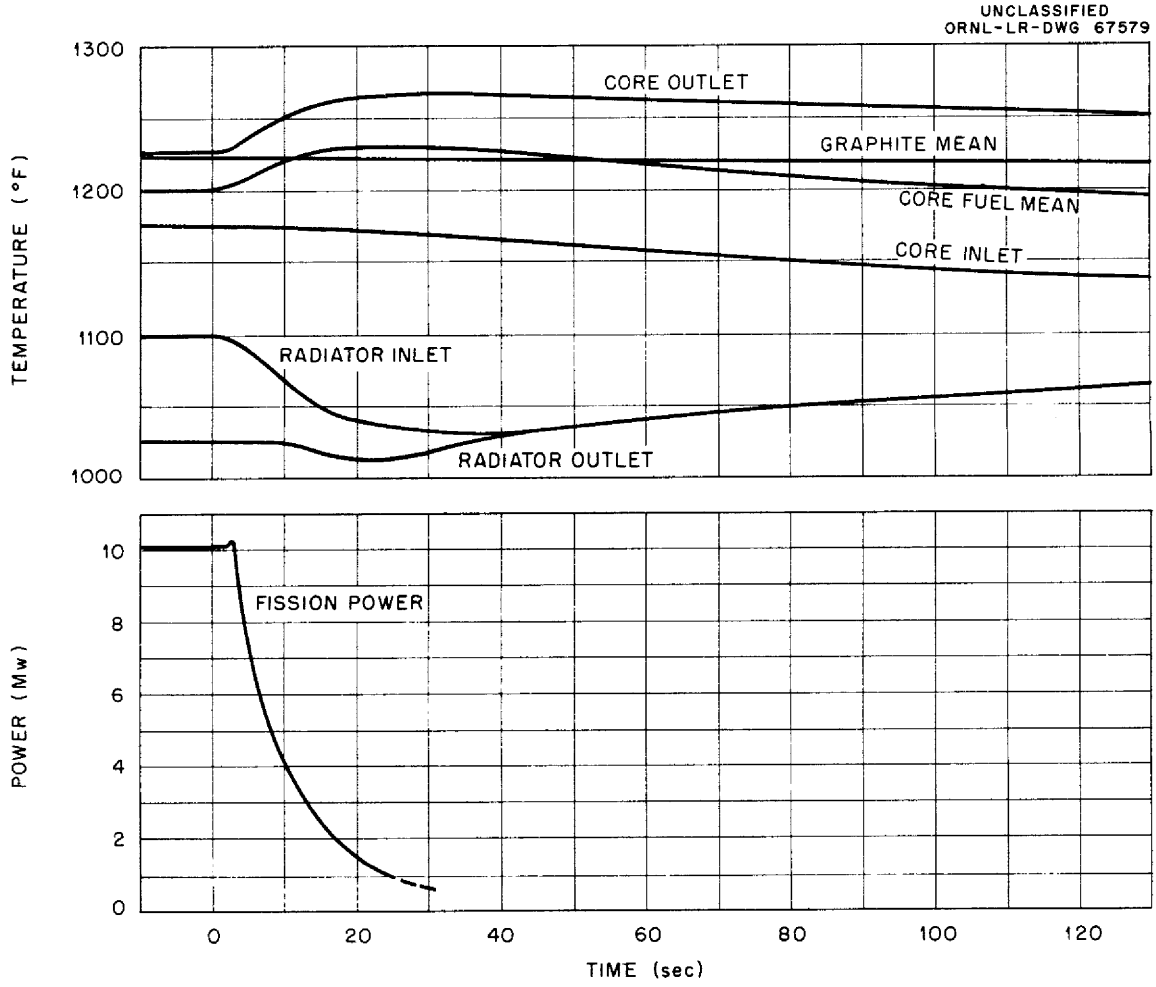

Fig. 12.11. Power and Temperature Transients Following Fuel Pump Power Failure at High Power; Radiator Doors Closed and Control Rods Driven in After Failure.

13. BIOLOGICAL SHIELDING

13.1 General

The basis for the design of all biological shielding is the recommended maximum permissible exposure to radiation of 100 mrem/week, or 2.5 mrem/hr based on a 40-hr work week. The criterion for the MSRE biological shield design is that the dose rate will not exceed 2.5 mrem/hr during normal operation at any point on the shield exterior that is located in an unlimited access area. This criterion inherently includes allowance for significant underestimation of the hot-spot dose, with the general area still below 2.5 mrem/hr.

As in most reactor designs (and particularly in the case of the MSRE, since it has to fit within an existing reactor containment cell and building) nuclear, mechanical, and structural requirements, as well as economics, preclude the design of permanently installed shielding that results in a dose rate that is less than the permissible rate at all points. Consequently, the final shield design allows for addition of shielding as needed to reduce the radiation level at localized hot spots.

13.2 Overhead Biological Shielding

The calculations which are described in this section on the biological shielding over the reactor cell were carried out at an early stage of the design.[41] The source strengths which were used, and which are reported in this section, differ somewhat from those obtained from the latest nuclear calculation (see Sec 13.3.4 for later results). The differences would make no significant change in the prescribed shielding. In this section, the calculations sometime refer to ordinary concrete, which was initially considered for use. The final shield design is composed of barytes concrete, ordinary concrete, and steel which is equivalent to about 9 ft of ordinary concrete and about 7 ft for neutrons.

13.2.1 Geometry

The basic shield construction is shown in Fig. 13.1. Two separate layers of concrete blocks are used; the majority of the lower blocks are

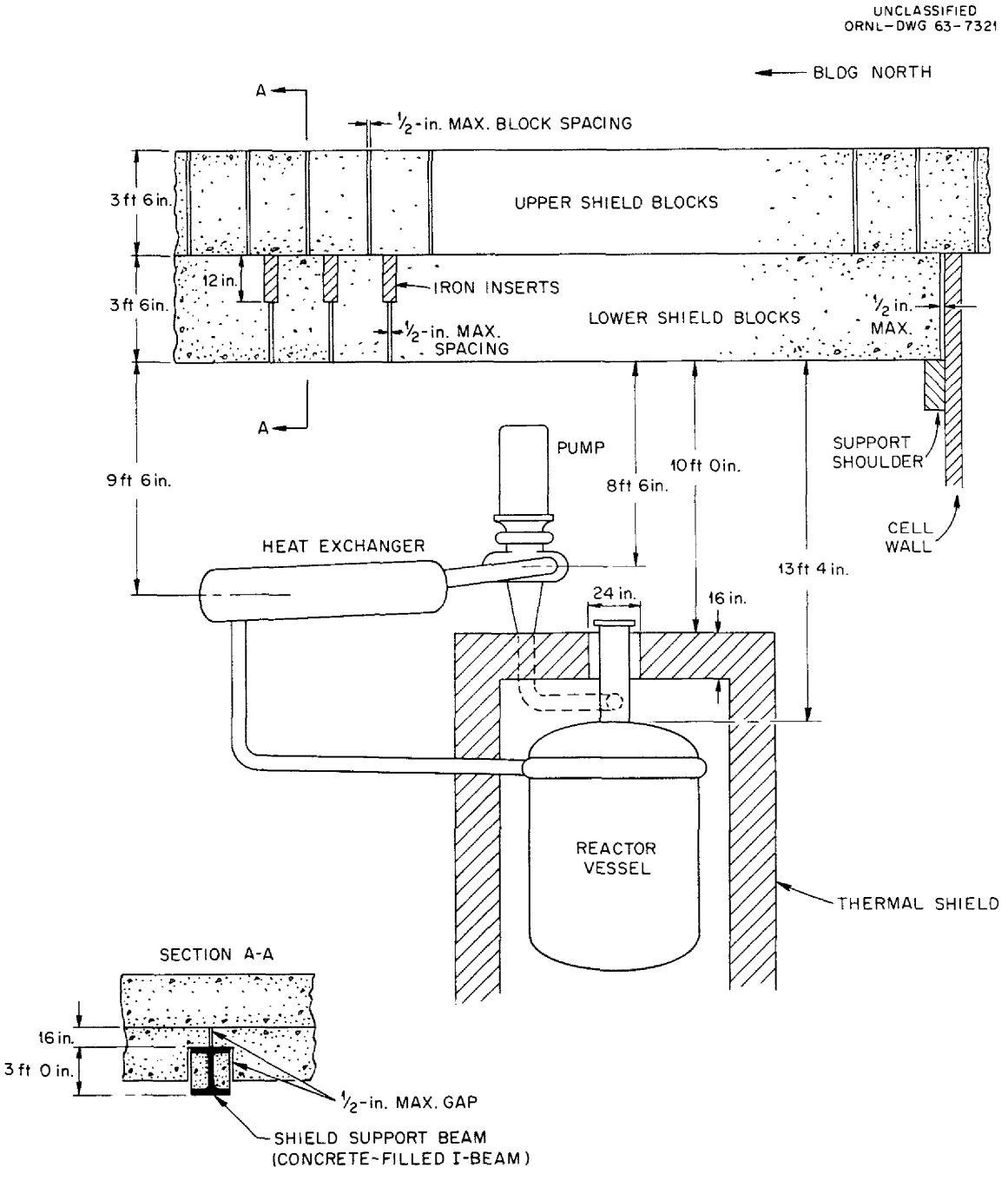

Fig. 13.1. Elevation View of Basic Overhead Shield.

23-1/2 in. wide and 3-1/2 ft thick, and are barytes concrete. These blocks do not extend completely across the cell but are intersected by two shield support beams, shown in Figs. 13.1 and 13.2, which run at right angles to the lower shield blocks. The top shield blocks are ordinary concrete, 23-1/2 in. wide and 3-1/2 ft thick, and extend completely across the cell. A thermal shield that is 16 in. thick and composed of about half water and half steel surrounds the reactor except for a 2-ft-diam

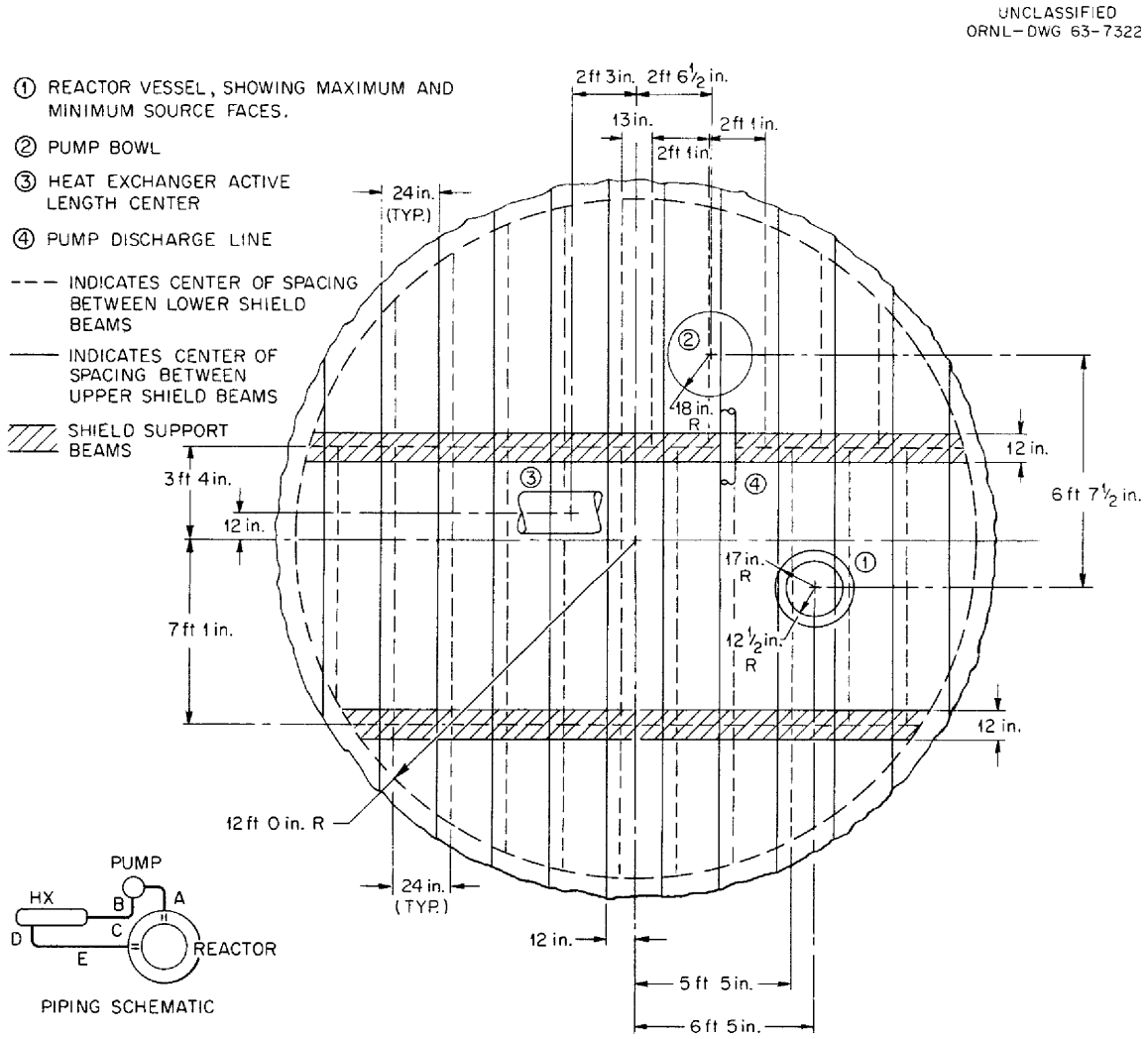

Fig. 13.2. Plan View of Basic Overhead Shield.

opening at the top. Obviously the maximum dose rate will exist over this opening, in an area limited by the thermal shield.

The dose rates that will exist on top of the shield are due to two conditions:

1. a general radiation level with the full thickness of the shield effective,
2. local peaks in the radiation level due to imperfections in the shield.

The general radiation levels above the shield have been based on the relations given below for a constant-source-strength disk source and for cylindrical and truncated right-circular cone constant-volume sources:[42]

disk source,

$$\phi = B(\mu t)\,\frac{S_A}{2}\,[E_1(\mu t) - E_1(\mu t \sec\theta)]\ ; \qquad (13.1)$$

cylindrical source,

$$\phi = B(\mu t)\,\frac{S_v R_o^2}{4(a + Z)}\,[F(\theta_1, \mu t) + F(\theta_2, \mu t)]\ ; \qquad (13.2)$$

truncated right-circular cone source,

$$\phi = B(\mu t)\,\frac{S_v}{2\mu_s}\left[E_2(\mu t) - \frac{E_2(\mu t \sec\theta)}{\sec\theta}\right]. \qquad (13.3)$$

(See Sec 13.6 for definition of symbols.)

Ordinary concrete dose buildup factors and standard attenuation coefficients were used for the gamma rays. The buildup factors may be used as indicated (constant for a particular case), since the solid angle involved is small.

Neutron attenuation was estimated using neutron removal cross sections with a buildup factor of unity.

Neutron and gamma sources are given in Sec 13.2.2 dealing with source strengths.

Estimates for the local peak dose rates that will occur above gaps between adjacent shield beams were determined using the methods given above for the solid shield with the appropriate effective source geometry.

The effective source geometry for a crack is illustrated in Fig. 13.3. For a given crack width, w, and a given distance, a, between the dose point and the source, a fraction of the source has direct line of sight to the dose point. This effective source is only attenuated by the partial thickness of the shield, t. In these estimates buildup of scattered photons has not been included, though the scattered photons make an appreciable contribution.

Figure 13.2 shows the location of the primary reactor system with respect to the spacings and locations of the shield blocks.

13.2.2 Source Strengths

The sources of radiation considered were fission product decay gammas, N^{16} decay gammas, prompt fission gammas, thermal neutron capture gammas, and fast neutrons. [The $F^{19}(n,\gamma)F^{20}$ reaction produces a 1.8-Mev photon, but its contribution to the dose rate through the top shield is negligible.]

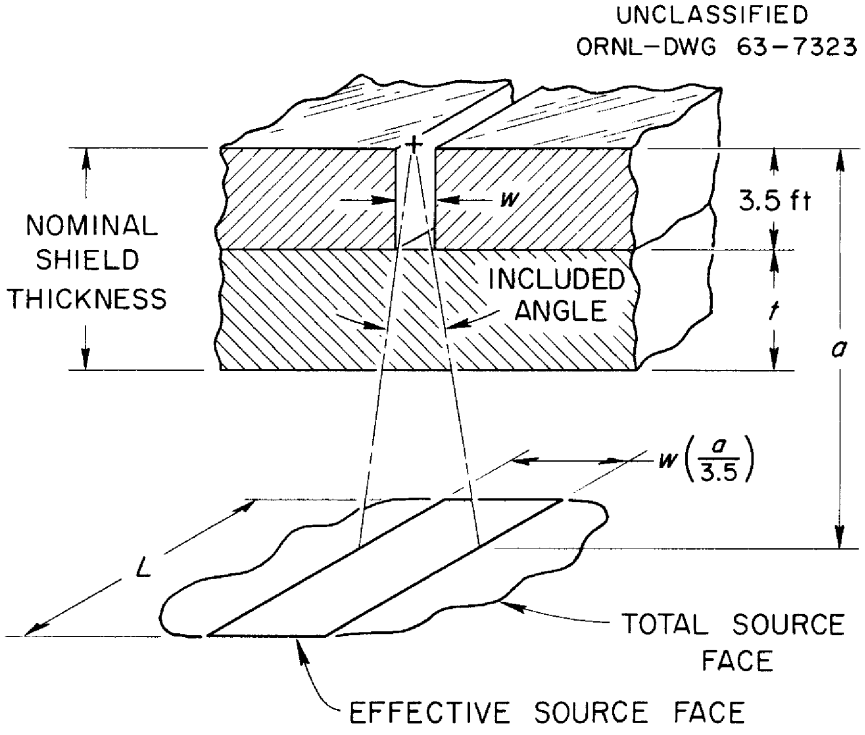

Fig. 13.3. Geometry for Determining an Effective Gap Source.

Fission Product Decay Gammas. – Goldstein[43] has reported the gammas from the fission products to have an exponential energy spectrum and a total energy decay rate of 5.5 Mev/fission at saturation. It was assumed that this spectrum and decay rate was constant through the primary system. Table 13.1 gives the fission product source strengths for a 10-Mw power level and a 62-ft^3 total fuel volume.

Nitrogen-16 Decay Gamma Activity. – The reaction $F^{19}(n,\alpha)N^{16}$ (7.36-sec half-life) is a high-energy reaction with an appreciable cross section above 3 Mev, going to a maximum of ~310 mb at ~5.8 Mev.[44]

The N^{16} production rate was determined by numerically integrating the neutron flux and reaction cross section over the energy range 3 to 10 Mev. Fast neutron fluxes over this energy range were obtained from multigroup reactor calculations.[45]

The activity in the primary system was based on Eq. (13.4), given below, using a constant production rate in each region of the reactor vessel.

Table 13.1. Saturated Fission Product Gamma-Ray Spectrum (10 Mw, 62 ft^3 fuel)

Energy Range (Mev)	Average Energy (Mev/photon)	Energy Emission Rate [Mev/(sec·cc)]
		× 10^{10}
0–1	0.41	31.5
1–2	1.41	36.1
2–3	2.41	20.5
3–4	3.41	9.66
4–5	4.41	4.16
5–5.4	5.1	0.88
	Total	103

The saturated activity at the reactor vessel exit is

$$\lambda N = \left[P_a(1 - e^{-\lambda t_a}) e^{-\lambda t_\ell} e^{-\lambda t_c} e^{-\lambda t_u} + P_\ell(1 - e^{-\lambda t_\ell}) e^{-\lambda t_c} e^{-\lambda t_u} + P_c(1 - e^{-\lambda t_c}) e^{-\lambda t_u} + P_u(1 - e^{-\lambda t_u}) \right] \div \left[1 - e^{-\lambda t_t} \right] . \quad (13.4)$$

The N^{16} production and decay rates are given in Table 13.2.

Neutron Leakage and Gamma Flux Core Sources. — The fast neutron leakage and gamma flux from the top of the core were obtained from two-group, two-dimensional reactor calculations.[45] The neutron leakage rates at 10 Mw are 1.36×10^{12} fast neutrons/(sec·cm^2) and 4.9×10^{10} thermal neutrons/(sec·cm^2); the gamma fluxes are listed in Table 13.3. These leakage rates and fluxes are at the surface of the reactor and should be representative of a cosine, or Fermi, source. It was assumed that they had a cosine distribution; therefore they were increased by factors of 4 and 2, respectively, and treated as an isotropic source.[46]

Table 13.2. N^{16} Saturated Activity

Region	Production Rate [atoms/(sec·cc)]	Average Decay Rate[a] [Mev/(sec·cc)]
Reactor outlet piping	0	2.7×10^{10}
Pump (bypass flow)	0	1.25×10^{15}[b]
Piping	0	2.42×10^{10}
Heat exchanger	0	2.20×10^{10}
Piping	0	1.97×10^{10}
Reactor inlet	0	1.82×10^{10}
Annulus	0.176×10^{10}	1.67×10^{10}
Lower header	0.176×10^{10}	1.52×10^{10}
Core	1.10×10^{10}	2.43×10^{10}
Upper header	0.176×10^{10}	3.0×10^{10}

[a] 6.13-Mev γ in 75.9% of decays and 7.10-Mev γ in 6.1% of decays.

[b] Units of Mev/sec, assuming all N^{16} in the bypass flow decays in the pump bowl.

Table 13.3. Gamma Fluxes from Top of Reactor Vessel, at 10 Mw Reactor Power

Energy (Mev)	Gamma Flux [Mev/(sec·cm^2)]
	$\times 10^{12}$
0.5	2.50
1	4.28
2	3.63
4	1.85
6	1.08
8	0.80
10	1.14

Iron and Concrete Capture Gammas. — The energy spectrum of the capture gammas was obtained from the data of Troubetzkoy and Goldstein.[47] In both the reactor thermal shield and the biological shield, the capture gamma source was assumed to be a plane isotropic disk source located two fast neutron relaxation lengths from the inside of the shield.[46]

13.2.3 Estimated Dose Rates

Tables 13.4–13.6 show the relative contributions of the individual sources as a function of the shield thickness and spacing between the blocks. These values have been compiled in Table 13.7 for a maximum block spacing (1/2 in.).

The results have been presented only as a function of ordinary concrete, assuming that for gamma attenuation the barytes concrete may be accounted for by a ratio of the densities. The attenuation of neutrons is essentially identical in either barytes or ordinary concrete, as shown by the data of Blizard.[46] Hence, for the neutron dose rate results, a given thickness of barytes concrete will have the same effect as the identical thickness of ordinary concrete.

Table 13.4. Gamma Dose Rates Above the Primary System Components for a Solid Shield, at 10 Mw Reactor Power

(All values given as tissue dose rates, mrem/hr)

Component	Thickness of Ordinary Concrete, ft		
	7	8	9
Pump bowl[a]			
Fission products	9.5 (5.3)	1.2 (0.68)	0.16 (0.09)
N^{16} bypass flow	8.0 (8.0)	1.5 (1.5)	0.28 (0.28)
N^{16} primary flow	6.3 (0)	1.2 (0)	0.22 (0)
Total	24 (13)	3.9 (2.2)	0.66 (0.37)
Heat exchanger			
Fission products	7.6	0.98	0.13
N^{16}	10	1.9	0.35
Total	18	2.9	0.48
Piping[b]			
A	3.2	0.52	0.09
B	4.0	0.64	0.11
C	2.0	0.32	0.05
D	1.0	0.17	0.03
E	2.7	0.44	0.07

[a]Values in parenthesis represent a possible lower limit.

[b]Locations shown in Fig. 13.2. Dose rates are for N^{16} activity and fission products.

Table 13.4 gives the gamma dose rates above the primary system components vs the shield thickness for a solid shield, at a 10-Mw reactor power level. Two values are given for the pump bowl, these represent estimates of an upper and lower limit, depending on how effective the pump motor and the internal pump shield are in reducing the dose.

The incremental dose above a given source due to adjacent sources has not been determined. Since the total dose rate will be less than the

Table 13.5. Dose Rates Above the Reactor Vessel for a Solid Shield, at 10 Mw Reactor Power

(All values given as tissue dose rates, mrem/hr)

Source	Thickness of Ordinary Concrete, ft		
	7	8	9
Gamma rays			
Core	136	28	6.2
N^{16}	15	2.8	0.51
Iron capture	86	17	3.4
Concrete capture	19		1.0
Neutrons from core	1.8	0.10	0.005

sum of the individual dose rates, an upper limit for the combination may be found by adding the dose rates directly above each of the sources; for example, the total dose rate above the heat exchanger, including piping lengths B and C, will be less than 0.64 mr/hr for 9 ft of concrete (0.64 = 0.48 + 0.11 + 0.05).

The dose rates directly above the reactor vs feed of ordinary concrete are given in Table 13.5, for a solid shield and a 10-Mw power level. The total dose rate is subdivided into the neutron and gamma contributions, as the shield is equivalent to ~9 ft of ordinary concrete for the gammas and ~7 ft for the neutrons.

The effect of spacing between the upper shield blocks is shown in Table 13.6 as a function of the nominal shield thickness and the face area of the source covered by the gap, wL. These estimates are essentially minimum values that may be expected above the gaps. Two factors that will make the actual gamma dose rate higher are:

1. Scattered radiation; since buildup and sources from scattering were not included in the estimate.
2. The uncollided radiation that is partially attenuated by the upper shield blocks; that is, photons traveling at an angle from the shield normal slightly greater than the included angle used to determine the effective source.

Table 13.6. Effect of Spacing Between Upper Shield Blocks on Dose Rates, at 10 Mw Reactor Power

(All values given as tissue dose rates)

Source	Thickness of Ordinary Concrete, ft		
	7	8	9
Reactor gamma rays [D/wL, mr/(hr·in.^{2})]			
Core	69	12	2.2
N^{16} activity	7.8	1.3	0.21
Fe capture	9.0	1.7	0.29
Concrete capture	240		
Reactor neutrons [D/wL, mrem/(hr·in.^{2})]	273	11	0.42
Pump bowl gamma rays [D/wL, mr/(hr·in.^{2})]			
Fission products	13	1.3	0.14
N^{16} activity	10	1.7	0.27
Heat exchanger gamma rays [D/w, mr/(hr·in.)]			
Fission products	78	8.1	0.89
N^{16} activity	46	7.7	1.2
Pump discharge line[a] [D/w^2, mr/(hr·in.^{2})]	680		

[a]Due to coincidence of upper shield block spacing and lower shield block and shield support beam spacing, shown in Fig. 13.2.

Table 13.7. Summary of Dose Rates Above Overhead Shield,[a] at 10 Mw Reactor Power

Source	Solid Shield	Peaking at Cracks	
		Minimum	Probable
Reactor			
Gammas	14	80	160
Neutrons	1.8	4600	6000
Pump bowl gammas	0.88	10	20
Heat exchanger gammas	0.65	1.5	3
Pump discharge piping gammas	0.15	170[b]	340[b]

[a] 3.5 ft of barytes concrete and 3.5 ft of ordinary concrete.

[b] Due to coincidence of gap between upper shield blocks with the gap between the lower shield blocks and shield support beam.

The second factor given will also tend to make the actual fast neutron dose rate higher.

The results given in Tables 13.4–13.6 have been interpolated and compiled in Table 13.7 to show the expected dose rate estimates above the present reactor shield. Effective source face areas were based on 1/2-in. gap spacings and source lengths, L, shown in Fig. 13.2. For the reasons discussed, neutron and gamma peak dose rates were arbitrarily increased by factors of 1.3 and 2.0, respectively, to give the "probable" values listed.

13.3 Lateral Biological Shielding

The biological shielding around the sides of the reactor and reactor cell is composed of steel, water, magnetite sand, ordinary concrete, and barytes concrete. The detailed arrangement of this shielding and the additional shielding requirements due to the induced activity in the coolant salt are discussed in the following sections.

13.3.1 Basic Shield Arrangement

Figure 13.4 shows the layout of the reactor cell, shielding, and adjacent areas in plan view. Most of the cell walls and shielding were built before the MSRE program, for an earlier reactor installation.

The thermal shield immediately surrounding the reactor vessel was installed specifically for the MSRE. It consists of a steel tank, 16 in. thick on the sides, filled with steel shot and water. The water is circulated to remove the heat generated in the shield.

The major part of the lateral shield is an ~3-ft-thick annulus formed by two concentric cylindrical steel tanks (inner tank, 2 in. thick; outer tank, 5/8 in. thick) enclosing the reactor cell. The hollow annular space (33 in.) is filled with a compacted magnetite sand–water mixture with a bulk density of at least 210 lb/ft^3. Except in two large areas where certain shield penetrations are located, the annulus is in turn surrounded by a monolithic concrete wall with a minimum thickness of 21 in. The two areas that lack the concrete portion of the shield are the south electrical service area and the coolant cell. The south electrical service area adjoins the north side of the reactor cell just below the transmitter room shown in Fig. 13.4. The coolant cell is southwest of the reactor cell and is connected by a passageway along the shield wall and by a 7- by 11-ft air duct to the blower house, or fan room, where the main cooling fans are located. The fan room walls on the west side and parts of the north and south sides are louvered to admit air.

13.3.2 South Electrical Service Room

Because of the gap in the concrete wall around the reactor cell, the dose rate in the south electrical service room will be too high for access during high-power operation. The room will therefore be sealed to prevent entry except when the reactor is shut down. The room itself is enclosed in 2 ft of concrete (except for the narrow passageway leading around the reactor cell to the northwest corner of the coolant cell). This should be adequate to reduce the dose rate to less than 2.5 mrem/hr in the north electrical service room and in the transmitter room located above. There exists a possibility, however, that some minor hot spots may occur in the north electrical service room along the 2-ft wall separating it from the

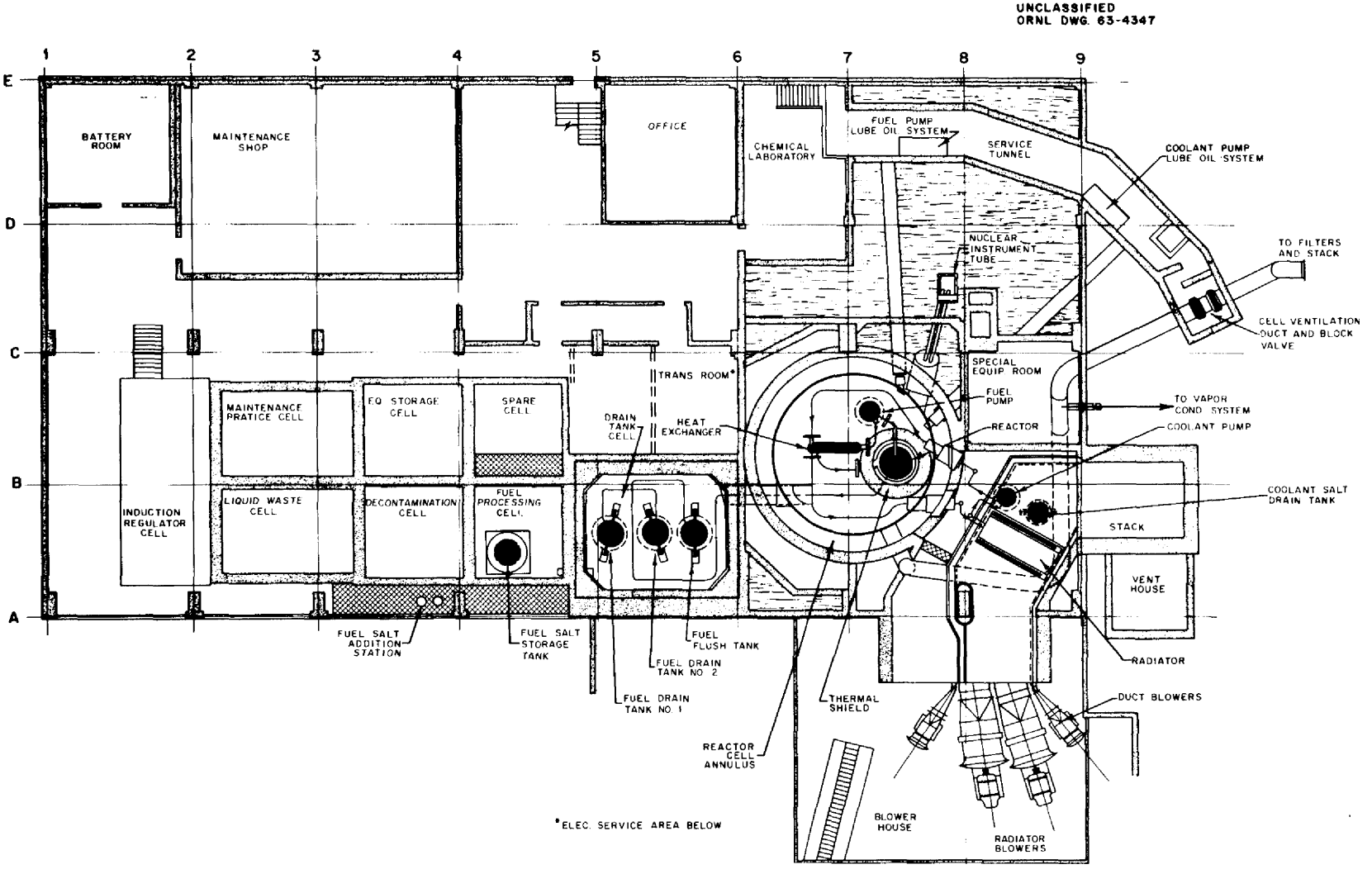

Fig. 13.4. Plan View of MSRE.

south electrical service room, due to the various penetrations in the annular shield. The dose would depend on the material in the penetrations and whether the penetrations could "see" a strong source. These possible hot spots would have only nuisance value and can be eliminated by localized stacking of concrete blocks on either side of the wall separating the two electrical service rooms. The 4-in.-diam holes that penetrate the wall separating the two electrical service areas will obviously require plugs.

The 2-ft-thick floor of the transmitter room located directly over the south electrical service room has a number of penetrations that will require special attention in the way of additional shielding. These include several 4-in.-diam holes, an 8- by 30-in. opening which is traversed by two electrical conduits, and the ventilating duct located on the south wall of the transmitter room.

13.3.3 Coolant Cell and Fan House

On the face of the annular shield where it is exposed to the coolant cell, there are two segmental indentations in the vicinity of the coolant line penetrations. These indentations are about 14 ft long and 4 ft high, with a maximum depth of nearly 9 in. On the inner side of the indentations the steel tank thickness was increased from 2 in. to 4 in., but this only partially compensates for the removal of the sand-water mixture where the indentation is deepest.

Because of the gap in the concrete wall and the reduced thickness of the annular shield, the dose rate in the coolant cell due to radiation from the reactor cell alone would be much too high for personnel access during power operation. Radiation in the coolant cell from this source can be reduced by additional stacked block shielding against the reactor cell wall, but there remains the gamma radiation from the circulating coolant salt, which becomes activated in passing through the fuel-coolant heat exchanger. Access to the coolant cell during operation is therefore prohibited.

Because of the very large duct connecting the coolant cell and the fan house, high radiation levels in the coolant cell lead to undesirably high dose rates in the fan house. A close estimate of the dose rates at

various points in the fan house cannot be made, because of the complicated geometry of sources and shielding. Using simplified line-of-sight methods of calculation, and assuming no additional shielding, the dose rate at the south louvered wall in the vicinity of No. 2 fan was estimated to be 140 mrem/hr. Contributions from various sources to this dose rate are itemized in Table 13.8.

The dose rate from the most important single source, the thermal shield, could be reduced by the addition of dissolved boron in the thermal shield water (10 g/liter would reduce the dose rate from 71 mr/hr to about 15 mr/hr, see Fig. 13.5), but the radiation from the other sources in the reactor cell would still be too high. Therefore, additional shielding will be added between the reactor cell and coolant cell to reduce the dose rate from all sources in the reactor cell to a negligible level, thus obviating the use of boron in the thermal shield water. A wall of stacked barytes concrete blocks with a minimum thickness of 16 in. will be used for this purpose.

With the additional shielding around the reactor cell, the dose rate in the fan house is controlled by the gamma activity of the circulating coolant salt. The highest dose rate from this source will be in the vicinity of No. 4 fan. It is estimated that the dose rate here would be 16 mr/hr from the radiator and 11 mr/hr from the coolant pump and piping. Most of the latter contribution will be eliminated by concrete blocks stacked in the area between the radiator housing and the reactor shield.

Table 13.8. Dose Rates Near No. 2 Fan During 10-Mw Operation (No additional shielding)

Source	Dose (mrem/hr)
Core neutrons	4
Core gammas	15
Circulating fuel gammas	35
Thermal shield capture gammas	71
Radiator and coolant piping gammas	15

Nothing can be done to reduce the dose rate in the fan house from the radiator without interfering with the air flow. However, there is normally no need for access to this area during power operation, so the fan house will be made a controlled-access area.

After the addition of the stacked block shielding described above, it is estimated that the dose rate along the west louvered wall will probably not exceed 2.5 mrem/hr and will exceed this value somewhat along the south louvered wall. If the dose outside the wall proves excessive, an existing concrete block wall located a few feet outside the louvered wall on the south side will be extended around the fan house as far as needed.

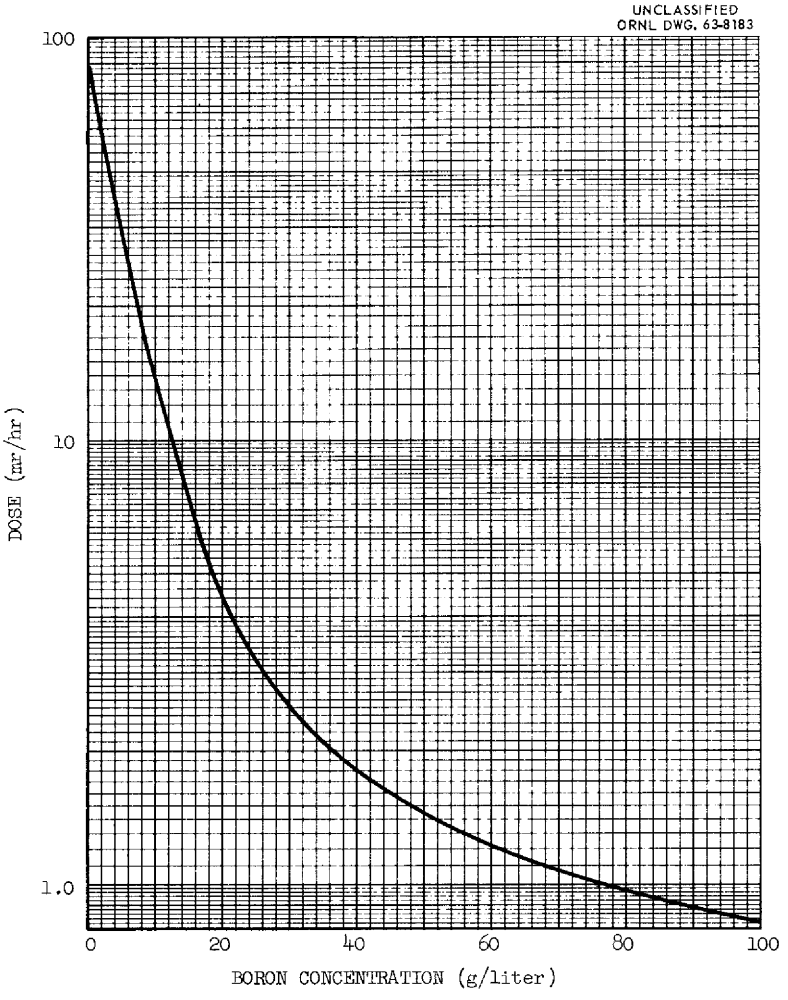

Fig. 13.5. Biological Dose from Thermal Shield Capture Gammas as a Function of Boron Concentration. Dose at louvered wall near No. 2 fan.

Adjoining the fan house on the north is a ramp leading down into the coolant cell. The large cell exhaust penetration in the annular shield is in line with this sloping passage. Although a 9-in. steel shadow shield is provided in front of the exhaust line, the radiation leaking from the reactor cell at this point will be unusually high. In addition, radiation will scatter into this area from the passageway leading from the south electrical service room. A stacked block wall, at least 1 ft thick, with a labyrinth passage, will be provided at the base of the ramp to reduce the dose rate outside to the tolerance level.

13.3.4 Source Strengths

The source strengths of the fuel salt activities and capture gammas from the thermal shield were different from those used in the top shield calculations. This reflects changes due to more recent calculations and a need for more sophisticated calculations for the capture gammas because of the more critical nature of the shielding in the fan house area.

Nitrogen-16 and Fluorine-20 Activity in Fuel Salt. — The source strengths of the N^{16} and F^{20} activities are summarized in Table 13.9.

Table 13.9. N^{16} and F^{20} Activities[a] in the Fuel Salt for 10-Mw Operation

	Activity [dis/(sec·cm^2)]	
	N^{16}	F^{20}
Reactor outlet	4.62×10^9	4.48×10^9
Pump bowl inlet	4.18×10^9	4.20×10^9
Inlet to reactor downcomer	2.67×10^9	3.13×10^9
Average activity in circulating fuel	3.56×10^9	3.73×10^9
Average activity in external loop	3.56×10^9	3.77×10^9
Average activity in reactor vessel	3.56×10^9	3.72×10^9
Total production rate (atoms/sec)	6.78×10^{15}	7.12×10^{15}

[a]Calculated using latest neutron balances from MODRIC and EQUIPOISE calculations for fuel B (see Chap. 3).

Capture Gammas in Thermal Shield. – The thermal flux distribution used in calculating the capture gamma source strength in the thermal shield is shown in Fig. 13.6. These values were calculated with the reactor code DTK, a one-dimensional S_n transport calculation.

Induced Activity in Coolant Salt. – Practically all of the activation of the coolant salt will occur in the heat exchanger, where it is exposed to neutrons resulting from decay of the delayed neutron precursors in the fuel salt and a small amount of fissioning.

For F^{20} and N^{16} during steady-state operation, the saturated specific activity, or source strength, of the circulating coolant at any time, t, after leaving the heat exchanger tubes is

$$S_v = p\left[\frac{1 - e^{-\lambda T_1}}{1 - e^{-\lambda(T_1+T_2)}}\right] e^{-\lambda t} , \qquad (13.5)$$

where p is the production rate per unit volume of coolant in the heat exchanger tubes, T_1 is the residence time in the heat exchanger tubes, and T_2 is the residence time of the circulating stream outside of the heat exchanger tubes. The saturated specific activity was calculated[48] to be 7.25×10^4 and 2.55×10^4 dis/(cm^3·sec) for N^{16} and F^{20} respectively.

13.3.5 Calculation Methods

The core gammas and core N^{16} activity were treated as uniform cylindrical sources and Eq. (13.2) was used for the dose rate calculation. It was possible to reduce all coolant salt dose rate calculations to simple point and line sources. The capture gammas from the thermal shield may be represented by a truncated right-circular cone source [Eq. (13.3)], but because of the distance to the louvered wall, point source approximations were used. The thermal shield was divided into 11 concentric cylinders, and each half of a cylindrical annulus was considered a disk with a radius of 5 ft. Because of the distance involved, each disk could then be closely approximated by a point source based on the flux at the midplane of the disk. The total dose rate is the sum of the contributions from each energy group and each disk.

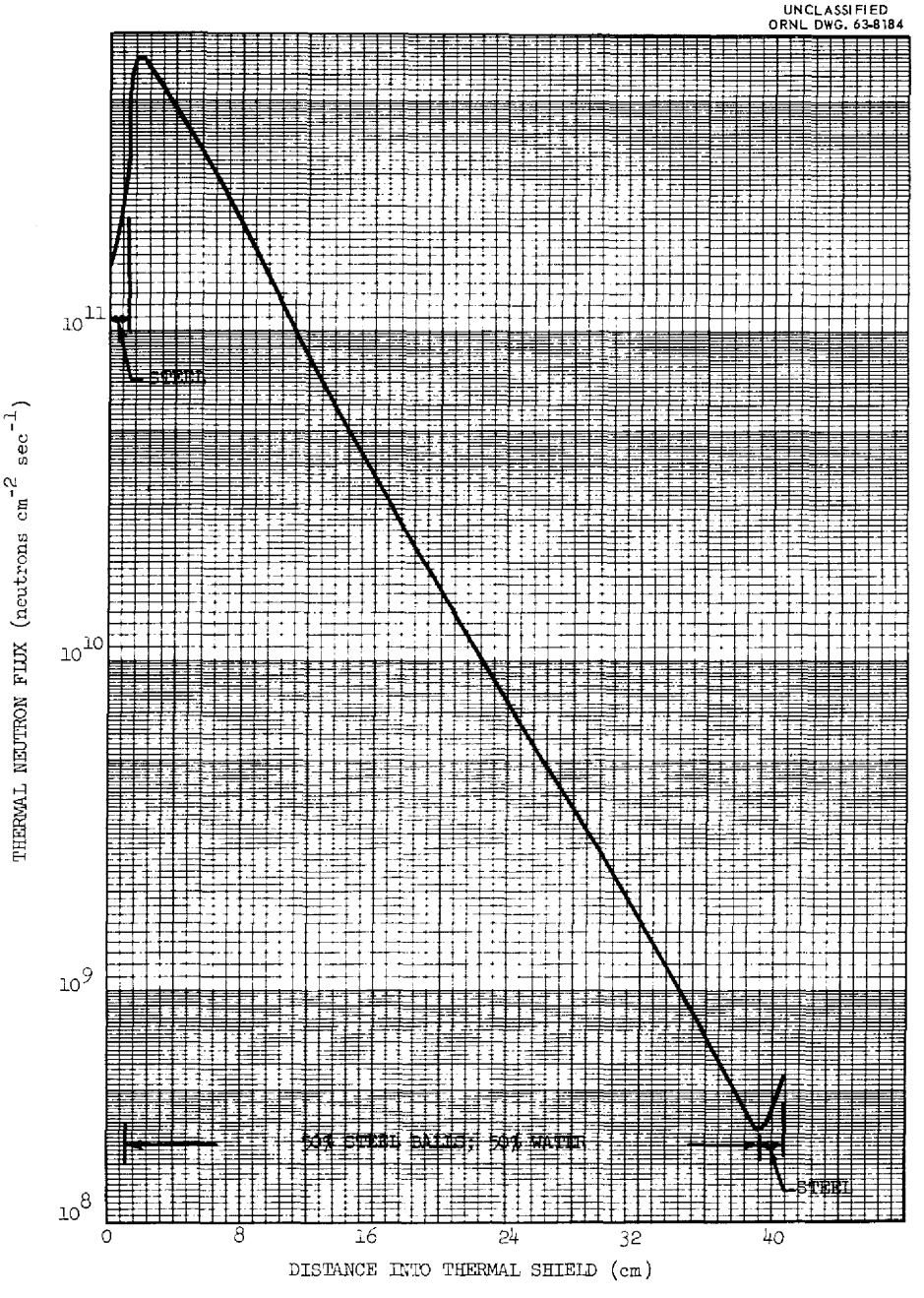

Fig. 13.6. Thermal Flux in Thermal Shield of MSRE.

13.4 Conditions After Reactor Shutdown

All areas external to the reactor cell will be accessible on an unlimited basis minutes after reactor shutdown except under one condition. When the coolant salt lines are drained, two 4-in.-diam holes are left in the shield. One of these coolant pipes (line 200) "looks" directly at the pump bowl; depending on the degree of drainage of the fuel salt, the dose rate in the vicinity of this line can be several rem/hr. The other coolant pipe (line 201) does not "see" any large source but will leak a few mrem/hr of scattered radiation. There is no practical way of providing permanent shielding for the drained condition. Temporary shadow shielding will be used for any maintenance work in the vicinity of these lines.

13.5 *Summary*

The solid portion of the overhead shield is sufficient to limit the dose rate to less than 2.5 mrem/hr except directly over the reactor core, where the dose rate was estimated to be 16 mrem/hr. Large dose rates up to 7 rem/hr could exist over some points where the 1/2-in. gaps overlap. However, it is planned to insert polyethylene and steel strips in the gaps existing in the critical areas and finally to stack concrete blocks as needed over any remaining hot spots.

The lateral shield with the additional 16-in. barytes block to be installed and further field addition of concrete blocks where needed should be adequate. If the dose rate at the louvered walls does exceed 2.5 mrem/hr, an existing concrete block wall located a few feet outside the south louvered wall can be extended quickly and easily as far around as needed.

13.6 Nomenclature for Biological Shielding Calculations

a	Distance from source to dose point
$B(\mu t)$	Buildup factor
D	Dose rate
$E_1(\mu t)$, $E_2(\mu t)$	Attenuation functions, tabulated in TID-7004[42]
$F(\theta_1, \mu t)$, $F(\theta_2, \mu t)$	Attenuation functions, tabulated in TID-7004[42]
L	Source length
N	Concentration per unit volume
p	Production rate per unit volume
R_o	Radius of disk or cylindrical source
S_A, S_v	Source strength, number per unit time per unit area, or unit volume
T_1	Residence time
T_2	Residence time
t	Time and thickness
w	Gap width
z	Self absorption distance
λ	Decay constant
μ	Attenuation coefficient
ϕ	Particle flux

Subscripts:

a	Annulus
c	Core
ℓ	Lower header
s	Source
t	Total
u	Upper header

14. MISCELLANEOUS

14.1 Radiation Heating of Core Materials

Heat produced in the graphite by absorption of beta and gamma radiation and the elastic scattering of fast neutrons amounts to about 7% of the total heat produced in the reactor. This heating of the graphite affects the overall kinetic behavior of the reactor through its effect on graphite temperature response. Heat produced in the INOR parts of the reactor, on the other hand, is a small fraction of the total and has little effect on overall behavior. It is important, however, from the standpoint of local temperatures.

The spatial distribution of the graphite heating was computed, with the results shown in Figs. 14.1 and 14.2. In these computations the main part of the core was treated as a homogeneous mixture, with gamma energy being absorbed at the point of origin. (This is a reasonable approximation for the MSRE, because the core is large and the channels are small in relation to the mean free path of gamma rays.) Capture gammas from the INOR control rod thimbles and core support grid were treated separately, because the sources were quite concentrated.

Gamma-ray heating of INOR at a number of points on and inside the reactor vessel was computed with digital computer codes NIGHTMARE[49] and 2DGH[50] (a two-dimensional version of NIGHTMARE). These computations obtained the gamma flux at one specified point by summing the contributions of gammas originating in all parts of the reactor, using appropriate attenuation and buildup factors. A multiregion model of the reactor similar to that described in Sec 3.2 was used in these computations. Values of gamma sources per fission and per capture were taken from ref 49. The source of fission product decay gammas was assumed to follow the same spatial distribution as the fissions. Results of these calculations are given in Table 14.1.

A summary of the nuclear energy sources and the places where the energy appears as heat is given in Table 14.2. The total energy which heats the fuel as it passes through the reactor vessel is 196.7 Mev per fission.

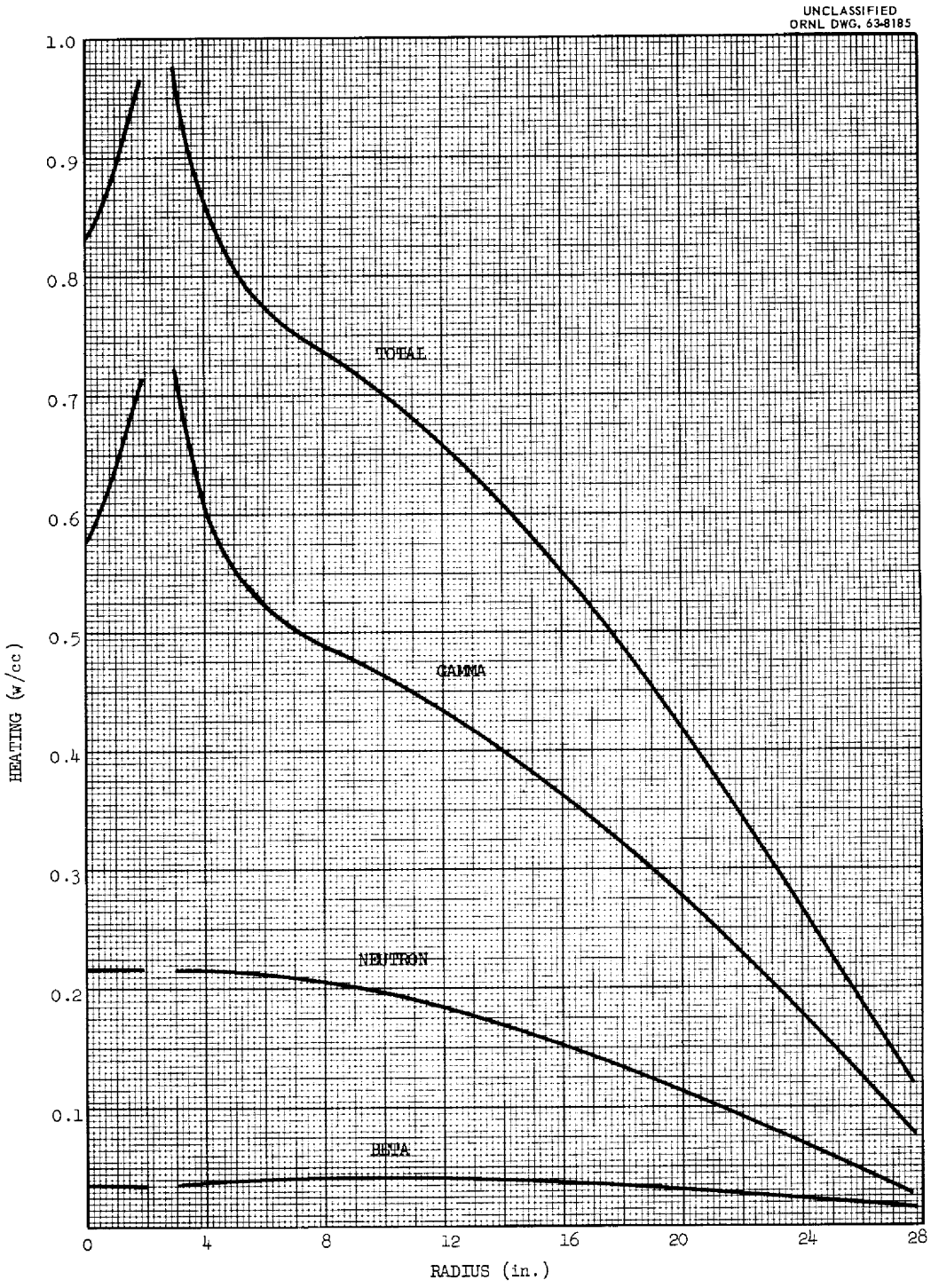

Fig. 14.1. Heating in Graphite: Radial Distribution near Midplane at 10 Mw.

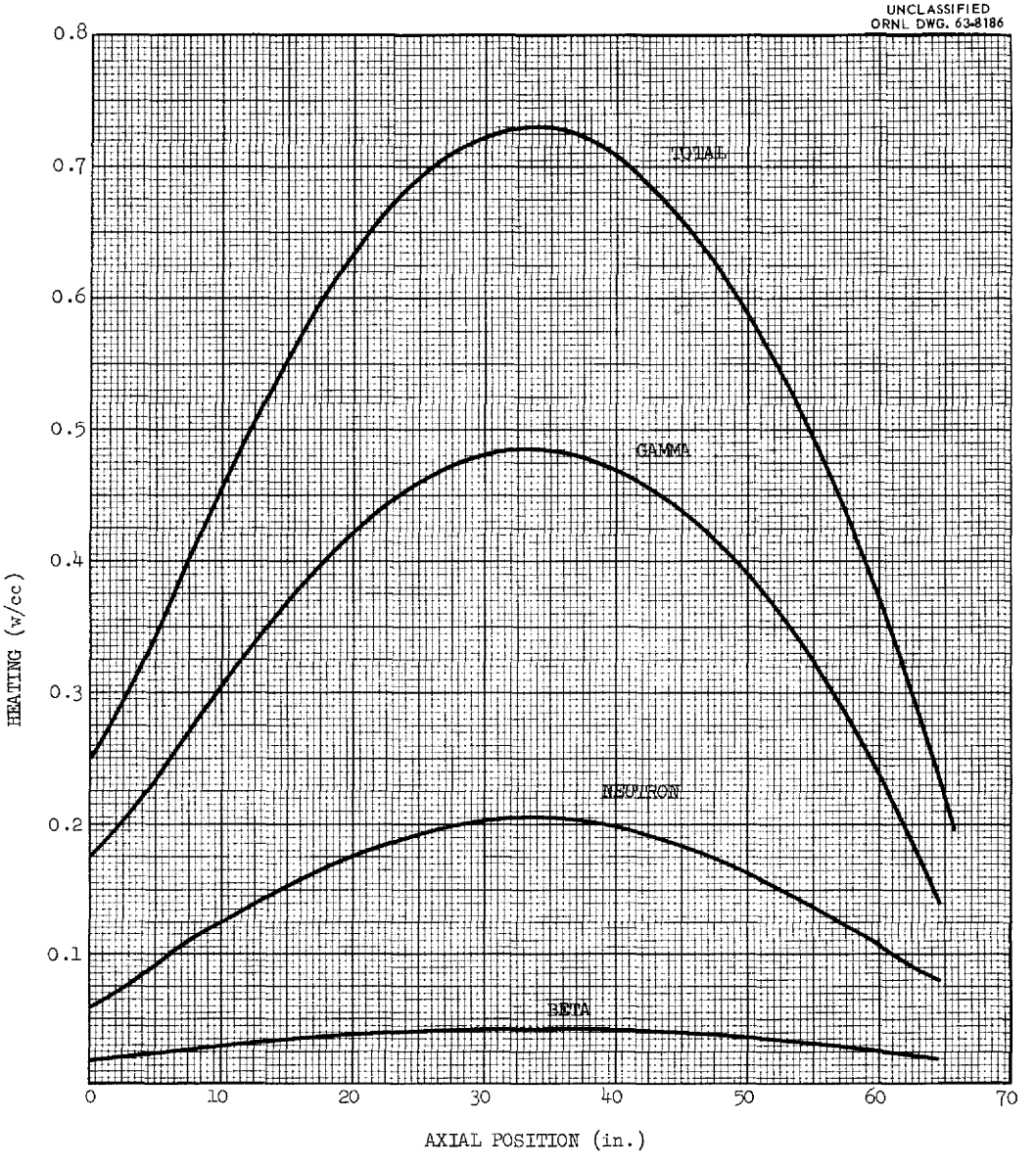

Fig. 14.2. Heating in Graphite: Axial Distribution 8.4 in. from Core Center Line at 10 Mw.

Table 14.1. Gamma Heating of INOR in MSRE, Operating at 10 Mw

Location	Heat Source (w/cm^3)	Calculation	
		Method	Reference
Rod thimble, midplane	2.5	NIGHTMARE	7
Core can, midplane	0.2	NIGHTMARE	4
Vessel, midplane	0.2	NIGHTMARE	4
Upper grid	2.2	NIGHTMARE	4
Lower grid	1.8	NIGHTMARE	4
Upper head at fuel outlet	0.1	2DGH	50

Table 14.2. Energy Sources and Deposition in MSRE

Source	Energy (Mev/fission)					
	Emitted	Absorbed				
		Fuel			Graphite	Cell and Shield
		Main Core	Peripheral Regions	External		
Fission fragments	168	149.5	18.5	0	0	0
Fast neutrons	4.8	0.8	0.1	0	3.5	0.4
Prompt fission gammas	7.2	1.9	0.7	0	4.5	0.1
Fission product decay gammas	5.5	0.7	2.2	0.7	1.6	0.3
Fission product decay betas	8.0	2.7	3.0	1.3	1.0	0
Capture gammas	6.2	1.2	2.2	0	2.6	0.2
Neutrinos	11	0	0	0	0	0
	210.7	156.8	26.7	2.0	13.2	1.0

14.2 Graphite Shrinkage

At the temperature of the MSRE core, fast-neutron irradiation causes graphite to shrink. Shrinkage is proportional to the total exposure and is greater in the direction of extrusion than in the direction normal to the axis of extrusion. Thus shrinkage will be nonuniform, leading to changes in the core dimensions and the distribution of fuel and graphite within the core. These changes produce slow changes in reactivity.

Available information on the behavior of MSRE graphite under nuclear irradiation did not permit a detailed analysis, but some of the reactivity effects were estimated, using preliminary information. The coefficient for shrinkage parallel to the axis of extrusion (axial shrinkage) for a grade of graphite similar to that to be used in the MSRE is about 2.06×10^{-24} per nvt for neutrons with energies greater than 0.1 Mev. The coefficient for EGCR graphite in the same temperature range, between 5 and 8×10^{21} nvt of neutrons with energies greater than 0.18 Mev, is about 1.8×10^{-24} per nvt. Also, for EGCR graphite the coefficient for shrinkage normal to the extrusion axis (transverse shrinkage) is about half that for axial shrinkage. On this basis the coefficients used in the analysis described below were 2.06×10^{-24} and 1.0×10^{-24} per nvt ($E >$ 0.18 Mev) for axial and transverse shrinkage, respectively. The neutron flux distributions for energies greater than 0.18 Mev calculated for fuel C were used (see Figs. 3.9 and 3.10). All of the reactivity effects were based on one full-power year of reactor operation.

Since the MSRE graphite stringers are mounted vertically, axial shrinkage causes, first of all, a shortening of the moderated portion of the core. The amount of shrinkage in individual stringers depends on the radial distribution of the fast flux, so that the top of the graphite structure will gradually take on a dished appearance. The maximum axial shrinkage was estimated to be about 0.14 in./yr. Even if the entire moderator structure were shortened by this amount, the effect on reactivity would not be detectable. In addition to shortening the stringers, axial shrinkage increases the effective graphite density in the main portion of the core. The total axial shrinkage is equivalent to a uniform density increase of 0.11% per year. This corresponds to a reactivity

increase of 0.08% Δk/k per year. The nonuniformity of the density change might increase the reactivity effect by as much as a factor of 2, but the resultant effect would still be negligible.

A third effect of axial contraction is bowing of the stringers, caused by the radial gradient in the neutron flux. This mechanism leads to an increase in the fuel volume fraction in the main portion of the core and has the same effect as increasing the fuel density. The maximum bowing has been estimated at 0.1 in./yr.[51] If it is assumed that the bowing causes a uniform radial expansion of the graphite assembly, this rate represents an equivalent increase in the fuel density of 3.2%/yr. The associated reactivity effect is 0.6% Δk/k per year. Since both ends of the graphite stringers are constrained from radial motion, uniform expansion of the assembly will not occur. Instead, the stringers which have the greatest tendency to bow will be partly restrained, while others, in regions where the radial flux gradient is smaller, will be bulged outward at the middle. The net result will be a much smaller fractional increase in fuel volume than would be predicted for a completely unconstrained assembly.

Shrinkage of the graphite transverse to the direction of extrusion adds to the effect produced by bowing. However, this effect is much smaller because of the smaller shrinkage coefficient. The calculated reactivity effect was 0.04% Δk/k per full-power year of operation.

14.3 Entrained Gas in Circulating Fuel

14.3.1 Introduction

The nuclear characteristics of the reactor are affected by the presence of entrained helium bubbles, which circulate with the fuel through the core. This gas, introduced through the action of the fuel spray ring in the fuel circulating pump, reduces the effective density of the fuel and makes the fuel-gas mixture compressible. The most important consequence is that there is a pressure feedback on reactivity, which is positive for rapid changes in pressure and temperature and negative for slow changes.

14.3.2 Injection and Behavior of Gas

A small fraction of the fuel pump discharge stream (50 gpm out of 1250 gpm) is diverted into a spray ring in the gas space in the pump bowl. The purpose of the spray, or stripper, is to provide contact so that Xe^{135} in the salt can escape into the gas space, which is continuously purged. Salt jetting from holes in the spray ring impinges on the surface of the liquid pool in the pump bowl with sufficient velocity to carry under considerable quantities of gas, and some of the submerged bubbles are swept through the ports at the pump suction into the main circulating stream of fuel. A steady state is reached when the helium concentration in the circulating stream has increased to the point where loss of helium through the stripper flow equals the rate of injection.

At steady state the volume fraction of gas in the circulating stream varies around the loop with the inverse of the local pressure, which changes with elevation, velocity, and head losses. Pump loop tests showed a volume fraction of 1.7 to 2.0% gas at the pump suction, which is normally at 21 psia in the reactor. In the core, where the pressure ranges from 39.4 psia at the lower ends of the fuel channels to 33.5 psia at the upper ends, the equivalent volume fraction of gas is about 1.2%. For rapid changes in core or loop pressure, the mass ratio of gas to liquid remains practically constant and the volume fraction of gas in the core decreases with increasing pressure. For very slow increases in loop pressure the volume of gas in the core increases, because the ratio of absolute pressures between the core and pump suction is reduced. (The steady-state volume fraction at the pump suction is presumably independent of pressure.)

14.3.3 Effects on Reactivity

The presence of the gas in the core has two effects on reactivity. First, by making the fuel compressible, the gas introduces a pressure coefficient of fuel density or reactivity. Secondly, the presence of the gas modifies the fuel temperature coefficient of reactivity, because the density of the salt-gas mixture changes with temperature at a different rate from the density of the salt alone.

A detailed description of the reactivity effects of entrained gas involves the following quantities:

f	Volume fraction of gas in fuel stream at pump suction
P	Absolute pressure in the core
P_s	Absolute pressure at the pump suction
T	Temperature of the fuel in the core
θ	Volume fraction of gas in fuel in core
ρ_ℓ	Density of liquid salt containing no gas
ρ_f	Density of the fuel salt–gas mixture
$-\alpha = \frac{1}{\rho_\ell}\frac{\partial \rho_\ell}{\partial T}$	Temperature coefficient of salt density
$\beta = \frac{\rho_f}{k}\frac{\partial k}{\partial \rho_f}$	Fuel density coefficient of reactivity
$-\gamma$	Contribution to fuel temperature coefficient of reactivity due to changes in neutron energies and microscopic cross sections

The core pressure is related to the reactivity through the mean fuel density in the core:

$$\frac{1}{k}\frac{\partial k}{\partial P} = \beta \frac{1}{\rho_f}\frac{\partial \rho_f}{\partial P} . \tag{14.1}$$

The fuel temperature affects the reactivity through the fuel density and also through its effect on thermal neutron energy and microscopic cross sections:

$$\frac{1}{k}\frac{\partial k}{\partial T} = \beta \frac{1}{\rho_f}\frac{\partial \rho_f}{\partial T} - \gamma . \tag{14.2}$$

The mean density of the fuel is given by

$$\rho_f = (1 - \theta)\rho_\ell . \tag{14.3}$$

(The gas adds practically nothing to the fuel density.)

If there is no gas in the core, $\theta = 0$, $\rho_f = \rho_\ell$, and the effect of pressure on density is negligible. With no gas in the fuel,

$$\frac{1}{k}\frac{\partial k}{\partial T} = -\alpha\beta - \gamma \ .$$

Rapid Changes. – During rapid changes in pressure and temperature, the mass ratio of gas to liquid remains practically constant. (The change in the amount of dissolved helium is negligible compared with the amount in the gas phase.) In this case ρ_f is approximated by

$$\rho_f = \frac{[1 - \alpha(T - T_0)]\rho_{\ell 0}}{1 + \frac{P_0}{T_0}\left(\frac{\theta_0}{1 - \theta_0}\right)[1 - \alpha(T - T_0)]\frac{T}{P}} , \tag{14.4}$$

where the subscript 0 refers to initial conditions. If Eq. (14.4) is used to obtain the partial derivatives of ρ_f required in (14.1) and (14.2), these equations become

$$\frac{1}{k}\frac{\partial k}{\partial P} = \frac{\beta[1 - \alpha(T - T_0)]}{\left[1 - \alpha(T - T_0) + \left(\frac{1 - \theta_0}{\theta_0}\right)\frac{T_0}{T}\frac{P}{P_0}\right]P} \tag{14.5}$$

and

$$\frac{1}{k}\frac{\partial k}{\partial T} = \frac{-\alpha\beta}{1 - \alpha(T - T_0)} - \frac{\left(\frac{1}{T} - 2\alpha + \alpha\frac{T_0}{T}\right)\beta}{1 - \alpha(T - T_0) + \left(\frac{1 - \theta_0}{\theta_0}\right)\frac{T_0}{T}\frac{P}{P_0}} - \gamma \ . \tag{14.6}$$

At the initial point, when $P = P_0$ and $T = T_0$,

$$\frac{1}{k}\frac{\partial k}{\partial P} = \frac{\beta\theta_0}{P_0} \tag{14.7}$$

and

$$-\frac{1}{k}\frac{\partial k}{\partial T} = \alpha\beta + \gamma + \left(\frac{1}{T_0} - \alpha\right)\theta_0\beta \ . \tag{14.8}$$

These equations show that for rapid changes there is a positive pressure coefficient of reactivity and that the magnitude of the negative temperature coefficient of reactivity is increased because the gas expands more than the liquid ($1/T_0$ is greater than α).

Slow Changes. – During gradual changes in fuel loop temperatures and pressure, f will probably remain equal to the volume fraction in the pump

bowl just outside the ports, which should be constant. The core mean pressure is 15.6 psi higher than the pump suction pressure; therefore

$$\theta = f\,\frac{P_s}{P} = f\left(\frac{P - 15.6}{P}\right), \tag{14.9}$$

$$\rho_f = \left(1 - f + \frac{15.6f}{P}\,\rho_\ell\right). \tag{14.10}$$

If the partial derivatives of ρ_f required in Eqs. (14.1) and (14.2) are obtained from Eq. (14.10), Eqs. (14.1) and (14.2) become

$$\frac{1}{k}\frac{\partial k}{\partial P} = \frac{-\beta}{P + \left(\frac{1 - f}{f}\right)\frac{P^2}{15.6}} \tag{14.11}$$

and

$$\frac{1}{k}\frac{\partial k}{\partial T} = -\alpha\beta - \gamma\ . \tag{14.12}$$

Thus for slow changes, there is a negative pressure coefficient of reactivity and the temperature coefficient is the same as if there were no entrained gas.

Magnitude. – The magnitudes of pressure and temperature coefficients of reactivity with entrained gas in the core are listed in Table 14.3 for three different fuel salts, at the conditions listed at the bottom of the table.

Importance. – During normal operation, the presence of entrained gas introduces additional reactivity "noise" because its compressibility converts fluctuations in core outlet pressure drop to reactivity perturbations. In power excursions, the gas enhances the negative temperature coefficient of reactivity. At the same time it superimposes a pressure coefficient which makes a positive contribution to reactivity during at least part of the power excursion. (See Sec 12.4.3 for discussion of pressure behavior during power excursions.) In any credible power excursion, the pressure rise, in psi, is numerically much smaller than the fuel temperature rise, in °F, and the net reactivity feedback from pressure and temperature is negative.

Table 14.3. Reactivity Coefficients with Entrained Gas in Core[a]

	Fuel A	Fuel B	Fuel C
Fuel density coefficient of reactivity, β	0.190	0.345	0.182
$\alpha\beta[(°F)^{-1}]$	-2.24×10^{-5}	-4.07×10^{-5}	-2.15×10^{-5}
$\gamma[(°F)^{-1}]$	-0.79×10^{-5}	-0.90×10^{-5}	-1.13×10^{-5}
Fuel temperature coefficient of reactivity $[(°F)^{-1}]$			
No gas or slow changes with gas	-3.03×10^{-5}	-4.97×10^{-5}	-3.28×10^{-5}
Rapid changes with gas	-3.14×10^{-5}	-5.17×10^{-5}	-3.39×10^{-5}
Pressure coefficient of reactivity (psi^{-1})			
Slow changes with gas	-3.8×10^{-5}	-7.0×10^{-5}	-3.7×10^{-5}
Rapid changes with gas	$+6.3 \times 10^{-5}$	$+11.4 \times 10^{-5}$	$+6.0 \times 10^{-5}$

[a]Evaluated at T = 1200°F, P = 36.5 psia (pump bowl pressure 5 psig), θ = 0.012, and $\alpha = 1.2 \times 10^{-4}(°F)^{-1}$.

14.4 Choice of Poison Material

There is available a wide variety of materials that have been used as neutron absorbers in reactor control rods. The choice of poison material for a given reactor application must be based primarily on the overall suitability of the poison, considering the physical and chemical, as well as the nuclear, environment. If several acceptable materials exist, the choice between them may be made on the basis of cost and ease of procurement of the required form.

14.4.1 Boron

The first poison material considered for use in the MSRE was boron because of its low cost, ready availability, and high neutron-capture cross section in both the thermal and epithermal energy ranges.

The shape of the poison elements was established by the mechanical design of the rod assemblies, which required short, hollow cylinders of poison. Pure boron carbide (B_4C) was tentatively selected as the poison material, to ensure long rod life. This material could easily be fabricated in the desired shape and also have the stability against thermal decomposition required for use at reactor temperatures. However, B_4C is highly abrasive and oxidizes in air at high temperature. These properties made it necessary to consider complete canning of the poison elements.

Essentially all of the poisoning by B_4C is due to neutron absorptions in B^{10}, where the predominant reaction is $B^{10}(n,\alpha)Li^7$. The alpha particle ends as a helium atom, so that each neutron absorption results in the replacement of a single atom by two of approximately the same size. This effect alone would lead to significant damage, due to volume increase in the poison elements after long exposure. However, the difficulty is compounded, particularly in the case of canned elements, by the fact that one of the nuclear reaction products is a gas. Only a fraction of the helium produced escapes from the poison elements, but this fraction increases with increasing neutron exposure. In addition, the amount escaping cannot be predicted reliably. Therefore, to be conservative, all calculations of gas pressure buildup were based on the assumption that all of the gas escapes. Calculations of the helium production rate in the MSRE control rods indicated that the rod life would be severely limited by the pressure buildup in completely sealed poison capsules. Since it appeared infeasible to vent the capsules because of the oxidation problem, the use of B_4C was abandoned in favor of a more radiation-stable material.

14.4.2 Gadolinium

The poison material finally selected for use in the MSRE was gadolinium, fabricated in ceramic cylinders containing 70 wt % Gd_2O_3 and 30 wt % Al_2O_3. This material has satisfactory nuclear properties and was selected over other, equally suitable materials on the basis of its moderate cost, ready availability, and the fact that it could be used without additional development.

Natural gadolinium has two isotopes (155 and 157) with extremely large thermal neutron-capture cross sections; the average 2200 m/sec

cross section for natural gadolinium is 46,600 barns. However, the neutron-capture products of both isotopes are stable gadolinium isotopes with very low cross sections, so that the neutron-capture efficiency is very low, about 0.3 neutrons per atom of natural gadolinium. Gadolinium also has a relatively low capture cross section for resonance-energy neutrons (about one-fourth that of boron). Thus, for rods which are "black" to thermal neutrons, a boron-containing rod will control somewhat more reactivity than one containing gadolinium.

Because of the large cross section, only a small amount of gadolinium is required for "blackness" to thermal neutrons. However, this same property results in very rapid burnout of a rod that is initially just barely "black." Therefore, such a rod must have built into it sufficient gadolinium to ensure that it remains "black" throughout its required lifetime. The low neutron-capture efficiency requires relatively large amounts of gadolinium for this purpose.

The individual ceramic poison capsules on the MSRE control rods are 0.84 in. ID by 1.08 in. OD by 1.315 in. long. The elements contain about sixty times the concentration of gadolinium required for "blackness" to 1200°F thermal neutrons. This is sufficient to maintain "blackness" in those portions that are continuously exposed to the neutron flux for the equivalent of about 50,000 full-power hours.

Since the end products of neutron absorption in gadolinium are other isotopes of the same element, there is essentially no volume change associated with its exposure to neutron bombardment. As a result this material may be expected to have reasonable resistance to radiation damage; at least the problem of gas production associated with the irradiation of boron is avoided. Structural strength of the poison is of secondary importance, because the elements are completely canned. However, completely leak-proof canning is less important with Gd_2O_3 than with B_4C, because of the greater chemical stability of the former.

14.5 Criticality in Drain and Storage Tanks

Molten fuel salt with the uranium concentration required for criticality in the core is not critical in the drain tanks or the storage tank. This is so because there is much less moderator in the tanks than in the

core and the tanks are of smaller diameter than the core, and these effects outweigh the increased fuel volume fraction in the tanks.

Normally, when fuel salt is stored in either the drain tanks or the storage tank, it is kept in the molten state. However, under some conditions it may be desirable to allow the salt to solidify in a tank and cool to ambient temperature. Simply cooling the salt causes the reactivity to increase because of the increased density and cross sections. In addition, if the salt is cooled extremely slowly, it is possible for a nonuniform composition to develop, with the uranium tending to be more concentrated in the remaining melt as the slow freezing progresses. It is conceivable that slow freezing could begin at the outside surfaces, leading to a condition in which the uranium is all concentrated in a central region surrounded by a neutron-reflecting layer of barren salt. Some additional neutron reflection would occur if the cell containing the tank were flooded with water. (The effectiveness of the water reflector is limited by the furnace structure which surrounds each of the tanks.) Under such abnormal conditions, criticality in the tanks is not impossible.

In order to outline the limiting conditions for criticality in the tanks, some calculations were made with the multigroup neutron diffusion program MODRIC. Effective multiplication constants were calculated for fuels B and C in the drain and storage tanks, at 20°C, for various degrees for uranium segregation.[52] A major uncertainty in these calculations was the density of the salt. In the absence of experimental information, a conservative approximation was made by computing the density of the unsegregated salt from the x-ray densities of the components. (The actual density should be lower because the salt will not be a perfect crystal, and cracks and voids will probably develop as the frozen salt cools.) Calculations were made in both cylindrical and spherical geometry for the case of uniform concentration, with the size of the sphere chosen to give the same multiplication as in a cylinder having the actual dimensions of the tanks. Calculations were made in spherical geometry with the uranium concentrated by factors of 2, 4, and 10. In these cases, the uranium and a stoichiometric amount of fluorine were assumed to be uniformly dispersed

in a sphere surrounded by a layer of uranium-free salt. The concentrations of the other components were assumed to be uniform in both the fueled and unfueled portions.

The results of the calculations are shown graphically for the storage tank and a fuel drain tank in Figs. 14.3 and 14.4, respectively. If all other conditions are equal, the reactivity is higher in the storage tank than in a drain tank, because of the INOR coolant thimbles in the latter. In the reflected cases, a practically infinite (50 cm) H_2O reflector was assumed. This gives an overestimate of k_{eff}, since the effective reflector thickness must be less because of the furnace. The amount of overestimation is not great, however, as shown by the comparison of the curves for fuel B in the storage tank, bare and reflected. In one calculation the salt density was assumed to be 95% of the upper limit used in the other calculations. This was for the case of fuel B, concentrated by a factor of 10 in the reflected storage tank, and gave a k_{eff} of 1.003, compared with 1.024 for the higher density. Similar reductions might be expected for the other cases.

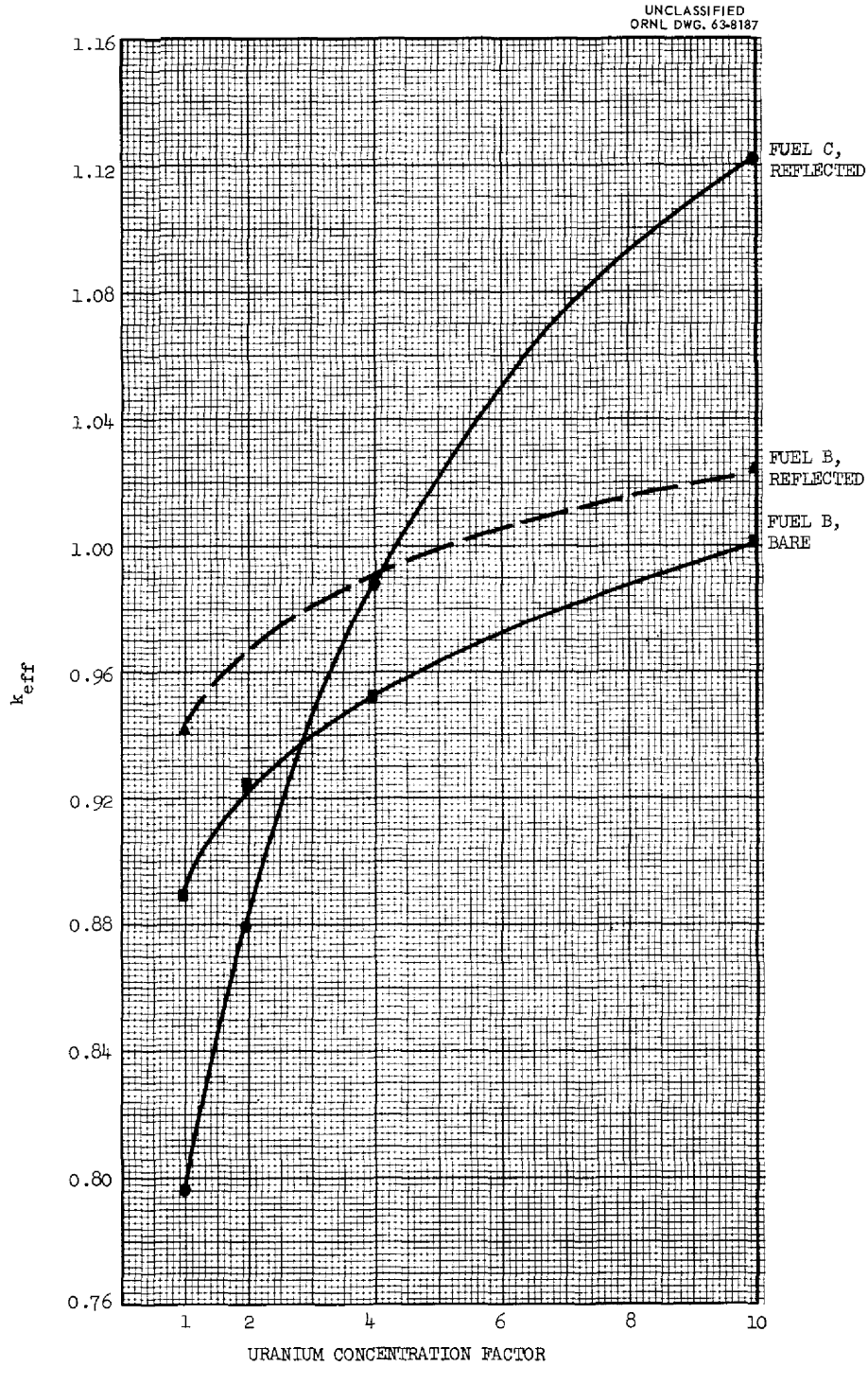

Fig. 14.3. Effect of Uranium Segregation on Criticality in Fuel Storage Tank at 20°C.

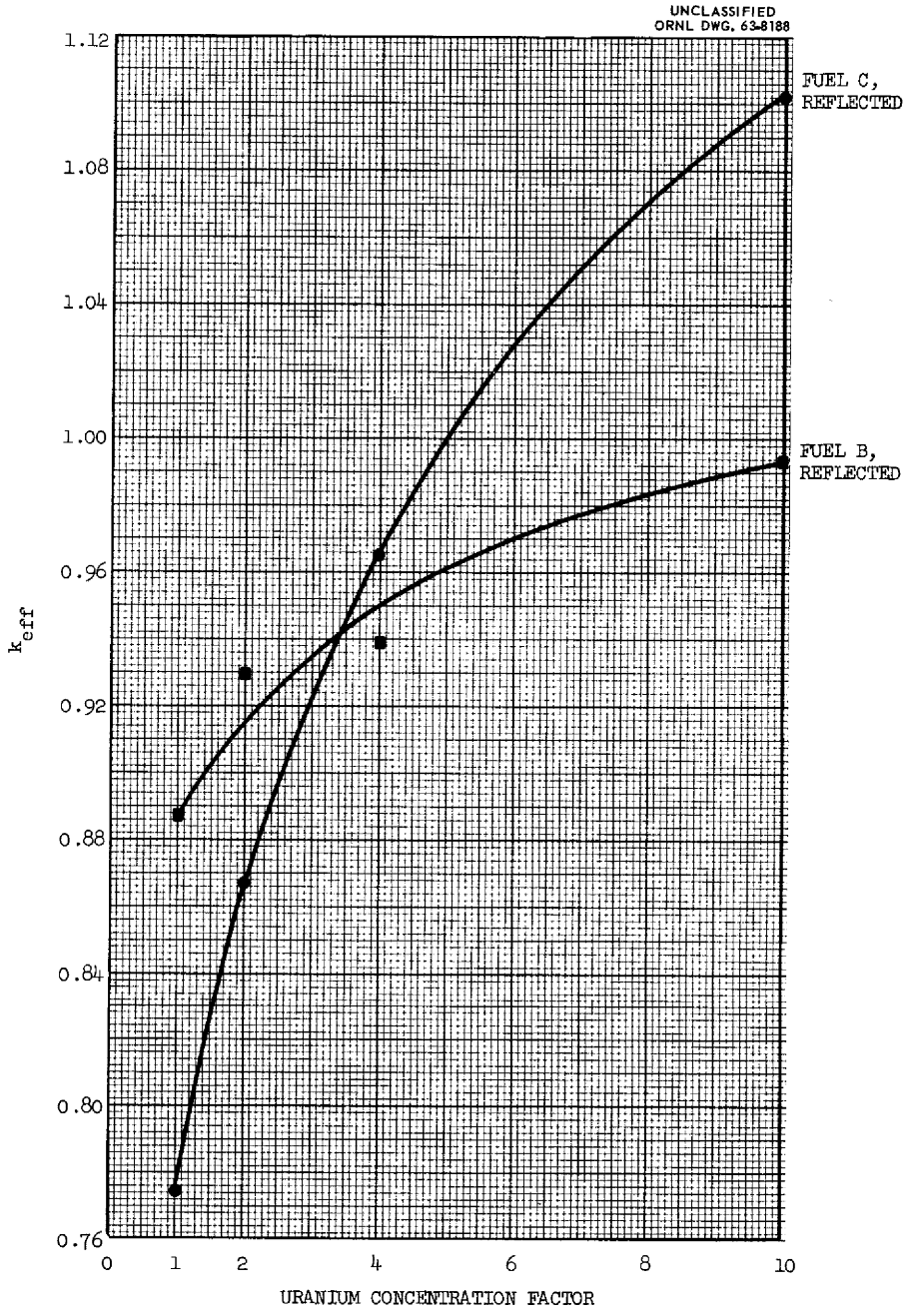

Fig. 14.4. Effect of Uranium Segregation on Criticality in Fuel Drain Tank at 20°C.

15. REFERENCES

1. C. L. Davis, J. M. Bookston, and B. E. Smith, "GNU-II – A Multigroup One-Dimensional Diffusion Program for the IBM-704," USAEC Report GMR-101, General Motors, November 12, 1957.

2. D. J. Hughes and R. B. Schwartz, "Neutron Cross Sections," USAEC Report BNL-325, Second Edition, Brookhaven National Laboratory, July 1958.

3. C. W. Nestor, Jr., "Multigroup Neutron Cross Sections," USAEC Report ORNL CF-60-3-35, Oak Ridge National Laboratory, March 1960.

4. Oak Ridge National Laboratory, "MSRP Quart. Progr. Rept. July 31, 1960," USAEC Report ORNL-3014, pp. 41–45.

5. C. W. Nestor, Jr., "A Computational Survey of Some Graphite-Moderated Molten Salt Reactors," USAEC Report ORNL CF-61-3-98, Oak Ridge National Laboratory, March 15, 1961.

6. Oak Ridge National Laboratory, "MSRP Progr. Rept. Aug. 1, 1960 to Feb. 28, 1961," USAEC Report ORNL-3122, p. 70.

7. Oak Ridge National Laboratory, "MSRP Progr. Rept. Mar. 1 to Aug. 31, 1961," USAEC Report ORNL-3215, pp. 83–89.

8. G. F. Kuncir, "A Program for the Calculation of Resonance Integrals," USAEC Report GA-2525, General Atomic, August 28, 1961.

9. G. I. Bell, "A Simple Treatment for Effective Resonance Absorption Cross Sections in Dense Lattices," Nucl. Sci. Eng., 5(2): 138–139 (February 1959).

10. G. D. Joanou and J. S. Dudek, "GAM-1: A Consistent P_1 Multigroup Code for the Calculation of Fast Neutron Spectra and Multigroup Constants," USAEC Report GA-1850, General Atomic, June 28, 1961.

11. H. C. Honeck, "THERMOS: A Thermalization Transport Theory Code for Reactor Lattice Calculations," USAEC Report BNL-5826, Brookhaven National Laboratory, September 1961.

12. D. E. Parks, J. R. Beyster, and N. F. Wikner, "Thermal Neutron Spectra in Graphite," Nucl. Sci. Eng., 13(4): 306–324 (August 1962).

13. James Replogle, "MODRIC: A One Dimensional Neutron Diffusion Code for the IBM-7090," USAEC Report K-1520, Union Carbide Nuclear Company, September 6, 1962.

14. T. B. Fowler and M. L. Tobias, "EQUIPOISE-3: A Two-Dimensional, Two-Group, Neutron Diffusion Code for the IBM-7090 Computer," USAEC Report ORNL-3199, Oak Ridge National Laboratory, February 7, 1962.

15. C. W. Nestor, Jr., "EQUIPOISE 3A," USAEC Report ORNL-3199 Addendum, Oak Ridge National Laboratory, June 6, 1962.

16. B. E. Prince and J. R. Engel, "Temperature and Reactivity Coefficient Averaging in the MSRE," USAEC Report ORNL TM-379, Oak Ridge National Laboratory, October 15, 1962.

17. G. H. Kear and M. H. Ruderman, "An Analysis of Methods of Control Rod Theory and Comparisons with Experiment," USAEC Report GEAP-3937, General Electric, May 27, 1962.

18. B. E. Prince, "Control Rod Worth in the MSRE," USAEC Report ORNL TM-___, Oak Ridge National Laboratory (in preparation).

19. R. V. Meghreblian and D. K. Holmes, Reactor Analysis, p. 656, McGraw-Hill, New York, 1960.

20. S. A. Kushneriuk and K. Jirlow, "The Linear Extrapolation Length and Blackness for Infinite Cylinders," J. Nucl. Energy, Pts. A and B, 16(9): 464–466 (September 1962).

21. J. R. Engel and P. N. Haubenreich, "Temperatures in the MSRE Core During Steady-State Power Operation," USAEC Report ORNL TM-378, Oak Ridge National Laboratory, November 5, 1962.

22. H. F. Poppendiek and L. D. Palmer, "Forced Convection Heat Transfer in Pipes with Volume Heat Sources Within the Fluids," USAEC Report ORNL-1395, Oak Ridge National Laboratory, December 2, 1952.

23. H. F. Poppendiek and L. D. Palmer, "Forced Convection Heat Transfer Between Parallel Plates and in Annuli with Volume Heat Sources Within the Fluids," USAEC Report ORNL-1701, Oak Ridge National Laboratory, May 21, 1954.

24. P. N. Haubenreich, "Prediction of Effective Yields of Delayed Neutrons in MSRE," USAEC Report ORNL TM-380, Oak Ridge National Laboratory, October 13, 1962.

25. Sidney Krasik, p. 8-4 in Nuclear Engineering Handbook, edited by Harold Etherington, McGraw-Hill, New York, 1958.

26. H. Goldstein, Fundamental Aspects of Reactor Shielding, p. 52, Addison-Wesley, Reading, Mass., 1959.

27. H. S. Weber, Oak Ridge National Laboratory, unpublished data.

28. B. E. Prince, "Methods of Computing the Reactivity Effects of Distributed Xenon, Graphite Shrinkage, and Fuel Soakup in the MSRE," USAEC Report ORNL TM-496, Oak Ridge National Laboratory (in preparation).

29. E. A. Nephew, "Thermal and Resonance Absorption Cross Sections of the U^{233}, U^{235}, and Pu^{239} Fission Products," USAEC Report ORNL-2869, Oak Ridge National Laboratory, January 18, 1960.

30. T. R. England, "Time-Dependent Fission-Product Thermal and Resonance Absorption Cross Sections," USAEC Report WAPD-TM-333, Bettis Atomic Power Laboratory, November 1962.

31. C. W. Nestor, "A Simple Formula for Computing Fission Product Thermal Cross Sections and Resonance Integrals," USAEC Report ORNL CF-60-4-30, Oak Ridge National Laboratory, April 7, 1960.

32. D. R. Harris, "Calculation of the Background Neutron Source in New, Uranium-Fueled Reactors," USAEC Report WAPD-TM-220, Bettis Atomic Power Laboratory, March 1960.

33. P. N. Haubenreich, "Inherent Neutron Sources in Clean MSRE Fuel Salt," USAEC Report ORNL TM-611, Oak Ridge National Laboratory, August 27, 1963.

34. J. O. Blomeke and M. F. Todd, "Uranium-235 Fission-Product Production as a Function of Thermal Neutron Flux, Irradiation Time, and Decay Time," USAEC Report ORNL-2127, Oak Ridge National Laboratory, August 19, 1957.

35. P. N. Haubenreich, J. R. Engel, and B. E. Prince, "MSRE Neutron Source Requirements," USAEC Report ORNL TM-___, Oak Ridge National Laboratory (in preparation).

36. C. W. Nestor, Jr., "MURGATROYD - An IBM 7090 Program for the Analysis of the Kinetics of the MSRE," USAEC Report ORNL TM-203, Oak Ridge National Laboratory, April 6, 1962.

37. C. W. Nestor, Jr., "ZORCH - An IBM 7090 Program for the Analysis of Simulated MSRE Power Transients with a Simplified Space-Dependent Kinetics Model," USAEC Report ORNL TM-345, Oak Ridge National Laboratory, September 18, 1962.

38. P. R. Kasten, "Operational Safety of the Homogeneous Reactor Test," USAEC Report ORNL-2088, Oak Ridge National Laboratory, July 3, 1956.

39. P. N. Haubenreich and J. R. Engel, "Safety Calculations for MSRE," USAEC Report ORNL TM-251, Oak Ridge National Laboratory, May 15, 1962.

40. J. R. Engel, P. N. Haubenreich, and S. J. Ball, "Analysis of Filling Accidents in MSRE," USAEC Report ORNL TM-497, Oak Ridge National Laboratory (in preparation).

41. D. W. Vroom, "Preliminary MSRE Gamma Ray Source and Biological Shielding Survey," USAEC Report ORNL CF-61-4-97, Oak Ridge National Laboratory, April 28, 1961.

42. T. Rockwell, Reactor Shielding Design Manual, Van Nostrand, New York, 1956.

43. H. Goldstein, Fundamental Aspects of Reactor Shielding, p. 60, Addison-Wesley, Reading, Mass., 1959.

44. D. J. Hughes and R. B. Schwartz, "Neutron Cross Sections," USAEC Report BNL-325, Brookhaven National Laboratory, July 1, 1958.

45. C. W. Nestor, Jr., Oak Ridge National Laboratory, unpublished data, May 1961.

46. E. P. Blizard, "Neutron Radiation Shielding," ORNL publication for ORSORT text, September 17, 1956.

47. E. Troubetzkoy and H. Goldstein, "Gamma Rays from Thermal Neutron Capture," Nucleonics, 18(11): 171–173 (November 1960).

48. P. N. Haubenreich and B. E. Prince, Oak Ridge National Laboratory, personal communication to H. C. Claiborne, Oak Ridge National Laboratory.

49. M. L. Tobias, D. R. Vondy, and Marjorie P. Lietzke, "Nightmare — An IBM 7090 Code for the Calculation of Gamma Heating in Cylindrical Geometry," USAEC Report ORNL-3198, Oak Ridge National Laboratory, February 9, 1962.

50. Oak Ridge National Laboratory, "MSRP Semiann. Progr. Rept. Feb. 28, 1962," USAEC Report ORNL-3282, pp. 68–71.

51. S. E. Moore, Oak Ridge National Laboratory, personal communication to R. B. Briggs, Oak Ridge National Laboratory (April 26, 1962).

52. J. R. Engel and B. E. Prince, "Criticality Factors in MSRE Fuel Storage and Drain Tanks," USAEC Report ORNL TM-___, Oak Ridge National Laboratory (in preparation).

INTERNAL DISTRIBUTION

1-2. Central Research Library
3-4. ORNL – Y-12 Technical Library
Document Reference Section
5-6. Reactor Division Library
7-9. Laboratory Records Department
10. Laboratory Records, ORNL R.C.
11. R. G. Affel
12. L. G. Alexander
13. C. F. Baes
14. S. E. Beall
15. M. Bender
16. E. S. Bettis
17. F. F. Blankenship
18. R. Blumberg
19. R. B. Briggs
20. S. Cantor
21. H. C. Claiborne
22. J. A. Conlin
23. W. H. Cook
24. L. T. Corbin
25. G. A. Cristy
26. J. L. Crowley
27. J. H. DeVan
28. S. J. Ditto
29. R. G. Donnelly
30. N. E. Dunwoody
31. J. R. Engel
32. E. P. Epler
33. J. H Frye
34. R. B. Gallaher
35. W. R. Grimes
36. A. G. Grindell
37. R. H. Guymon
38. P. H. Harley
39-48. P. N. Haubenreich
49. E. C. Hise
50. P. P. Holz
51. J. P. Jarvis
52. R. J. Kedl
53. S. S. Kirslis
54. J. W. Krewson
55. J. A. Lane
56. C. E. Larson
57. R. B. Lindauer
58. M. I. Lundin
59. R. N. Lyon
60. H. G. MacPherson
61. W. B. McDonald
62. H. F. McDuffie
63. C. K. McGlothlan
64. W. R. Mixon
65. R. L. Moore
66. P. Patriarca
67. H. R. Payne
68. A. M. Perry
69. B. E. Prince
70. J. L. Redford
71. M. Richardson
72. R. C. Robertson
73. M. W. Rosenthal
74. H. W. Savage
75. J. E. Savolainen
76. D. Scott
77. J. H. Shaffer
78. M. J. Skinner
79. A. N. Smith
80. P. G. Smith
81. I. Spiewak
82. J. A. Swartout
83. A. Taboada
84. J. R. Tallackson
85. R. E. Thoma
86. D. B. Trauger
87. W. C. Ulrich
88. C. F. Weaver
89. H. S. Weber
90. B. H. Webster
91. A. M. Weinberg
92. J. C. White
93. L. V. Wilson

EXTERNAL DISTRIBUTION

94-95. D. F. Cope, Reactor Division, AEC, ORO
96. R. L. Philippone, Reactor Division, AEC, ORO
97. H. M. Roth, Research and Development Division, AEC, ORO
98. W. L. Smalley, Reactor Division, AEC, ORO
99. M. J. Whitman, Atomic Energy Commission, Washington
100-114. Division of Technical Information Extension, AEC, ORO